NAVAL POSTGRADUATE SCHOOL
Monterey, California

THESIS

S2436

MONTEREY BAY ACOUSTIC TOMOGRAPHY:
SIGNAL PROCESSING USING
MULTI-CHANNEL DATA-SYNCHRONIZED
QUADRATURE PHASE DEMODULATION

by

Kevin P. Schaaff

September 1989

Thesis Advisor: James H. Miller

Approved for public release; distribution is unlimited.

REPORT DOCUMENTATION PAGE

1a Report Security Classification: Unclassified	1b Restrictive Markings
2a Security Classification Authority	3 Distribution Availability of Report: Approved for public release; distribution is unlimited
2b Declassification/Downgrading Schedule	
4 Performing Organization Report Number(s)	5 Monitoring Organization Report Number(s)
6a Name of Performing Organization: Naval Postgraduate School; 6b Office Symbol (If Applicable): 62Mr	7a Name of Monitoring Organization: Naval Postgraduate School
6c Address (city, state, and ZIP code): Monterey, CA 93943-5000	7b Address (city, state, and ZIP code): Monterey, CA 93943-5000
8a Name of Funding/Sponsoring Organization; 8b Office Symbol (If Applicable)	9 Procurement Instrument Identification Number
8c Address (city, state, and ZIP code)	10 Source of Funding Numbers: Program Element Number; Project No; Task No; Work Unit Accession No

11 Title (Include Security Classification) MONTEREY BAY ACOUSTIC TOMOGRAPHY: SIGNAL PROCESSING USING MULTI-CHANNEL DATA-SYNCHRONIZED QUADRATURE PHASE DEMODULATION

12 Personal Author(s) Kevin P. Schaaff

13a Type of Report	13b Time Covered	14 Date of Report (year, month, day)	15 Page Count
Master's Thesis	From To	September 1989	257

16 Supplementary Notation The views expressed in this thesis are those of the author and do not reflect the official policy or position of the Department of Defense or the U.S. Government.

17 Cosati Codes			18 Subject Terms (continue on reverse if necessary and identify by block number)
Field	Group	Subgroup	acoustic tomography, quadrature phase demodulator, maximal-length sequences, internal waves, surface wave spectra

19 Abstract (continue on reverse if necessary and identify by block number)

An ocean acoustic tomography experiment was conducted in Monterey Bay from December 12-16, 1988 and had the following goals: 1) validate theories describing the relationship between acoustic travel time fluctuations and ocean waves, both surface and internal , 2) determine the effects of the complex bathymetry of Monterey Bay Submarine Canyon on acoustic propagation, and 3) test the first shore-based acoustic tomography data acquisition system. This thesis developed a multi-channel data-synchronized quadrature phase demodulator for pre-processing the acoustic data. The demodulator fed the resulting baseband signals to a Zenith personal computer equipped with an A/D board for further processing. Preliminary results of the data analysis for one of the receiving stations is given to demonstrate the system effectiveness.

20 Distribution/Availability of Abstract	21 Abstract Security Classification	
[X] unclassified/unlimited [ ] same as report [ ] DTIC users	Unclassified	
22a Name of Responsible Individual: James H. Miller	22b Telephone (Include Area code): (408) 646-2384	22c Office Symbol: 62Mr

DD FORM 1473, 84 MAR 83 APR edition may be used until exhausted
All other editions are obsolete

T246007
T246008

Approved for public release; distribution is unlimited.

MONTEREY BAY ACOUSTIC TOMOGRAPHY: SIGNAL PROCESSING USING MULTI-CHANNEL DATA-SYNCHRONIZED QUADRATURE PHASE DEMODULATION

by

Kevin P. Schaaff
Lieutenant, United States Navy
B.S., United States Naval Academy, 1981

Submitted in partial fulfillment
of the requirements for the degree of

MASTER OF SCIENCE IN ENGINEERING ACOUSTICS

and

MASTER OF SCIENCE IN APPLIED SCIENCE

from the

NAVAL POSTGRADUATE SCHOOL
September 1989

ABSTRACT

An ocean acoustic tomography experiment was conducted in Monterey Bay from December 12-16, 1988 and had the following goals: 1) validate theories describing the relationship between acoustic travel time fluctuations and ocean waves, both surface and internal, 2) determine the effects of the complex bathymetry of Monterey Bay Submarine Canyon on acoustic propagation, and 3) test the first shore-based acoustic tomography data acquisition system. This thesis developed a multi-channel data-synchronized quadrature phase demodulator for pre-processing the acoustic data. The demodulator fed the resulting baseband signals to a Zenith personal computer equipped with an A/D board for further processing. Preliminary results of the data analysis for one of the receiving stations is given to demonstrate the system effectiveness.

Thesis
S2436
C.1

TABLE OF CONTENTS

I. INTRODUCTION 1
A. THESIS OVERVIEW 1

II. BACKGROUND 4
A. OCEAN ACOUSTIC TOMOGRAPHY 4
1. General Description 4
2. Signal Processing 6
a. Signal Propagation 6
b. Signal Design 8
(1) Resolution. 8
(2) Response. 8
(3) Modulation. 10
(4) Arrival Time Error. 10
c. Signal Parameters 10
B. MONTEREY BAY ACOUSTIC TOMOGRAPHY EXPERIMENT . . 11
1. General Overview 11
a. Source and Receiver Placement 19
2. Signal Processing 19

III. DEMODULATOR DESIGN 26
A. MULTI-CHANNEL DATA-SYNCHRONIZED QUADRATURE PHASE DEMODULATOR 26
1. General description 26
2. Schematic 29
3. Timing Channel 29
a. Phase Locked Loop 29
b. RS-232 35
c. Monostable Multivibrator 36
d. Counters 37

(1) Divide by 16. 37
(2) Divide by 7. 37
(3) Invertor. 37
(4) Divide by 2. 38
e. Timer 38
f. Low Pass Filter 39
(1) Butterworth Filter 40
(2) VCVS Filter 44
g. Buffer Amplifier 44
4. Data Channel 45
a. Preamplifier 45
b. Bandpass Filter 46
(1) State-Variable Filter. 48
c. Multiplier 48
d. Low Pass Filter 49
(1) Phase Response. 50
5. Power Supply 50
a. Power Requirements 50
(1) +5 Volt DC Power Supply. 55
(2) ± 15 Volt DC Power Supply. . . . 55
(3) ± 12 Volt DC Power Supply. . . . 55

IV. PERFORMANCE 56
A. SPECIFICATIONS 56
1. Input Specifications 56
2. Output Specifications 56
B. TESTING OVERVIEW 56
C. TEST RESULTS 57
1. Timing Channel 57
2. Data Channel 57
D. RELIABILITY 57
1. Mean Time Between Failures 57
E. DIMENSIONS 57
F. COST 57

V. DATA PROCESSING 58
A. GENERAL SUMMARY OF THE DATA 58
1. Acoustic Data 58
2. Surface Wave Data 59
3. Sound Speed Profile and Current Measurements 59
B. STATION L DATA 59
1. Station L Eigenray Prediction 59
2. Measured Sound Speed Profiles 60
3. Received Acoustic Signal 64
4. Travel Time Fluctuations 64
C. ANALYSIS OF ARRIVAL TIME FLUCTUATIONS AT SURFACE WAVE FREQUENCIES 65
D. ANALYSIS OF ARRIVAL TIME FLUCTUATIONS AT INTERNAL WAVE FREQUENCIES 72

VI. CONCLUSIONS AND RECOMMENDATIONS 85
A. CONCLUSIONS 85
1. Signal Processing Objectives 85
2. Tomography Experiment Objectives 85
B. RECOMMENDATIONS 86
1. Design Changes 86
a. Carrier Frequency 86
b. Bandwidth 86
c. Timing Channel 86
d. Data Channel 87

APPENDIX A. MAXIMAL-LENGTH SEQUENCES 88
A. MAXIMAL LENGTH SHIFT-REGISTER SEQUENCE 88
1. Properties 88
a. Periodic Property 88
b. Balance Property 88
c. Pseudo-Random Property 88
(1) Amplitude Modulation. 90

APPENDIX B. SCHEMATIC 92

APPENDIX C. VCR-PCM SPECIFICATIONS 99
A. VCR/PCM SPECIFICATIONS 99
1. General 99

APPENDIX D. ADDITIONAL DATA FOR STATION L 100
A. MATCHED-FILTERED ACOUSTIC SIGNAL 100
B. ARRIVAL TIME ESTIMATES 148
C. MATLAB PROGRAMS 221
1. Arrest1 221
2. Varloop2 221
3. Perturb 222
4. Pwrspec1 222

LIST OF REFERENCES 223

INITIAL DISTRIBUTION LIST 225

LIST OF TABLES

Table 1: Signal parameters for various acoustic tomography experiments [from Ref. 4]. . . . 12

LIST OF FIGURES

Figure 1: Top view of source and receiver pairs from the 1981 Bermuda Experiment. Each slice may contain on the order of ten eigenrays connecting each source and receiver pair.[from Ref.3] . . . 5

Figure 2: Comparison of arrivals for resolved and unresolvable pulses. 9

Figure 3: Monterey Bay Acoustic Tomography Experiment 12-16 December 1988. 13

Figure 4: Monterey Bay showing the positions of the transmitter and receivers. The transmitter is at station A, all others are receivers. . 14

Figure 5: 224 Hz resonant tomography signal transmitter 16

Figure 6: Modified AN/SSQ-57 sonobuoy. 17

Figure 7: Sonobuoy data recording system located in the van. This system receives the sonobuoy radio transmission, converts it to analog sound, and then records it on videotape using pulse code modulation. 18

Figure 8: The low-pass spectrum $X_{LP}(f)$ and the band-pass spectrum $X_{BP}(f)$ which do not overlap [from Ref.13]. 22

Figure 9: Quadrature demodulation of input band-pass signal [from Ref. 13]. 24

Figure 10: Diagram of signal processing performed by control program AMORE after tomography signal enters computer. 25

Figure 11: Diagram of acoustic tomography signal processing system. 27

Figure 12: Block diagram of Multi-channel, Data Synchronized, Quadrature Phase Demodulator timing channel. 28
Figure 13: Block Diagram of Multi-channel, Data Synchronous, Quadrature Phase Demodulator data channel (x4). 30
Figure 14: Phase-locked loop. 31
Figure 15: Type I, Exclusive-OR-gate phase detector [from Ref. 14]. 32
Figure 16: Lag-lead filter [from Ref. 14]. 34
Figure 17: Phase-locked loop. 35
Figure 18: Monostable multivibrator. 36
Figure 19: Divide by 16 counters. 38
Figure 20: Divide by 7 counter. 39
Figure 21: Invert and divide by 2 circuit. 40
Figure 22: Timer circuit. 41
Figure 23: Ideal low-pass filter amplitude and phase response. 42
Figure 24: Amplitude and phase response for varying orders of butterworth filters. 43
Figure 25: Fourth order VCVS low-pass filter. 45
Figure 26: Data channel preamplifier. 46
Figure 27: Single, second-order stage of band-pass filter. 47
Figure 28: State-variable active filter normalized to 1 ohm and 1 rad/s. 49
Figure 29: Phase response comparison of Butterworth, Chebyshev, and Elliptic band-pass filters. . 51
Figure 30: Phase response comparison of various order Butterworth band-pass filters. 52
Figure 31: Multiplier circuit. 53
Figure 32: Low-pass filter phase response comparison of Butterworth, Chebyshev, and Elliptic. . . . 54
Figure 33: ± 12 V power supply. 55

Figure 34: Monterey Bay, Station L, deep water sound velocity profile taken at position 36°32.906N-122°16.210W. 61
Figure 35: Monterey Bay, Station L, shallow water sound velocity profile taken at position 36°51.095N-122°04.798W. 62
Figure 36: Two-dimensional eigenray path for Station L predicted using MPP.[from Ref.5] 63
Figure 37: Received acoustic signal after matched-filtering for maximal-length sequence from Station L, 14Dec88 1805 to 1859 PST. Each line is 31 seconds of data coherently averaged to one 1.9375 second period. 66
Figure 38: Received acoustic signal after matched-filtering for maximal-length sequence from Station L, 14Dec88 1907 to 2001 PST. . 67
Figure 39: Arrival time estimate for Station L, 14Dec88 1824 to 1924 PST. The fast fluctuations in arrival time are due to surface waves changing the path length. 68
Figure 40: Arrival time estimate for Station L, 14Dec88 1924 to 2024. The fast fluctuations are due to the surface waves changing the path length. 69
Figure 41: Arrival time power spectrum for Station L. Spectrum from arrival time series, 1824 to 2024 14Dec88 PST. 70
Figure 42: Surface wave power spectrum in Monterey Bay.. 71
Figure 43: Arrival time perturbation data, Station L 1100-1700 PST 13Dec88, low-pass filtered to .00258 Hz (periods > 6.4 minutes). 74
Figure 44: Arrival time perturbation data, Station L 1600-2300 PST 13Dec88, low-pass filtered to .00258 Hz (periods > 6.4 minutes). 75

Figure 45: Arrival time perturbation data, Station L 1900-2400 PST 13Dec88, low-pass filtered to .00258 Hz (periods > 6.4 minutes). 76
Figure 46: Arrival time perturbation data, Station L 0000-0500 PST 14Dec88, low-pass filtered to .00258 Hz (periods > 6.4 minutes). 77
Figure 47: Arrival time perturbation data, Station L 0400-1100 PST 14Dec88, low-pass filtered to .00258 Hz (periods > 6.4 minutes). 78
Figure 48: Arrival time perturbation data, Station L 1000-1700 PST 14Dec88, low-pass filtered to .00258 Hz (periods > 6.4 minutes). 79
Figure 49: Arrival time perturbation data, Station L 1600-2200 PST 14Dec88, low-pass filtered to .00258 Hz (periods > 6.4 minutes). 80
Figure 50: Arrival time perturbation data, Station L 0000-0400 PST 15Dec88, low-pass filtered to .00258 Hz (periods > 6.4 minutes). 81
Figure 51: Arrival time perturbation data, Station L 0400-0800 PST 15Dec88, low-pass filtered to .00258 Hz (periods > 6.4 minutes). 82
Figure 52: Arrival time perturbation data, Station L 0930-1330 PST 15Dec88, low-pass filtered to .00258 Hz (periods > 6.4 minutes). 83
Figure 53: Arrival time perturbation data, Station L 1600-2200 PST 15Dec88, low-pass filtered to .00258 Hz (periods > 6.4 minutes). 84
Figure 54: Autocorrelation of M-sequence. 89
Figure 55: Binary shift register for generating a fifth order M-Sequence. 90
Figure 56: Tomographic signal, coherently averaged 16 times then magnitude squared. Station L, 1048 to 1042 13Dec88. 100

Figure 57: Tomographic signal, coherently averaged 16 times then magnitude squared. Station L, 1154 to 1248 13Dec88. 101
Figure 58: Tomographic signal, coherently averaged 16 times then magnitude squared. Station L, 1254 to 1348 13Dec88. 102
Figure 59: Tomographic signal, coherently averaged 16 times then magnitude squared. Station L, 1354 to 1448 13Dec88. 103
Figure 60: Tomographic signal, coherently averaged 16 times then magnitude squared. Station L, 1500 to 1554 13Dec88. 104
Figure 61: Tomographic signal, coherently averaged 16 times then magnitude squared. Station L, 1600 to 1654 13Dec88. 105
Figure 62: Tomographic signal, coherently averaged 16 times then magnitude squared. Station L, 1636 to 1730 13Dec88. 106
Figure 63: Tomographic signal, coherently averaged 16 times then magnitude squared. Station L, 1736 to 1830 13Dec88. 107
Figure 64: Tomographic signal, coherently averaged 16 times then magnitude squared. Station L, 1842 to 1936 13Dec88. 108
Figure 65: Tomographic signal, coherently averaged 16 times then magnitude squared. Station L, 1949 to 2036 13Dec88. 109
Figure 66: Tomographic signal, coherently averaged 16 times then magnitude squared. Station L, 2049 to 2136 13Dec88. 110
Figure 67: Tomographic signal, coherently averaged 16 times then magnitude squared. Station L, 2148 to 2242 13Dec88. 111

Figure 68: Tomographic signal, coherently averaged 16 times then magnitude squared. Station L, 2218 to 2312 13Dec88. 112
Figure 69: Tomographic signal, coherently averaged 16 times then magnitude squared. Station L, 2324 13 Dec88 to 0018 14Dec88. 113
Figure 70: Tomographic signal, coherently averaged 16 times then magnitude squared. Station L, 0024 to 0118 14Dec88. 114
Figure 71: Tomographic signal, coherently averaged 16 times then magnitude squared. Station L, 0124 to 0218 14Dec88. 115
Figure 72: Tomographic signal, coherently averaged 16 times then magnitude squared. Station L, 0230 to 0324 14Dec88. 116
Figure 73: Tomographic signal, coherently averaged 16 times then magnitude squared. Station L, 0418 to 0518 14Dec88. 117
Figure 74: Tomographic signal, coherently averaged 16 times then magnitude squared. Station L, 0518 to 0618 14Dec88. 118
Figure 75: Tomographic signal, coherently averaged 16 times then magnitude squared. Station L, 0624 to 0724 14Dec88. 119
Figure 76: Tomographic signal, coherently averaged 16 times then magnitude squared. Station L, 0724 to 0824 14Dec88. 120
Figure 77: Tomographic signal, coherently averaged 16 times then magnitude squared. Station L, 0824 to 0924 14Dec88. 121
Figure 78: Tomographic signal, coherently averaged 16 times then magnitude squared. Station L, 0924 to 1024 14Dec88. 122

Figure 79: Tomographic signal, coherently averaged 16 times then magnitude squared. Station L, 1024 to 1124 14Dec88. 123
Figure 80: Tomographic signal, coherently averaged 16 times then magnitude squared. Station L, 1124 to 1218 14Dec88. 124
Figure 81: Tomographic signal, coherently averaged 16 times then magnitude squared. Station L, 1224 to 1318 14Dec88. 125
Figure 82: Tomographic signal, coherently averaged 16 times then magnitude squared. Station L, 1330 to 1424 14Dec88. 126
Figure 83: Tomographic signal, coherently averaged 16 times then magnitude squared. Station L, 1430 to 1524 14Dec88. 127
Figure 84: Tomographic signal, coherently averaged 16 times then magnitude squared. Station L, 1530 to 1624 14Dec88. 128
Figure 85: Tomographic signal, coherently averaged 16 times then magnitude squared. Station L, 1703 to 1757 14Dec88. 129
Figure 86: Tomographic signal, coherently averaged 16 times then magnitude squared. Station L, 2109 to 2103 14Dec88. 130
Figure 87: Tomographic signal, coherently averaged 16 times then magnitude squared. Station L, 2257 to 2351 14Dec88. 131
Figure 88: Tomographic signal, coherently averaged 16 times then magnitude squared. Station L, 0203 to 0257 15Dec88. 132
Figure 89: Tomographic signal, coherently averaged 16 times then magnitude squared. Station L, 0330 to 0424 15Dec88. 133

Figure 90: Tomographic signal, coherently averaged 16 times then magnitude squared. Station L, 0359 to 0459 15Dec88. 134
Figure 91: Tomographic signal, coherently averaged 16 times then magnitude squared. Station L, 0501 to 0601 15Dec88. 135
Figure 92: Tomographic signal, coherently averaged 16 times then magnitude squared. Station L, 0603 to 0703 15Dec88. 136
Figure 93: Tomographic signal, coherently averaged 16 times then magnitude squared. Station L, 0705 to 0805 15Dec88. 137
Figure 94: Tomographic signal, coherently averaged 16 times then magnitude squared. Station L, 0807 to 0907 15Dec88. 138
Figure 95: Tomographic signal, coherently averaged 16 times then magnitude squared. Station L, 0951 to 1045 15Dec88. 139
Figure 96: Tomographic signal, coherently averaged 16 times then magnitude squared. Station L, 1053 to 1147 15Dec88. 140
Figure 97: Tomographic signal, coherently averaged 16 times then magnitude squared. Station L, 1155 to 1249 15Dec88. 141
Figure 98: Tomographic signal, coherently averaged 16 times then magnitude squared. Station L, 1257 to 1351 15Dec88. 142
Figure 99: Tomographic signal, coherently averaged 16 times then magnitude squared. Station L, 1359 to 1453 15Dec88. 143
Figure 100: Tomographic signal, coherently averaged 16 times then magnitude squared. Station L, 1501 to 1555 15Dec88. 144

Figure 101: Tomographic signal, coherently averaged 16 times then magnitude squared. Station L, 1702 to 1756 15Dec88. 145
Figure 102: Tomographic signal, coherently averaged 16 times then magnitude squared. Station L, 1804 to 1858 15Dec88. 146
Figure 103: Tomographic signal, coherently averaged 16 times then magnitude squared. Station L, 1906 to 2000 15Dec88. 147
Figure 104: Arrival time estimate for Station L from 1100 to 1200 PST 13Dec88. The fast fluctuations in the arrival time are caused by surface waves changing the path length. 148
Figure 105: Arrival time estimate for Station L from 1200 to 1312 PST 13Dec88. The fast fluctuations in the arrival times are caused by surface waves changing the path length. 149
Figure 106: Arrival time estimate for Station L from 1312 to 1406 PST 13Dec88. The fast fluctuations in the arrival times are caused by surface waves changing the path length. 150
Figure 107: Arrival time estimate for Station L from 1200 to 1312 PST 13Dec88. The fast fluctuations in the arrival times are caused by surface waves changing the path length. 151
Figure 108: Arrival time estimate for Station L from 1624 to 1700 PST 13Dec88. The fast fluctuations in the arrival times are caused by surface waves changing the path length. 152

Figure 109: Arrival time estimate for Station L from 1748 to 1848 PST 13Dec88. The fast fluctuations in the arrival times are caused by surface waves changing the path length. 153
Figure 110: Arrival time estimate for Station L from 1854 to 1954 PST 13Dec88. The fast fluctuations in the arrival times are caused by surface waves changing the path length. 154
Figure 111: Arrival time estimate for Station L from 2000 to 2100 PST 13Dec88. The fast fluctuations in the arrival times are caused by surface waves changing the path length. 155
Figure 112: Arrival time estimate for Station L from 2112 to 2206 PST 13Dec88. The fast fluctuations in the arrival times are caused by surface waves changing the path length. 156
Figure 113: Arrival time estimate for Station L from 2209 to 2224 PST 13Dec88. The fast fluctuations in the arrival times are caused by surface waves changing the path length. 157
Figure 114: Arrival time estimate for Station L from 0424 to 0524 PST 14Dec88. The fast fluctuations in the arrival times are caused by surface waves changing the path length. 158

Figure 115: Arrival time estimate for Station L from 0536 to 0630 PST 14Dec88. The fast fluctuations in the arrival times are caused by surface waves changing the path length. 159
Figure 116: Arrival time estimate for Station L from 0636 to 0736 PST 14Dec88. The fast fluctuations in the arrival times are caused by surface waves changing the path length. 160
Figure 117: Arrival time estimate for Station L from 0748 to 0848 PST 14Dec88. The fast fluctuations in the arrival times are caused by surface waves changing the path length. 161
Figure 118: Arrival time estimate for Station L from 0848 to 0948 PST 14Dec88. The fast fluctuations in the arrival times are caused by surface waves changing the path length. 162
Figure 119: Arrival time estimate for Station L from 0954 to 1024 PST 14Dec88. The fast fluctuations in the arrival times are caused by surface waves changing the path length. 163
Figure 120: Arrival time estimate for Station L from 1036 to 1136 PST 14Dec88. The fast fluctuations in the arrival times are caused by surface waves changing the path length. 164

Figure 121: Arrival time estimate for Station L from 1136 to 1236 PST 14Dec88. The fast fluctuations in the arrival times are caused by surface waves changing the path length. 165
Figure 122: Arrival time estimate for Station L from 1248 to 1348 PST 14Dec88. The fast fluctuations in the arrival times are caused by surface waves changing the path length. 166
Figure 123: Arrival time estimate for Station L from 1348 to 1448 PST 14Dec88. The fast fluctuations in the arrival times are caused by surface waves changing the path length. 167
Figure 124: Arrival time estimate for Station L from 1500 to 1554 PST 14Dec88. The fast fluctuations in the arrival times are caused by surface waves changing the path length. 168
Figure 125: Arrival time estimate for Station L from 1557 to 1612 PST 14Dec88. The fast fluctuations in the arrival times are caused by surface waves changing the path length. 169
Figure 126: Arrival time estimate for Station L from 1612 to 1712 PST 14Dec88. The fast fluctuations in the arrival times are caused by surface waves changing the path length. 170

Figure 127: Arrival time estimate for Station L from 1712 to 1812 PST 14Dec88. The fast fluctuations in the arrival times are caused by surface waves changing the path length. 171
Figure 128: Arrival time estimate for Station L from 1824 to 1924 PST 14Dec88. The fast fluctuations in the arrival times are caused by surface waves changing the path length. 172
Figure 129: Arrival time estimate for Station L from 1924 to 2024 PST 14Dec88. The fast fluctuations in the arrival times are caused by surface waves changing the path length. 173
Figure 130: Arrival time estimate for Station L from 2036 to 2136 PST 14Dec88. The fast fluctuations in the arrival times are caused by surface waves changing the path length. 174
Figure 131: Arrival time estimate for Station L from 2136 to 2206 PST 14Dec88. The fast fluctuations in the arrival times are caused by surface waves changing the path length. 175
Figure 132: Arrival time estimate for Station L from 2200 to 2300 PST 14Dec88. The fast fluctuations in the arrival times are caused by surface waves changing the path length. 176

Figure 133: Arrival time estimate for Station L from 0012 to 0112 PST 15Dec88. The fast fluctuations in the arrival times are caused by surface waves changing the path length. 177
Figure 134: Arrival time estimate for Station L from 0124 to 0224 PST 15Dec88. The fast fluctuations in the arrival times are caused by surface waves changing the path length. 178
Figure 135: Arrival time estimate for Station L from 0224 to 0324 PST 15Dec88. The fast fluctuations in the arrival times are caused by surface waves changing the path length. 179
Figure 136: Arrival time estimate for Station L from 0330 to 0406 PST 15Dec88. The fast fluctuations in the arrival times are caused by surface waves changing the path length. 180
Figure 137: Arrival time estimate for Station L from 0400 to 0512 PST 15Dec88. The fast fluctuations in the arrival times are caused by surface waves changing the path length. 181
Figure 138: Arrival time estimate for Station L from 0512 to 0612 PST 15Dec88. The fast fluctuations in the arrival times are caused by surface waves changing the path length. 182

Figure 139: Arrival time estimate for Station L from 0618 to 0718 PST 15Dec88. The fast fluctuations in the arrival times are caused by surface waves changing the path length. 183
Figure 140: Arrival time estimate for Station L from 0724 to 0824 PST 15Dec88. The fast fluctuations in the arrival times are caused by surface waves changing the path length. 184
Figure 141: Arrival time estimate for Station L from 0836 to 0936 PST 15Dec88. The fast fluctuations in the arrival times are caused by surface waves changing the path length. 185
Figure 142: Arrival time estimate for Station L from 0936 to 1000 PST 15Dec88. The fast fluctuations in the arrival times are caused by surface waves changing the path length. 186
Figure 143: Arrival time estimate for Station L from 1000 to 1100 PST 15Dec88. The fast fluctuations in the arrival times are caused by surface waves changing the path length. 187
Figure 144: Arrival time estimate for Station L from 1100 to 1200 PST 15Dec88. The fast fluctuations in the arrival times are caused by surface waves changing the path length. 188

Figure 145: Arrival time estimate for Station L from 1212 to 1312 PST 15Dec88. The fast fluctuations in the arrival times are caused by surface waves changing the path length. 189
Figure 146: Arrival time estimate for Station L from 1324 to 1424 PST 15Dec88. The fast fluctuations in the arrival times are caused by surface waves changing the path length. 190
Figure 147: Arrival time estimate for Station L from 1424 to 1524 PST 15Dec88. The fast fluctuations in the arrival times are caused by surface waves changing the path length. 191
Figure 148: Arrival time estimate for Station L from 1524 to 1554 PST 15Dec88. The fast fluctuations in the arrival times are caused by surface waves changing the path length. 192
Figure 149: Arrival time estimate for Station L from 1612 to 1712 PST 15Dec88. The fast fluctuations in the arrival times are caused by surface waves changing the path length. 193
Figure 150: Arrival time estimate for Station L from 1712 to 1812 PST 15Dec88. The fast fluctuations in the arrival times are caused by surface waves changing the path length. 194

Figure 151: Arrival time estimate for Station L from 1824 to 1924 PST 15Dec88. The fast fluctuations in the arrival times are caused by surface waves changing the path length. 195
Figure 152: Arrival time estimate for Station L from 1924 to 2024 PST 15Dec88. The fast fluctuations in the arrival times are caused by surface waves changing the path length. 196
Figure 153: Arrival time estimate for Station L from 2036 to 2136 PST 15Dec88. The fast fluctuations in the arrival times are caused by surface waves changing the path length. 197
Figure 154: Arrival time power spectrum for Station L. Spectrum from 2.2 hours of arrival time series, 1100 to 1312 PST 13Dec88 including 95% confidence interval. 198
Figure 155: Arrival time power spectrum for Station L. Spectrum from 2.2 hours of arrival time series, 1312 to 1524 PST 13Dec88 including 95% confidence interval. 199
Figure 156: Arrival time power spectrum for Station L. Spectrum from 2.2 hours of arrival time series, 1524 to 1748 PST 13Dec88 including 95% confidence interval. 200
Figure 157: Arrival time power spectrum for Station L. Spectrum from 2.2 hours of arrival time series, 1748 to 2000 PST 13Dec88 including 95% confidence interval. 201

Figure 158: Arrival time power spectrum for Station L. Spectrum from 2.2 hours of arrival time series, 0024 to 0236 PST 14Dec88 including 95% confidence interval. 202
Figure 159: Arrival time power spectrum for Station L. Spectrum from 2.2 hours of arrival time series, 0236 to 0448 PST 14Dec88 including 95% confidence interval. 203
Figure 160: Arrival time power spectrum for Station L. Spectrum from 2.2 hours of arrival time series, 0412 to 0624 PST 14Dec88 including 95% confidence interval. 204
Figure 161: Arrival time power spectrum for Station L. Spectrum from 2.2 hours of arrival time series, 0624 to 0836 PST 14Dec88 including 95% confidence interval. 205
Figure 162: Arrival time power spectrum for Station L. Spectrum from 2.2 hours of arrival time series, 0836 to 1048 PST 14Dec88 including 95% confidence interval. 206
Figure 163: Arrival time power spectrum for Station L. Spectrum from 2.2 hours of arrival time series, 1048 to 1300 PST 14Dec88 including 95% confidence interval. 207
Figure 164: Arrival time power spectrum for Station L. Spectrum from 2.2 hours of arrival time series, 1300 to 1512 PST 14Dec88 including 95% confidence interval. 208
Figure 165: Arrival time power spectrum for Station L. Spectrum from 2.2 hours of arrival time series, 1512 to 1724 PST 14Dec88 including 95% confidence interval. 209

Figure 166: Arrival time power spectrum for Station L. Spectrum from 2.2 hours of arrival time series, 1724 to 1936 PST 14Dec88 including 95% confidence interval. 210
Figure 167: Arrival time power spectrum for Station L. Spectrum from 2.2 hours of arrival time series, 1936 to 2148 PST 14Dec88 including 95% confidence interval. 211
Figure 168: Arrival time power spectrum for Station L. Spectrum from 2.2 hours of arrival time series, 2148 to 2400 PST 14Dec88 including 95% confidence interval. 212
Figure 169: Arrival time power spectrum for Station L. Spectrum from 2.2 hours of arrival time series, 0212 to 0424 PST 15Dec88 including 95% confidence interval. 213
Figure 170: Arrival time power spectrum for Station L. Spectrum from 2.2 hours of arrival time series, 0424 to 0636 PST 15Dec88 including 95% confidence interval. 214
Figure 171: Arrival time power spectrum for Station L. Spectrum from 2.2 hours of arrival time series, 0848 to 1100 PST 15Dec88 including 95% confidence interval. 215
Figure 172: Arrival time power spectrum for Station L. Spectrum from 2.2 hours of arrival time series, 1124 to 1312 PST 15Dec88 including 95% confidence interval. 216
Figure 173: Arrival time power spectrum for Station L. Spectrum from 2.2 hours of arrival time series, 1312 to 1524 PST 15Dec88 including 95% confidence interval. 217

Figure 174: Arrival time power spectrum for Station L. Spectrum from 2.2 hours of arrival time series, 1524 to 1736 PST 15Dec88 including 95% confidence interval. 218
Figure 175: Arrival time power spectrum for Station L. Spectrum from 2.2 hours of arrival time series, 1736 to 1948 PST 15Dec88 including 95% confidence interval. 219
Figure 176: Arrival time power spectrum for Station L. Spectrum from 2.2 hours of arrival time series, 1948 to 2200 PST 15Dec88 including 95% confidence interval. 220

ACKNOWLEDGMENT

It is difficult to mention everyone that has contributed to the completion of this thesis, therefore I would like to first express my gratitude to everyone that has in some way contributed. I would like to thank my thesis advisor, Dr. James H. Miller for his enthusiasm, encouragement and confidence in my ability to successfully complete the demodulator design in the time available. I would also like to thank Tom Walton, George Steelman, and Mary Ann Stroub of the Mitre Corporation for sponsoring my experience tour where I developed the preliminary design of the demodulator. I thank Sönke Paulsen for his electronic and computer troubleshooting expertise. I thank Bob Dees for his advice on some of the demodulator design modifications. I thank Dave Shafer, Greg Pless, and Floyd York for their equipment and logistical support throughout this project. I especially thank my wife Irena for her love, patience, understanding and total support, her many hours of proof reading on a difficult subject, and who more than anyone understands the importance of this engineering degree to me. Finally, I dedicate this thesis to my mother Emma Mae Schaaff.

I. INTRODUCTION

A. THESIS OVERVIEW

The main obstacle to understanding ocean circulation is our inability to observe it. The ocean is opaque to most of the electromagnetic spectrum. However, the ocean is transparent to low frequency acoustic waves. The navies of the world have utilized this fact to detect submarines with sound since 1918. Recently, oceanographers and engineers have looked to acoustics for assistance in observing the ocean circulation.[Ref. 1]

In 1979, Munk and Wunsch proposed a scheme for large scale monitoring of the ocean and named it ocean acoustic tomography [Ref. 2]. Ocean acoustic tomography can observe the mesoscale dynamics of the ocean by measuring the changes in the travel time of narrow-band acoustic signals transmitted over various paths. Tomography derives from the Greek root meaning "to slice" or image the interior of a body. Ocean acoustic tomography is analogous to medical x-ray computer-assisted tomography (CAT).

Until recently, ocean acoustic tomography has been restricted to the deep ocean imaging mesoscale features such as fronts and eddies. This thesis is part of an effort by the Naval Postgraduate School (NPS) and Woods Hole Oceanographic Institution (WHOI) to use tomography in coastal regions. In particular, an experiment was held in Monterey Bay, California in December, 1988. Among the experiment goals were:

1. Determine experimentally the relationship between surface waves and fast fluctuations in acoustic arrival times of tomography signals;

2. Determine the effect of internal waves on tomography signals in a coastal environment;

3. Determine the effect of the complex bathymetry of the Monterey Submarine Canyon on acoustic propagation, and;

4. Test the first real-time shore-based acoustic tomography data acquisition system.

The experiment had a single acoustic tomography source located off Point Sur and ten receivers located around the rim of the Monterey Canyon between Point Piños and Santa Cruz. The principle investigators were Professors James H. Miller and Ching-Sang Chiu of NPS and Professor James F. Lynch of WHOI. Also involved in the experiment were the National Data Buoy Center, Spartan Corporation, and the Mitre Corporation.

This thesis describes the analog signal processing system developed for the experiment focusing on the signal demodulation. The goal of the thesis was to design and build a low-cost, reliable, multi-channel quadrature demodulator. That goal has been met. This demodulator receives the raw recorded acoustic data, preamplifies, bandpass filters, demodulates the narrow-band tomography signal, and provides the demodulates to a Zenith Z-248 PC equipped with an analog-to-digital converter. All the processing is done synchronous to a 7168 Hz square wave recorded on all data tapes. The synchronization is necessary to eliminate any timing errors introduced by the recording system.

In Chapter II, details of ocean acoustic tomography and the 1988 Monterey Bay Acoustic Tomography Experiment are given. In Chapter III, the design of the Multi-Channel Data-Synchronized Quadrature Phase Demodulator is presented. The performance of the Demodulator is given in Chapter IV. Results of processing data from one of the receivers in the

experiment are shown in Chapter V. Finally, Chapter VI presents conclusions and recommendations for signal processing in a future tomography experiment.

II. BACKGROUND

A. OCEAN ACOUSTIC TOMOGRAPHY

1. General Description

The ability to understand the world's oceans is predominately limited by our ability to observe it. There is currently no large-scale ocean monitoring network. A major reason is the cost of ship time is prohibitive. Monitoring an area 1000 km x 1000 km, approximately one third the area of the Mediterranean Sea, by taking in-situ measurements would require approximately ten ships employed full-time. In-situ sensors are difficult to use because the ocean is opaque to the majority of the electromagnetic spectrum resulting in only a limited area of measurement.[Ref. 3]

It is known that the majority of the ocean's kinetic energy is associated with the mesoscale variability. The ocean mesoscales are disturbances with horizontal scales of approximately 100 km and time scales from 50-150 days [Ref. 4]. Mesoscale variability in the ocean is analogous to weather systems in the atmosphere. The ocean problem is more difficult due to the smaller scale structure (100 km versus 1000 km for the atmosphere) and the longer time scales (100 days versus 3 days for the atmosphere). Current satellite technology provides accurate surface mapping of the ocean but this is only accurate to a depth of a few centimeters. The critical need for real time measurements of the ocean's interior can be fulfilled by ocean acoustic tomography because the ocean is essentially transparent to sound.[Ref. 5]

The concept of ocean acoustic tomography was first, formally presented by Munk and Wunsch in 1977 as a means of large scale ocean monitoring[Ref. 2]. The method involves

large scale ocean monitoring[Ref. 2], using the travel time of acoustic pulses transmitted between multiple points in the ocean to reconstruct the intervening sound field (Figure 1). The speed of sound in water is dependent on temperature, pressure and salinity. Sound propagating through the water is affected by these properties and any mesoscale variability. Linear inverse theory provides a method to use the travel time fluctuations caused by the mesoscale variability to estimate its scope. This method is similar to that used in medical x-ray tomography except that x-rays tend to follow straight paths while the acoustic energy travels along curved paths.[Ref. 6]

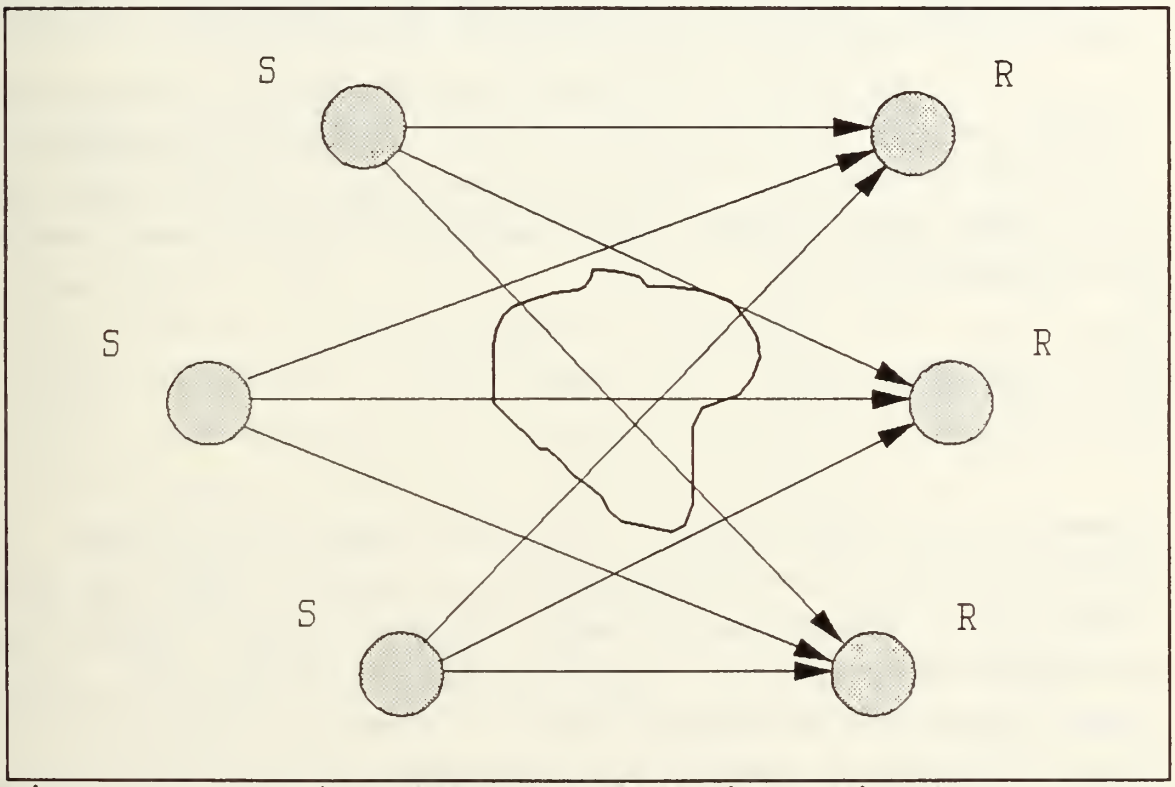

Figure 1: Top view of source and receiver pairs from the 1981 Bermuda Experiment. Each slice may contain on the order of ten eigenrays connecting each source and receiver pair.[from Ref.3]

2. Signal Processing

a. Signal Propagation

In ocean acoustic tomography, travel time is the measurement of interest and can be represented as the time-varying impulse response of the source-receiver channel,

$$h(t,T) = \sum_{i=1}^{P} a_i \delta(t-\tau_i) \qquad (1)$$

where T represents geophysical time and τ_i represents total travel time for each P multipath with amplitude a_i. The channel parameters change with T in response to ocean variations, but during the time of the tomographic measurement which is short relative to geophysical time, the impulse response can be considered fixed.[Ref. 6]

Acoustic tomographic measurements are made by deploying transmitters and receivers around the periphery of an ocean volume. The transmitter sends an acoustic signal and the total travel time τ_i along each eigenray to each receiver is measured

$$\tau_i = \int_i [c+u]^{-1} ds \qquad (2)$$

where c is sound speed, u is the current speed along the path, and ds, the differential arc-length along the path. Each pulse travels along many eigenray paths joining each source-receiver pair; a typical number of resolvable paths is ten. Therefore N sources and M receivers will result in approximately 10xNxM pieces of information versus N+M pieces of information from conventional in-situ measurements. Instruments do not need to be distributed vertically because each source-receiver pair provides vertical resolution. The

travel time τ_i of each eigenray and their time spread τ_s depends on source-receiver geometry and intervening sound field perturbations. It has been estimated that the previously discussed representative 1000 square kilometer piece of ocean could be monitored with as few as four acoustic tomographic source-receiver pairs.[Ref. 6]

The sound speed can be modelled as a perturbation about a mean c_o,

$$c = c_o + \delta c \tag{3}$$

for the mesoscale, c_o is the climatological mean (approximately 1500 m/s) and δc is variability (approximately 10 m/s). The current field is usually an order of magnitude smaller. Therefore the perturbation in travel time is

$$\delta\tau_i = \int_i c_o^{-2} \delta c \, ds \tag{4}$$

where the path of integration is assumed the same as the unperturbed path in (2). Errors associated with the linearization (4) can be shown to be small (3). The inverse problem estimates c or δc based on τ_i or $\delta\tau_i$ from equations (2) or (4) depending on whether absolute or differential travel times are measured, respectively.[Ref. 6]

Several techniques for inverting equations of the form of (4) have been developed. Linear optimal estimation theory is the method normally used to invert ocean acoustic tomographic data. The method assumes apriori information of the mean field and its covariance function and produces an estimator that minimizes the mean square differences between the actual field and the estimate.[Ref. 6]

b. Signal Design

In ocean acoustic tomography the signal used is normally a phase modulated carrier. The phase modulation is determined by a linear maximal-length, binary, shift-register sequence. The signal is designed to achieve specified performance goals in the face of equipment limitations. In order to detect travel time perturbations due to mesoscale variability, long term timing stability is needed.[Ref. 6]

(1) Resolution. The resolution of the system is approximately equal to the reciprocal of the bandwidth, 1/B, which is 62.5 milliseconds for the Monterey Bay Experiment. The environment of the Monterey Bay was previously studied as the subject of a Master's Thesis by Theresa M. Rowan in preparation for the December 1988 experiment. The results of her thesis predict arrival time separations between 2 and 500 milliseconds for consecutive rays with the majority of the arrivals separated by greater than 80 milliseconds [Ref. 7]. Therefore, impulses arriving with less than 62.5 milliseconds separation will appear as one arrival and will not be resolved (Figure 2).[Ref. 8]

(2) Response. Impulsive excitation is a useful mathematical tool for determining the travel time through the ocean medium. Unfortunately, an impulse is not easily created. The practical, physical solution is to use a finite length pulse signal and then pass it through a matched filter which effectively compresses the signal. The maximal length sequence or M-sequence is a way of producing pseudorandom noise with unique properties and is an excellent technique for producing a practical impulse.

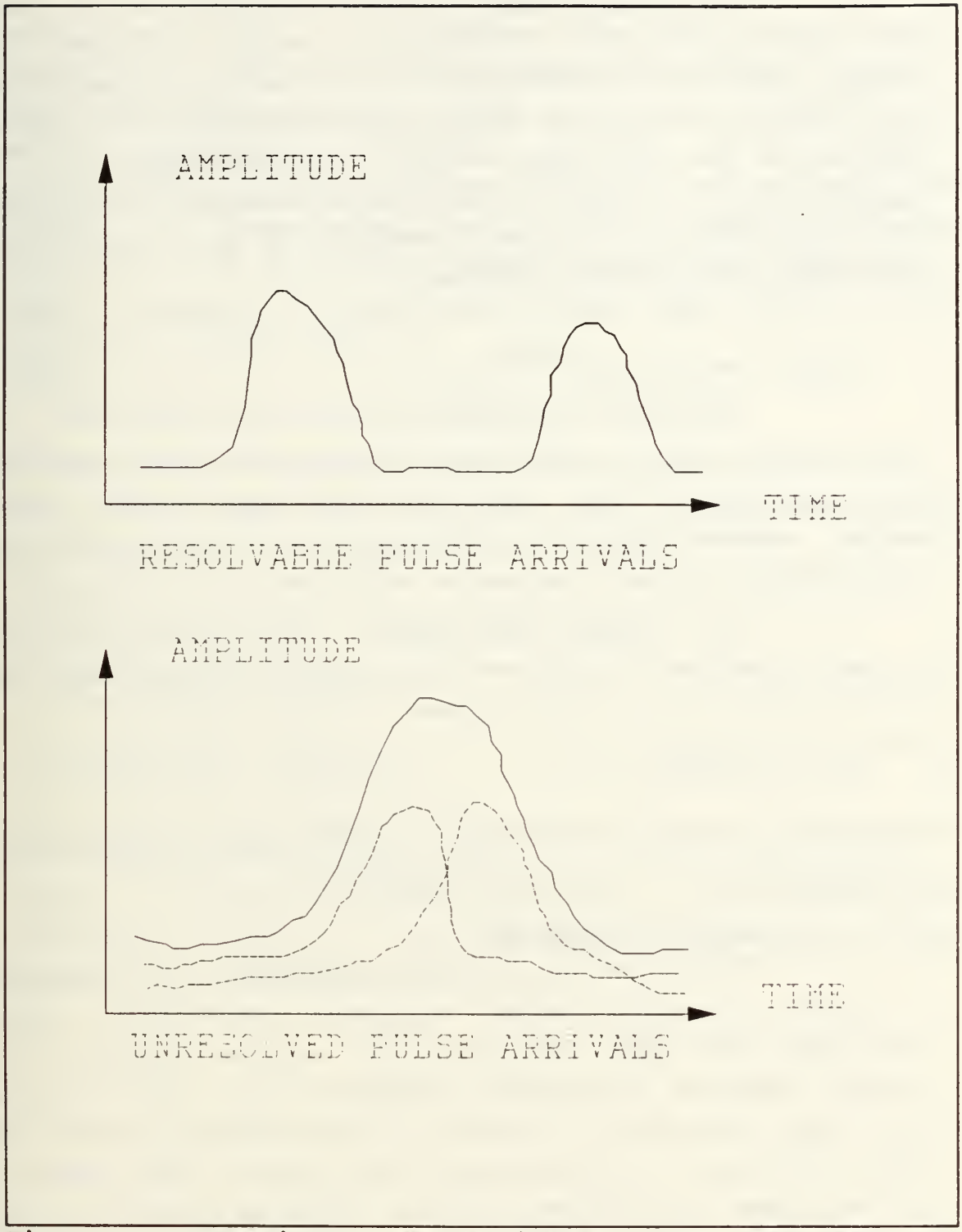

Figure 2: Comparison of arrivals for resolved and unresolvable pulses.

(3) Modulation. The M-sequence is used to phase modulate the carrier by switching the phase between two values. The values are determined by the modulating waveform, m(t). Each value of the carrier phase corresponds to either the one or the zero value of m(t). The M-sequence {0,1} is mapped to {1,-1} before it is used to modulate the carrier. The modulated signal can be represented by S(t), and s(t) is the associated baseband waveform,

$$S(t) = \mathrm{Re}[s(t)(\sqrt{2}e^{-j2\pi f_c t})]. \quad (5)$$

The received signal is then autocorrelated with the M-sequence which produces a peak where the code and received signal match. A more complete description of M-sequences and modulation is given in Appendix A.[Ref. 9]

(4) Arrival Time Error. The arrival time error σ_t is a function of the received signal to noise ratio SNR and the bandwidth B of the signal,

$$\sigma_t = [2\pi B\sqrt{SNR}]^{-1}. \quad (6)$$

Using the parameters from Table 1 and Equation (6) the arrival time error σ_t is 1.9 milliseconds.[Ref. 6]

c. Signal Parameters

The selection of signal parameters is a balancing of signal processing gains, equipment limitations, limits resulting from signal decorrelation, and the spread of the impulse response. The signal processing gains are a function of 10logN, where $N=2^r-1$, but are also determined by N=L/d. The digit duration, d, is set by the relationship $d=D/f_c$ where D, is the number of integral carrier frequency cycles for each digit in m(t) and f_c is the carrier frequency in Hz. L is the period of m(t). Generally, the value for d is set to utilize

the full bandwidth of the transmitter and a value of N is chosen such that L is greater than the channel time dispersion τ_s. Various signal parameters for several different tomography experiments are shown in Table 1, including the Monterey Bay Acoustic Tomography Experiment. It is important to note that in this experiment, unlike previous ones, the signal is transmitted continuously. The continuous transmission of the signal limits the aliasing effects of higher frequency internal and surface waves on the lower frequency spectrum.[Ref. 6]

B. MONTEREY BAY ACOUSTIC TOMOGRAPHY EXPERIMENT

1. General Overview

This thesis developed a major signal processing component for the December 1988 Monterey Bay Acoustic Tomography Experiment. The experiment had four objectives:

1. test the acoustic tomography system;
2. determine the effects of surface waves on acoustic tomography signals;
3. determine the effects of internal waves on acoustic tomography signals;
4. determine the effects of complex bathymetry on acoustic propagation.

Figure 3 provides a graphic overview of the Monterey Bay experiment. Figure 4 provides relative source-receiver geometry for the experiment.[Ref. 10]

Table 1: Signal parameters for various acoustic tomography experiments [from Ref. 4].

	1981 Density Tomography	1984 Gulf Stream Tomography	1984 Marginal Ice Zone Tomography	1988 Monterey Bay Tomography
Carrier, f_c (Hz)	224	400	224	224
Digits, N	127	511	63	31
Digit duration, d (s)	0.0625	0.01	0.0625	0.0625
Sequence duration, L = Nd (s)	7.9375	5.11	3.9375	1.9375
Repetitions, R	24	42	1828	continuous
Modulation angle, θ_o (degrees)	75	87.5	85	79.8179
Pulse compression gain (dB)	21	27	18	15
Coherent averaging gain (dB)	13.8	16.3	20(?)	6
Total signal processing gain (dB)	34.8	43.8	38(?)	21
3 dB bandwidth (Hz)	16	100	16	16
Spectral line spacing (Hz)	0.126	0.196	0.254	0.516
Arrival time error, σ_t (ms)	1.0	0.06	0.7(?)	1.9

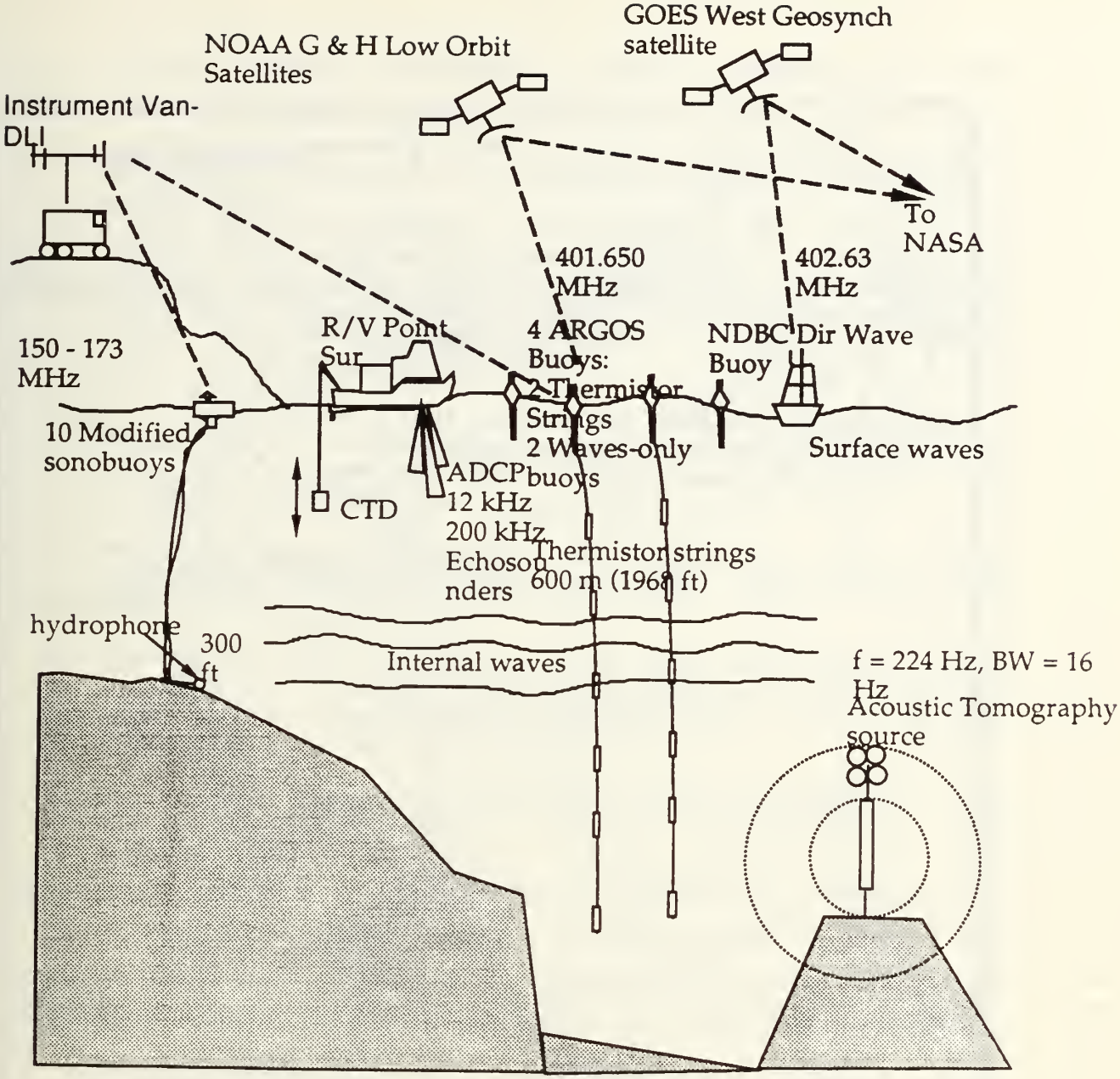

Figure 3: Monterey Bay Acoustic Tomography Experiment 12-16 December 1988

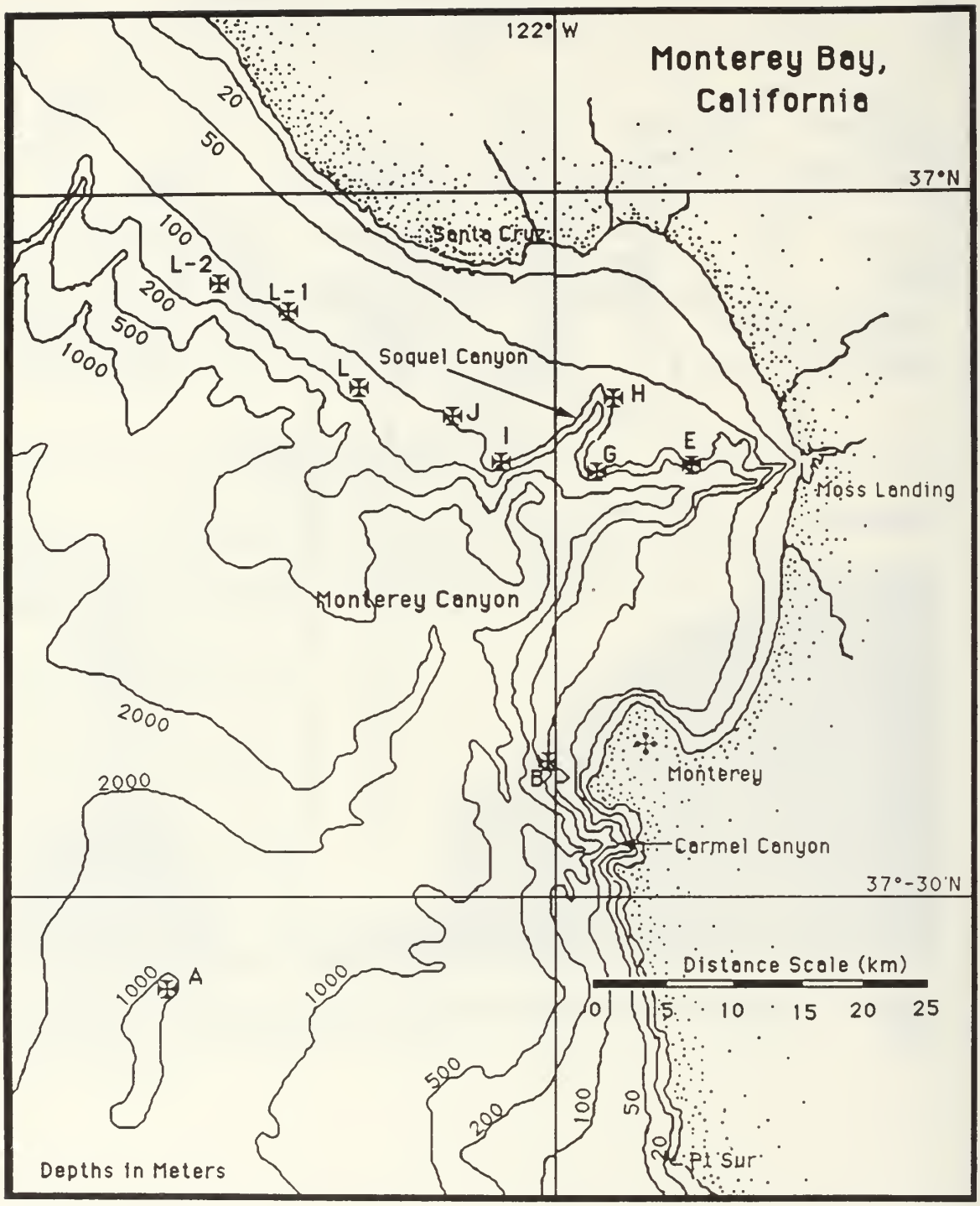

Figure 4: Monterey Bay showing the positions of the transmitter and receivers (positions are marked with ✠). The transmitter is at station A, all others are receivers. The shore station position is marked by ✣ .

The acoustic tomography system consists of the following components:

1. a 224 Hz moored, battery powered, microprocessor controlled, resonant tube tomographic source (Figure 5);

2. eleven SSQ-57A sonobuoys, manufactured and modified by Spartan Electronics of Jackson Michigan to extend their battery life to one week, equipped with a new sonobuoy float and bottom mooring system designed and built by Woods Hole Oceanographic Institution (WHOI) of Woods Hole, Maine (Figure 6);

3. a van-mounted Sonobuoy Receiving System, the AN/ARR-72 which is a 31 channel sonobuoy receiver designed for use in U. S. Navy S3A and P3C aircraft, used to monitor the sonobuoys (Figure 7);

4. multiple video cassette recorders with pulse code modulation (VCR-PCM), used to record and playback the data;

5. the Multi-Channel Data-Synchronized Quadrature Phase Demodulator, used to reduce the data as it was played back, to its demodulates which are then sent to an ADC installed in a Zenith Z-248; and

6. the Zenith Z-248 performed an autocorrelation of the demodulated data with the original code and stored the reduced data.

This thesis dealt with the demodulator described in (5) above. A 31 bit maximal length, binary, shift-register sequence was used to phase modulate a 224 Hz tomographic source. The phase modulated signal was received using the modified sonobuoys. The sonobuoys performed no signal processing, transmitting all data to the van via VHF. The raw data was received by the van and recorded on the VCR-PCM's (Figure 7). The VCR-PCM's record and play at only one speed so the data processing rate at playback is set by this limitation. The Zenith Z-248 used has an Intel 80286 cpu running at 6 MHz with an 80287 coprocessor. The computer is equipped with a Metrobyte DASH16F analog to digital converter (ADC).

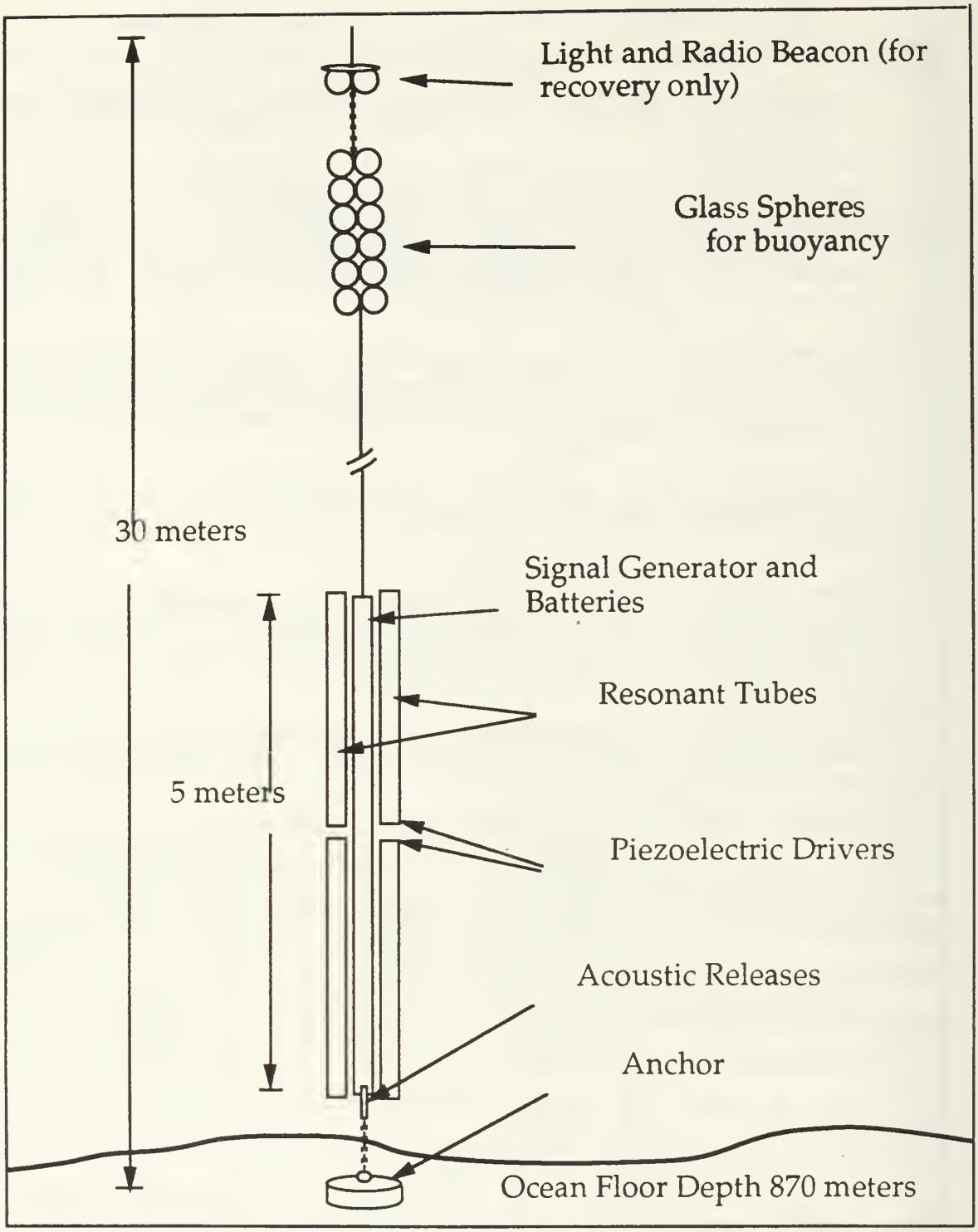

Figure 5: 224 Hz resonant tomography signal transmitter.

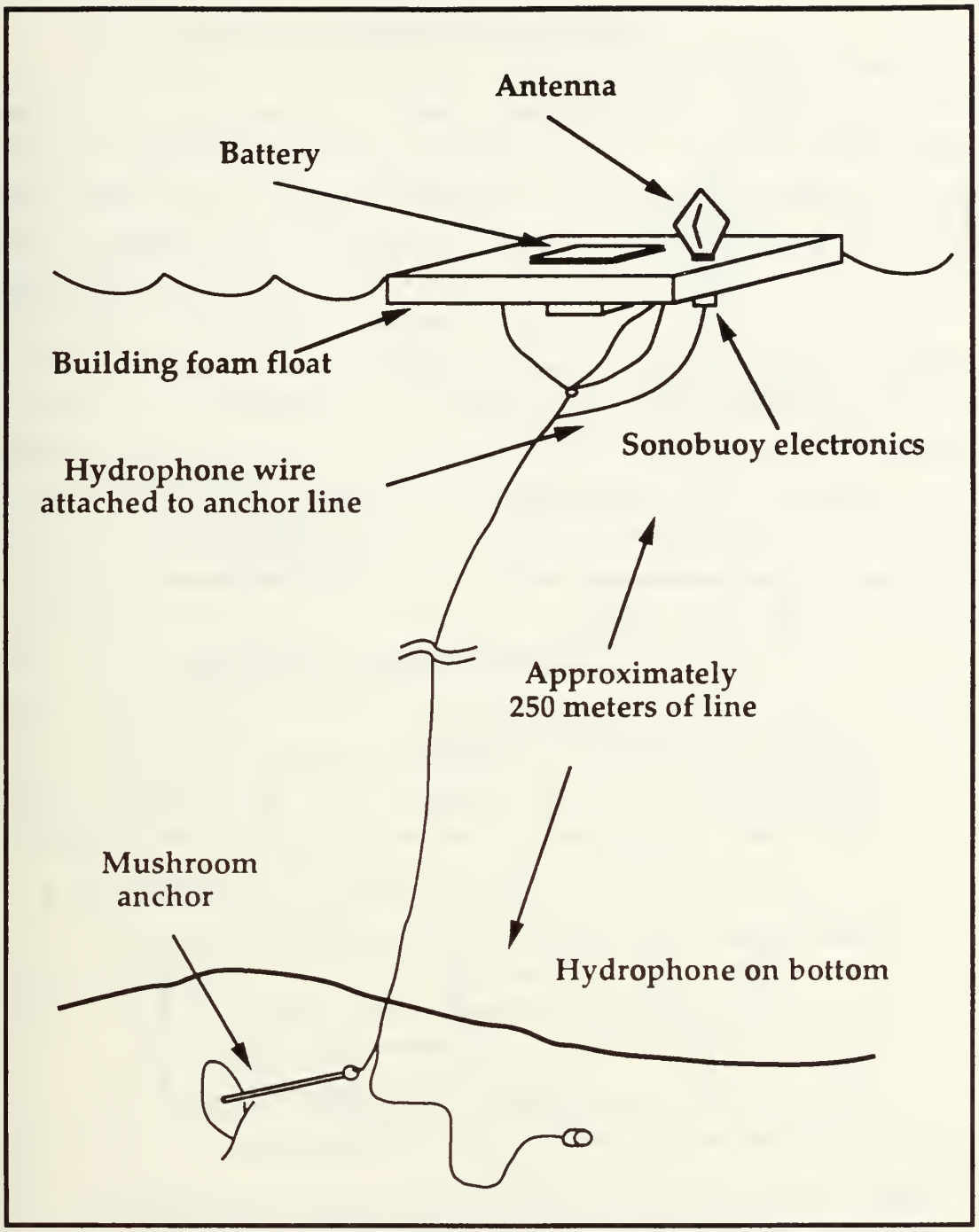

Figure 6: Modified AN/SSQ-57 sonobuoy .

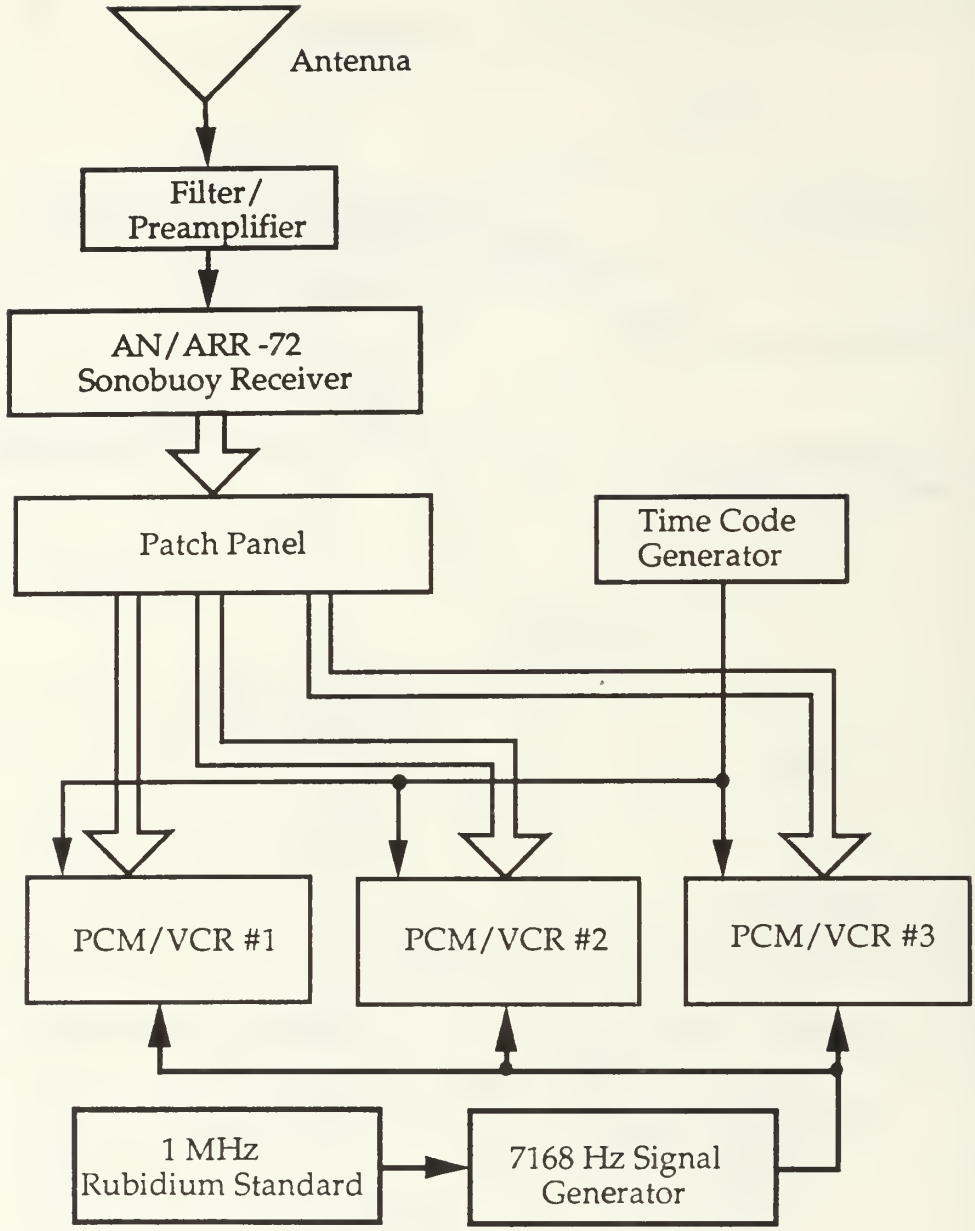

Figure 7: Sonobuoy data recording system located in the van. This system receives the sonobuoy radio transmission, converts it to analog sound, and then records it on videotape using pulse code modulation.

a. Source and Receiver Placement

The environment of the Monterey Bay was previously studied by Theresa M. Rowan to determine optimum source-receiver geometry based on a fixed source location. The source was placed on an unnamed seamount 36 kilometers west of Point Sur at a depth of 870 meters. The source transmitted the phase modulated signal for four days continuously at a source level of 172 dB re 1μPa at 1 meter.

The general receiver locations were determined as a result of Reference 7 (Figure 4). The eigenrays for the geometry particular to this experiment were generated using the Multiple Profile Ray-Tracing Program (MPP) used by Scripps Institute, Woods Hole Oceanographic Institution, and the Naval Postgraduate School. MPP is a range dependent, two-dimensional ray trace program that calculates eigenray arrivals and travel times for specified source-receiver locations using given sound velocity profiles and bathymetry. MPP is only capable of giving rough estimates due to the complex bathymetry of the Monterey Bay which cannot be accurately modelled due to the two-dimensional limitation of this program.[Ref. 7]

2. Signal Processing

The Multi-Channel Data-Synchronized Quadrature Phase Demodulator provides the link between the VCR-PCM's and the Zenith Z-248. There was no signal processing performed at the time of the experiment. The signal was only monitored to determine sonobuoy status and quality of reception. Large quantities of raw data were recorded and stored as a result. Attempting to have the Z-248 perform all the signal processing after the analog to digital conversion would have exceeded the capabilities of the computer. The demodulator processes each channel of data and outputs an in-phase and quadrature component. It is this demodulated data which is then sent to the Z-248.

The signal processing begins with the phase demodulation in the demodulator. The signal is sampled at twice the Nyquist rate and digitized by the ADC. The signal is then cross-correlated and coherently averaged by the PC. The Monterey Bay Acoustic Tomography Experiment differs from the other experiments presented in Table 1 because all the data from the receivers was transmitted prior to any signal processing and then stored in analog format for later signal processing. It is in the autocorrelation and coherent averaging that the properties of the M-sequence are fully exploited.

The output of the Multi-channel, Data Synchronized, Quadrature Phase Demodulator is the complex envelope of the input from the VCR-PCMs. The real bandpass signal can be represented by its complex envelope:

$$\tilde{x}(t) \doteq [x(t)+j\hat{x}(t)]e^{-j2\pi f_c t} \tag{7}$$

where $\hat{x}(t)$ is the Hilbert transform of $x(t)$. The Hilbert transform must be calculated prior to computing the complex envelope. The Hilbert transform can be calculated by taking the inverse Fourier transform:

$$\hat{x}(t) = F_f^{-1}\{-j\,\mathrm{sgn}(f)X(f)\} \tag{8}$$

where sgn(f) is the sign function. Therefore, the Hilbert transform can be represented as a $\pm$ 90° phase shifter where the phase lead or lag is dependent on the sign of f in the frequency domain. Using this knowledge and returning to the

time domain, the Hilbert transform of the cosine and sine functions can now be represented by:

$$H\{\cos(2\pi f_c t+\theta_o)\} = \sin(2\pi f_c t+\theta_o) \quad (9)$$

and

$$H\{\sin(2\pi f_c t+\theta_o)\} = -\cos(2\pi f_c t+\theta_o) \quad (10)$$

and θ_o is in radians. Note that if

$$x(t) = x_{LP}(t)x_{BP}(t) \quad (11)$$

where $x_{LP}(t)$ is a low-pass and $x_{BP}(t)$ is a band-pass signal, and if the amplitude spectra $|X_{LP}(f)|$ and $|X_{BP}(f)|$ do not overlap (Figure 8), then

$$\hat{x}(t) = x_{LP}(t)\hat{x}_{BP}(t), \quad (12)$$

that is, only the band-pass signal is Hilbert transformed.[Ref. 11]

Now consider the signal used in the Monterey Bay Acoustic Tomography Experiment. The signal can be represented by

$$x(t) = A(t)\cos[2\pi f_c t+\theta(t)] \quad (13)$$

where $\theta(t)$ includes the phase shift from the M-sequence and the phase shift due to the time-varying impulse response of the ocean medium. Now using a trigonometric identity we can

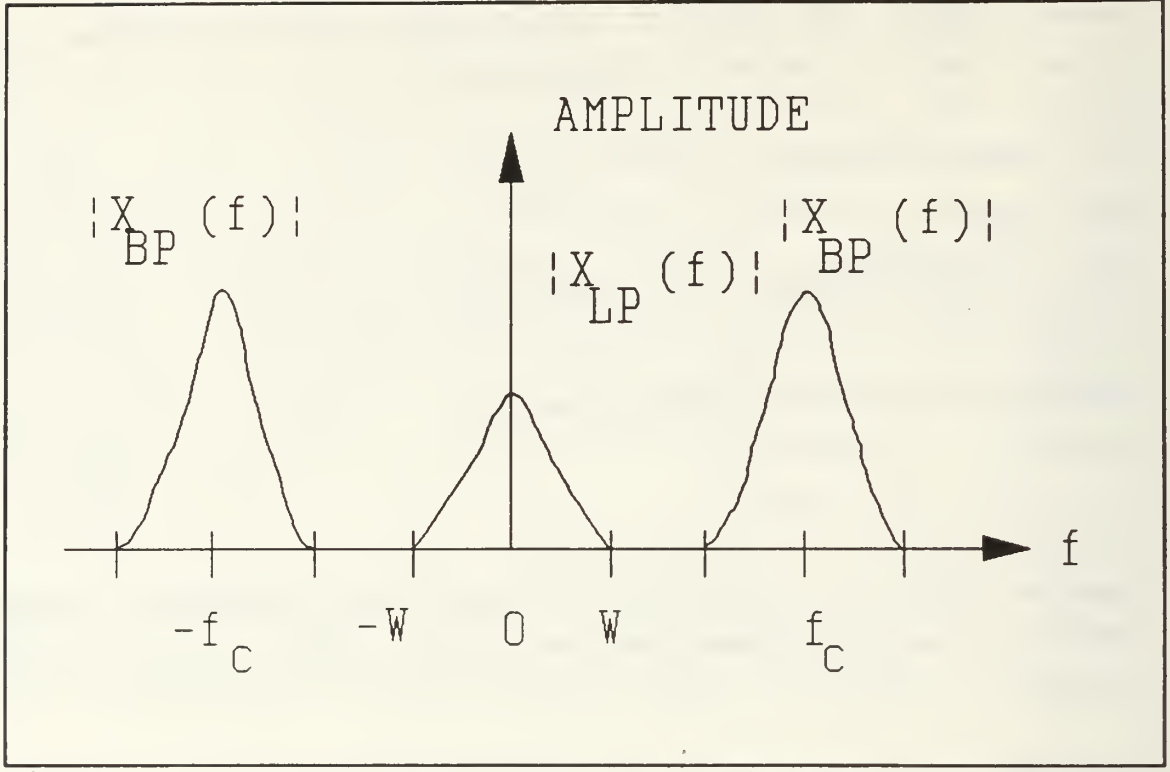

Figure 8: The low-pass spectrum $X_{LP}(f)$ and the band-pass spectrum $X_{BP}(f)$ which do not overlap [from Ref.11].

rewrite Equation 13 as

$$x(t) = x_c(t)\cos(2\pi f_c t) - x_s(t)\sin(2\pi f_c t) \qquad (14)$$

where

$$x_c(t) = A(t)\cos[\theta(t)] \qquad (15)$$

and

$$x_s(t) = A(t)\sin[\theta(t)]. \qquad (16)$$

Equations 15 and 16 are the in-phase and quadrature components respectively. Since Equations 15 and 16 both represent low-pass signals we can use Equations 9, 10, and 11

to write the Hilbert transform as

$$\hat{x}(t) = x_c(t)\sin(2\pi f_c t)+x_s(t)\cos(2\pi f_c t) \qquad (17)$$

and from this and by using Equation 7 we obtain the complex envelope

$$\tilde{x}(t) = x_c(t)+jx_s(t). \qquad (18)$$

This entire process is performed by the hardware in the data channels of the Multi-Channel Data-Synchronized Quadrature Phase Demodulator (Figure 9).[Ref. 11]

The signal is first passed through a band-pass filter to eliminate the noise outside the pass-band. It is next multiplied against both the cosine and minus sine of the original signal where it is Hilbert transformed. The signal is then low-pass filtered leaving only the baseband signal which is output as an In-phase (I) and Quadrature (Q) channel for each input. This output is then sent to the Zenith Z-248.

The Zenith Z-248 receives the demodulates from the ADC, both an In-phase (I) and Quadrature (Q) output for each input channel. The demodulates are then treated separately but processed identically by the control program. The demodulates are first digitized and then the code concurrently correlated by the Fast Hadamard Transform. Following the code correlation the in-phase and quadrature components are combined and stored as magnitude and phase. The signal is also coherently averaged over the number of repetitions (R), for the Monterey Bay Acoustic Tomography Experiment, R was continuous so R=16 was used for signal processing,

$$X_j = \sum_{r=1}^{U} X_{rN} \qquad (19)$$

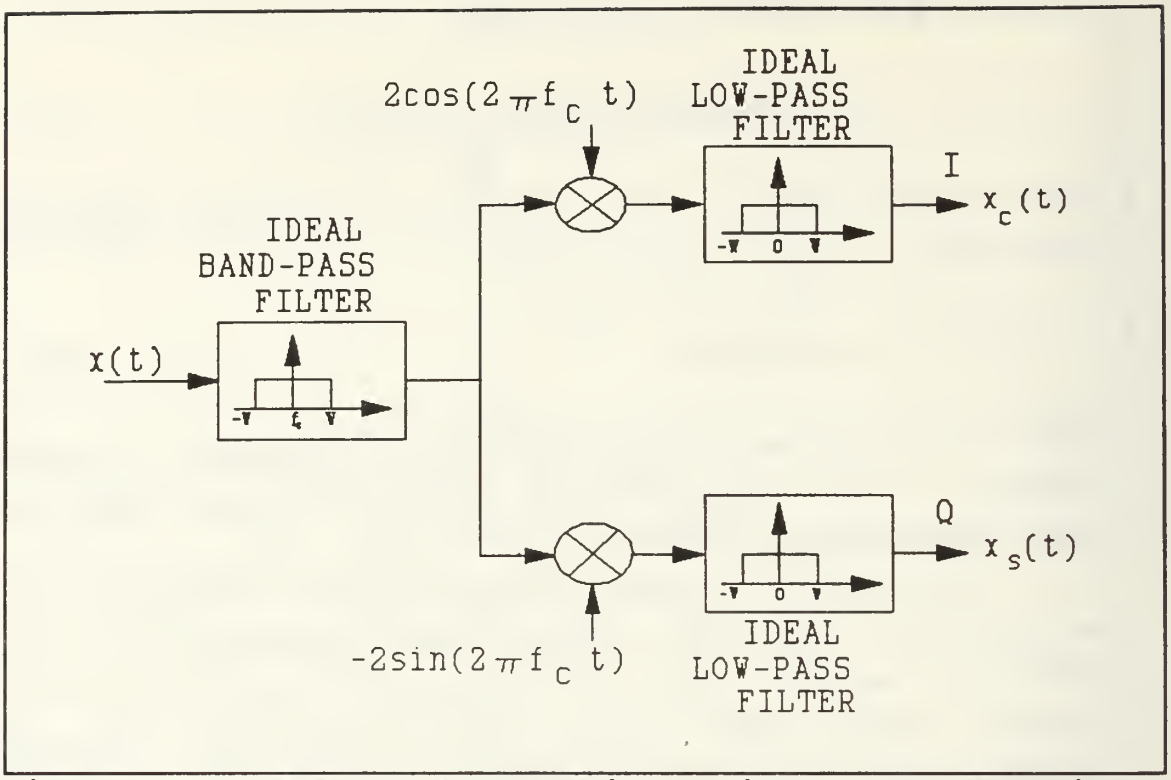

Figure 9: Quadrature demodulation of input band-pass signal [from Ref. 11].

for j=1,..2N this produces a 10log(R) dB signal processing gain. The data is then stored on 20 Megabyte Bernoulli Cartridges (Figure 10).[Ref. 6]

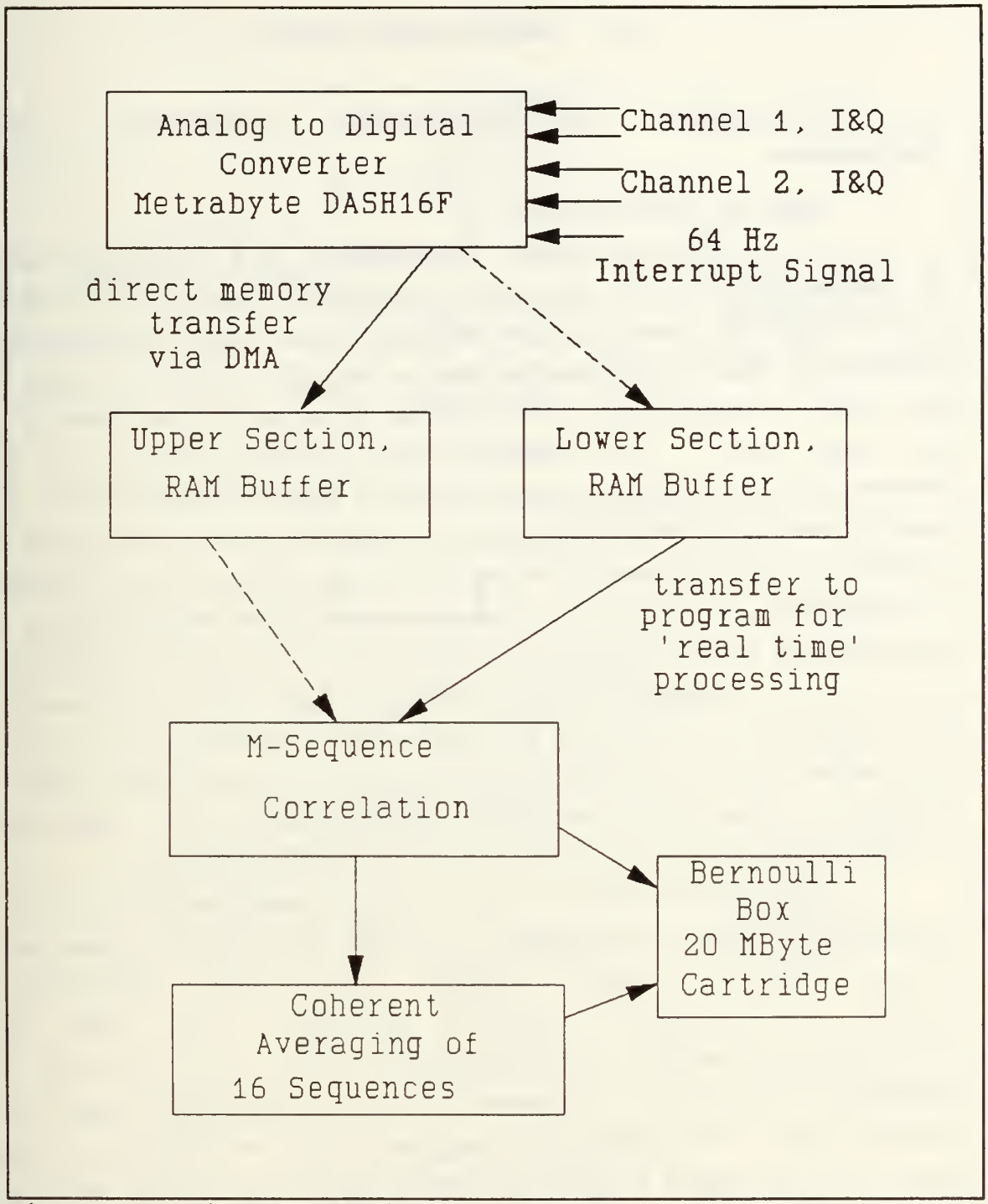

Figure 10: Diagram of signal processing performed by control program AMORE after tomography signal enters computer.

III. DEMODULATOR DESIGN

A. MULTI-CHANNEL DATA-SYNCHRONIZED QUADRATURE PHASE DEMODULATOR

1. General description

The quadrature phase demodulator is a practical means of reducing the data flow to a level that can be processed with a desktop computer. The Multi-Channel Data-Synchronized Quadrature Phase Demodulator uses a signal recorded on one of the video channels of the VCR-PCMs to synchronize itself to the data as it is replayed for demodulation. If the synchronizing channel is lost during phase demodulation the demodulator automatically switches during this input lapse to synchronous phase demodulation until the synchronizing channel is regained. The switch in demodulation from synchronized to synchronous inputs a known and predictable error in the output that can be compensated for later in the signal processing. The alternative would be to lose signal demodulation during the lapse which produces an unpredictable jump in the output. Figure 11 shows the interrelationship between all components in the Acoustic Tomography Signal Processing System.

The Multi-Channel, Data Synchronized Quadrature Phase Demodulator can be described by subdividing it into two main circuit types, a timing circuit and a data demodulation circuit. The timing circuit's function is to take the synchronizing signal and convert it so it can be used to demodulate the data and generate a 64 Hz interrupt signal for the ADC and, if necessary, generate its own synchronizing signal if the input signal is lost (Figure 12). There are four

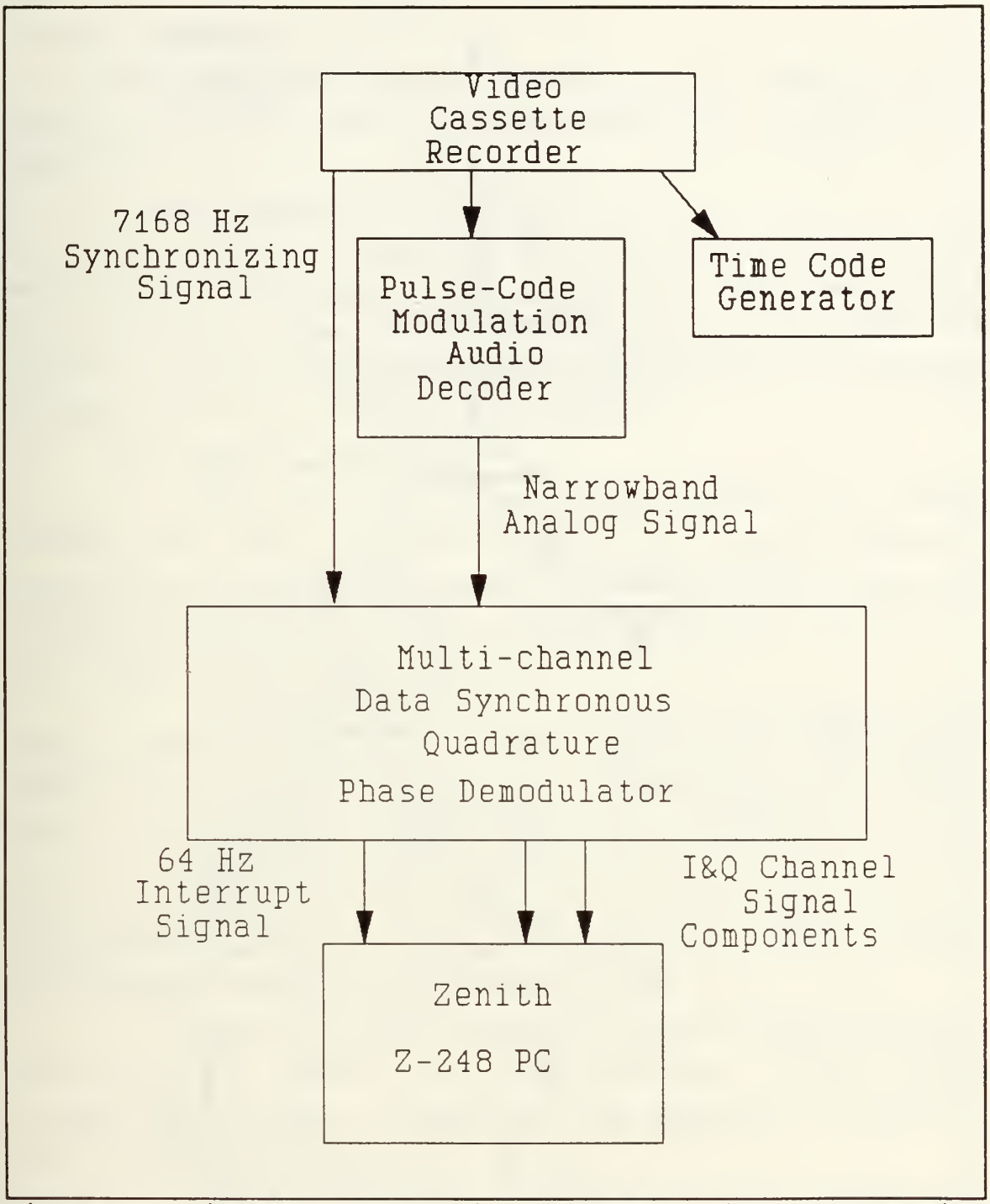

Figure 11: Diagram of acoustic tomography signal processing system.

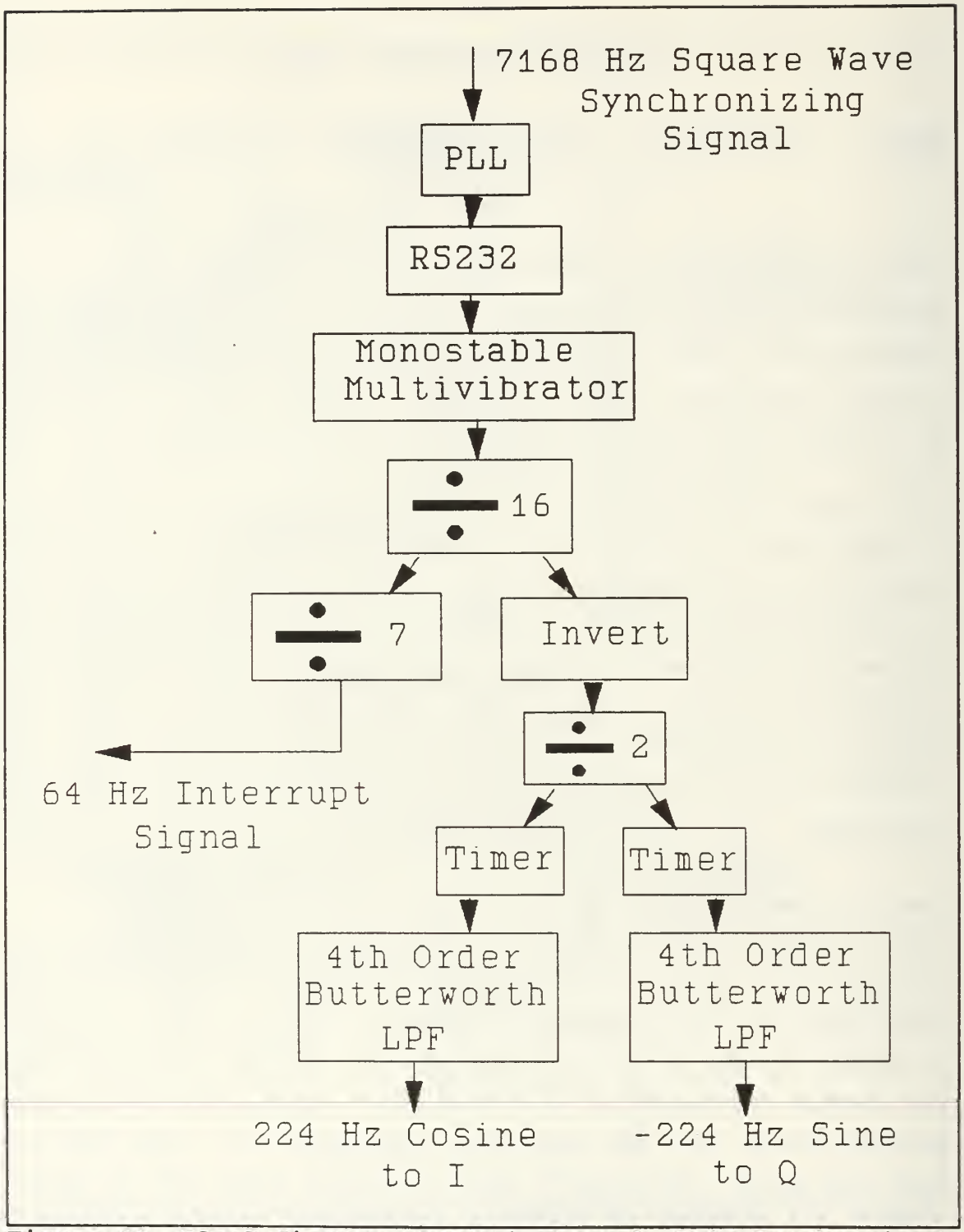

Figure 12: Block diagram of Multi-channel, Data Synchronized, Quadrature Phase Demodulator timing channel.

identical data demodulation circuits, one per channel, and their function is to phase demodulate the signal (Figure 13).

2. Schematic

A complete schematic drawing of the Multi-Channel Data-Synchronized Quadrature Phase Demodulator is provided in Appendix B.

3. Timing Channel

The Timing Channel is the critical circuit in the Multi-Channel Data-Synchronized Quadrature Phase Demodulator. It synchronizes the phase demodulation and provides the automatic switching to synchronous demodulation in the event of the loss of the synchronizing channel.

a. Phase Locked Loop

The front end of the Timing Channel is a Phase Locked Loop (PLL). The PLL consists of a phase detector, amplifier and voltage-controlled oscillator (VCO). Figure 14 illustrates the standard PLL configuration. The PLL used in this application is the LM565CN.

The phase detectors used in PLLs are of two basic types normally referred to as Type I and II. The Type I phase detector is designed for use with analog signals or square waves and is the type used in this application. The Type II is edge-triggered by digital transitions. The Type I is the simplest type of phase detector and is an exclusive-OR gate, Figure 15. These type of phase detectors are linear in phase and excellent for lock-in detection.[Ref. 12]

The VCO is controlled by the phase detector output. The VCO in the LM565CN is a low distortion, stable, highly linear design. The frequency can be set with an external capacitor and resistor.[Ref. 12]

The synchronizing frequency recorded on the VCR-PCM data tapes was a 7168 Hz square wave, measured with a

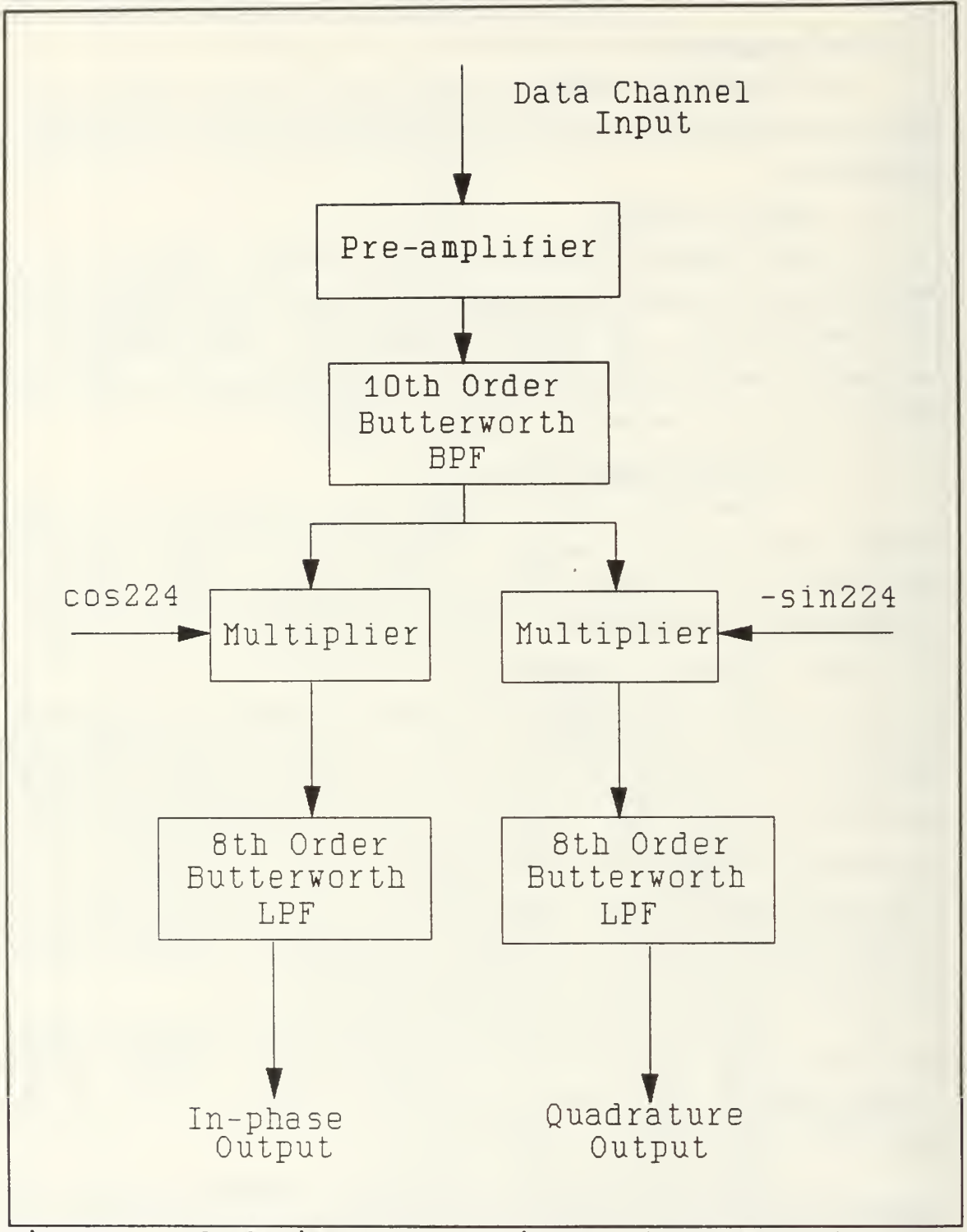

Figure 13: Block Diagram of Multi-channel, Data Synchronous, Quadrature Phase Demodulator data channel (x4).

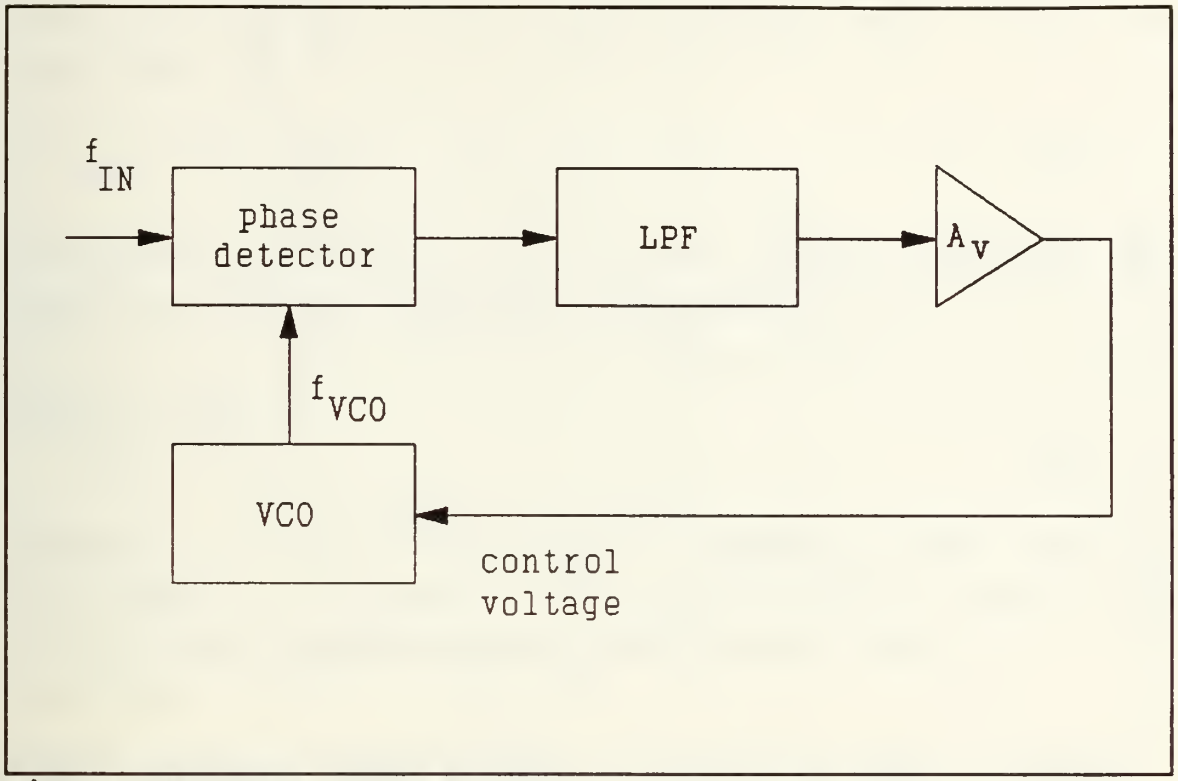

Figure 14: Phase-locked loop.

frequency counter and spectrum analyzer. The measured synchronizing frequency on playback was 7160 ± .5 Hz. The PLL was used to lock-on this frequency and in the event of signal loss, to output 7168 Hz, thus producing a predictable error. This was necessary because on several of the tapes there are periods as long as 10 seconds where the signal is completely overcome by a noise source of unknown origin. The unknown noise source caused the counters to miss count thus inducing a time shift in the data output that could not be compensated for, or predicted.

In this design application of the SE565F the design parameters of interest are:

FREE RUNNING FREQUENCY

$$f_o = 1/(3.7R_oC_o) \qquad (20)$$

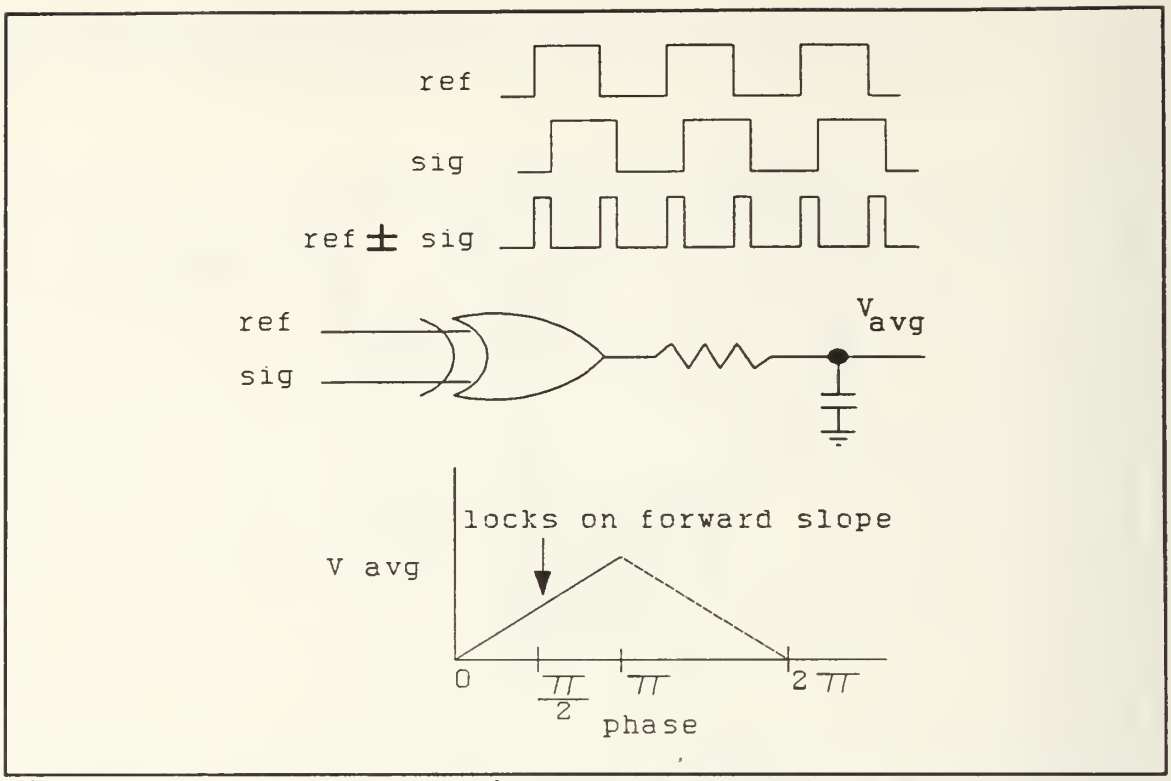

Figure 15: Type I, Exclusive-OR-gate phase detector [from Ref. 14].

for a free running frequency of 7168 Hz and choosing a value of C_o=.01 μF, the value of R_o should be 3.8 kΩ. A 5 kΩ potentiometer was substituted for the 3.8 kΩ resistor to allow for fine tuning of the free running VCO output.

LOOP GAIN

$$\text{Loop Gain} = K_o K_D (1/\text{sec}) \qquad (21)$$

K_o = oscillator sensitivity [(radians/sec)/volt]

K_D = phase detector sensitivity (volts/radian)

The loop gain of the SE565F is dependent on the free running

frequency and the total supply voltage (V_c). It may be calculated by:

$$K_o K_D = 33.6 f_o / V_c \qquad (22)$$

The SE565F is powered by a ± 12 V power supply. Therefore, the loop gain for this application is 1.0×10^4.

HOLD IN RANGE

$$f_H = \pm 8 f_o / V_c \qquad (23)$$

The Hold In Range is the range of frequencies that the loop will remain in lock after initially gaining lock. Substituting in the values for this application yields a value of ± 2389 Hz.

LOOP FILTER

It is usually desirable to filter the output of the phase detector. In narrow band applications involving a slowly varying carrier where narrow noise bandwidth is desired a lag-lead filter is used, Figure 16.

The natural bandwidth (f_n), of the closed loop response is:

$$f_n = \frac{1}{2\pi}\sqrt{\frac{K_o K_D}{R_1 C_1 K_o K_D}}. \qquad (24)$$

An arbitrary value of 10 Hz was selected for f_n since ideally there should be very little frequency drift and this value is well within the circuit's operating range. There is also a damping factor δ, associated with f_n:

$$\delta = \frac{1}{2}\sqrt{\frac{1}{R_1 C_1 K_o K_D}}. \qquad (25)$$

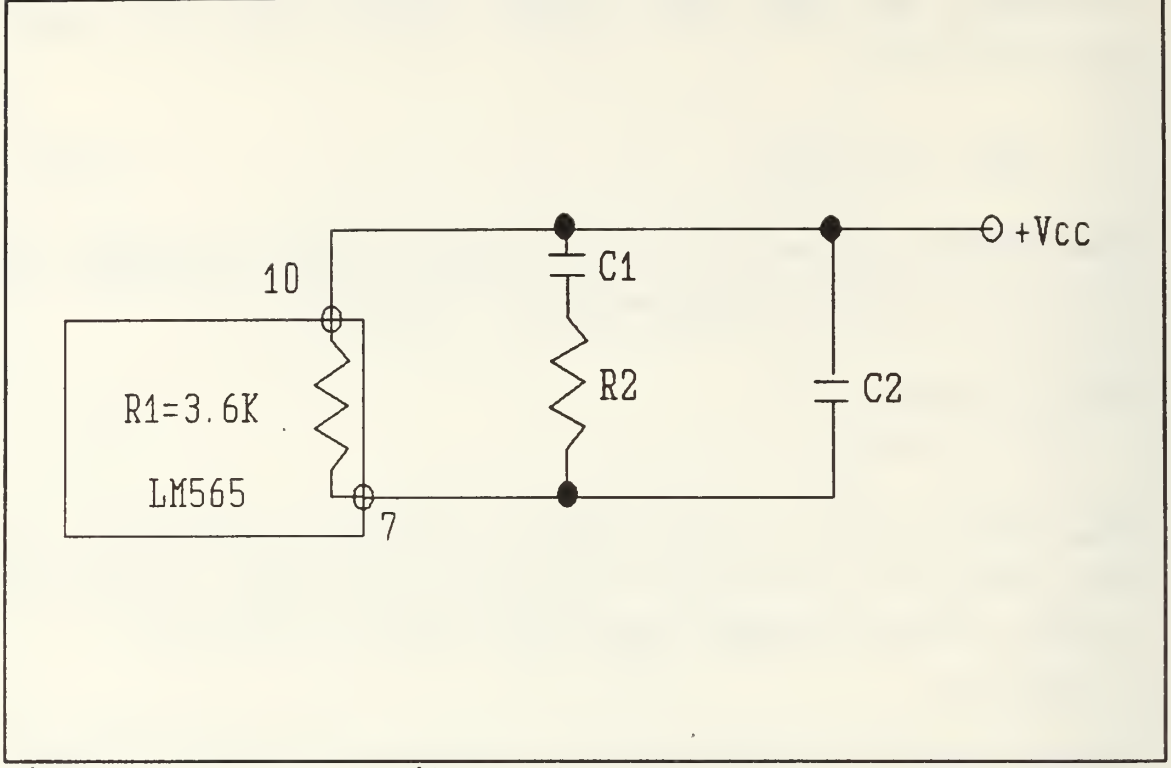

Figure 16: Lag-lead filter [from Ref. 14].

The desired value of δ is between 0.5 and 1.0. The value of R_2 is selected to produce this result. The damping factor can also be found from the approximation:

$$\delta = \pi \tau_2 f_n \tag{26}$$

$$\tau_2 = R_2 C_1 \tag{27}$$

Using Equations 26 and 27 and choosing R_2=10 ohms, C_1=3.1 μF. Now using Equations 28 and 29 the value of R_1 can be determined, R_1=2.7 MΩ.

$$f_n = \frac{1}{2\pi}\sqrt{\frac{K_o K_D}{\tau_1+\tau_2}} \tag{28}$$

$$\tau_1+\tau_2 = (R_1+R_2)C_1 \quad (29)$$

Figure 17 illustrates the connections for the PLL.[Ref. 12]

b. RS-232

The output from the PLL is a 7161 Hz square wave which is then sent to a RS232 serial interface. The RS232 used is the MAX232CPE, which is a +5 V powered RS232 that meets EIA RS-232C and CCITT V.28 specifications and requires no external components. The MAX232CPE converts the bipolar ± 12 V input to unipolar, 5 V TTL/CMOS output.[Ref. 13]

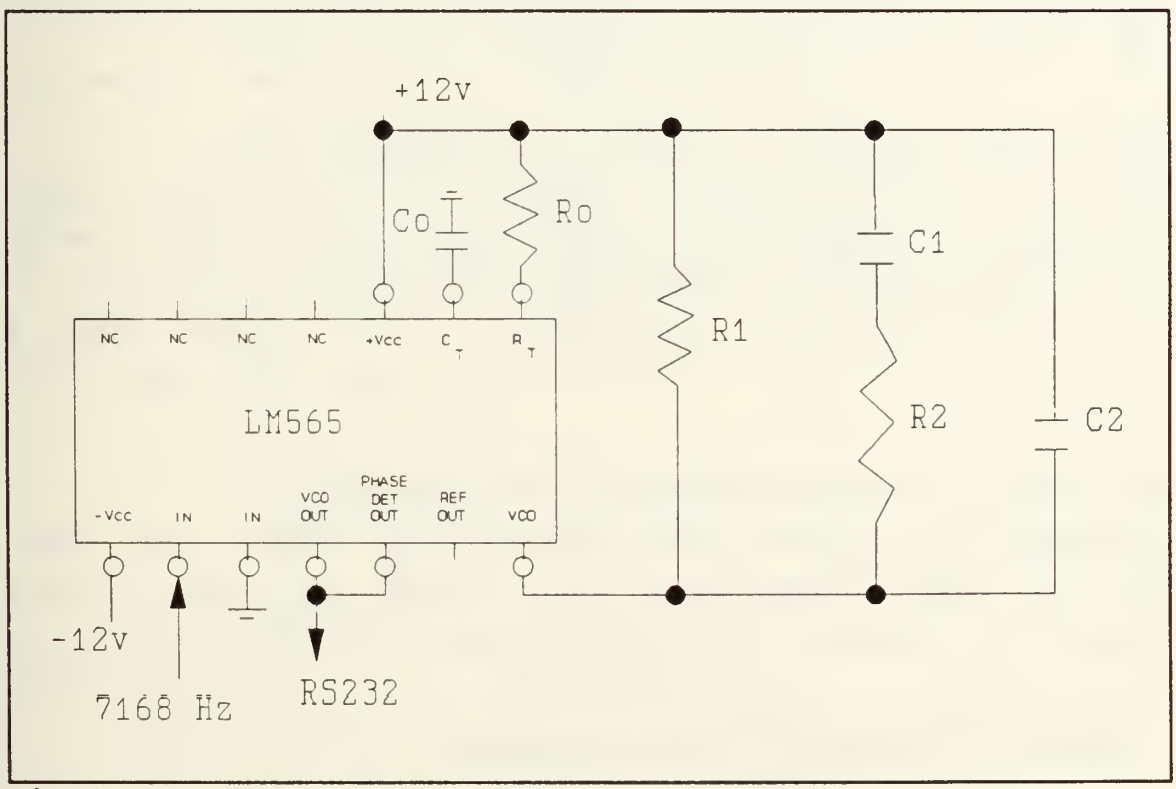

Figure 17: Phase-locked loop.

c. Monostable Multivibrator

The RS232 output is received by a Monostable Multivibrator with a Schmitt-Trigger input. The Monostable Multivibrator, SN74121N, was added to the circuit to noise isolate the Counters which are susceptible to false triggering due to noise transients. The Schmitt-Trigger input circuitry provides excellent noise immunity up to 1.2 V. Internal latching circuitry also provides V_{cc} noise immunity up to 1.5 V. The Monostable Multivibrator once triggered holds the output high over 90% of the cycle. During this time the output is independent of further input transitions and is only a function of the timing components. Therefore during this time the circuit is immune to noise transients at the input. Figure 18 shows the SN74121N connections.[Ref. 14]

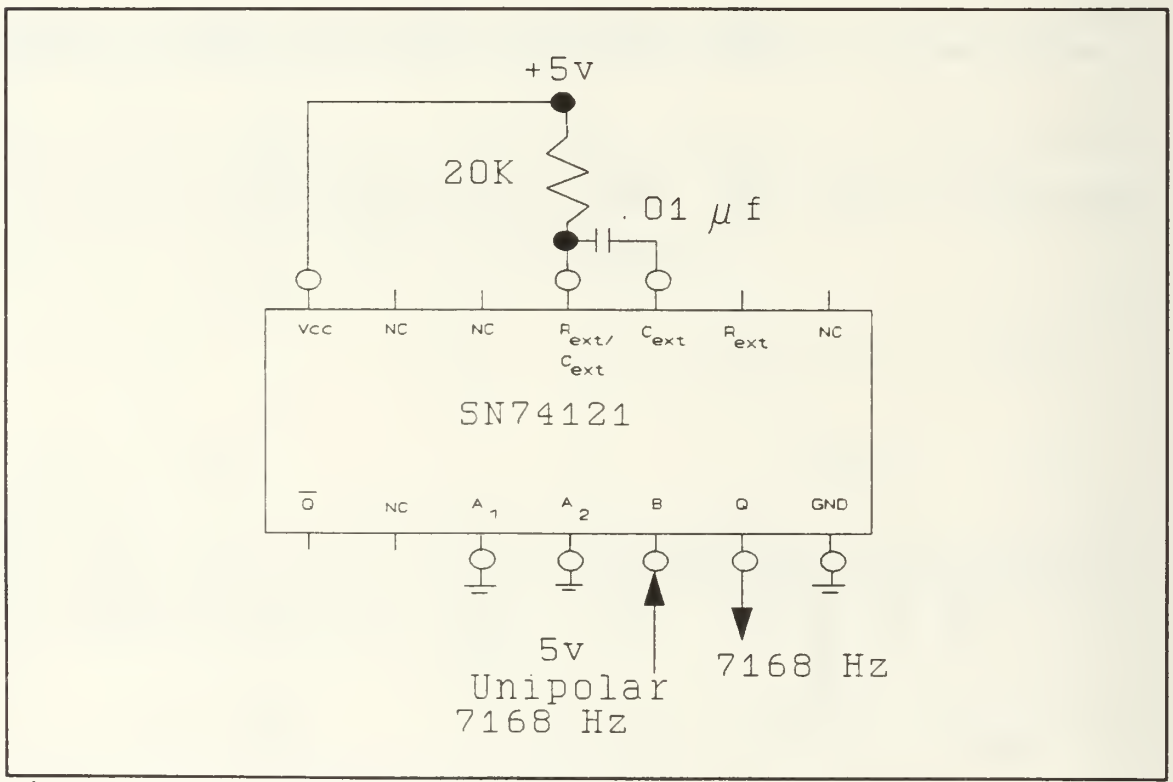

Figure 18: Monostable multivibrator.

d. Counters

The square wave is next processed by a series of positive edge triggered counters which reduce the frequency. The counters reduce the frequency in order to perform two functions. The first function is to generate the 64 Hz sampling frequency for the ADC installed in the Zenith Z-248. Their second function is to regenerate the 224 Hz carrier frequency to be used in the phase demodulation.

(1) Divide by 16. The 7168 Hz square wave output of the Monostable Multivibrator is received by a pair of Synchronous 4-Bit Up/Down Binary Counters connected in series. The counters used for the divide by 16 application were the 74AC169 with each counter performing a divide by 8. The synchronous mode of operation for these counters eliminates the output counting spikes normally associated with asynchronous counters. The output from this set of counters is a 448 Hz square wave (Figure 19), which is then sent to the divide by 7 counter and the invertor.[Ref. 15]

(2) Divide by 7. The 448 Hz square wave is the input to the divide by 7 circuit which is a Modulo 16 4-Bit Up/Down Binary Synchronous Counter, the 74F169. The counter is configured to count down to output the desired divide by 7 result which is the 64 Hz interrupt signal for the ADC (Figure 20).[Ref. 16]

(3) Invertor. The 448 Hz square wave is also the input to a simple hex invertor, the N74F04N. The inverted signal is required later in the phase demodulation. The 448 Hz inverted output is then sent to the divide by 2 circuit (Figure 21).[Ref. 15]

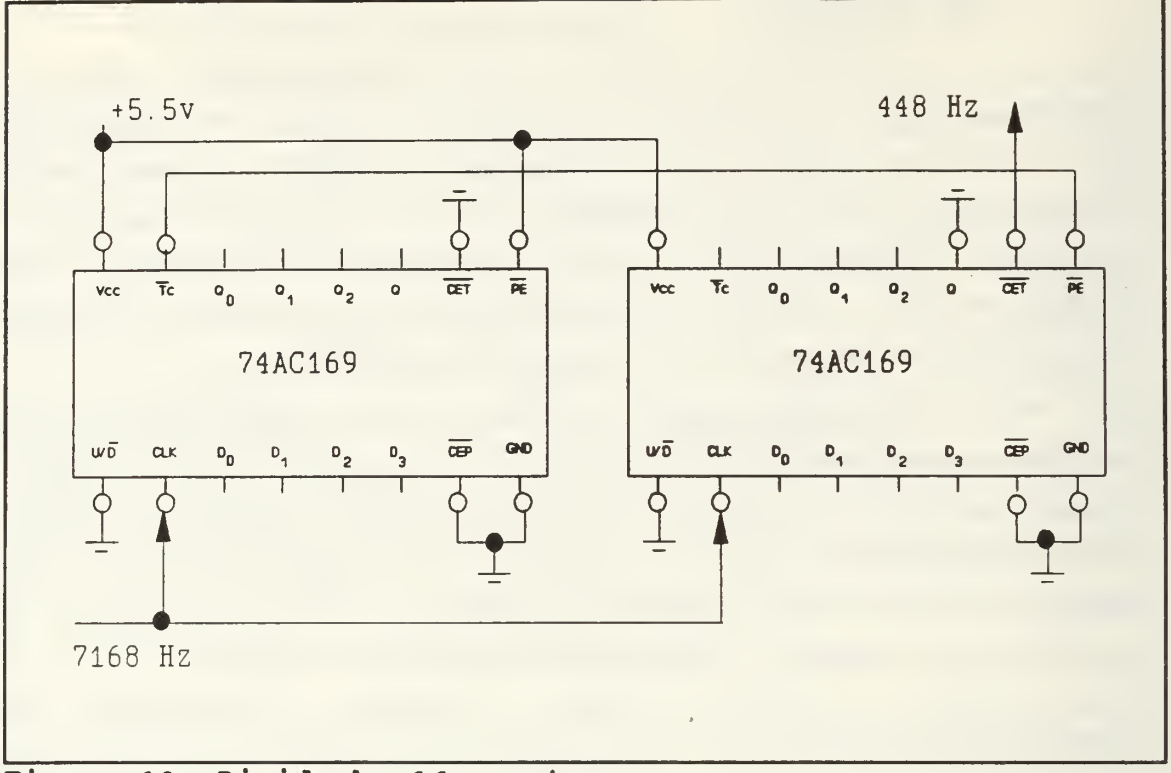

Figure 19: Divide by 16 counters.

(4) Divide by 2. The ± 448 Hz is now divided by 2 and two separate outputs differing in phase by 90 degrees and opposite in sign are produced. A D-Type Flip Flop, the N74F74N, is used for this part of the signal processing (Figure 21). The end result is what will become the 224 Hz cosine and minus sine waves used by the multipliers to perform the first part of the demodulation.[Ref. 15]

e. Timer

There are two timers, one with the 224 Hz square wave input and the other with the 224 Hz inverted, 90 degree phase lagged, square wave input. The timers used are the NE555V in the astable mode [Ref. 17]. The timers are configured in this

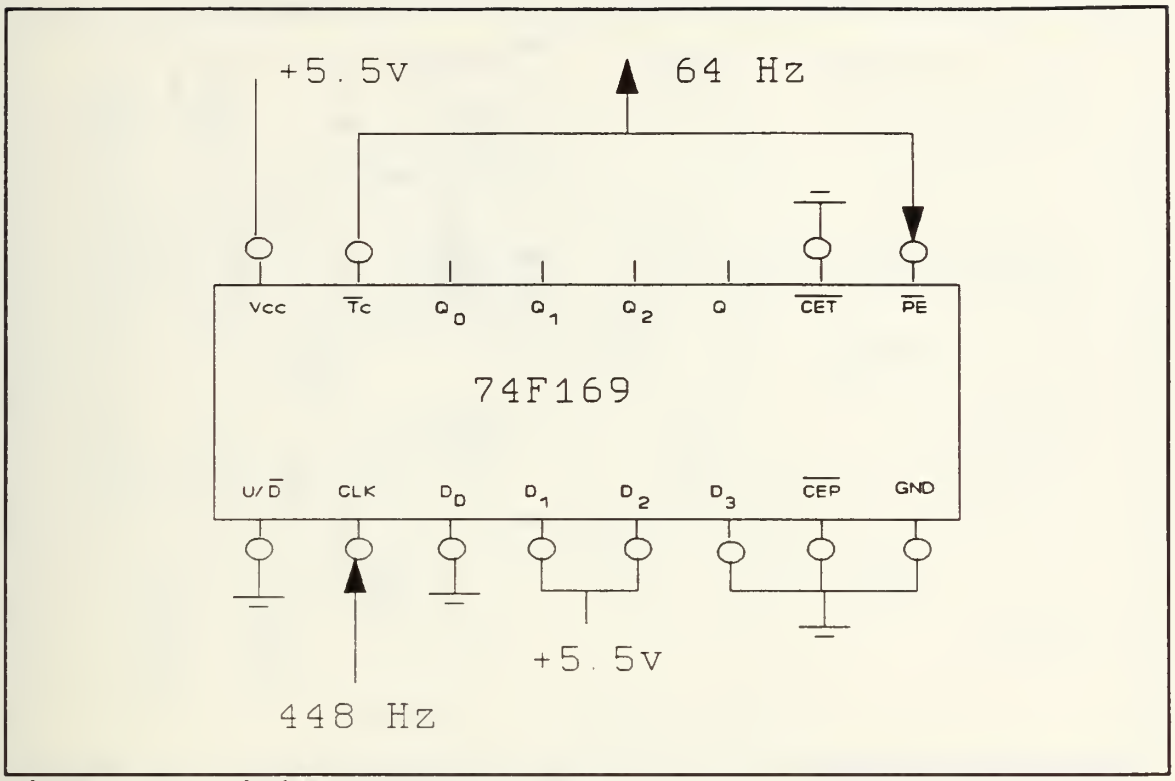

Figure 20: Divide by 7 counter.

mode to operate as repeat cycle timers with the output taken from the high side of the timing capacitor. The RC values in the circuit were adjusted to produce a symmetric triangle wave output followed by a blocking capacitor to remove the DC. An example is shown in Figure 22.[Ref. 18]

f. Low Pass Filter

The triangle wave outputs from the timers are then low pass filtered producing sinusoidal outputs. The filter design required a nearly linear phase response with the maximum amplitude rolloff practical without sacrificing phase characteristics. The filter design chosen was a Fourth Order Butterworth Voltage-Controlled Voltage Source (VCVS) Low-pass filter because of its linear phase response characteristics. The filter design was based on the CA747CE which is a general-

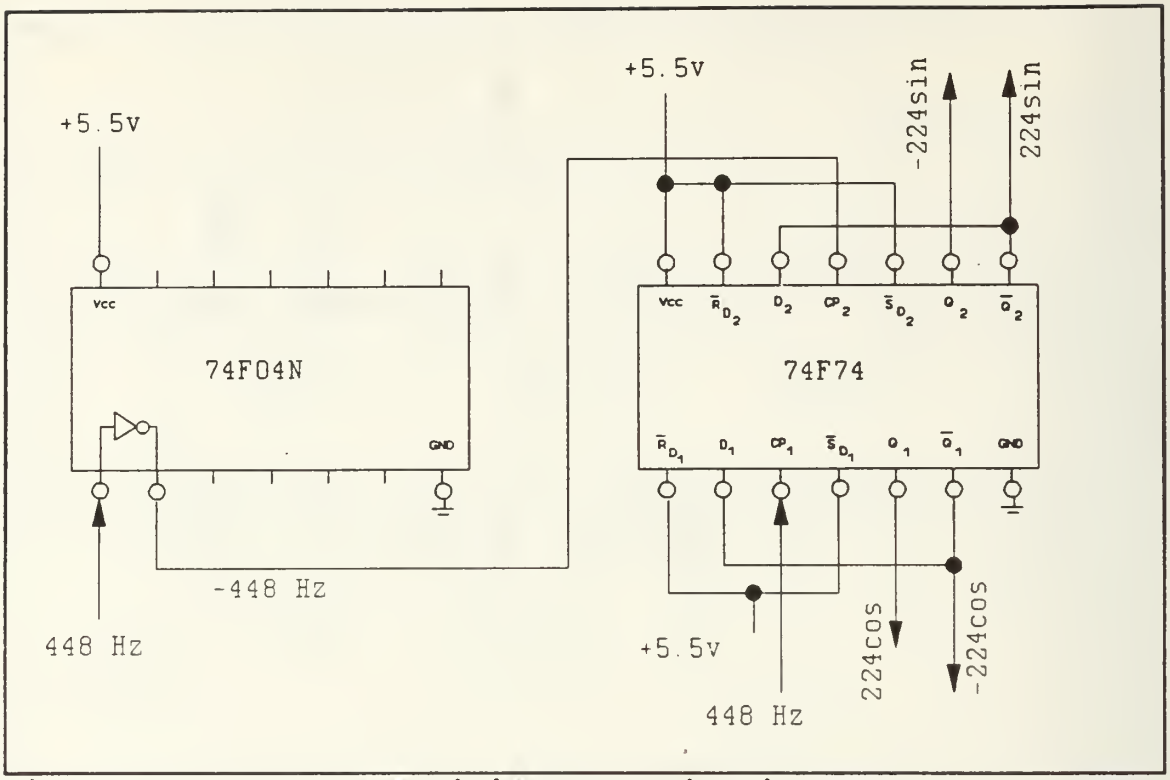

Figure 21: Invert and divide by 2 circuit.

purpose, high-gain, dual operational amplifier [Ref. 19]. In all filter discussions throughout this thesis the cutoff frequency, ω_c, is defined as the point where the loss α in dB of the amplitude function equals -3 dB.[Ref. 9]

(1) Butterworth Filter. An ideal low-pass amplitude and phase response is shown in Figure 23. A realizable $|H(jw)|^2$ that approximates the desired amplitude and phase response of Figure 23 is

$$|H(j\omega)|^2 = \frac{A}{1+f(\omega^2)} \qquad (30)$$

where A=1 in most cases and

$$f(\omega^2) >> 1, \qquad \omega>1$$

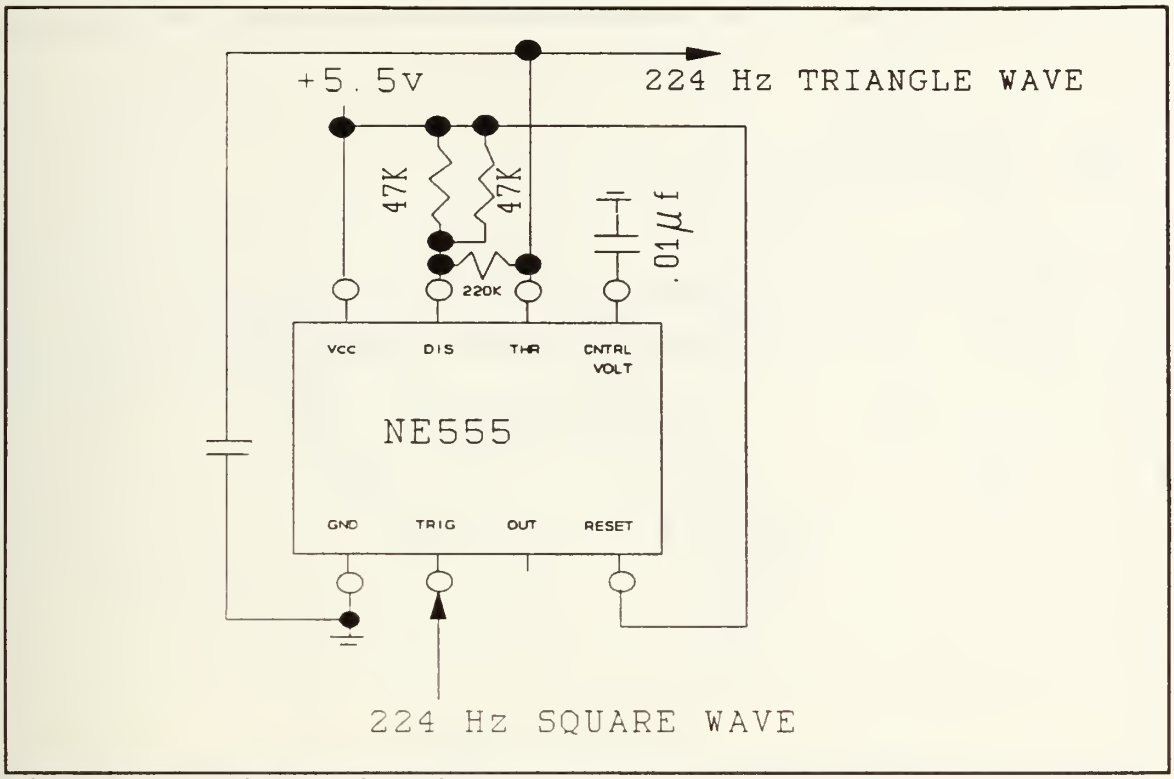

Figure 22: Timer circuit.

$$0 < f(\omega^2) << 1, 0 < \omega < 1,$$

The Butterworth function $f(\omega)=\omega^{2n}$ for n=1, 2, 3.. generally satisfies the criteria of Equation 30. Substituting this function into Equation 30 yields:

$$|H(j\omega)| = \frac{1}{\sqrt{1+\omega^{2n}}} \qquad (31)$$

the amplitude response for an nth-order Butterworth low-pass filter. The function in Equation 31 decreases monotonically, with its maximum value at $\omega=0$. For $\omega>>1$, the approximate loss, α in dB for the Butterworth amplitude function is:

$$\alpha_{dB}(\omega) = 20n\log\omega \qquad (32)$$

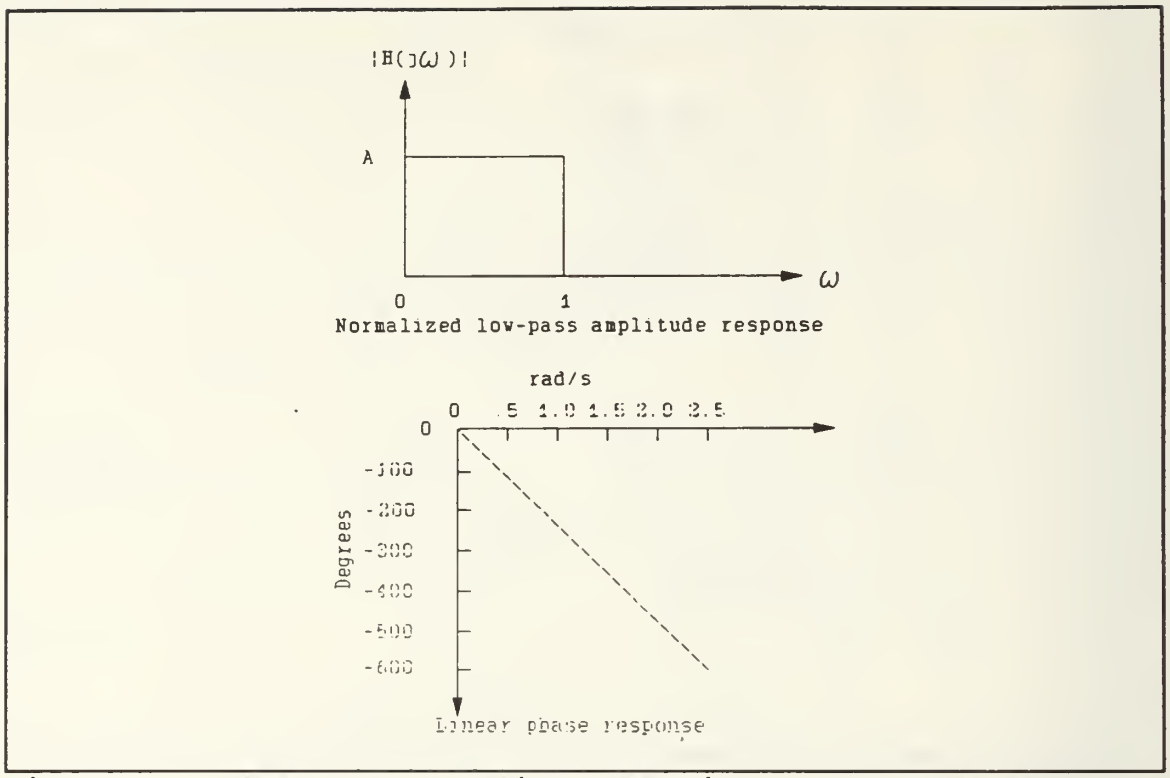

Figure 23: Ideal low-pass filter amplitude and phase response.

for large ω, $\alpha_{dB}(\omega)$ has a slope of 20n dB/decade. Figure 24 shows the amplitude and phase response for a different orders of Butterworth Low-pass Filters. Replacing ω^2 in Equation 32 by $-s^2$ yields

$$H(s)H(-s) = \frac{1}{1+(-s^2)^n}. \qquad (33)$$

So now

$$H(s) = 1/Q(s) \qquad (34)$$

and Q(s) is the Hurwitz polynomial that satisfies the condition

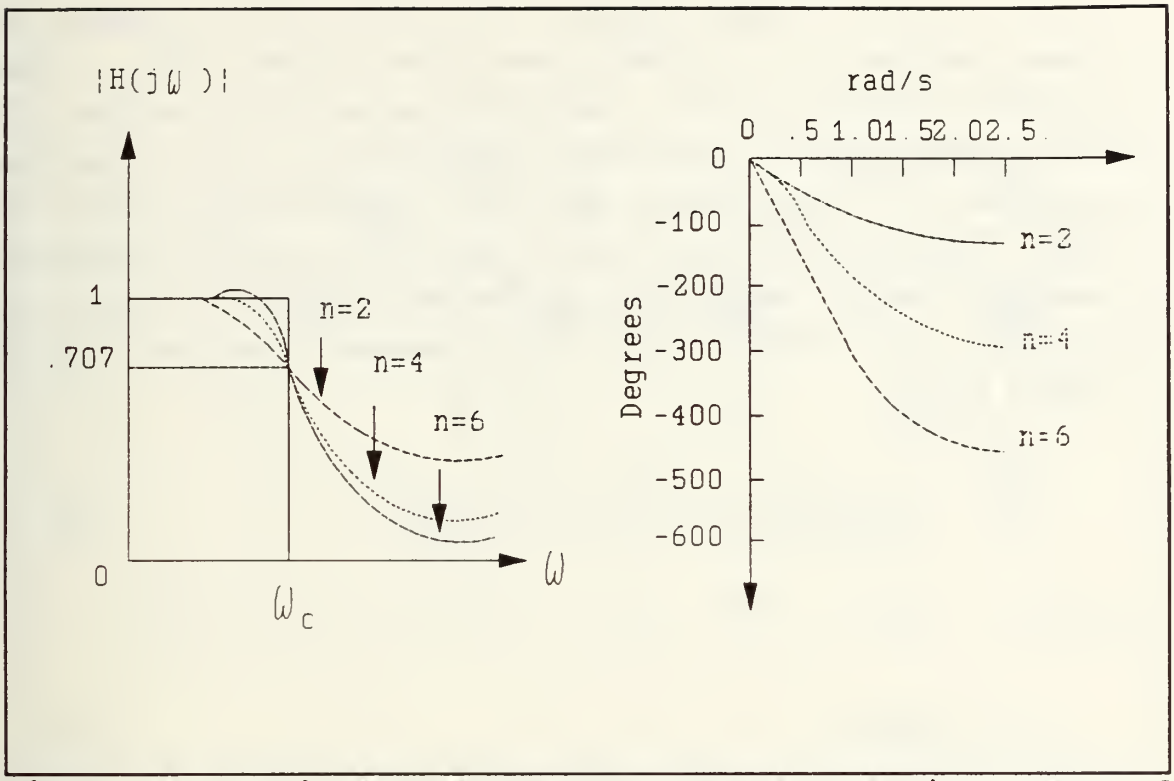

Figure 24: Amplitude and phase response for varying orders of butterworth filters.

$$Q(s)Q(-s) = 1+(-s^2)^n. \tag{35}$$

Q(s), for the general case, is

$$Q(s) = s^n+b_{n-1}s^{n-1}+ \ldots +b_1s+b_o. \tag{36}$$

Substituting back into Equation 34 yields the transfer function for the n^{th} order general case. Therefore, the transfer function for a n^{th} order Butterworth low-pass filter is

$$H(s) = \frac{Kb_o}{s^n+b_{n-1}s^{n-1}+\ldots+b_1s+b_o} \tag{37}$$

where K is a constant for the filter.[Ref. 20]

(2) VCVS Filter. The VCVS filter design was chosen because it is widely used with higher order filters achieved by sequentially cascading second-order stages. The VCVS is also easy to construct requiring only one operational amplifier, two capacitors, and four resistors per stage. The simple design makes the filter easy to tune and there are numerous design handbooks available. Figure 25 shows the design of the VCVS filter. The transfer function for the filter is

$$H(s) = \frac{G^2 b_o^2}{s^4+2b_1 s^3+s^2(2b_o+b_1^2)+2b_1 b_o s+b_o^2} \tag{38}$$

where

$$b_o = \frac{1}{R_1 R_2 C_2 C_1} \tag{39}$$

$$b_1 = \frac{1}{R_2 C_1}(1-\upsilon) + \frac{1}{R_1 C_2} + \frac{1}{R_2 C_2} \tag{40}$$

and

$$G = \upsilon = 1 + \frac{R_4}{R_3} \tag{41}$$

and μ is the gain of the VCVS and the filter.[Ref. 21]

g. Buffer Amplifier

The output of the filters is a sinusoid which is then sent to the buffer amplifier. The buffer amplifier was required because the filters could not supply sufficient current for the multiplier input.

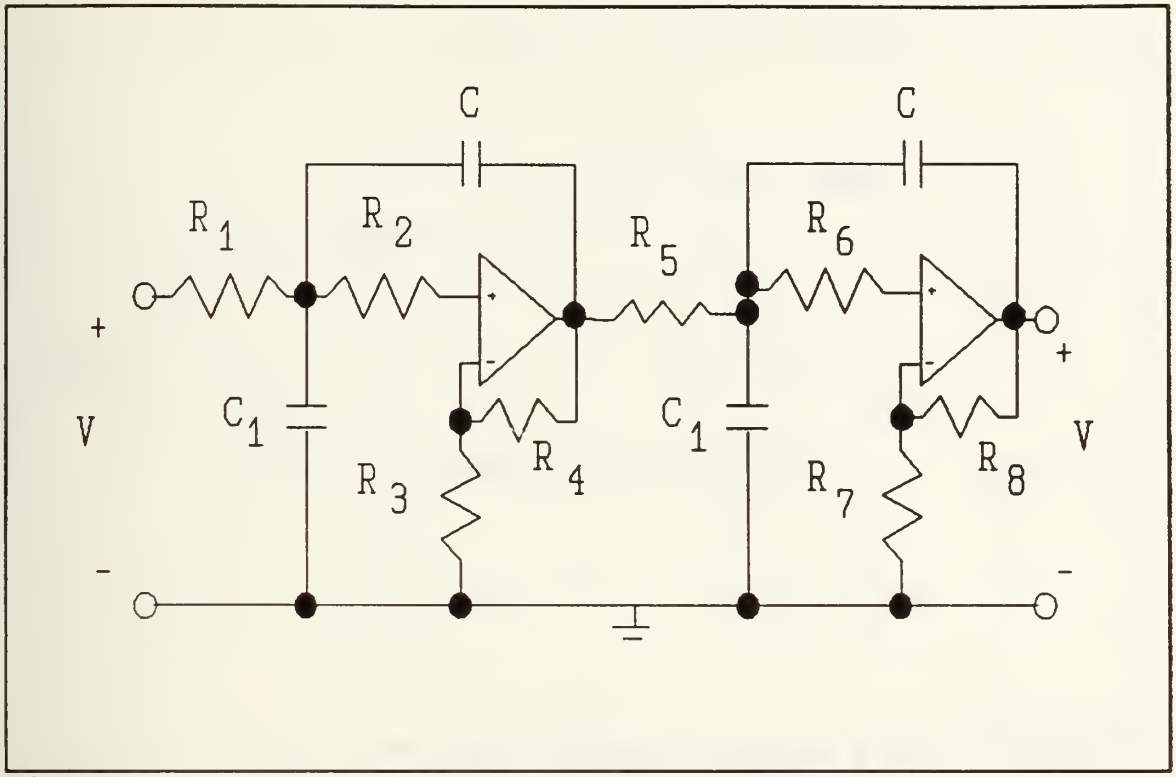

Figure 25: Fourth order VCVS low-pass filter.

4. Data Channel

The Multi-Channel Data-Synchronized Quadrature Phase Demodulator is capable of processing four channels of data simultaneously. The design can easily be expanded to more channels if necessary, by simply adding more data channels since the design of all the data channels is identical.

a. Preamplifier

The input from the VCR-PCMs is received first by the preamplifiers. The preamplifiers were required because the output amplitude of the VCR-PCMs was insufficient for the band-pass filters. Figure 26 shows the preamplifier configuration.

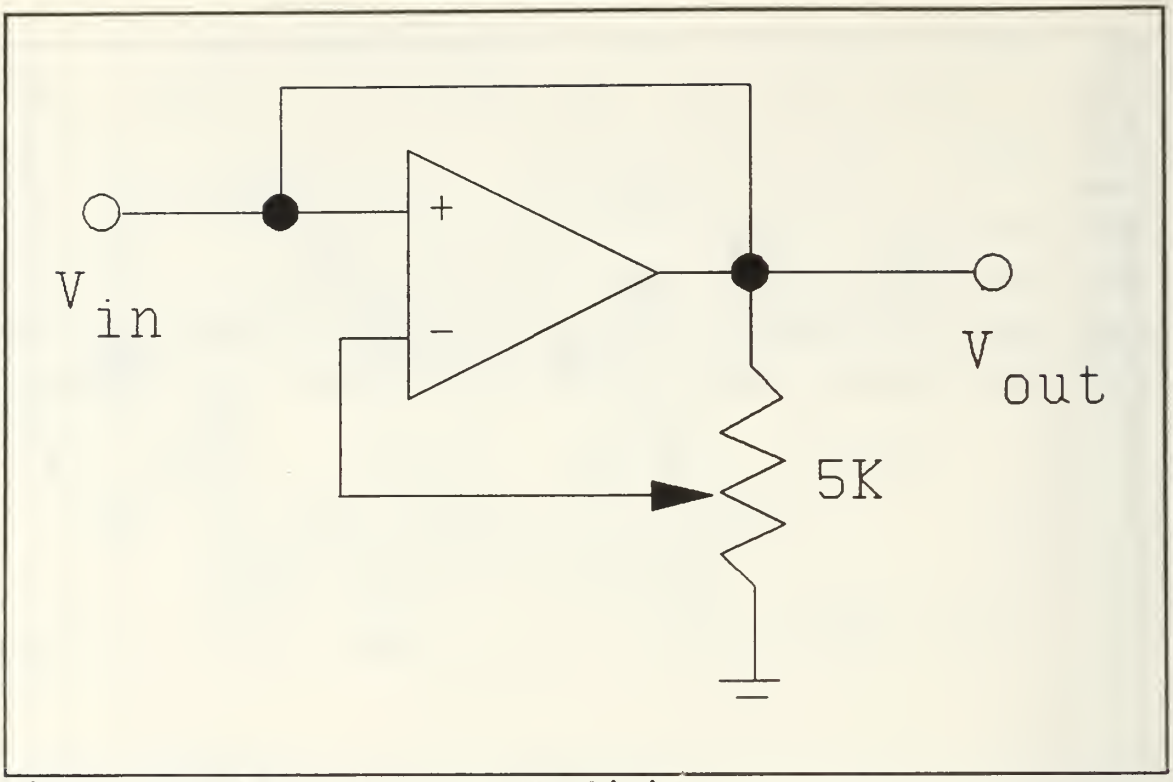

Figure 26: Data channel preamplifier.

b. Bandpass Filter

In order to minimize the noise outside the passband of the signal, a 10^{th} order Butterworth band-pass filter was placed in the input after the preamplifier. The filter was constructed using the AF100-1CN universal active filter integrated circuit. Figure 27 shows the basic second order configuration of the circuit. Multiple stages are cascaded by varying the values of R_{in} and R_f to match the Q's between stages with the 1MΩ potentiometer and 10 kΩ resistor connected to +IN only on the last stage to eliminate any bias. The AF100-1CN is a state-variable active filter. The filter can realize any of the classic filter configurations such as Butterworth, Chebyshev or Bessel with low-pass, band-pass, and high-pass functions all available simultaneously at separate outputs. The filter is programmed in most applications using only four external resistors which are determined through the use of a computer program that is supplied with the integrated

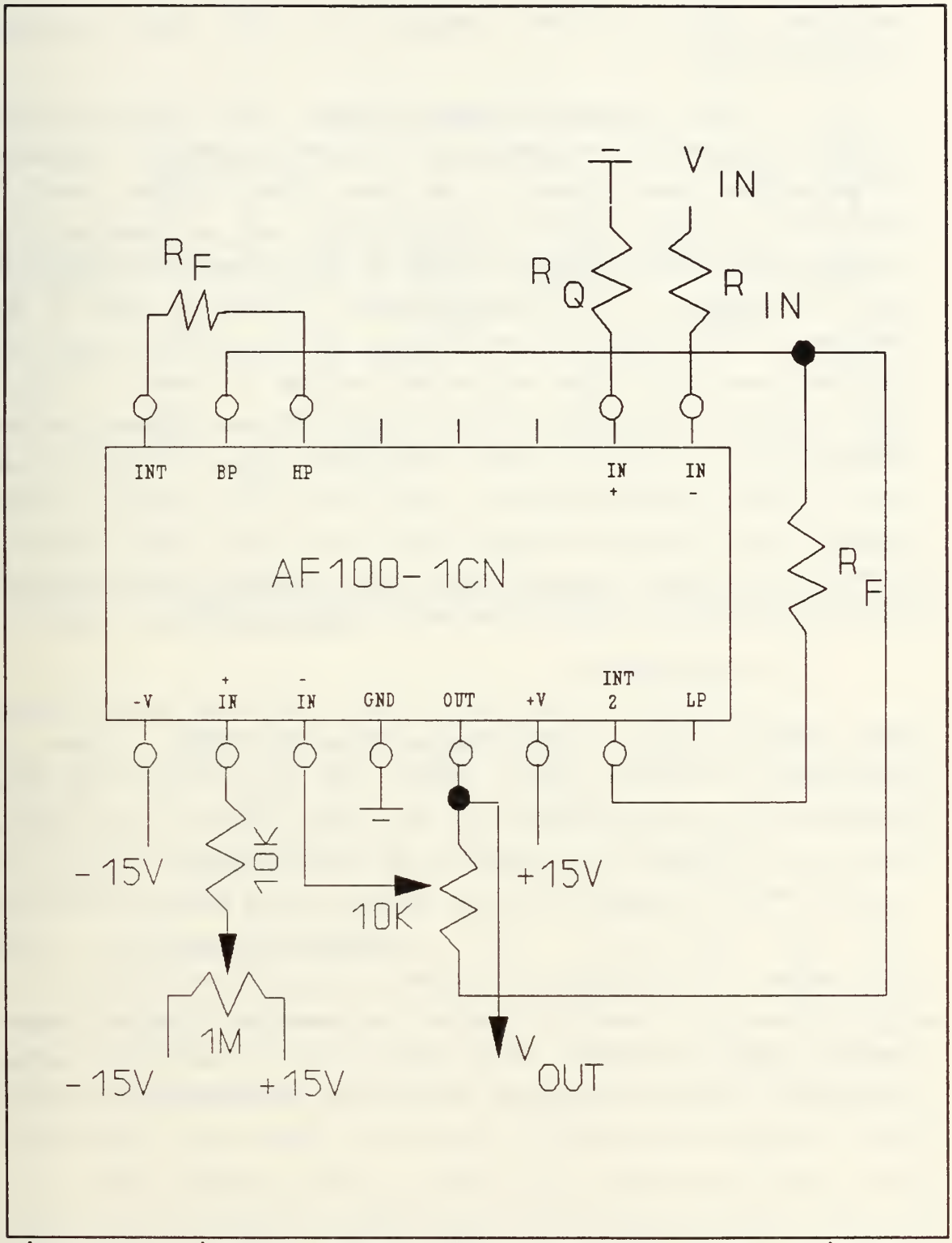

Figure 27: Single, second-order stage of band-pass filter.

circuit. Higher order filters are realized by cascading sections with 8^{th} order low-pass and 18^{th} order bandpass possible.[Ref. 22]

(1) State-Variable Filter. The state-variable filter is a general second order lumped RC network with three outputs that uses three IC op amps. The filter itself is composed of two cascaded integrators and a summing block (Figure 28), with an added op amp at the output for additional gain if needed. The state-variable filter is also a good choice for this application because it requires low open loop gain at resonance from the op amp making it ideal for high Q applications. Figure 29 shows amplitude and phase response comparisons for Butterworth, Chebyshev, and Elliptic band-pass filter configurations of the AF100-1CN. The Butterworth response was chosen because it was the most linear.Figure 30 compares the phase responses if the filter order is varied including the 10^{th} order Butterworth band-pass filter.[Ref. 23]

c. Multiplier

There are two multipliers for each data channel. The signal is split after the band-pass filter to feed each multiplier. The multiplier takes the output from the band-pass filter and multiplies it with the cosine of the carrier for the In-phase (I) channel and the negative sine of the carrier for the Quadrature (Q) channel. The multiplier chosen for this application was the AD534K Internally Trimmed Precision IC Multiplier (Figure 31). The AD534K is a monolithic four-quadrant laser trimmed multiplier with a maximum multiplication error of ± 0.5%. The AD534K offers excellent supply rejection, low noise, and gains up to 100.

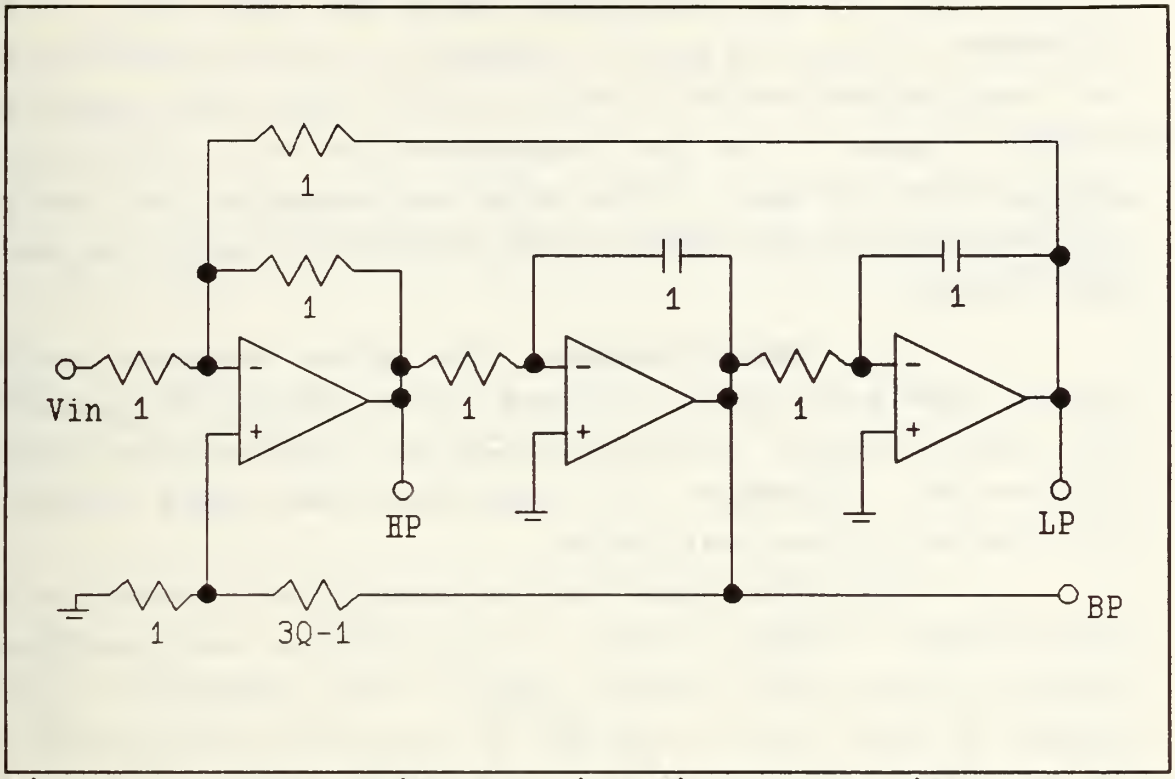

Figure 28: State-variable active filter normalized to 1 ohm and 1 rad/s.

When the I and Q components of the bandpass signal are multiplied with the cos(224t) and sin(224t) the bandpass signal is shifted down to the baseband and to twice the carrier. These demodulated signals are then sent to low-pass filters to remove the twice-carrier components.[Ref. 24]

d. Low Pass Filter

The output from each multiplier is sent to an eighth order Butterworth low-pass filter to remove the upper spectrum with only the baseband being passed. Again, prior to filter construction the phase response of the Butterworth, Chebyshev, and Elliptic Low-pass Filters were compared (Figure 32). The filter used is again the state-variable filter constructed using the AF100-1CN integrated circuit. The eight order Butterworth is the highest realizable order low-pass

filter that can be constructed using the AF100-1CN. It was important to have as good a low-pass filter as possible due to large ambient noise in the 50-60 Hz range that masked the signal. Figure 27 is also representative of a second order stage of the low-pass filter with the exception that for the low-pass filter the output used is the low-pass vice band-pass output.

(1) Phase Response. The phase response for the eighth order Butterworth low-pass filter (Figure 32), exhibits the same favorable characteristics as the band-pass filter (Figure 29). Therefore, the Butterworth was again chosen as the type of filter realization.

The output from the low-pass filters completes the demodulation process. There is an In-phase and Quadrature output for each data channel input to the demodulator. This output is then sent to the ADC in the Zenith Z-248 where it is sampled and digitized for further processing.

5. Power Supply

The demodulator requires 120 VAC 60 Hz to operate. It incorporates built in transformers which convert the power to the various DC voltages required.

a. Power Requirements

The integrated circuits used in the demodulator required three different voltages to function. The TTL Logic requires +5 VDC. The PLL requires ± 12 VDC to operate. All the other integrated circuits use ± 15 VDC. These voltages can all be produced by a single power supply. Unfortunately, due to time constraints and parts availability, three small power supplies were used instead.

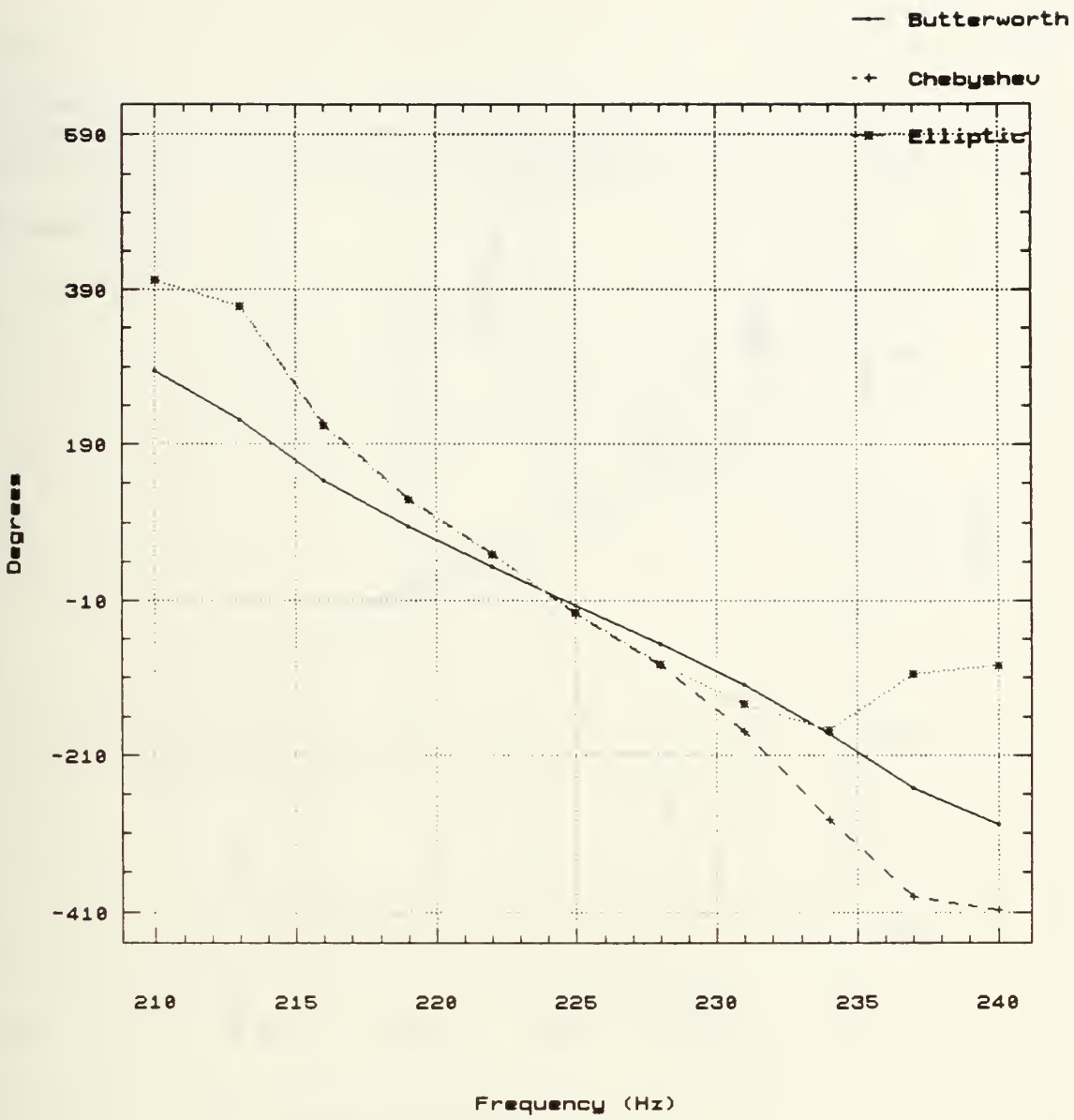

Figure 29: Phase response comparison of Butterworth, Chebyshev, and Elliptic band-pass filters.

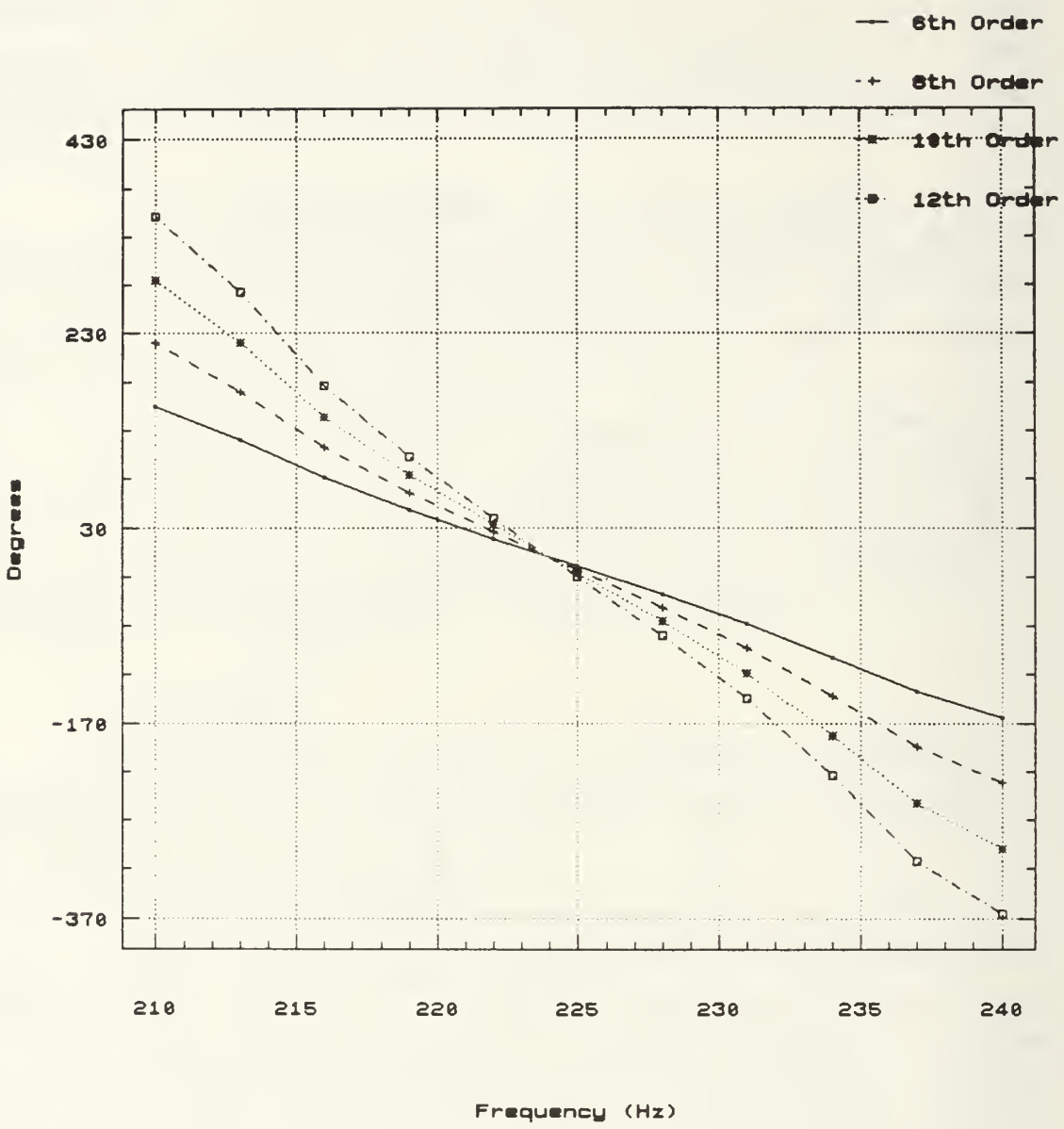

Figure 30: Phase response comparison of various order Butterworth band-pass filters.

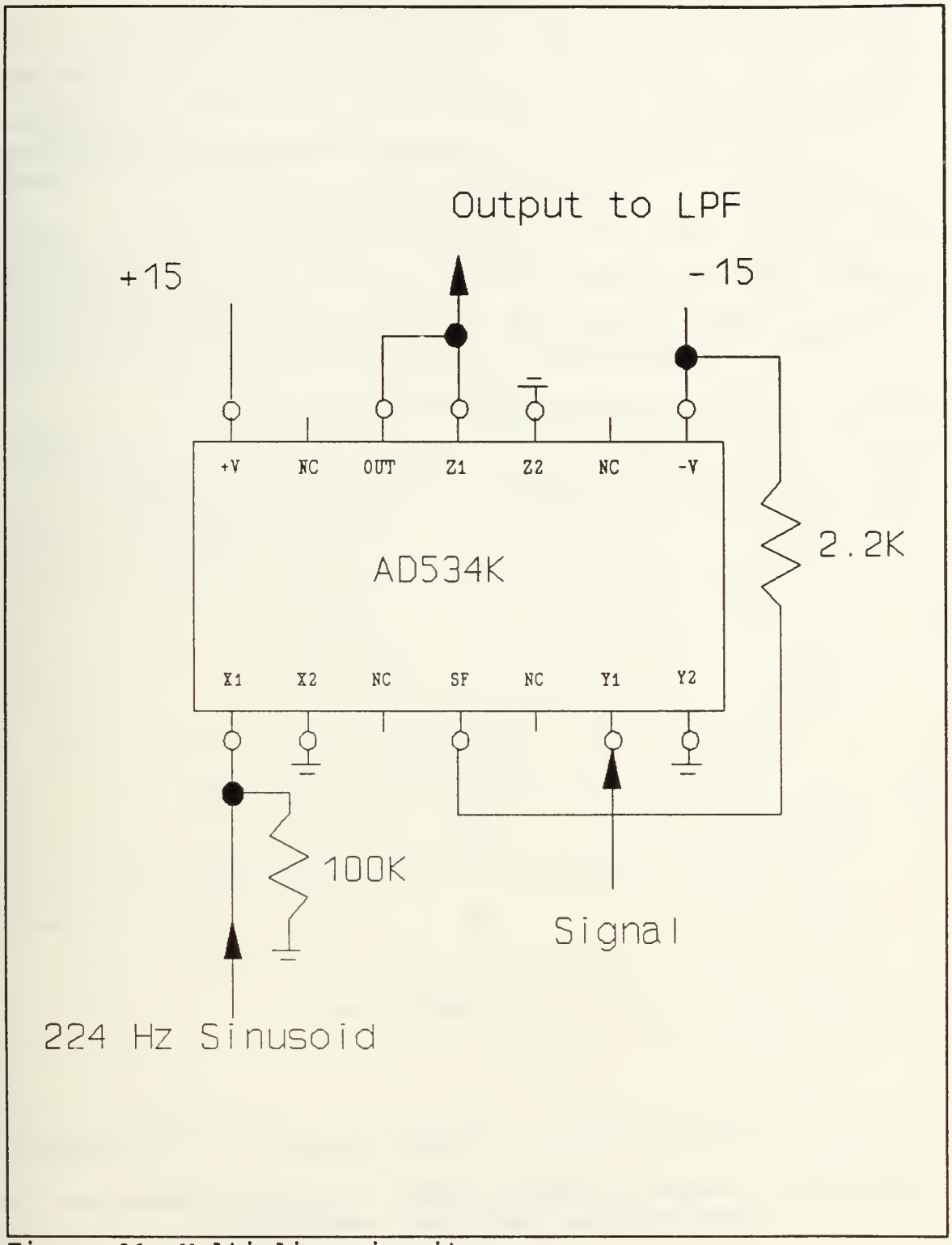

Figure 31: Multiplier circuit.

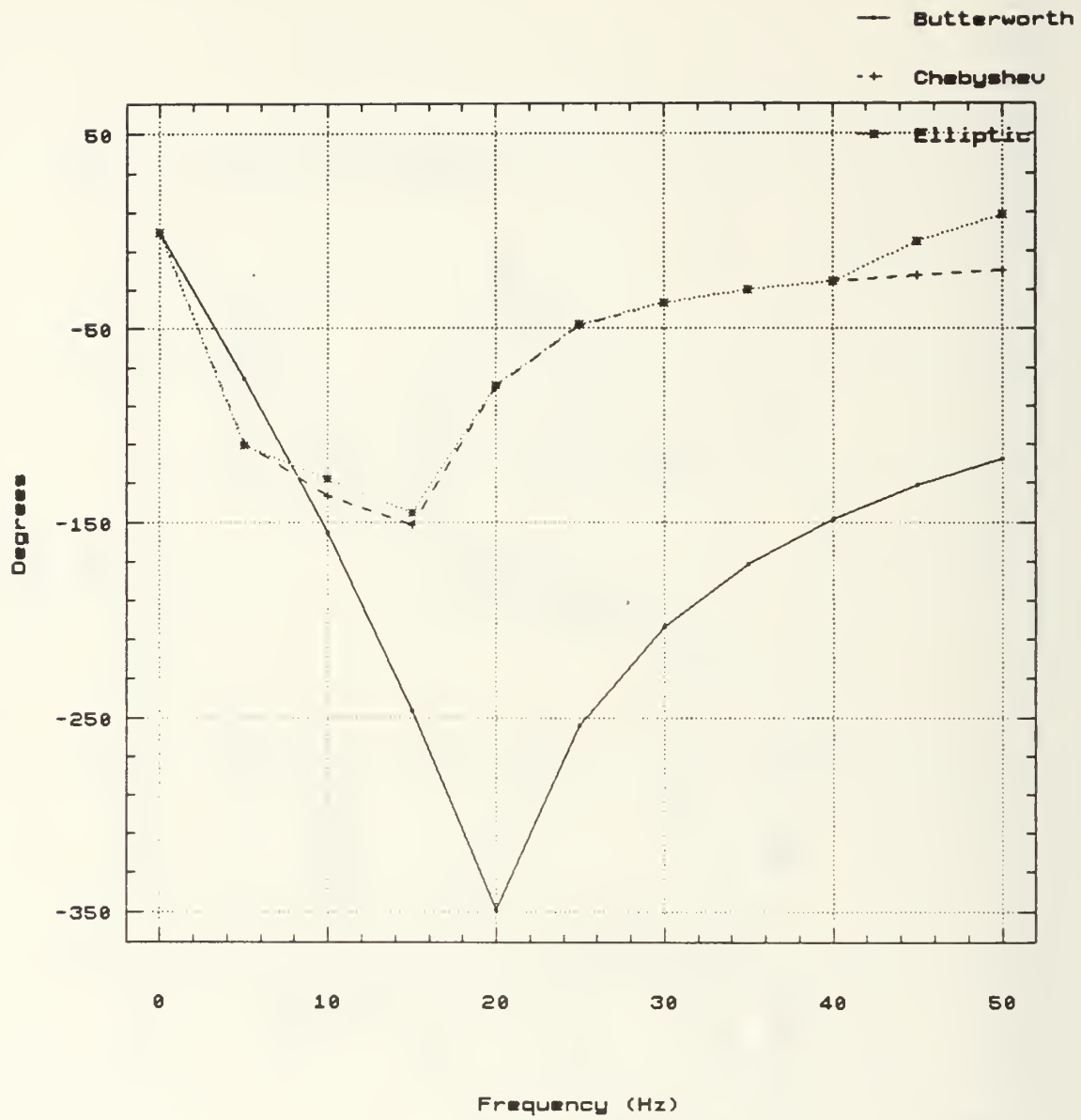

Figure 32: Low-pass filter phase response comparison of Butterworth, Chebyshev, and Elliptic.

(1) +5 Volt DC Power Supply. The +5 V power supply used is an Electrostatics, Inc. Model 10-5. The supply is rated at +4.5-5.5 V, 1.2 A. It features 0.05% voltage regulation with a full load change, less than 250 μV ripple, and automatic current limiting.

(2) ± 15 Volt DC Power Supply. The ± 15 V power supply used is an Electrostatics, Inc. Model 10-1818. The supply is rated at ± 17-19 V, 0.35 A. The output was adjusted using potentiometers built into the unit to output ± 15 V. It has the same features as the +5 V power supply.

(3) ± 12 Volt DC Power Supply. The ± 12 V power supply was constructed using a UA7912 and a UA7812 and four 0.1 μF capacitors (Figure 33). This circuit takes a ± 15 V input and steps it down to ± 12 V. The ± 12 V is required to operate the PLL.

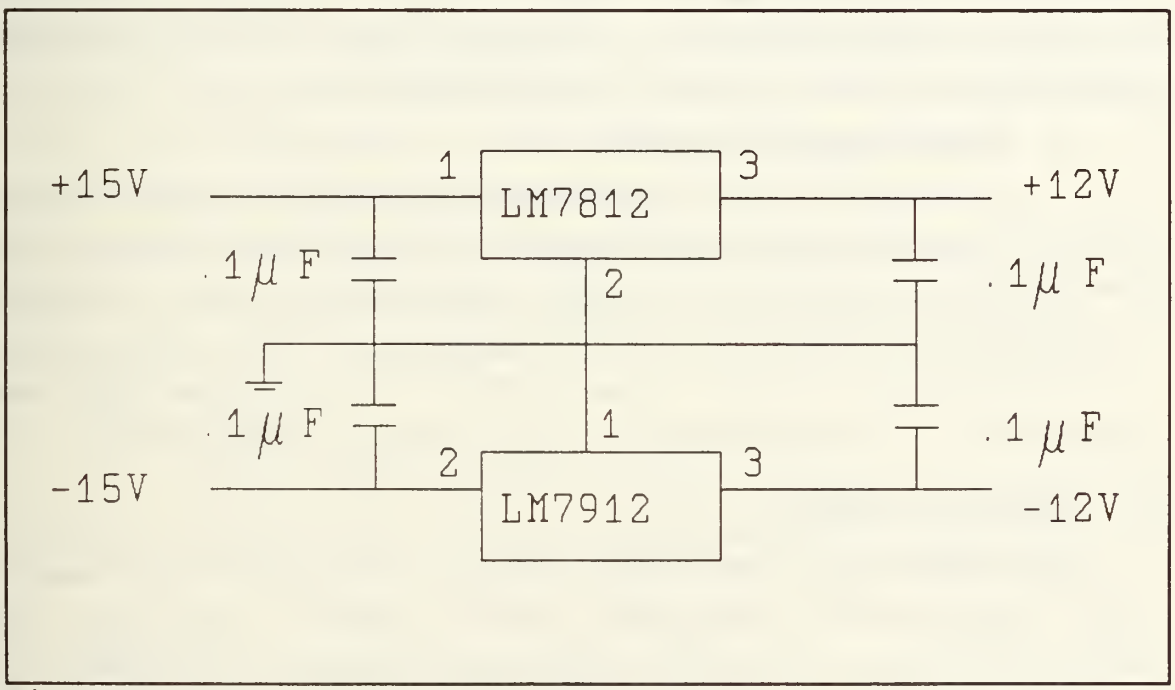

Figure 33: ± 12 V power supply.

IV. PERFORMANCE

A. SPECIFICATIONS

1. Input Specifications

The demodulator was designed to receive the output from the VCR-PCM. Each VCR-PCM is capable of reproducing three data channels plus a synchronizing channel. The demodulator was designed for four data channels to provide redundancy if needed. Each VCR-PCM consists of a modified Yamaha Hi-Fi Stereo Videocassette recorder (YV-1000) which records two audio channels plus two digital pulse code modulated (PCM) audio channels using a Sony PCM-501ES Digital Audio Processor which is wired into the circuit and a time code signal. Maxell XL Hi-Fi 120 videocassette tapes were used to record six hours of data on extended play. A listing of the relevant VCR-PCM specifications can be found in Appendix C.

2. Output Specifications

The demodulator was designed to output to a Metrabyte DASH 16F Analog to Digital Converter. This greatly simplified the design because all channels required only one volt peak to peak output with 75 ohm load impedance. The channel gain is adjustable to allow fine tuning to eliminate bias and compensate for differences in input channel gain.

B. TESTING OVERVIEW

The demodulator was tested using a phase modulated signal that simulated the tomographic source signal. The signal was generated using a HP3325A Synthesizer/Function Generator in the phase modulated mode generating a 224 Hz sine wave. The sine wave was phase modulated using a HP3312A Function Generator generating a 16 Hz square wave.

C. TEST RESULTS

1. Timing Channel

The PLL was easily able to lock on to a synchronizing signal with amplitudes as low as 150 mV below this value it would drop lock. This was not a problem since the synchronizing signal had an amplitude of approximately 800 mV.

2. Data Channel

The data channels had preamplifiers in the input which allowed processing of signals as low as 50 mV. Again this was adequate because the signal normally varied in amplitude from 250-500 mV. The preamplifiers were adjusted to provide adequate gain for input levels as low as 200 mV.

D. RELIABILITY

The reliability of the Multi-Channel Data-Synchronized Quadrature Phase Demodulator was a critical issue since there was only one demodulator and all the data had to be processed by it. For redundancy, a fourth channel was built in.

1. Mean Time Between Failures

The demodulator successfully demodulated over 396 hours of Tomographic data with no failures. Therefore, the demodulator has demonstrated a high degree of reliability.

E. DIMENSIONS

The demodulator measures 17 inches long by 13 inches wide and is 4 inches high. The total weight of the demodulator is 8 pounds 12 ounces. This makes the unit easily transportable.

F. COST

The demodulator uses all off the shelf components requiring no special parts, this minimizes the overall cost of parts for the demodulator. The total cost of the demodulator was approximately $1045.00.

V. DATA PROCESSING

Data analysis was not actually part of this thesis since the thesis dealt with the signal processing and was hardware oriented. However, the demodulator cannot be fully tested with only a laboratory test signal. Therefore to fully determine if the demodulator is functioning properly a real signal must be processed. The actual data analysis for this experiment was the subject of a Master's Thesis by Robert C. Dees (Reference 23) and this chapter will very closely follow the development of Chapter IV from that thesis except data from Station L will be analyzed vice Station J [Ref. 25].

A. GENERAL SUMMARY OF THE DATA

1. Acoustic Data

Approximately 300 hours of acoustic data was stored on videocassette tapes for later signal processing. The data quality varied because of receiver location and equipment inconsistencies. Ambient noise was high at all stations often higher than the 224 Hz signal but, after signal processing all functioning receivers showed some ray arrival structure. There were many sources of ambient noise both biologic and man-made of which only the noise generated by local fishing boats adversely affected signal reception. Radio frequency interference (RFI) occurred more than anticipated with most channels experiencing minor interference and some having their signal completely jammed for several minutes.

Station L was operating from 1030 13 December to 2000 15 December. The data from this channel will be analyzed in this section. There were generally four arrivals with good signal to noise ratio but the two strongest are sometimes unresolved. This station had the simplest bathymetry with a

steady upslope in shallow water after crossing the canyon. A faulty PCM encoder caused loss of the signal over some of the time, however, back up audio tapes recorded on a Honeywell 101E 24 track tape recorder were used to recover the data during those periods. It is interesting to note that although the Honeywell had better specifications than the VCR-PCM, a direct comparison of the data revealed no significant difference in the quality of the two recordings.[Ref.25]

2. Surface Wave Data

The NDBC moored surface wave buoy operated as designed throughout the duration of the experiment and provided hourly reports via satellite downlink of surface wave power spectral density, wave direction, barometric pressure, and temperature. It is this data that will be compared with the tomography data in the same frequency band.[Ref.25]

3. Sound Speed Profile and Current Measurements

The Woods Hole Oceanographic Institution is currently analyzing the data taken during conductivity, temperature, and density (CTD) measurements and by the acoustic Doppler profiler. The sound speed profile results from Reference 5 for two positions near the path of Station L will be shown (Figures 34 and 35).[Ref. 25]

B. STATION L DATA

1. Station L Eigenray Prediction

The two-dimensional bathymetry and MPP eigenray prediction between the source and receiver for Station L are shown in Figure 36. The eigenrays were predicted using a historical sound speed data base. The measured profile very closely matched the historical data base therefore the MPP prediction will be used until the three dimensional prediction is available. The two predicted arrivals have no surface and only one bottom interaction in the deep water but once across

the canyon and into the shallow water there are numerous surface and bottom interactions as expected. It is important to note that while the deep water prediction is reasonable, a small error in the shallow water prediction can dramatically change the number of interactions and therefore greatly effect the transmission loss.[Ref. 25]

2. Measured Sound Speed Profiles

Sound speed profiles measured at two positions near the ray path for Station L are shown in Figures 36 and 37. Figure 34 is the deep water profile and was taken at 36°32.906N 122°16.210W, near the source. Figure 35 is the shallow water profile and was taken at 36°51.095N 122°04.798W, near the receiver. Both figures show two traces, one while the CTD is descending and one while it is ascending. The difference between the curves is due to the effect of internal waves. The difference in depth of a particular sound speed gives a minimum vertical displacement for the internal wave but no amplitude or frequency information. On Figure 35 the 30 meter points are 4 minutes apart based on a 30 meter per minute descent/ascent rate for the CTD while on Figure 34 the 100 meter points are one hour apart based on a 45 minute descent/ascent rate for the CTD. The Brunt-Väisälä frequency can be calculated at the density gradient using the CTD measurements as

$$n = \sqrt{-\frac{gdp}{\rho dz}} \qquad (42)$$

for depth z, density ρ, and gravitational acceleration g. The Brunt-Väisälä frequency is directly proportional to the gradient both reaching a maximum at the same time. For the shallow water case (Figure 35), and using Equation 42 the minimum period is 8.3 minutes.[Ref. 25]

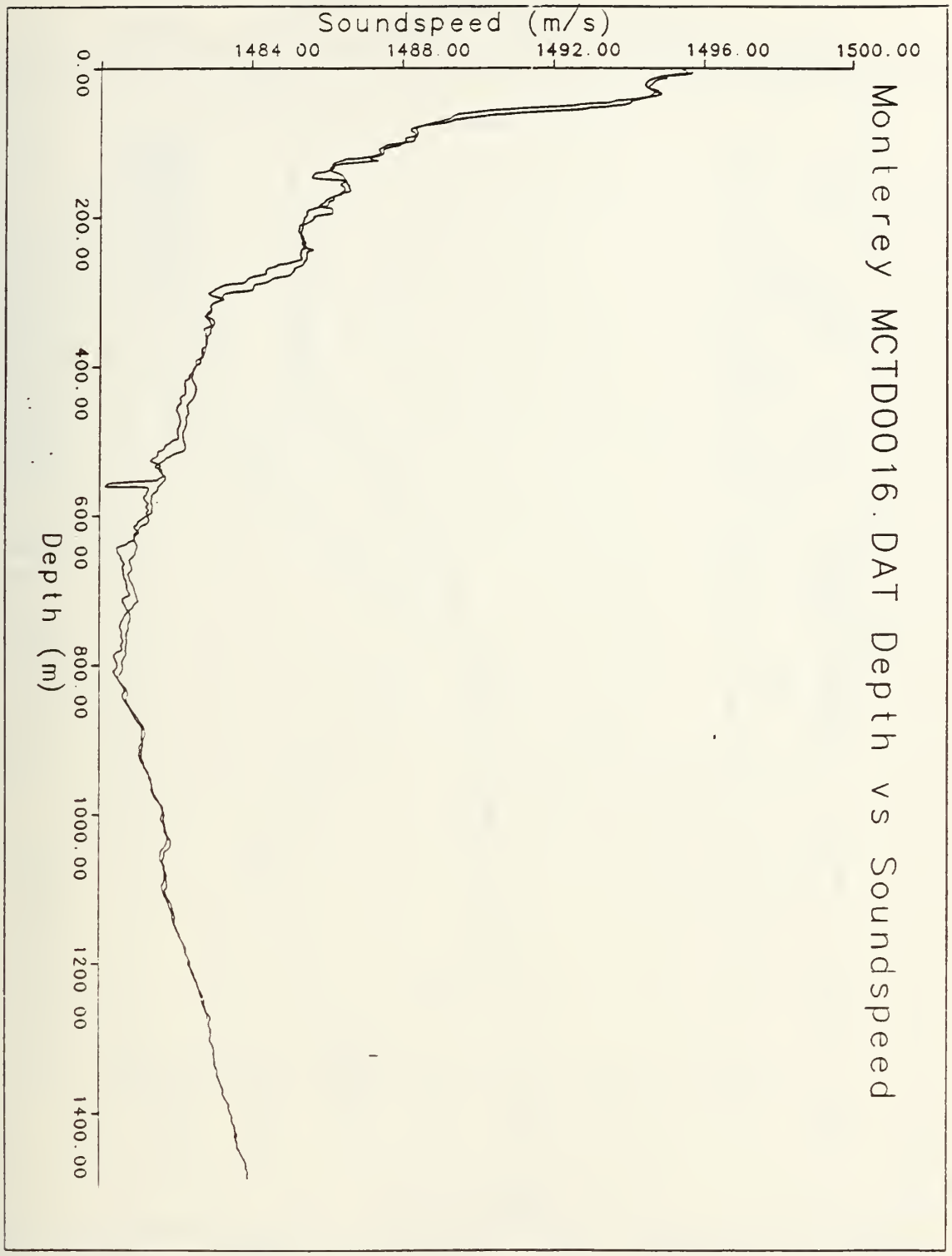

Figure 34: Monterey Bay, Station L, deep water sound velocity profile taken at position 36°32.906N-122°16.210W.

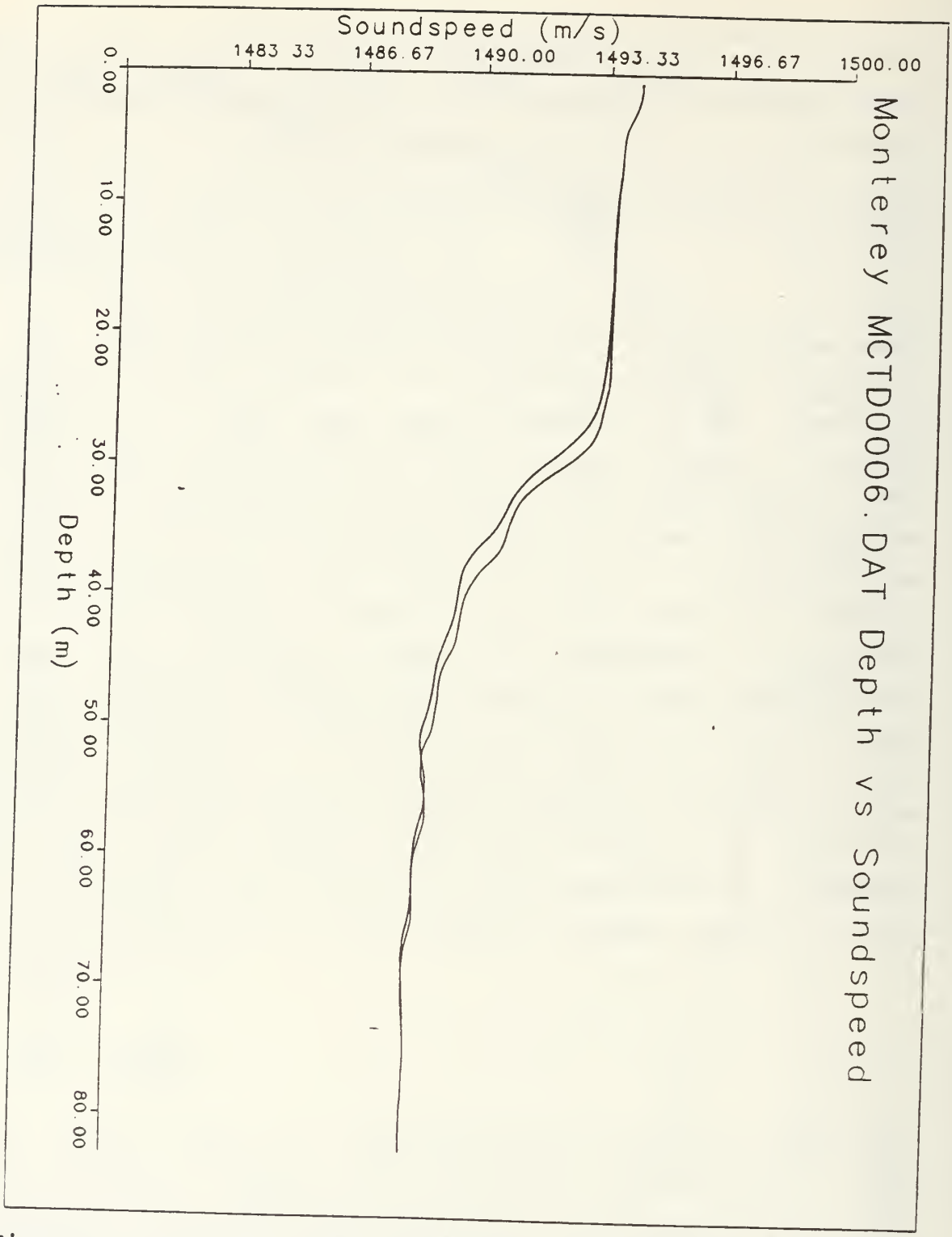

Figure 35: Monterey Bay, Station L, shallow water sound velocity profile taken at position 36°51.095N-122°04.798W.

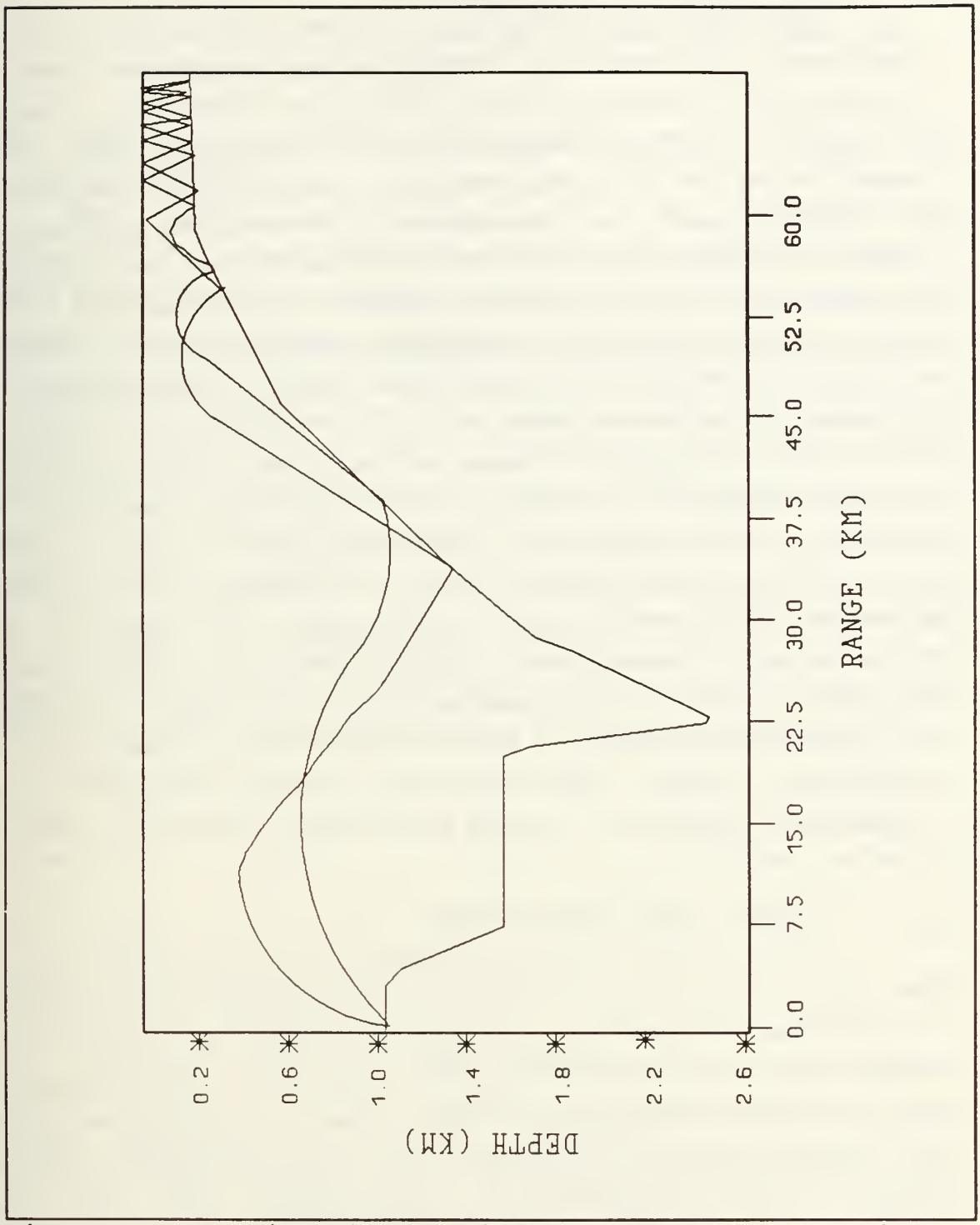

Figure 36: Two-dimensional eigenray path for Station L predicted using MPP.[from Ref.5]

3. Received Acoustic Signal

The data from Station L spans the length of the experiment. The number of received eigenrays varies from two as predicted to as many as four during the experiment. Figures 37 and 38 show an example of the received data after demodulation and 16 times coherent averaging for the period 1800-2000 14Dec88. The data spans 62 minutes per plot and is used to determine which arrival to track for the peak picking. The remaining VCR-PCM data for Station L is in Appendix D. The data from the different videotapes have arbitrary starting points for arrival estimations. The exact starting point is unimportant for ocean perturbations with periods less than six hours. The individual eigenray arrivals for stable paths can be determined for different videotapes by observing the arrival relative to others. The analysis of one arrival will be performed using Figures 37 and 38 to demonstrate the data processing for travel time fluctuations. In Figure 37 the selected arrival has a peak approximately 0.62 seconds after the start point on the sequence repetition scale. In Figure 38 the selected arrival is occurs about 0.61 seconds after the start point. While the SNR varies during the time of the experiment the path is always present so the arrival can be tracked.[Ref. 25]

4. Travel Time Fluctuations

The arrival time is estimated by picking the peak of the ray arrival with the Fortran program ACRIB. This program is the same as the Fortran program ACRID in Reference 25 except that in the program ACRIB the duration of peak picking can be varied. The absolute travel time is unimportant and is not measured. The fluctuation in the absolute travel time is equal to the fluctuation in the arrival time from the arbitrary starting point, therefore it is the latter measurement that is of interest. Arrival time estimation for

the selected arrivals versus time are shown in Figures 39 and 40. The uncertainty calculated using the SNR varies from 2.5 to 4.5 milliseconds.[Ref. 25]

C. ANALYSIS OF ARRIVAL TIME FLUCTUATIONS AT SURFACE WAVE FREQUENCIES

The power spectral density of the arrival time fluctuations caused by the surface waves should be similar to the power spectral density measured by the NDBC buoy. The power spectral density of the arrival time perturbations can be estimated using a segmented Fast Fourier Transform. The individual segments are 64 samples long to match the resolution of the NDBC data. Approximately 2.2 hours of data provides 64 segments with 128 degrees of freedom. Figure 41 shows the arrival time power spectrum with a resolution bandwidth of 0.00806 Hz. Dividing by this value can be used to normalize the data so that direct comparison is possible with other data of differing resolution bandwidths. The segmented Fast Fourier transform method sums the result so that the total power contributes to the magnitude.[Ref. 25]

The power spectrum from the NDBC buoy is presented in Figure 42 with a resolution of 0.01 Hz. Additional data is presented in Appendix D. Comparing the arrival time and surface wave power spectra shows agreement in general shape and frequency distribution. The largest concentration of power is in the long period swell frequency of 0.07 to 0.09 Hz. The arrival time spectrum also shows a significant peak at 0.03 Hz. This period is longer than normal for the Pacific and is possibly due to "beating" between two systems of long period swell propagating in different directions. The source could be swell that is refracted or reflected off the shoreline along the north side of the Monterey Bay.[Ref. 25]

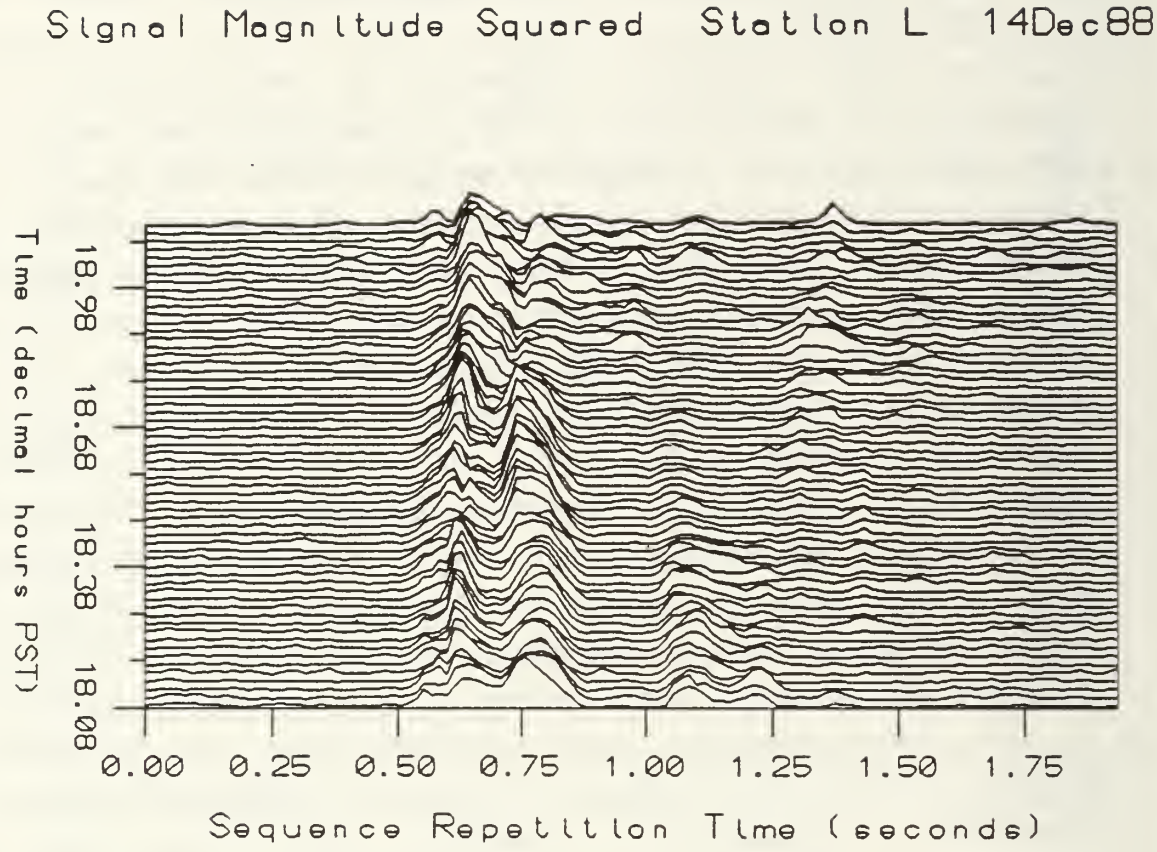

Figure 37: Received acoustic signal after matched-filtering for maximal-length sequence from Station L, 14Dec88 1805 to 1859 PST. Each line is 31 seconds of data coherently averaged to one 1.9375 second period.

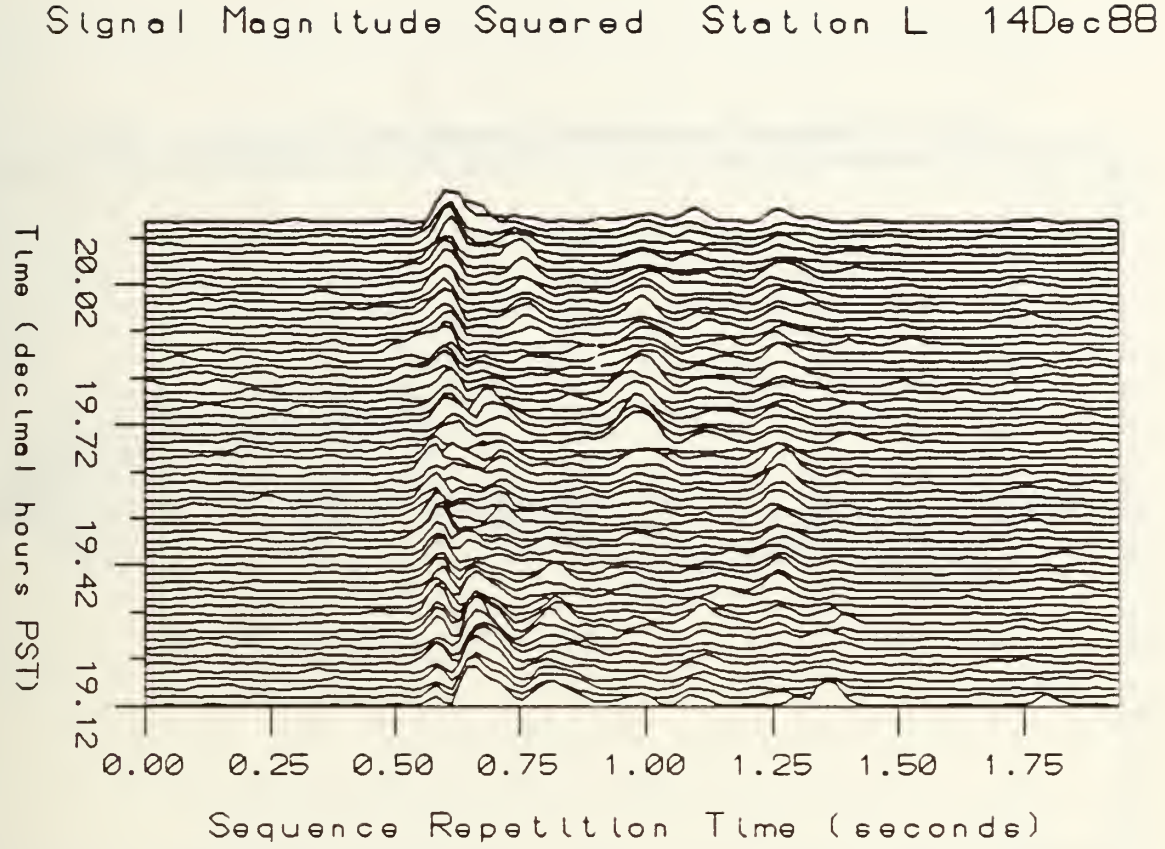

Figure 38: Received acoustic signal after matched-filtering for maximal-length sequence from Station L, 14Dec88 1907 to 2001 PST.

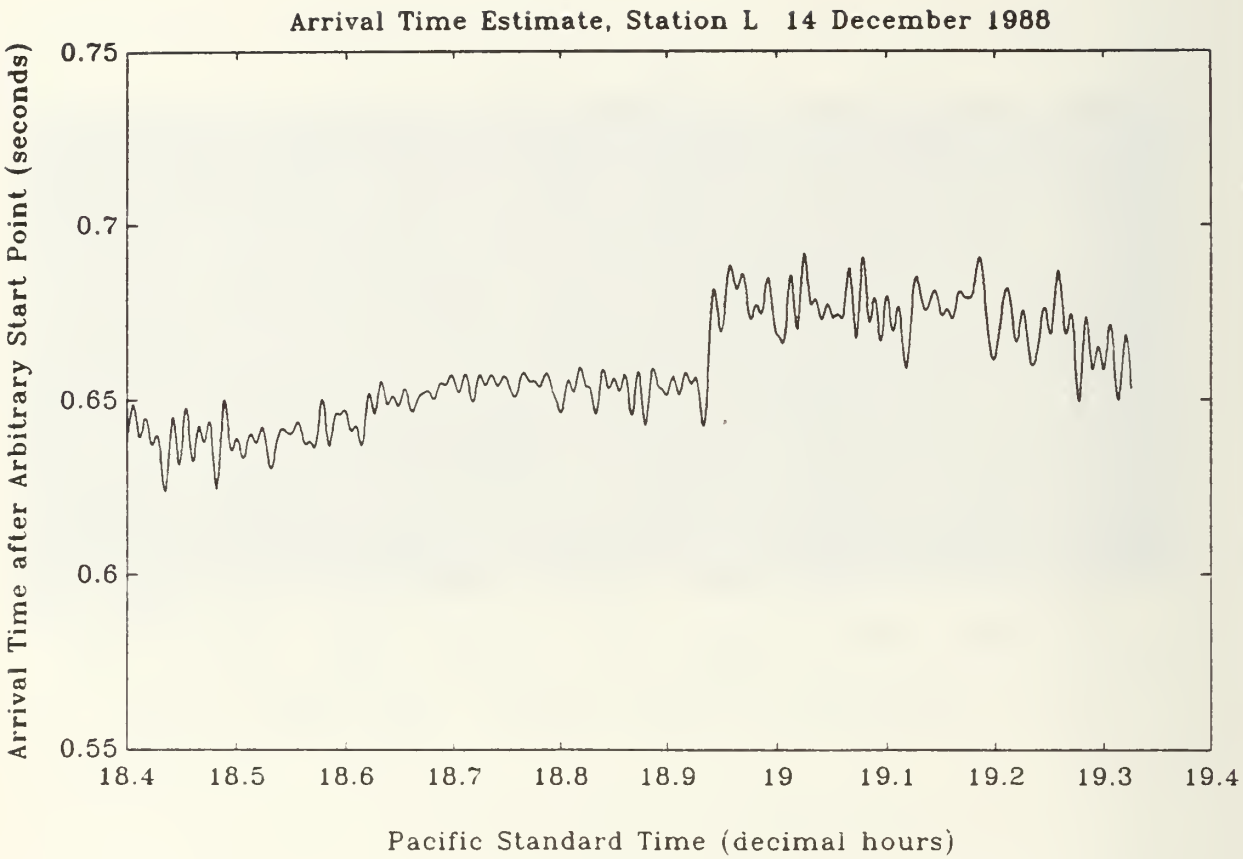

Figure 39: Arrival time estimate for Station L, 14Dec88 1824 to 1924 PST. The fast fluctuations in arrival time are due to surface waves changing the path length.

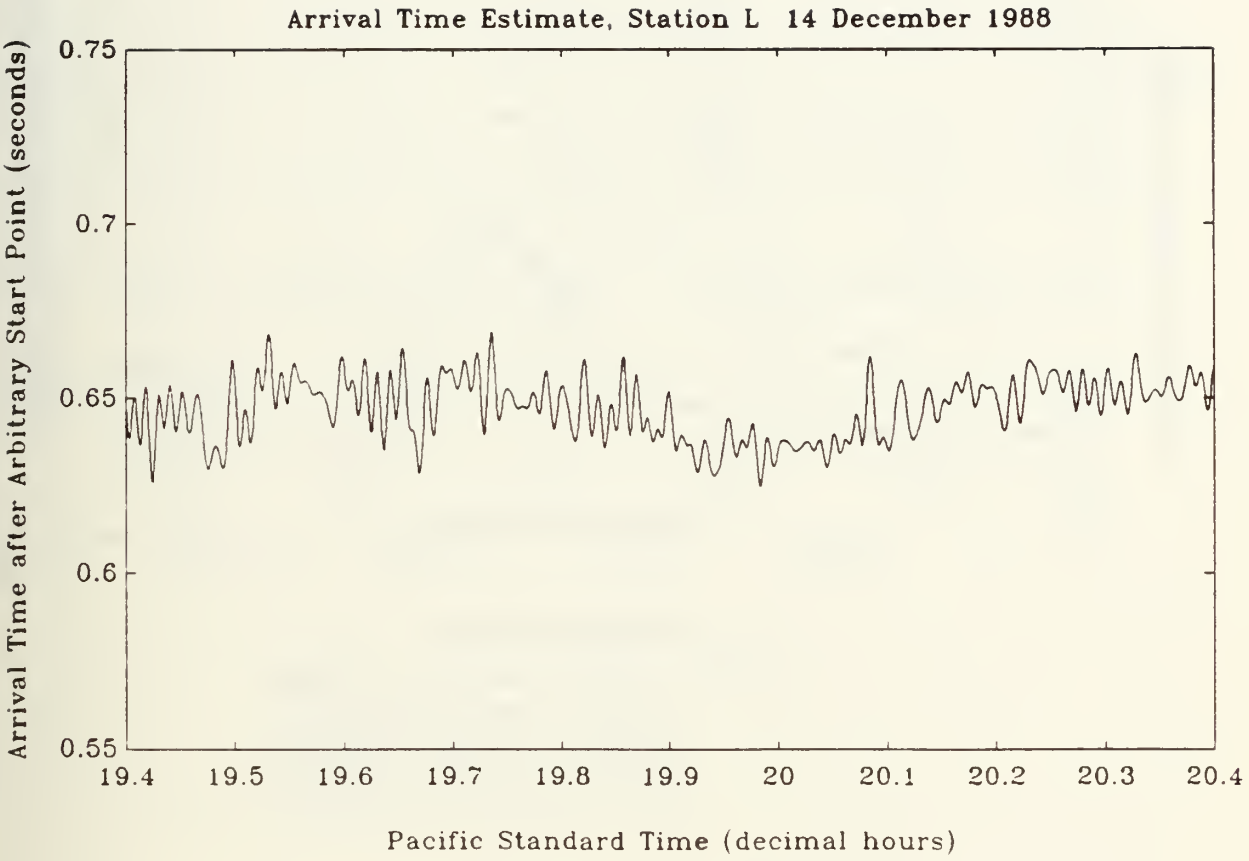

Figure 40: Arrival time estimate for Station L, 14Dec88 1924 to 2024. The fast fluctuations are due to the surface waves changing the path length.

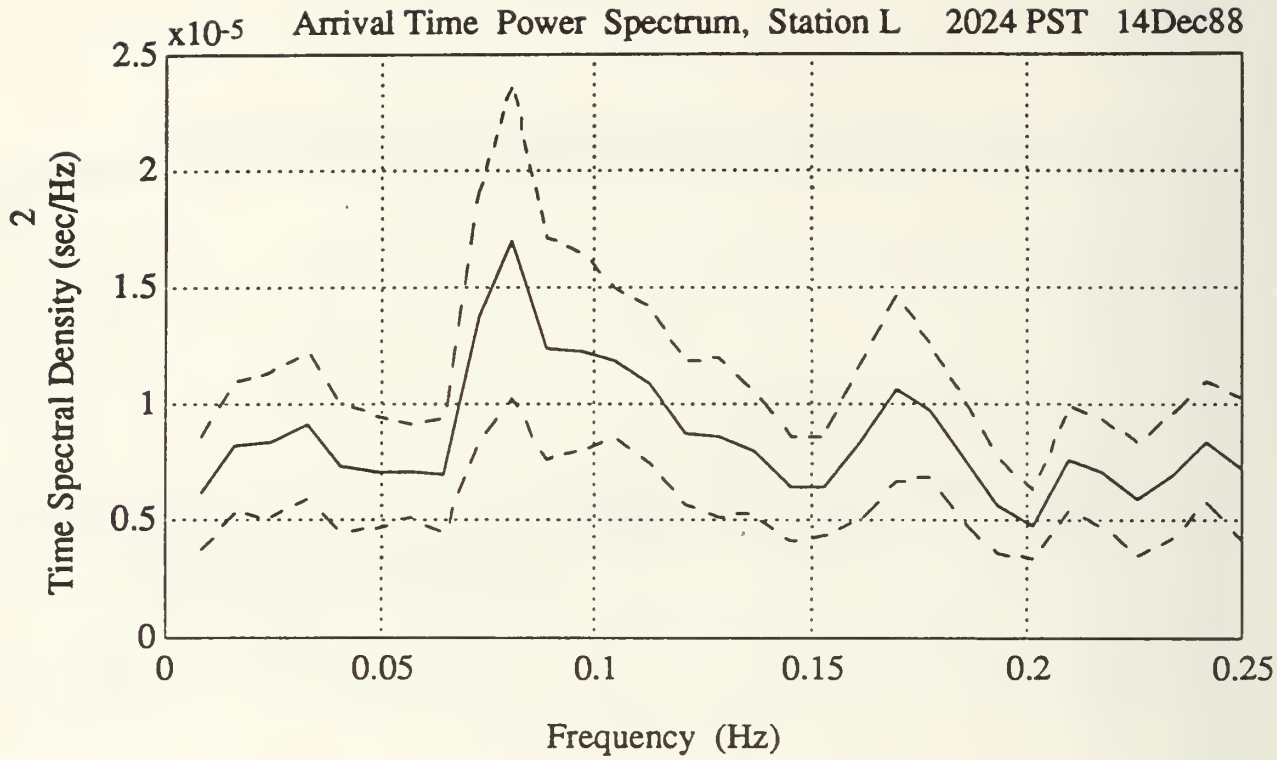

Figure 41: Arrival time power spectrum for Station L. Spectrum from arrival time series, 1824 to 2024 14Dec88 PST.

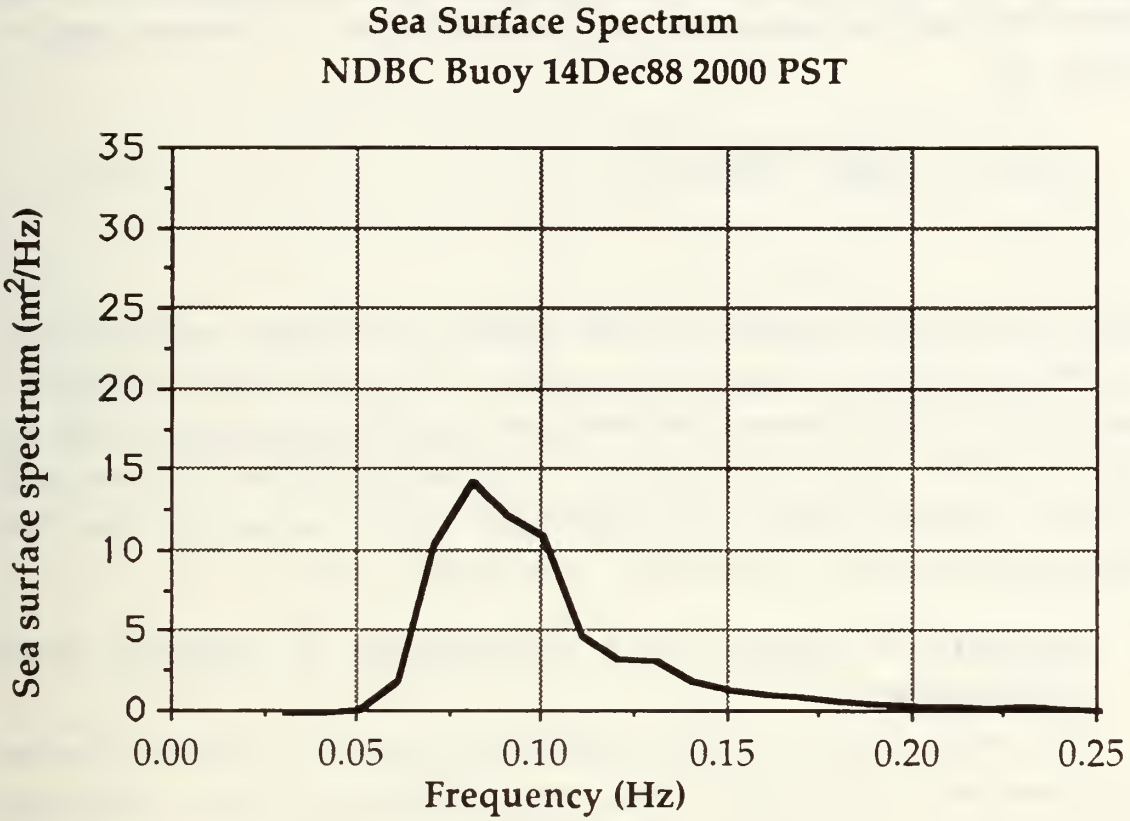

Significant Wave Height 4.10 m
Average Period 9.67 sec
Dominant Period 12.50 sec
Dominant Direction 308 N

Figure 42: Surface wave power spectrum in Monterey Bay.

The relationship between the travel time perturbation spectrum and the frequency-direction spectrum for the case where the wave propagation is perpendicular to the ray can be given by

$$T(\Omega) = \left(\frac{2\sin\theta}{c_o\Omega}\right)^2 \frac{M2\pi g}{r} F(\Omega,0) \qquad (43)$$

where Ω is the frequency, M the number of surface reflections, g the acceleration due to gravity, r the ray skip distance, and $F(\Omega,0)$ the frequency-direction spectrum perpendicular to the ray path. Before performing this calculation the wave and arrival spectra must be normalized and a solution for the number of surface reflections found.[Ref. 25]

D. ANALYSIS OF ARRIVAL TIME FLUCTUATIONS AT INTERNAL WAVE FREQUENCIES

The magnitude of time fluctuations due to internal waves is expected to be lower than the fluctuation due to surface waves. Figure 35 shows a difference in sound speed of only 5 meters per second across the thermocline which is a change of only 0.33%. The surface wave time perturbation is 300 greater than the same amplitude time perturbation due to an internal wave. The time perturbation data was detrended by subtracting the mean and then low-pass filtering with an Eighth Order Chebyshev digital filter with a cutoff frequency of 0.01 of the original maximum digital frequency. Oscillations of periods greater than 6.4 minutes pass through the filter including internal wave perturbations. The arrival time perturbations over the duration of the experiment for Station L are shown in Figures 43-53. The data analysis was performed using MATLAB, a computer software product of The Mathworks, Inc. of Sherborn, MA. which is a powerful mathematical and

signal processing package that can be programmed to perform data analysis. The programs used in MATLAB are included in Appendix E.

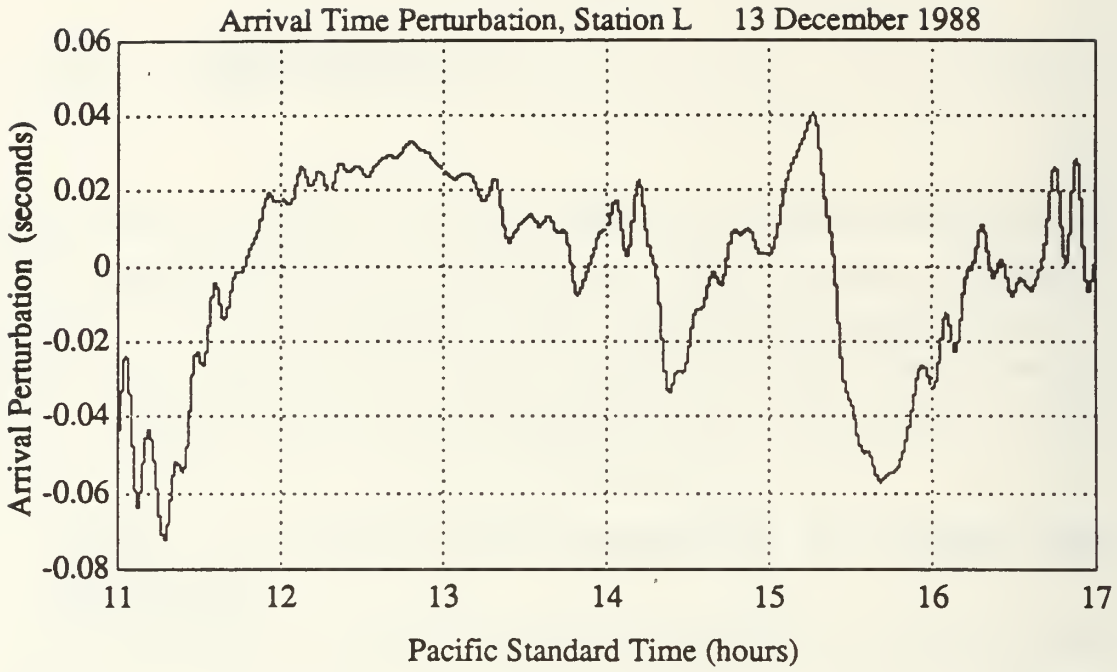

Figure 43: Arrival time perturbation data, Station L 1100-1700 PST 13Dec88, low-pass filtered to .00258 Hz (periods > 6.4 minutes).

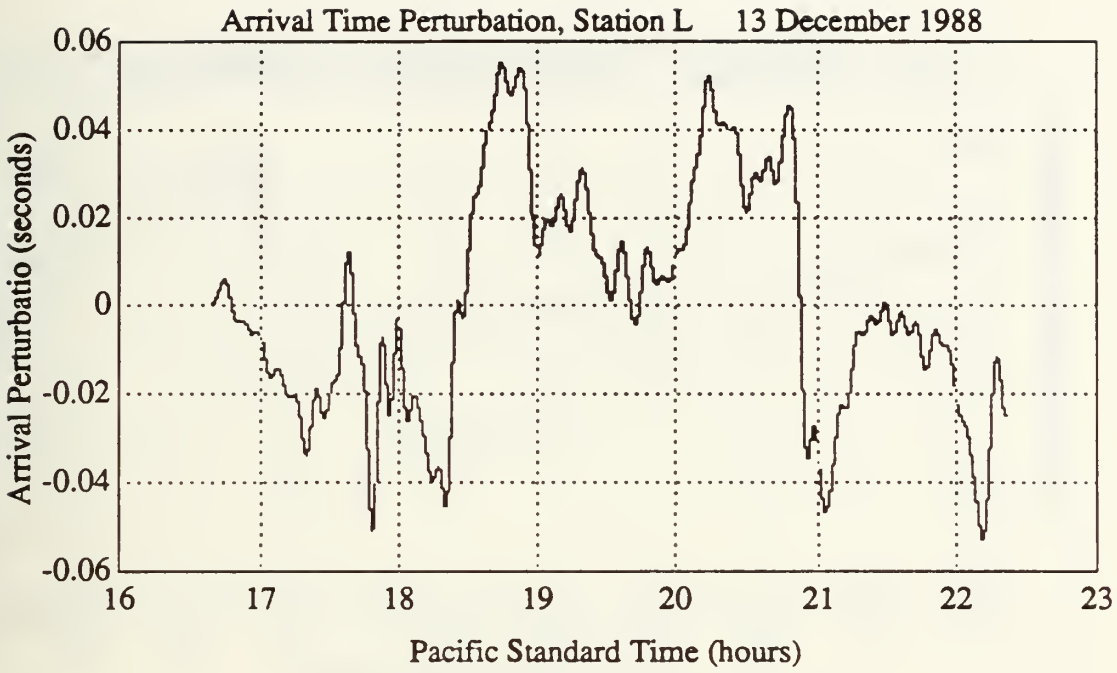

Figure 44: Arrival time perturbation data, Station L 1600-2300 PST 13Dec88, low-pass filtered to .00258 Hz (periods > 6.4 minutes).

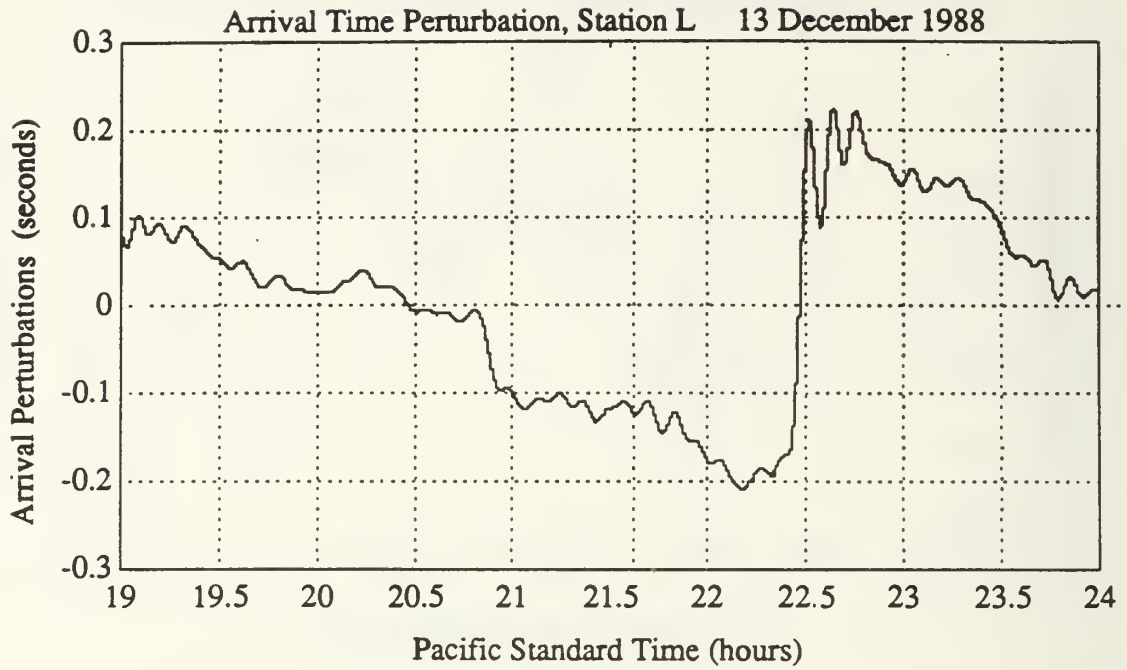

Figure 45: Arrival time perturbation data, Station L 1900-2400 PST 13Dec88, low-pass filtered to .00258 Hz (periods > 6.4 minutes).

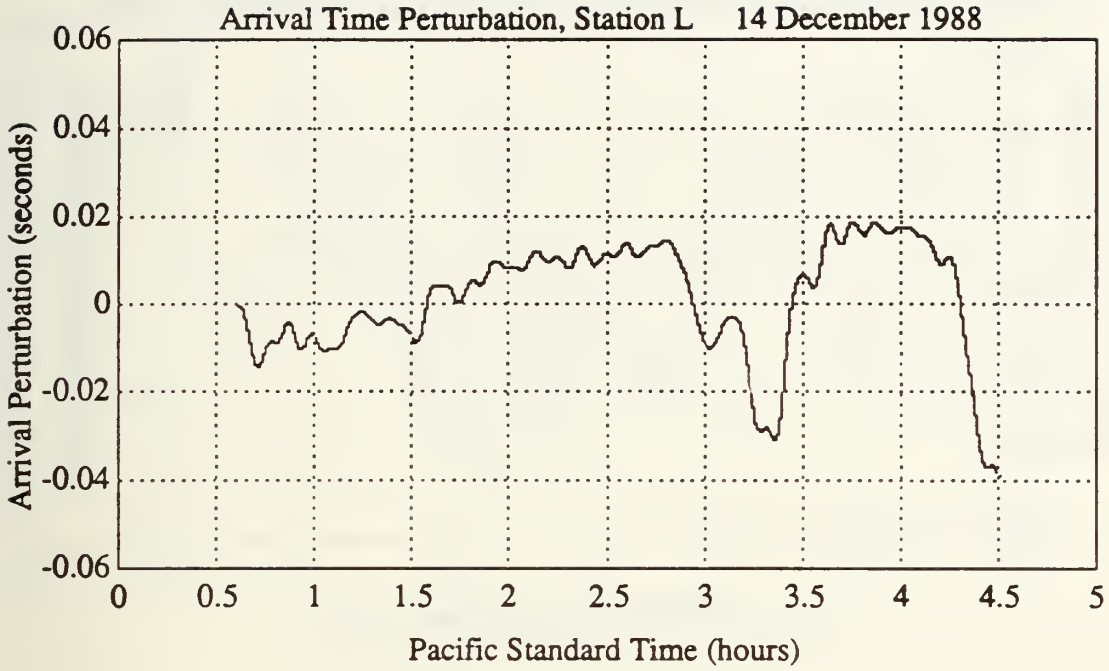

Figure 46: Arrival time perturbation data, Station L 0000-0500 PST 14Dec88, low-pass filtered to .00258 Hz (periods > 6.4 minutes).

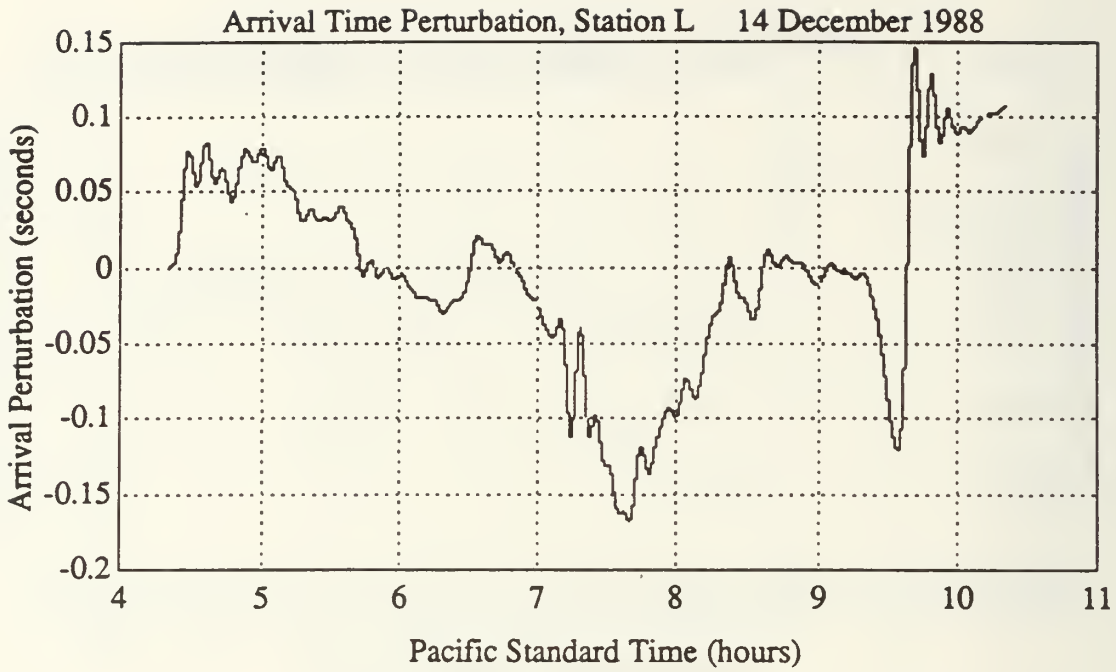

Figure 47: Arrival time perturbation data, Station L 0400-1100 PST 14Dec88, low-pass filtered to .00258 Hz (periods > 6.4 minutes).

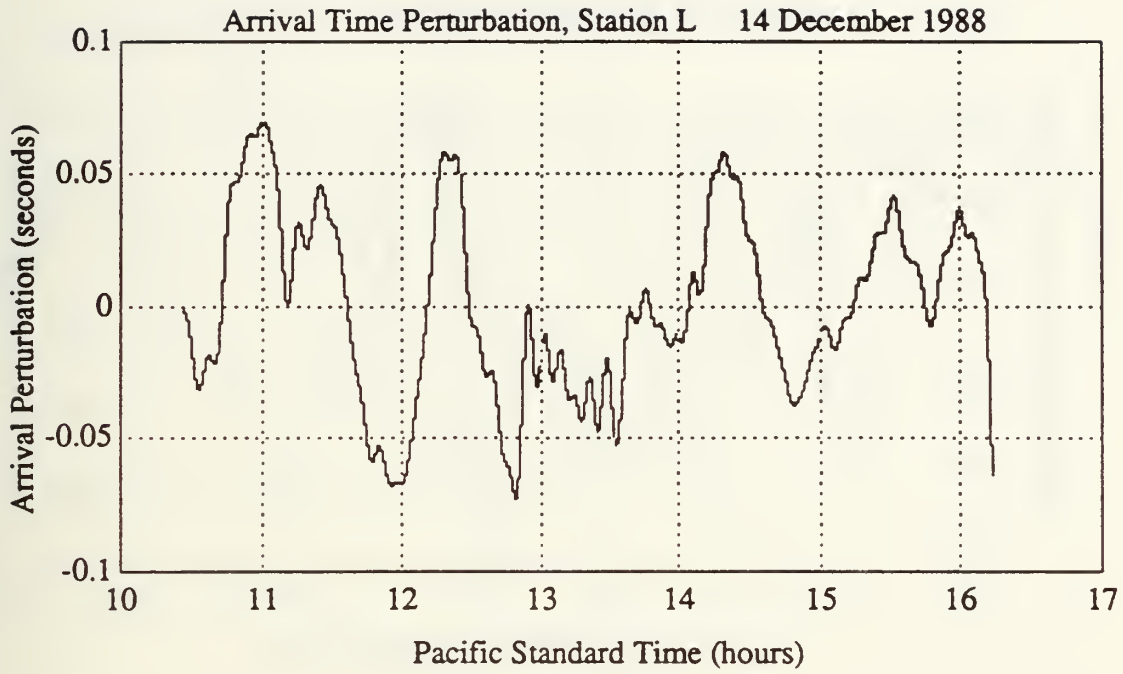

Figure 48: Arrival time perturbation data, Station L 1000-1700 PST 14Dec88, low-pass filtered to .00258 Hz (periods > 6.4 minutes).

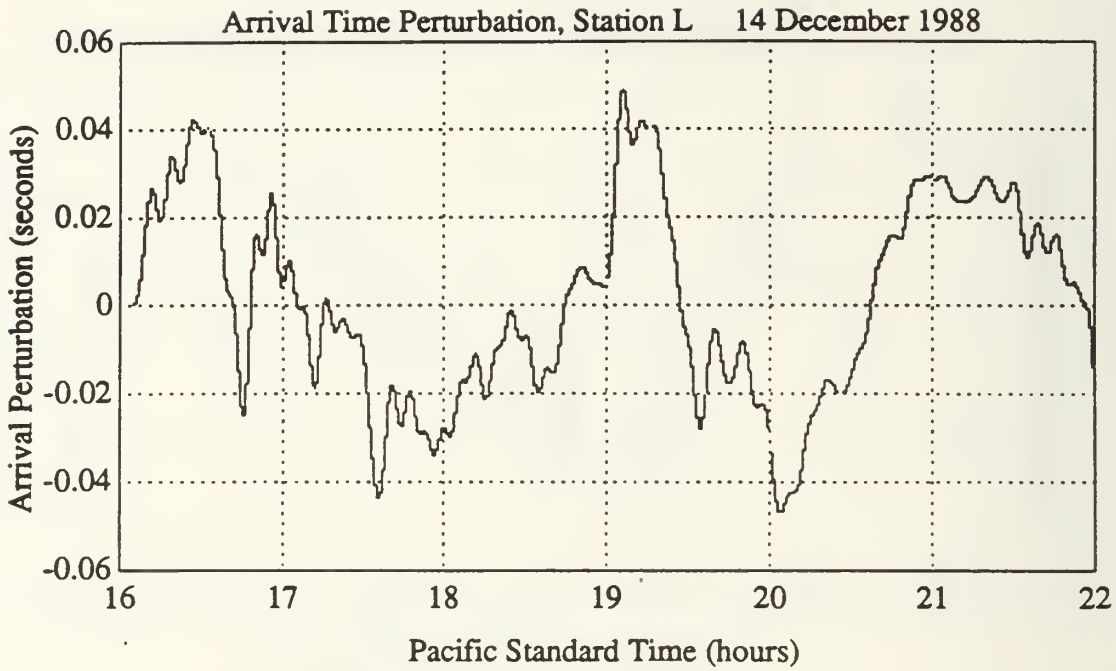

Figure 49: Arrival time perturbation data, Station L 1600-2200 PST 14Dec88, low-pass filtered to .00258 Hz (periods > 6.4 minutes).

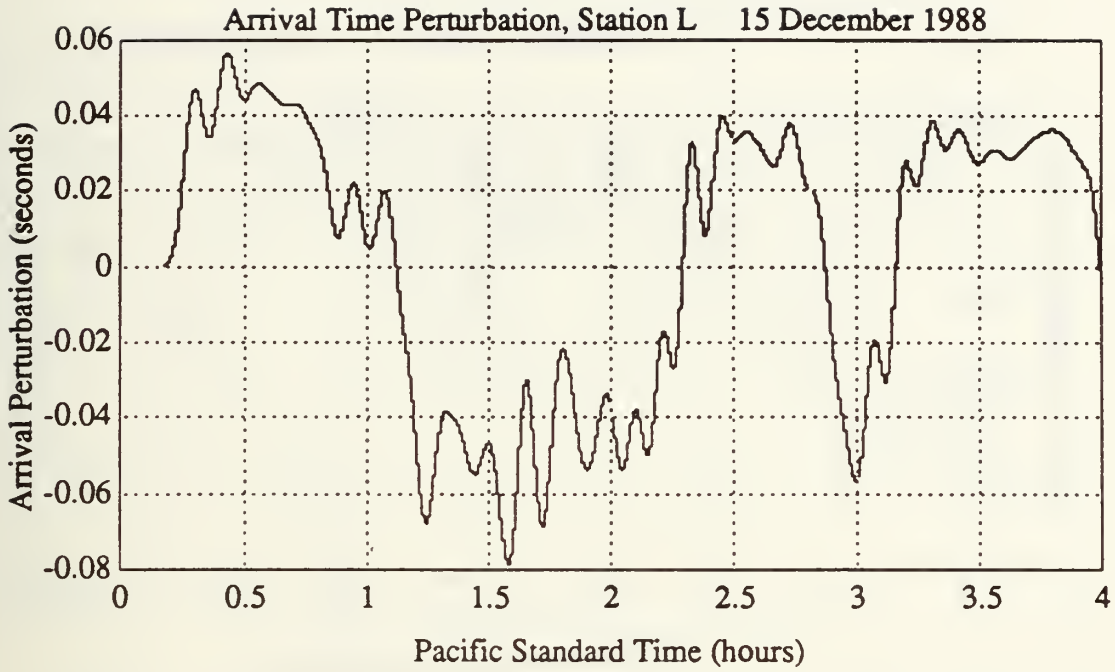

Figure 50: Arrival time perturbation data, Station L 0000-0400 PST 15Dec88, low-pass filtered to .00258 Hz (periods > 6.4 minutes).

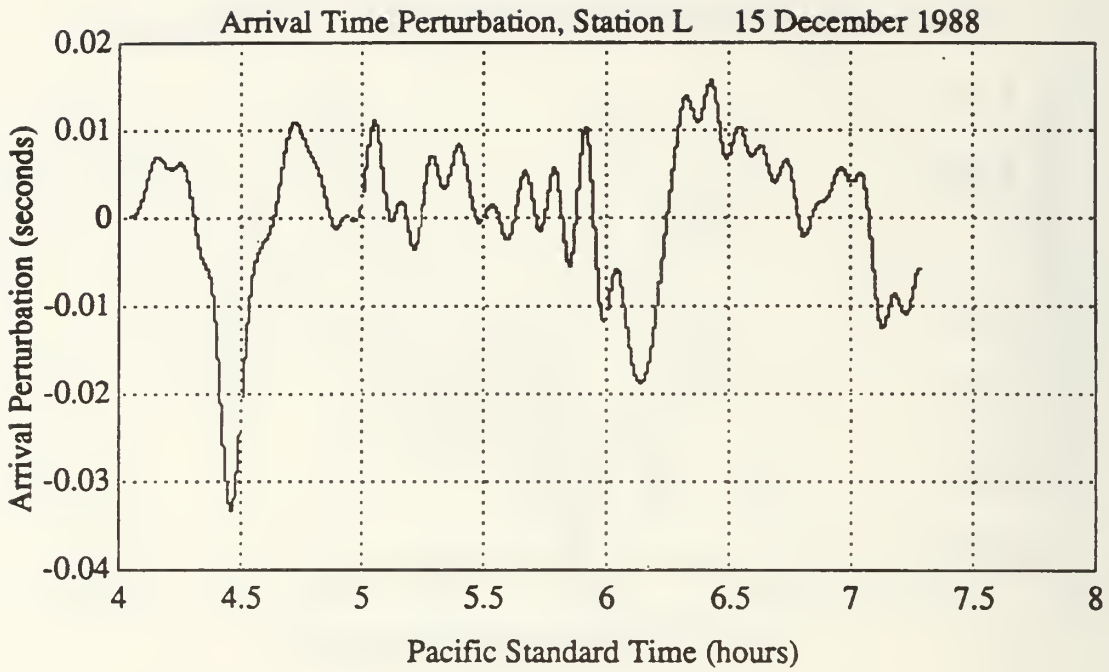

Figure 51: Arrival time perturbation data, Station L 0400-0800 PST 15Dec88, low-pass filtered to .00258 Hz (periods > 6.4 minutes).

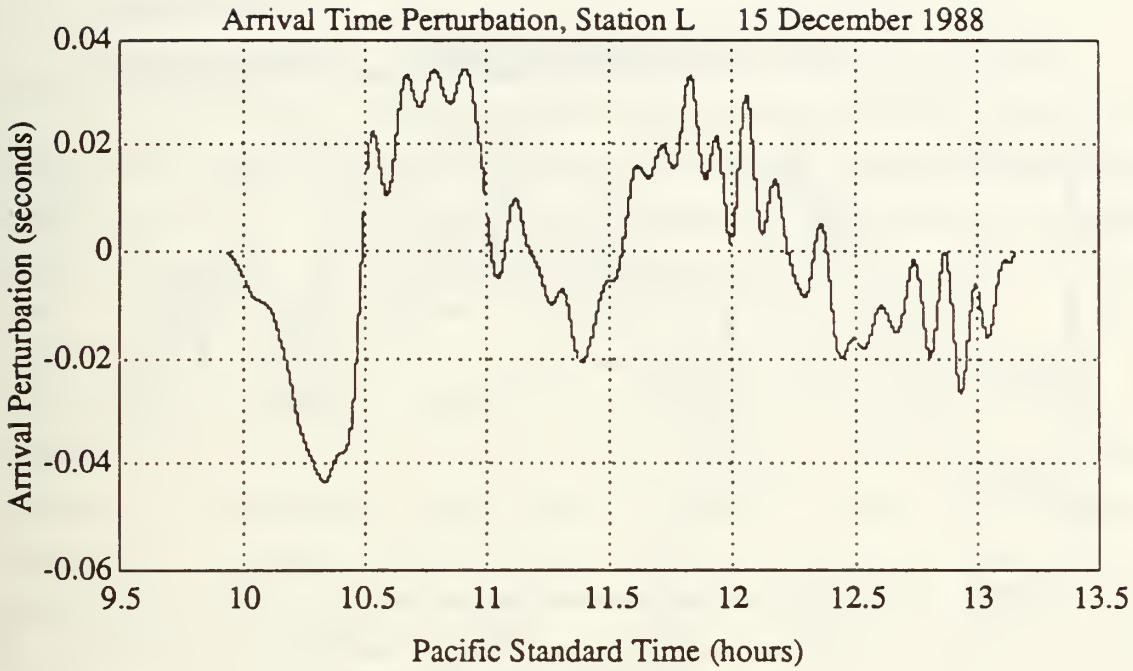

Figure 52: Arrival time perturbation data, Station L 0930-1330 PST 15Dec88, low-pass filtered to .00258 Hz (periods > 6.4 minutes).

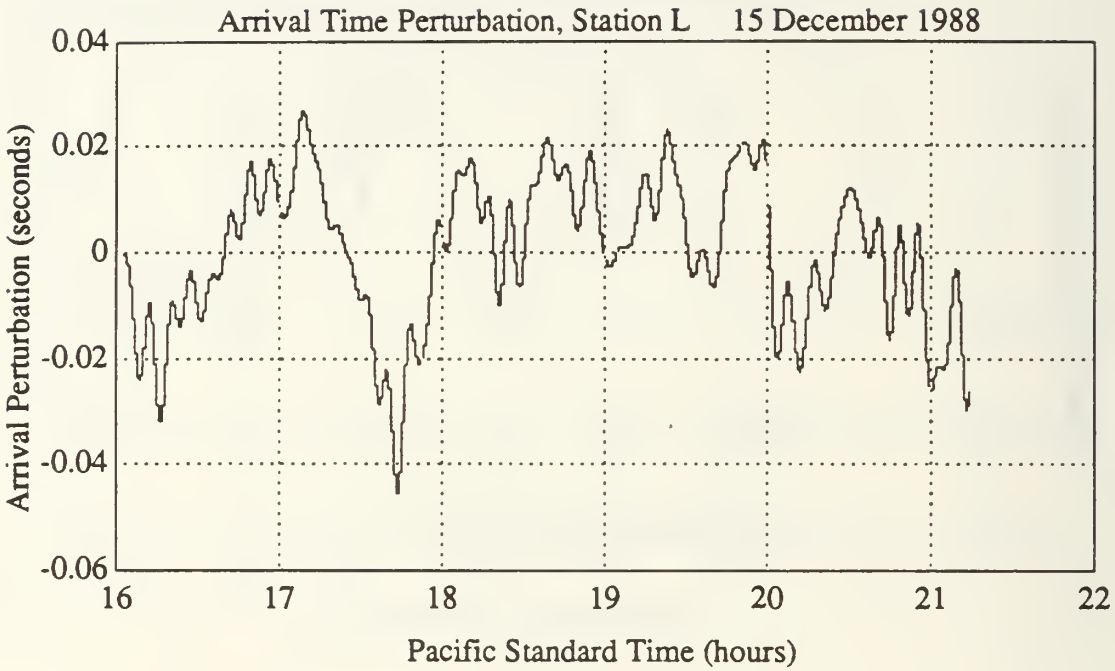

Figure 53: Arrival time perturbation data, Station L 1600-2200 PST 15Dec88, low-pass filtered to .00258 Hz (periods > 6.4 minutes).

VI. CONCLUSIONS AND RECOMMENDATIONS

A. CONCLUSIONS

1. Signal Processing Objectives

The overall Tomographic Signal Processing System, of which the Multi-Channel Data-Synchronized Quadrature Phase Demodulator is a part of, is capable of meeting its design objectives and can accurately reproduce data within ± 1 ms over a six hour period. The SNR for the majority of the channels is between 7-10 dB after signal processing which is acceptable although lower than predicted of about 15 dB. The system precision is within 2-4 ms which is adequate for density tomography. The Multi-Channel Data-Synchronized Quadrature Phase Demodulator design is very reliable, processing over 396 hours of data with no failures. The design is easily reproducible due to its wire wrap construction and modular board layout. The design can be altered without difficulty to accept more channels or different operating frequencies relatively quickly. The small size of the demodulator makes it easily transportable. The Multi-Channel Data-Synchronized Quadrature Phase Demodulator is a viable and effective means of effectively increasing the computing power of a personal computer. Therefore, this thesis has completed its original objective of making Acoustic Tomographic Signal Processing possible with a personal computer.

2. Tomography Experiment Objectives

The experiment successfully demonstrated that the new tomography system is capable of taking sufficiently accurate measurements in real-time. The effects of surface and internal waves have been measured but data processing of the tomographic inversion is not yet complete. The effect of the

complex bathymetry has been observed but analysis will not be complete until the three-dimensional ray tracing program is ready to predict the complex propagation paths expected.

B. RECOMMENDATIONS

1. Design Changes

There are several design changes that can be made to the demodulator that would improve performance, decrease chip count, and adapt the demodulator to be used in the Norwegian Sea 1992 experiment.

a. Carrier Frequency

If the carrier frequency were to be changed to 400 Hz then using the same factor as the Monterey Bay Experiment the new synchronizing frequency would be 12.8 kHz. This frequency would be a good choice because it still is in the mid-range of the frequency response of the VCR-PCM's. However, another alternative would be to record the 400Hz carrier frequency directly on the videotape. The 400 Hz carrier frequency could then be used for sampling and for the demodulation which would eliminate the need for the timing channel to perform a frequency step down and would simplify the circuit.

b. Bandwidth

If the bandwidth of the signal is changed to 100 Hz the new sampling rate should then be at least 400 Hz. If a higher sampling rate is used, digital filtering may be possible. The limiting factor would be the speed of the personal computer used.

c. Timing Channel

It is recommended to use the PLL with a Divide by N circuit to drive a VCO which produces a sinusoidal output directly thus eliminating the need for filters. If filters are used, it is recommended to use either the AF100-1CN in this

circuit also or, if possible, the LMF60 which is a Sixth Order Butterworth Filter.

d. Data Channel

The data channel could be improved by using a more accurate multiplier than the AD534K. The signal could also be improved by again switching to the LMF60 if possible which would allow 18 and 24th order filter realizations by cascading circuits. The chip count would also be reduced because the LMF60 requires no external components.

APPENDIX A. MAXIMAL-LENGTH SEQUENCES

A. MAXIMAL LENGTH SHIFT-REGISTER SEQUENCE

The impulse response is a simple tool for determining the travel time through a medium. Unfortunately the impulse response is not easily realizable. The M-sequence is a solution to this problem. The M-sequence is a means of generating pseudo-random noise that is the equivalent of white noise which closely approximates an impulse response.

1. Properties

It is these unique properties that make it ideal for use in tomography. The most important properties of the M-sequence are:

a. Periodic Property

The period N of a M-sequence is,

$$N=2^r+1 \qquad r=1,2,3, \ldots \qquad (44)$$

where r is also the number of stages in the shift register.

b. Balance Property

The number of 1's during one period of an M-sequence is

$$(N+1)/2=2^{r-1} \qquad (45)$$

the number of 0's during the same period is

$$(N-1)/2=2^{r-1}-1 \qquad (46)$$

c. Pseudo-Random Property

The frequency of 1's and 0's has the appearance of being random but is actually following a complex pattern.[Ref. 26]

Finally, the most important property of the M-sequence is that its autocorrelation is a constant equal to -1/N except

at a shift of zero where it equals one (Figure 54). The peak at zero is significantly larger in magnitude than the rest of the sequence making the arrival time easier to determine. The autocorrelation of the code with the received signal produces a peak where the code and received signal match. The amplitude of this peak is effected by the number of digits in the code with a longer code producing a larger peak. The complete set of properties for the M-sequence are listed in Reference 26.

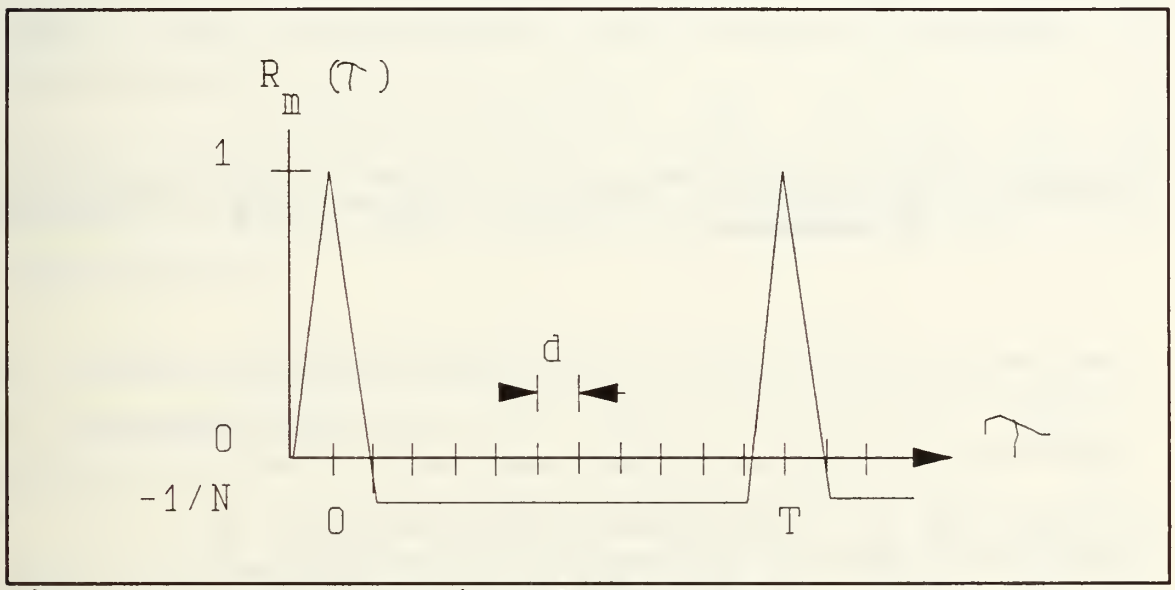

Figure 54: Autocorrelation of M-sequence.

The M-sequence is generated with a r-stage shift register using Mod-2 arithmetic. These sequences have the form of a primitive polynomial, g(x). The signal for the Monterey Bay Acoustic Tomography Experiment was based on an r=5 order polynomial,

$$g(x)=x^5+x^3+x+1 \qquad (47)$$

this results in the shift register configuration in Figure 55.

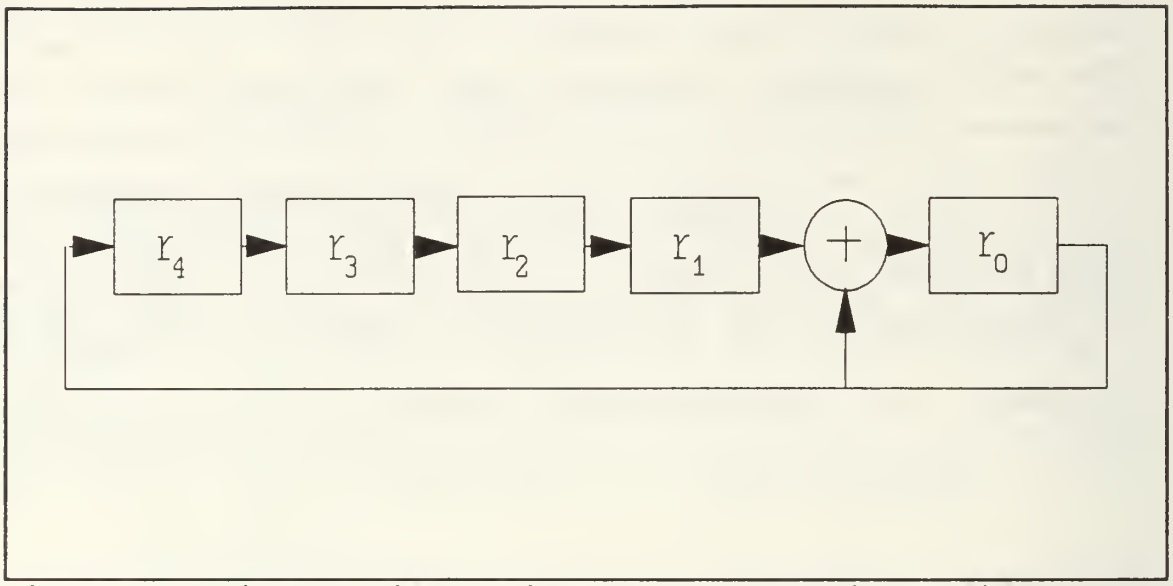

Figure 55: Binary shift register for generating a fifth order M-Sequence.

The r-stage shift register has a cycle with period $N=2^r-1$, for r=5 this results in a 31 digit binary sequence. Therefore, all the states are passed through and there is only one possible cycle. The initial conditions are variable and result in different phases of the same M-sequence.[Ref. 27]

(1) Amplitude Modulation. Amplitude Modulation (AM), is the easiest type of modulation because it only involves turning the carrier on or off depending on the value of m(t). All the cycles of an amplitude modulated carrier will have identical amplitudes for the case of a unipolar, binary M-sequence. In the amplitude modulated case

$$S(t) = \{[1+m(t)]/2\}\sqrt{2}\sin(2\pi f_c t) \quad (48)$$

$$s(t) = j[1+m(t)]/2 \quad (49)$$

for AM, the amplitude switches between +1 and +1/2 as the values of m(t) vary between +1 and 0.[Ref. 27]

(2) Phase Modulation. Phase Modulation (PM) is a type of modulation in which the angle of the carrier is varied linearly by the baseband signal, m(t), while the amplitude remains constant. It is closely related to Frequency Modulation (FM), the difference being that in FM the instantaneous frequency of the carrier is varied linearly with m(t) instead of the angle. There are two general types of PM used, Biphase and Complement-Phase, although these are not the only forms of PM. The main advantage of PM is that it provides better noise discrimination and is less susceptible to interference than AM.[Ref. 28]

In Biphase Modulation (BM), the angle of the carrier switches between $+\pi/2$ and $-\pi/2$ as m(t) switches between +1 and 0. The carrier and baseband signal can be represented as,

$$S_B(t) = \sqrt{2}\cos[2\pi f_c t - m(t)\pi/2] \quad (50)$$

$$s_b(t) = jm(t) \quad (51)$$

In Complement-Phase Modulation (CM), the angle of the carrier switches between $+\pi/4$ and $-\pi/4$ as m(t) switches between +1 and 0. The carrier and baseband signal can be represented as,

$$S_c(t) = \sqrt{2}\cos[2\pi f_c t - m(t)/4] \quad (52)$$

$$s_c(t) = |1+jm(t)|/\sqrt{2} \quad (53)$$

In the Monterey Bay Acoustic Tomography Experiment, the phase modulating the carrier varied between ± 79.8179°.[Refs. 27,28]

APPENDIX B. SCHEMATIC

The complete schematic for the Multi-Channel Data-Synchronized Quadrature Phase Demodulator is presented on the following six pages. The first three pages show the timing channel and the last three show one data channel. The data channels are all identical so the schematic for only one is presented.

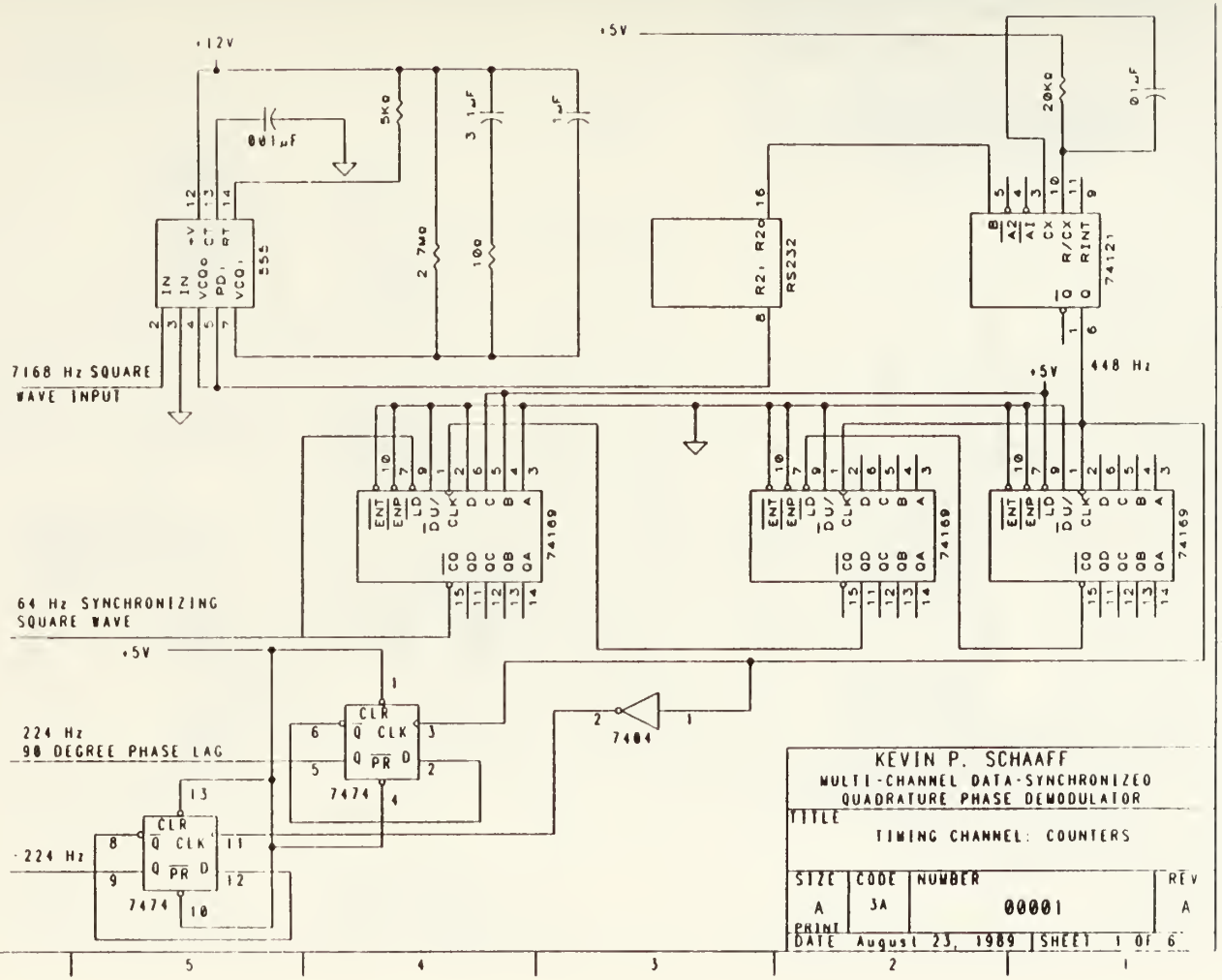
+12V
+5V
5KΩ
.001μF
3.1μF
1μF
2.7MΩ
100
555
20KΩ
.01μF
R2, R20
RS232
74121
7168 Hz SQUARE WAVE INPUT
448 Hz
74169
64 Hz SYNCHRONIZING SQUARE WAVE
224 Hz 90 DEGREE PHASE LAG
224 Hz
7474
7404
KEVIN P. SCHAAFF
MULTI-CHANNEL DATA-SYNCHRONIZED QUADRATURE PHASE DEMODULATOR
TITLE
TIMING CHANNEL: COUNTERS
SIZE
A
CODE
3A
NUMBER
00001
REV
A
DATE August 23, 1989
SHEET 1 OF 6

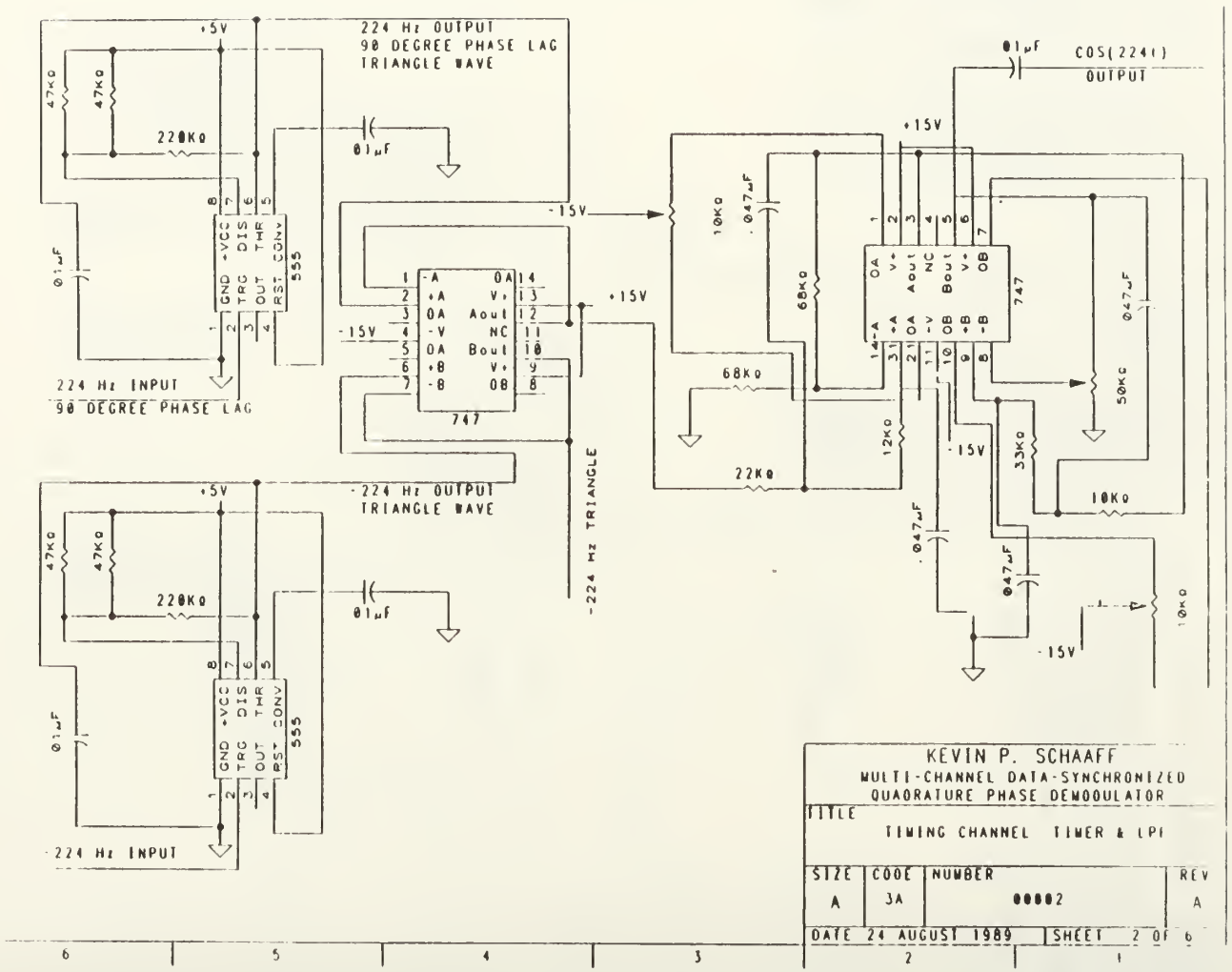
+5V
224 Hz OUTPUT
90 DEGREE PHASE LAG
TRIANGLE WAVE
47KΩ
47KΩ
220KΩ
.01μF
.01μF
GND +VCC DIS TRG OUT THR RST CONV
555
224 Hz INPUT
90 DEGREE PHASE LAG
-15V
+15V
-A
+A
OA
-V
OA
+B
-B
OA
+V
Aout
NC
Bout
+V
OB
747
-224 Hz OUTPUT
TRIANGLE WAVE
-224 Hz TRIANGLE
-224 Hz INPUT
.01μF
COS(2241)
OUTPUT
10KΩ
.047μF
68KΩ
22KΩ
12KΩ
33KΩ
50KΩ
.047μF
.047μF
10KΩ
KEVIN P. SCHAAFF
MULTI-CHANNEL DATA-SYNCHRONIZED
QUADRATURE PHASE DEMODULATOR
TITLE
TIMING CHANNEL TIMER & LPI
SIZE
A
CODE
3A
NUMBER
00002
REV
A
DATE 24 AUGUST 1989
SHEET 2 OF 6
6
5
4
3
2
1

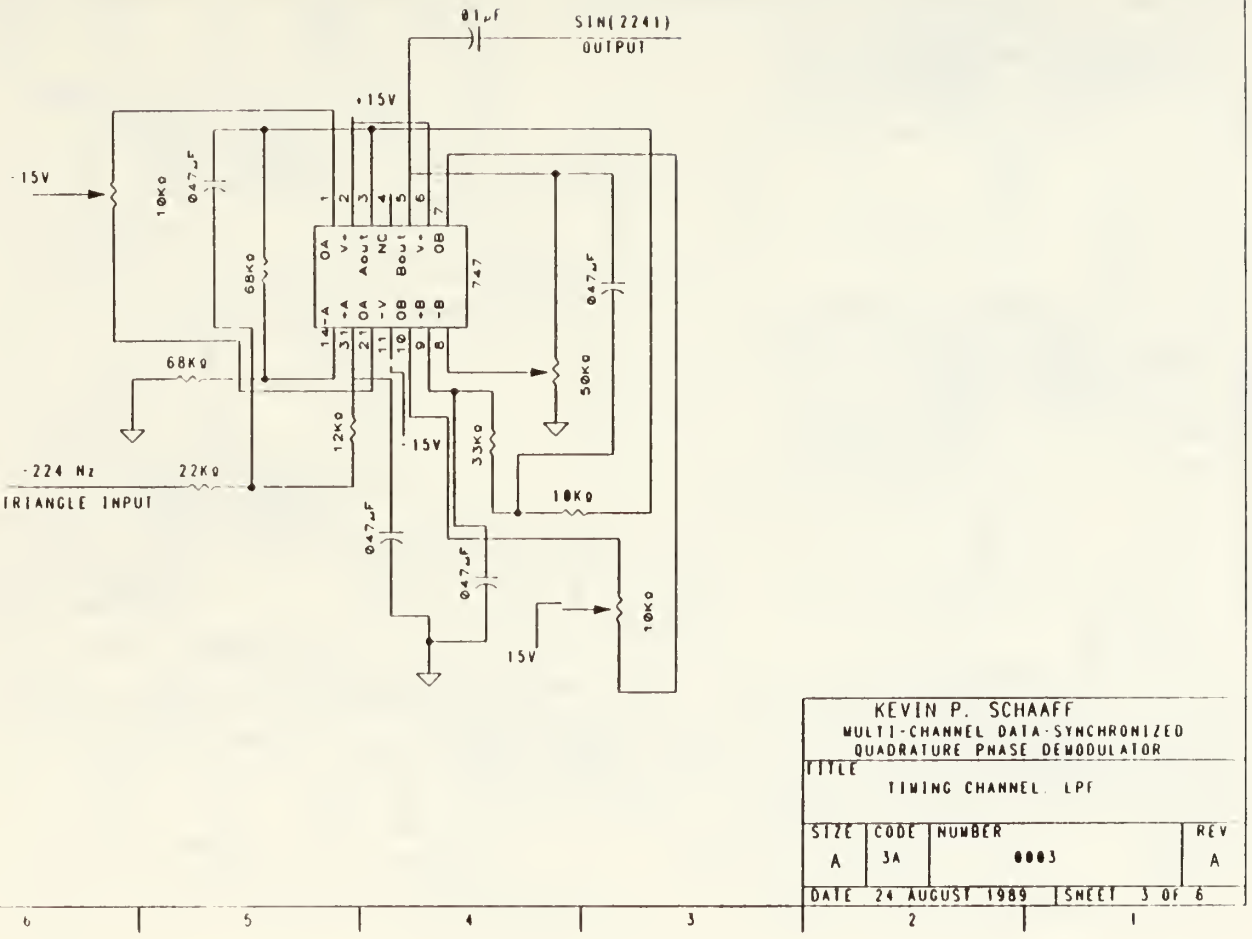
.01μF
SIN(2241)
OUTPUT
+15V
-15V
10KΩ
.047μF
68KΩ
747
OA
V+
Aout
NC
Bout
V-
OB
14-A
+A
OA
-V
OB
+B
-B
50KΩ
.047μF
68KΩ
12KΩ
-15V
33KΩ
-224 Hz
22KΩ
TRIANGLE INPUT
10KΩ
.047μF
.047μF
15V
10KΩ
KEVIN P. SCHAAFF
MULTI-CHANNEL DATA-SYNCHRONIZED
QUADRATURE PHASE DEMODULATOR
TITLE
TIMING CHANNEL LPF
SIZE
A
CODE
3A
NUMBER
0003
REV
A
DATE 24 AUGUST 1989
SHEET 3 OF 6

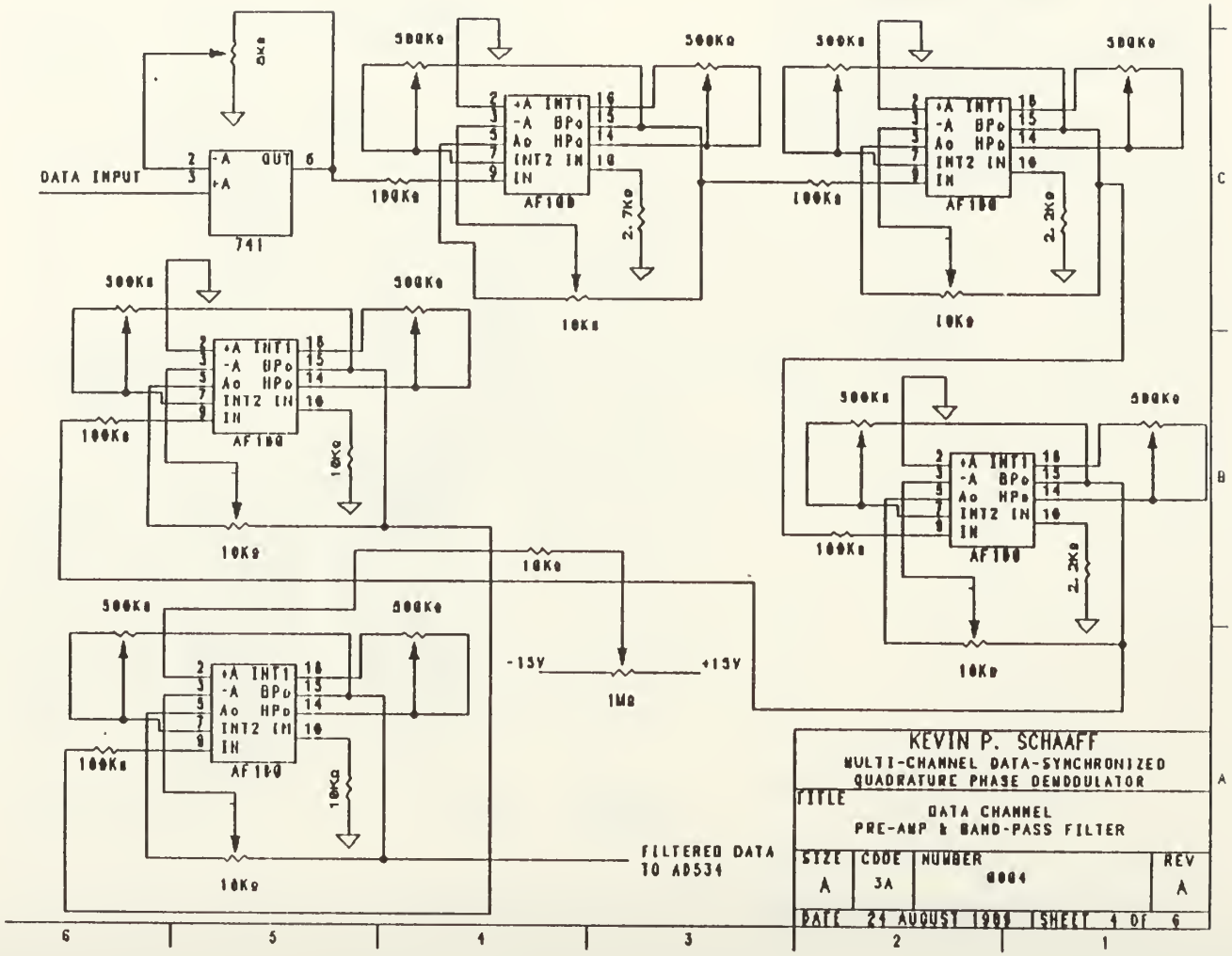
DATA INPUT
741
AF100
500Kø
100Kø
10Kø
2.7Kø
2.2Kø
1Mø
-15V
+15V
FILTERED DATA
TO AD534
KEVIN P. SCHAAFF
MULTI-CHANNEL DATA-SYNCHRONIZED
QUADRATURE PHASE DEMODULATOR
TITLE
DATA CHANNEL
PRE-AMP & BAND-PASS FILTER
SIZE
A
CODE
3A
NUMBER
0004
REV
A
DATE 24 AUGUST 1988 SHEET 4 OF 6

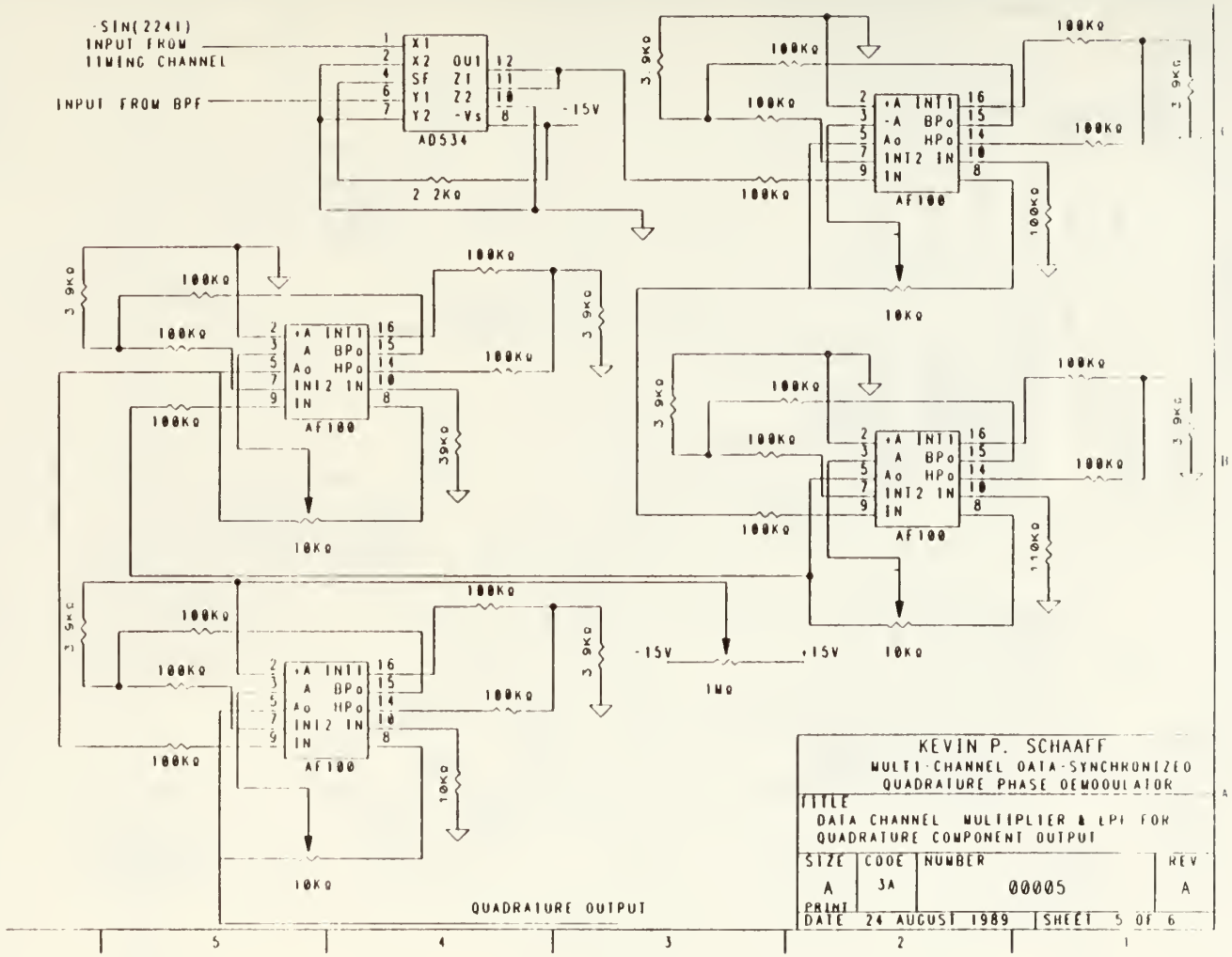
-SIN(2241)
INPUT FROM
TIMING CHANNEL
INPUT FROM BPF
AD534
AF100
2.2KΩ
100KΩ
3.9KΩ
39KΩ
10KΩ
1MΩ
-15V
+15V
QUADRATURE OUTPUT
KEVIN P. SCHAAFF
MULTI-CHANNEL DATA-SYNCHRONIZED
QUADRATURE PHASE DEMODULATOR
TITLE
DATA CHANNEL MULTIPLIER & LPF FOR
QUADRATURE COMPONENT OUTPUT
SIZE A
CODE 3A
NUMBER 00005
REV A
PRINT
DATE 24 AUGUST 1989
SHEET 5 OF 6

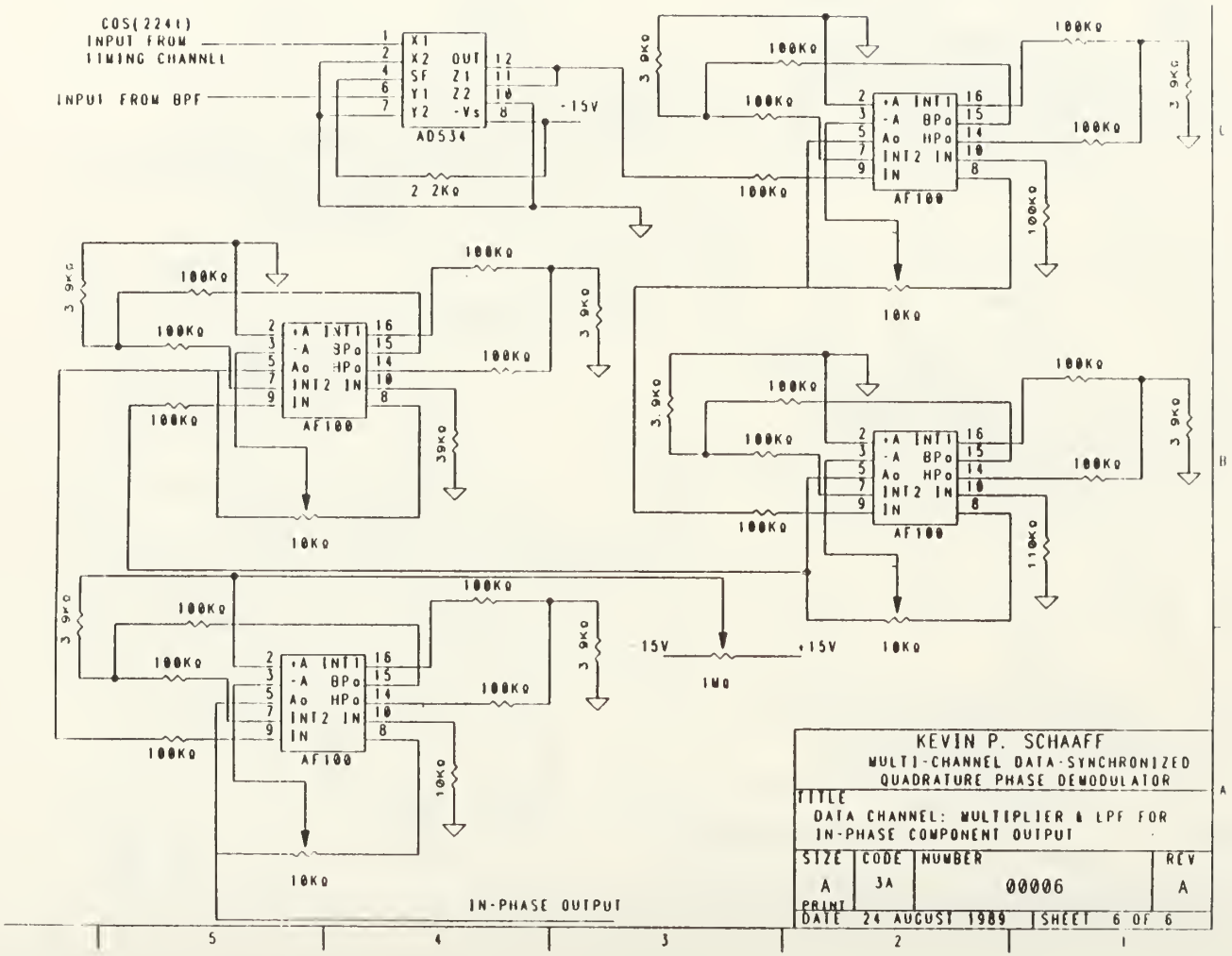
COS(2241)
INPUT FROM
TIMING CHANNEL
INPUT FROM BPF
X1
X2 OUT
SF Z1
Y1 Z2
Y2 -Vs
AD534
-15V
2 2KΩ
100KΩ
3.9KΩ
+A INT1
-A BPo
Ao HPo
INT2 IN
IN
AF100
10KΩ
39KΩ
110KΩ
15V
+15V
1MΩ
IN-PHASE OUTPUT
KEVIN P. SCHAAFF
MULTI-CHANNEL DATA-SYNCHRONIZED
QUADRATURE PHASE DEMODULATOR
TITLE
DATA CHANNEL: MULTIPLIER & LPF FOR
IN-PHASE COMPONENT OUTPUT
SIZE
A
CODE
3A
NUMBER
00006
REV
A
PRINT
DATE 24 AUGUST 1989
SHEET 6 OF 6

APPENDIX C. VCR-PCM SPECIFICATIONS

A. VCR/PCM SPECIFICATIONS

1. General

Sampling Frequency	44.1 kHz
Quantization	16-bit linear quantizing
Frequency Response	20-20,000 Hz ± 0.5 dB
Harmonic Distortion	< 0.005%
Dynamic Range	> 80 dB
Channel Separation	> 60 dB
Wow and Flutter	< 0.005% WRMS

APPENDIX D. ADDITIONAL DATA FOR STATION L

A. MATCHED-FILTERED ACOUSTIC SIGNAL

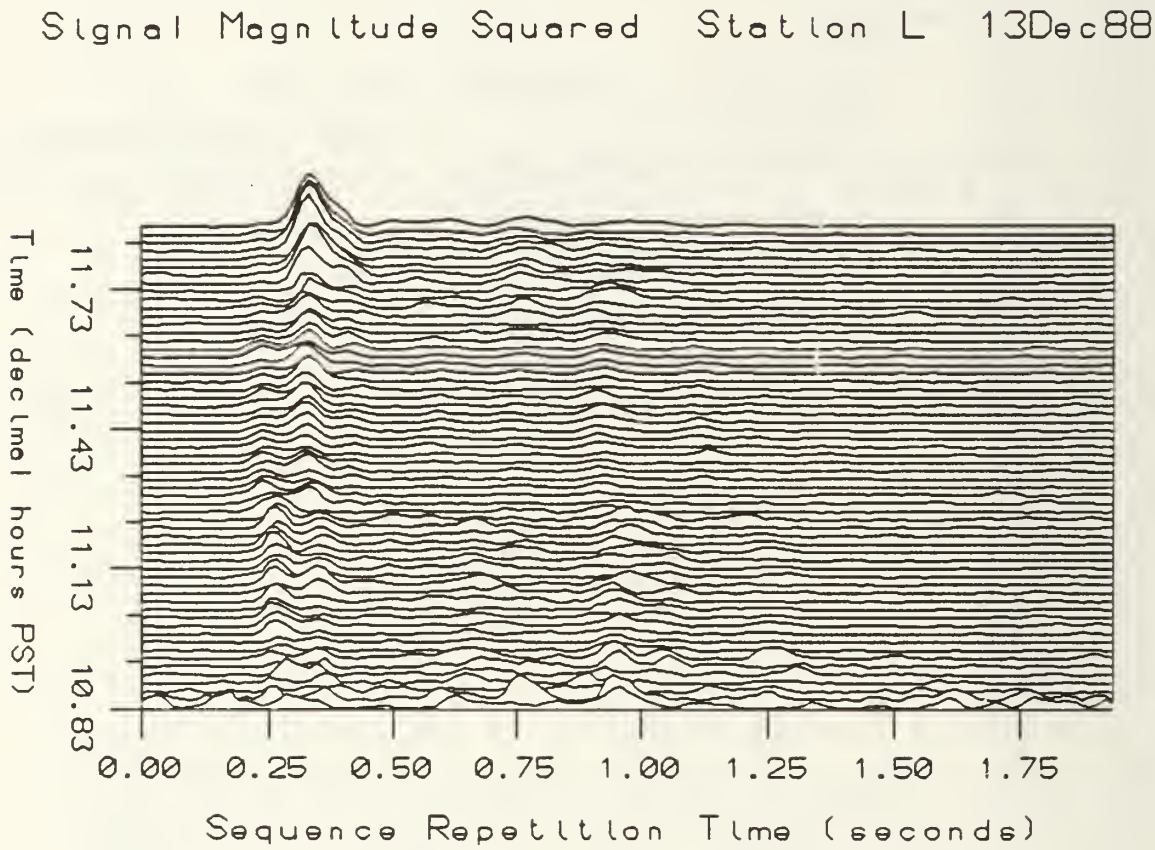

Figure 56: Tomographic signal, coherently averaged 16 times then magnitude squared. Station L, 1048 to 1042 13Dec88.

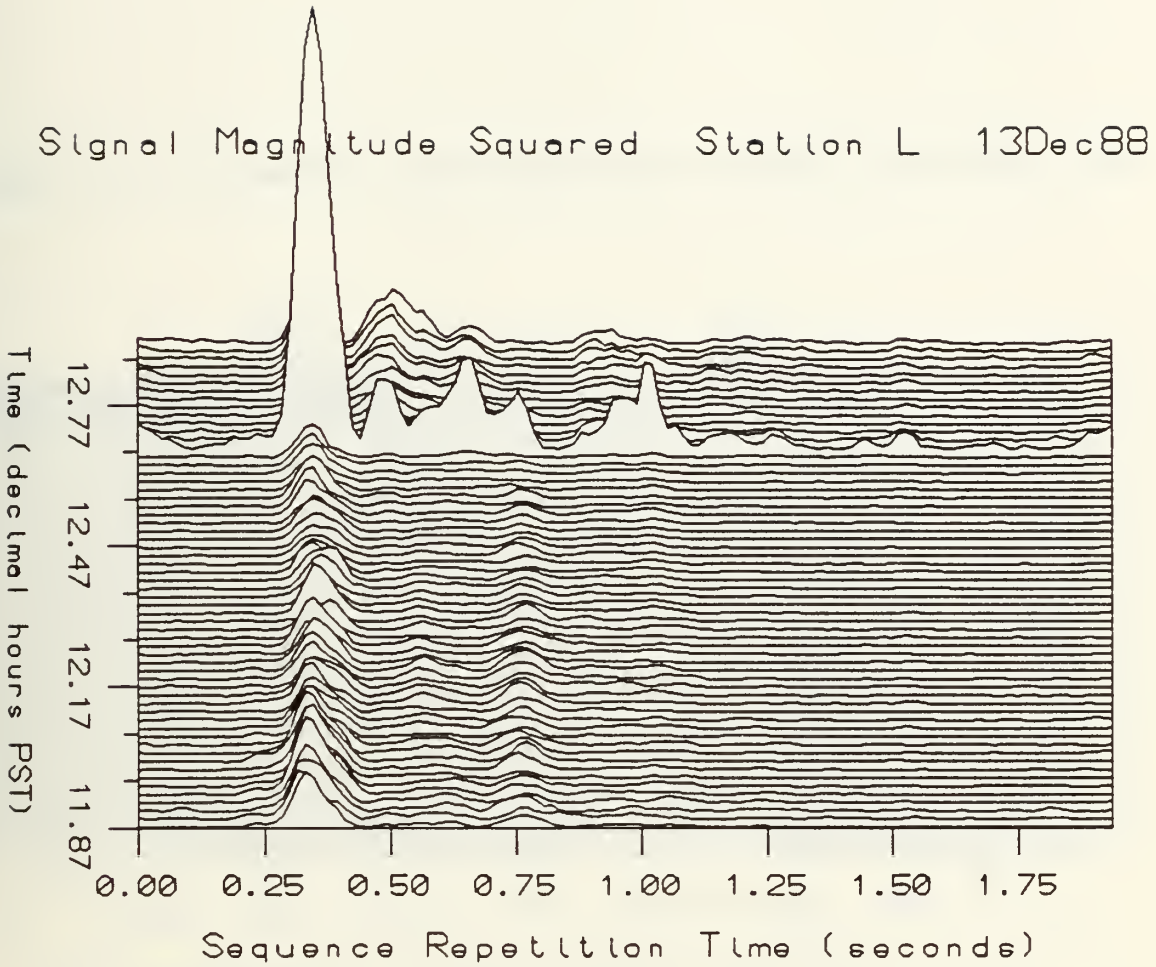

Figure 57: Tomographic signal, coherently averaged 16 times then magnitude squared. Station L, 1154 to 1248 13Dec88.

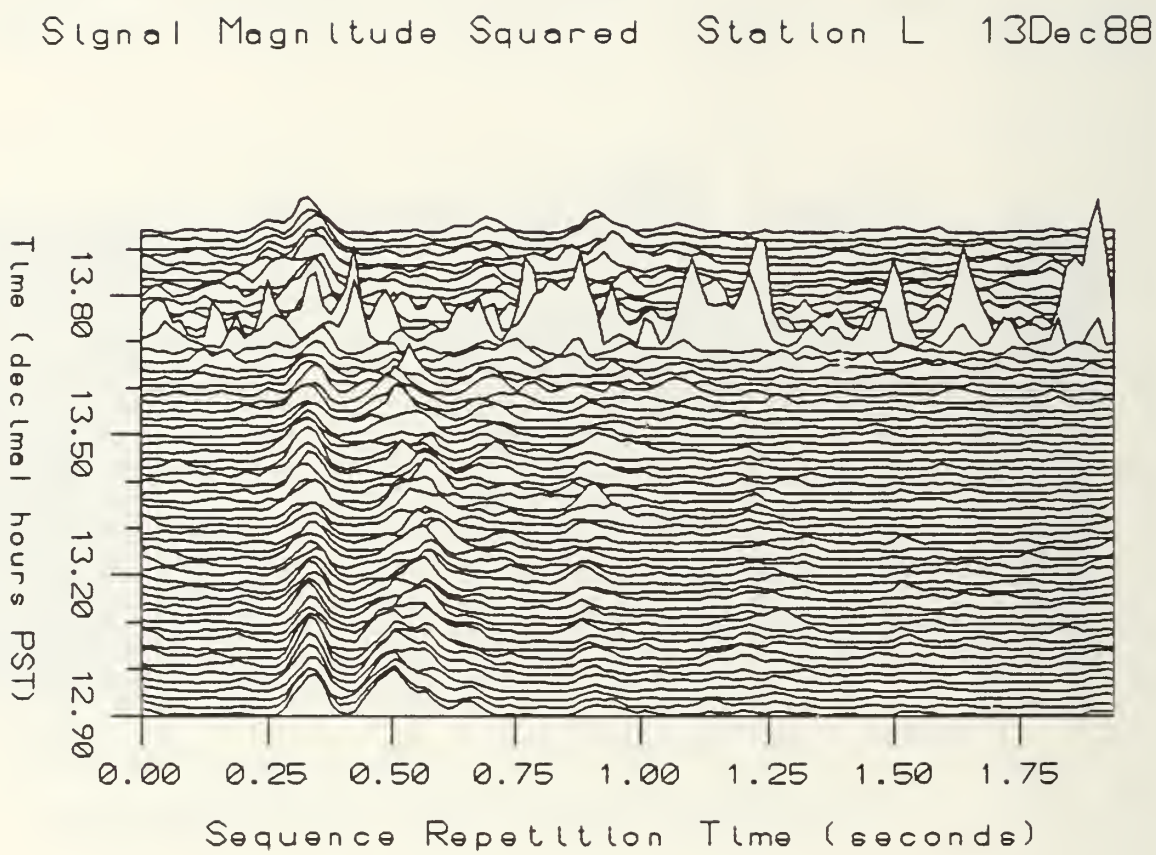

Figure 58: Tomographic signal, coherently averaged 16 times then magnitude squared. Station L, 1254 to 1348 13Dec88.

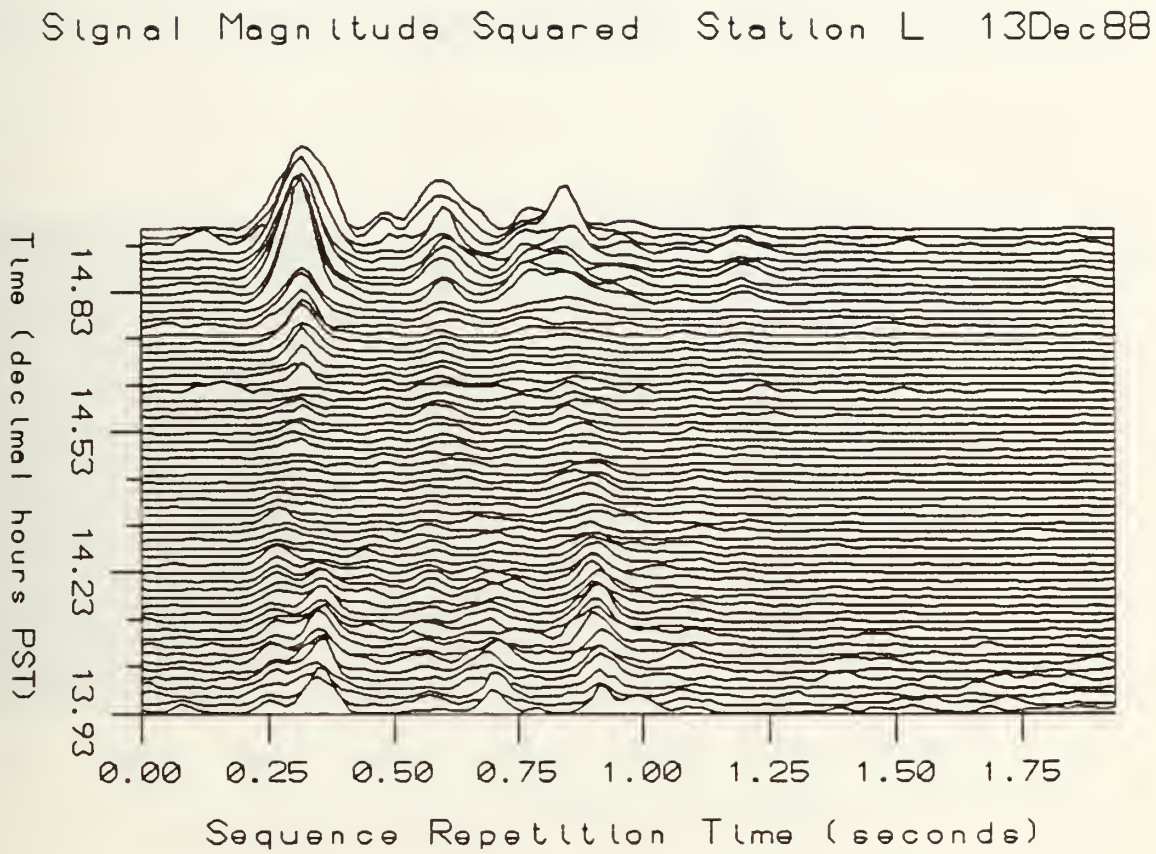

Figure 59: Tomographic signal, coherently averaged 16 times then magnitude squared. Station L, 1354 to 1448 13Dec88.

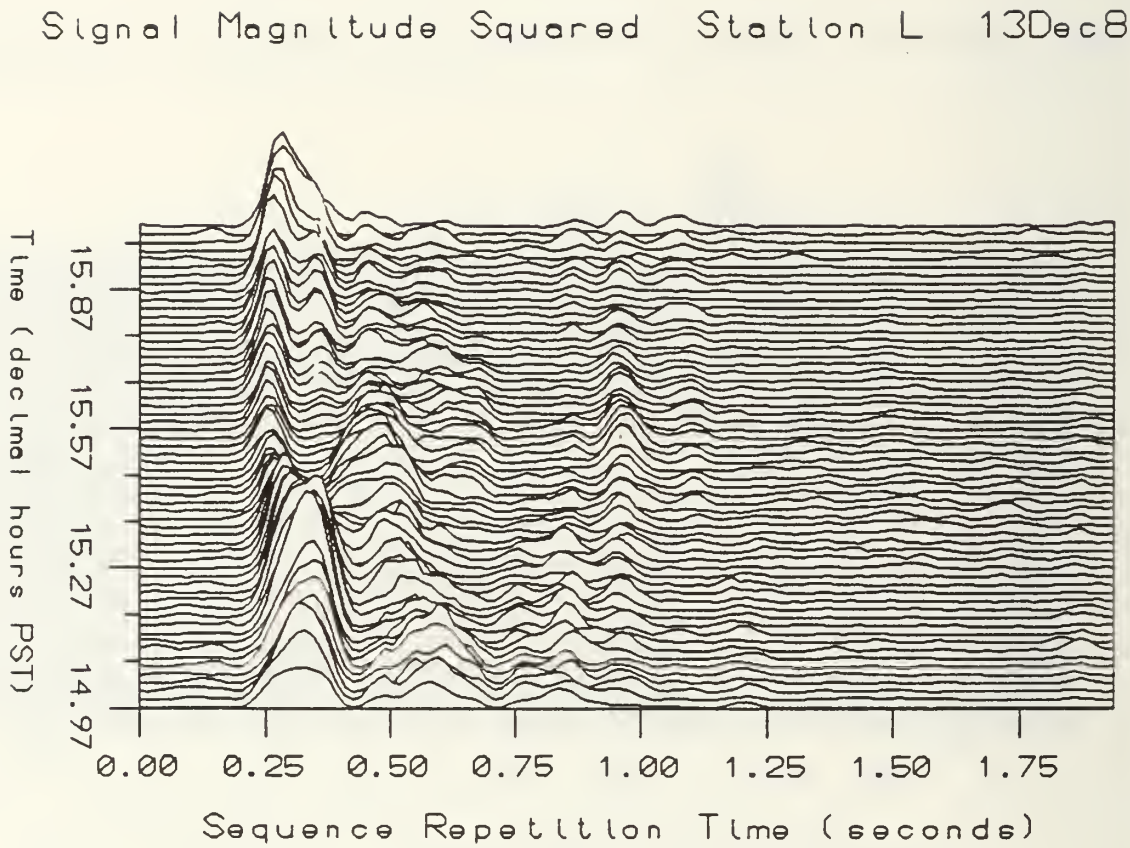

Figure 60: Tomographic signal, coherently averaged 16 times then magnitude squared. Station L, 1500 to 1554 13Dec88.

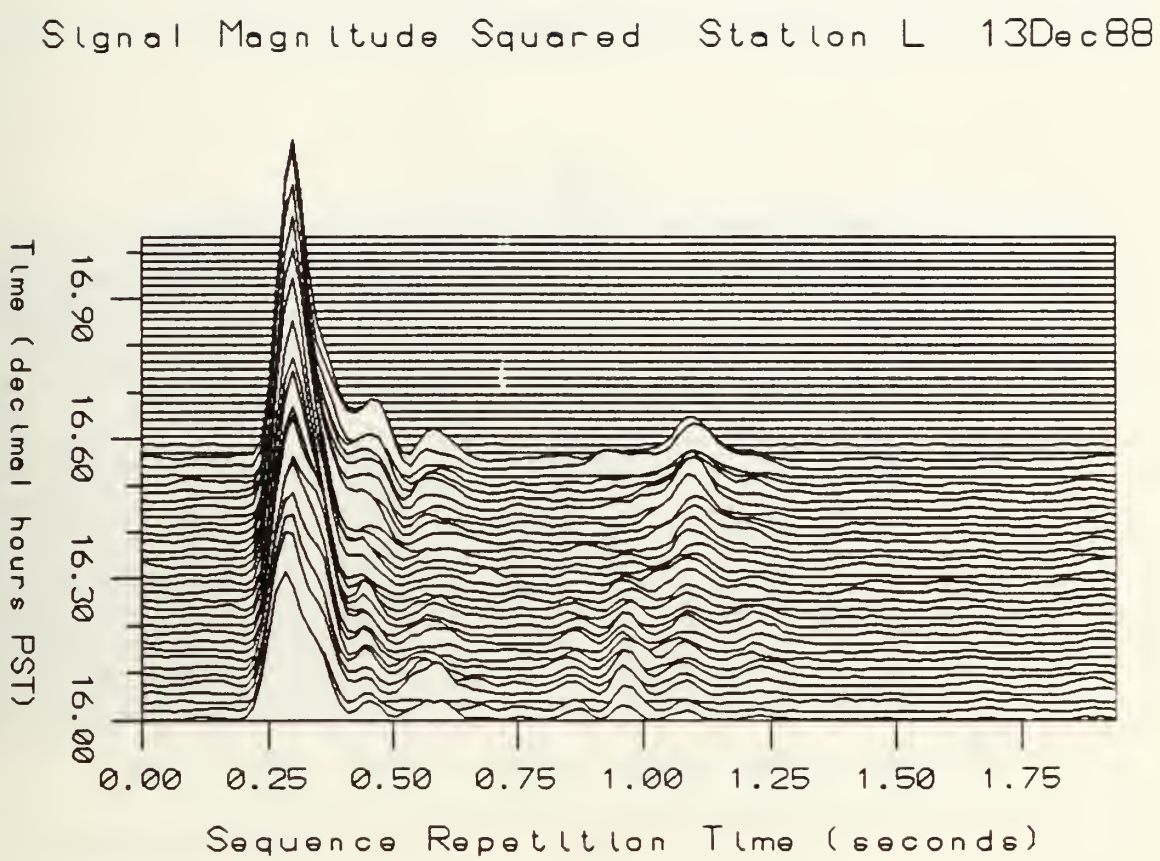

Figure 61: Tomographic signal, coherently averaged 16 times then magnitude squared. Station L, 1600 to 1654 13Dec88.

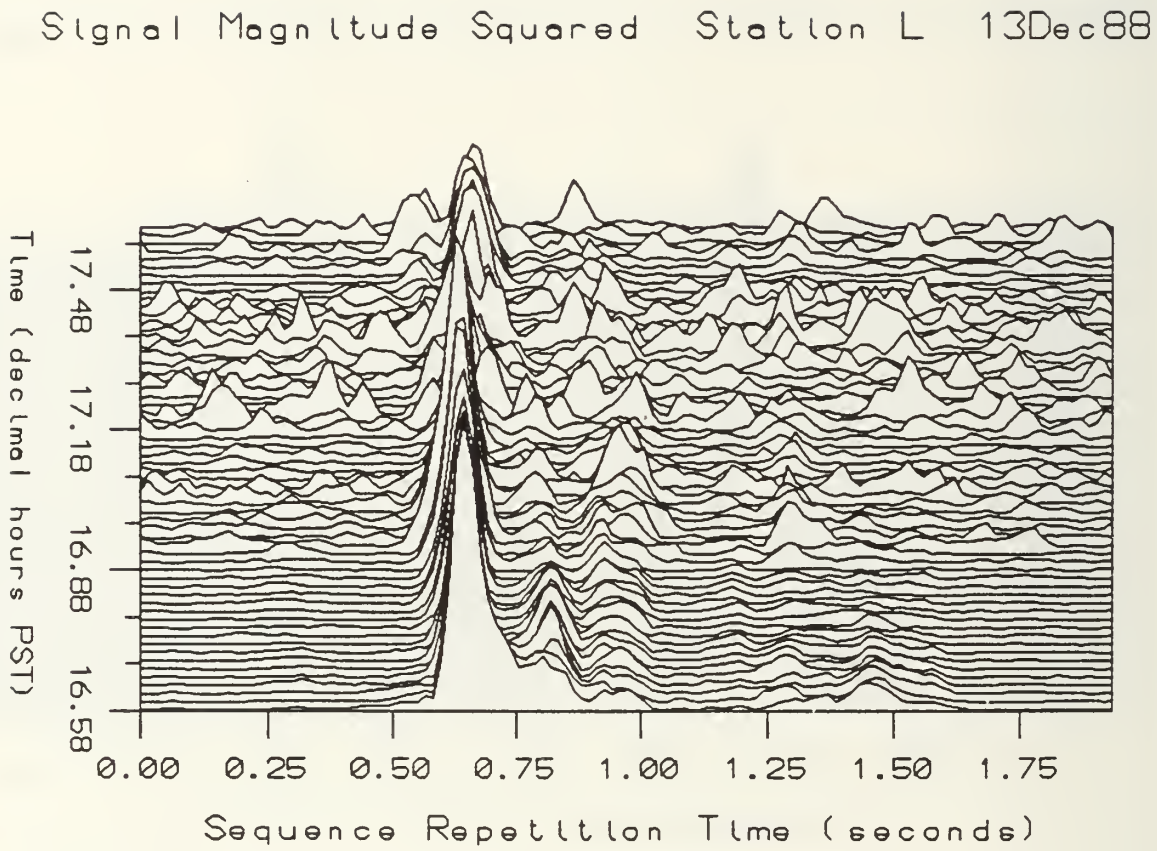

Figure 62: Tomographic signal, coherently averaged 16 times then magnitude squared. Station L, 1636 to 1730 13Dec88.

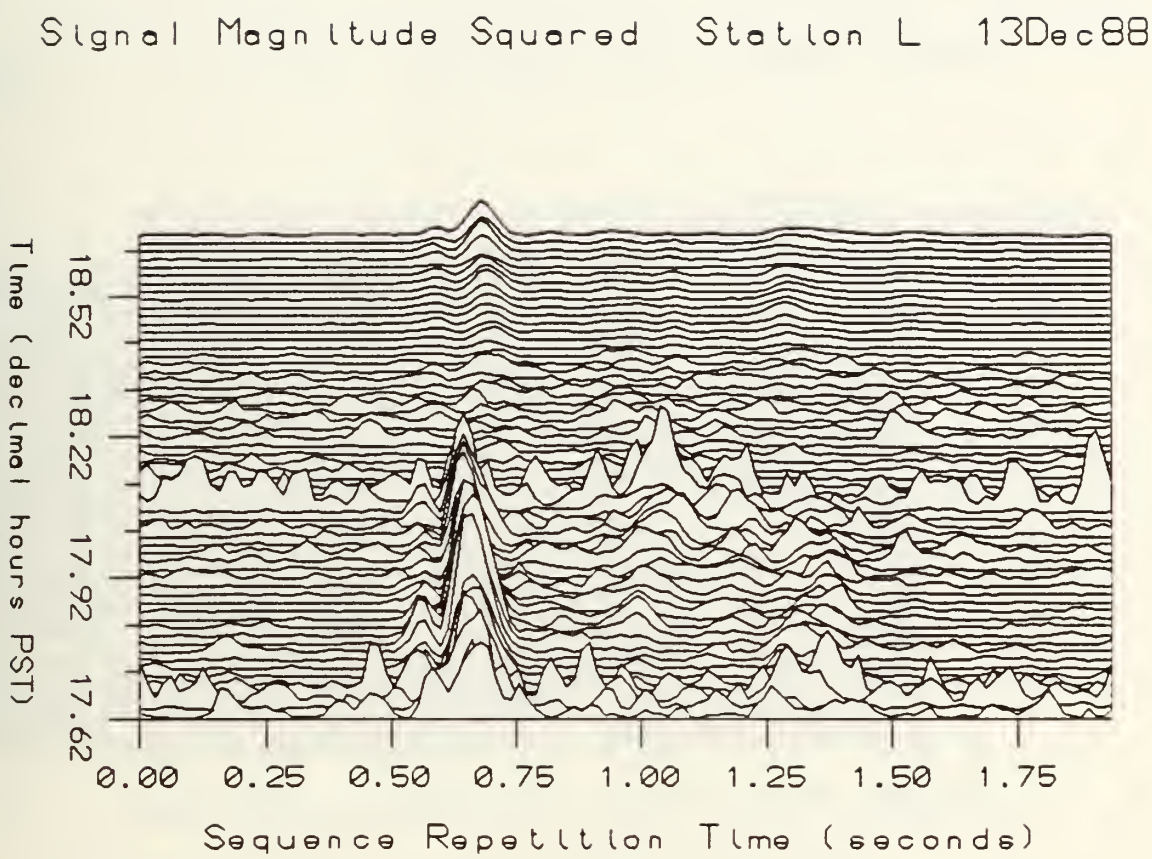

Figure 63: Tomographic signal, coherently averaged 16 times then magnitude squared. Station L, 1736 to 1830 13Dec88.

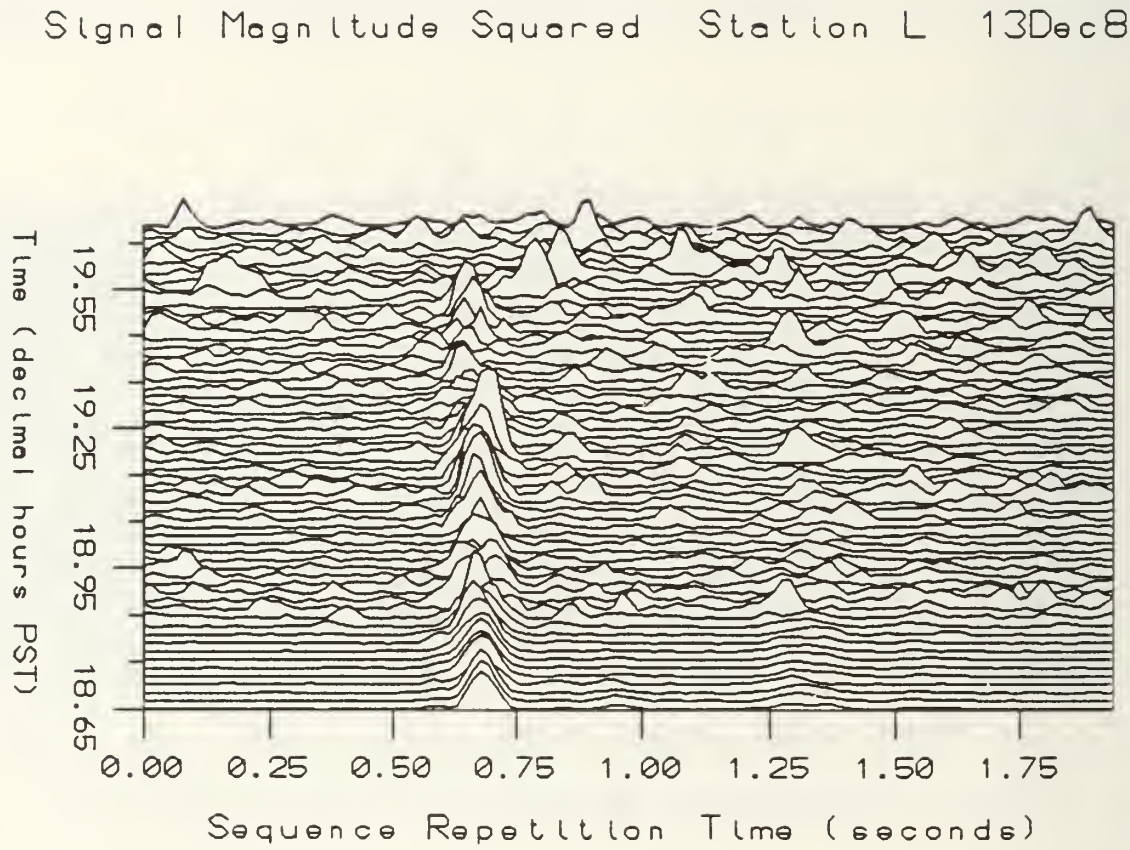

Figure 64: Tomographic signal, coherently averaged 16 times then magnitude squared. Station L, 1842 to 1936 13Dec88.

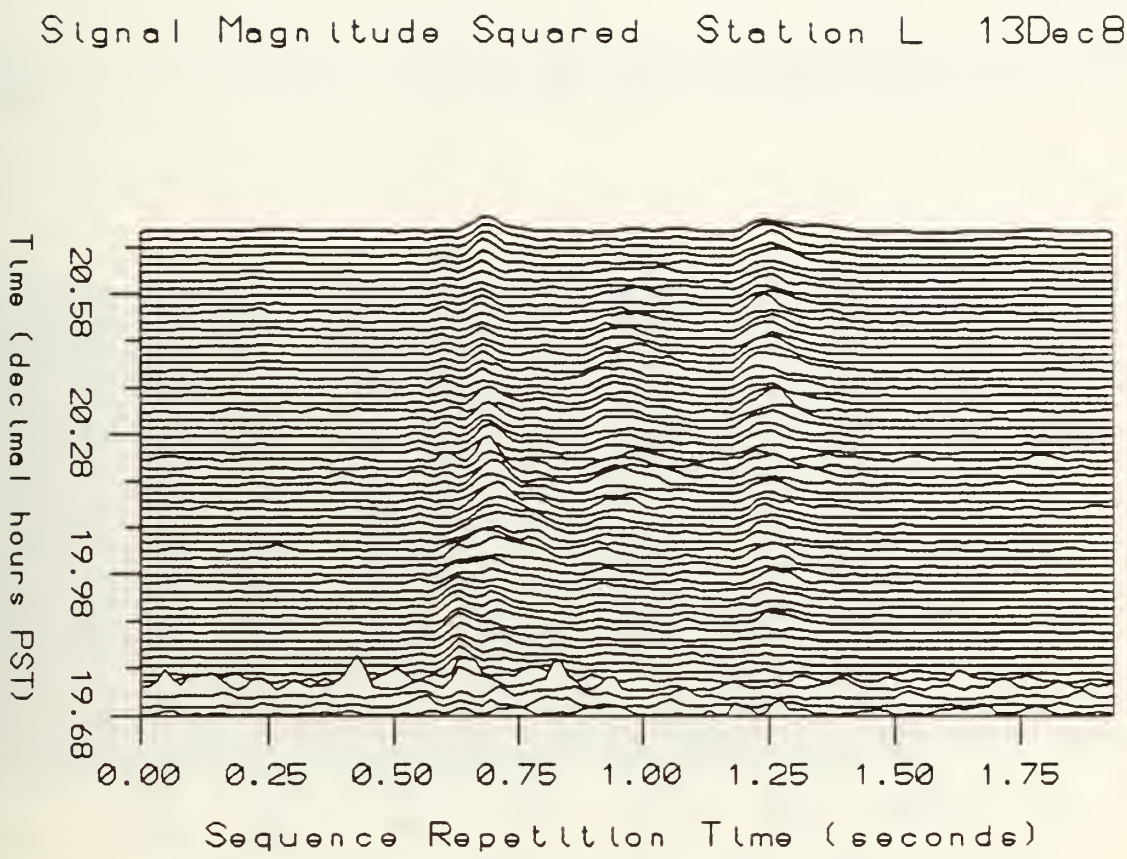

Figure 65: Tomographic signal, coherently averaged 16 times then magnitude squared. Station L, 1949 to 2036 13Dec88.

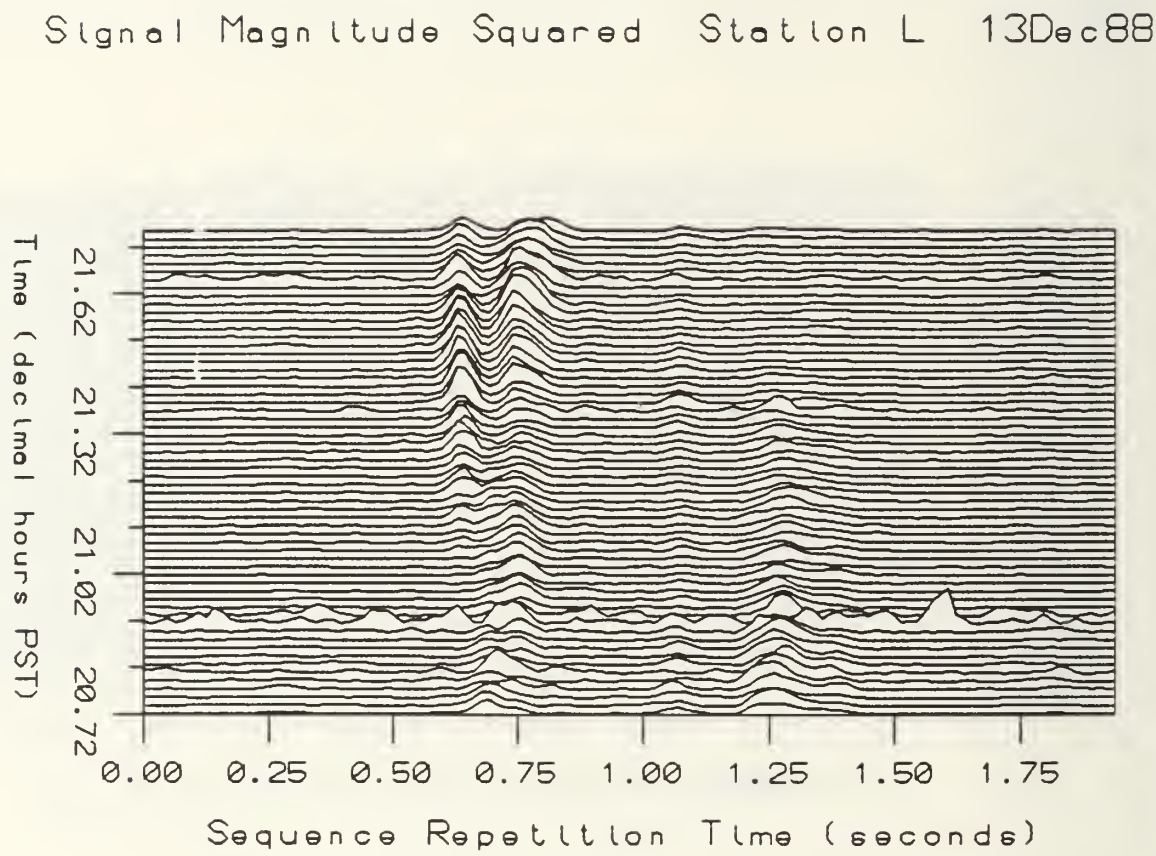

Figure 66: Tomographic signal, coherently averaged 16 times then magnitude squared. Station L, 2049 to 2136 13Dec88.

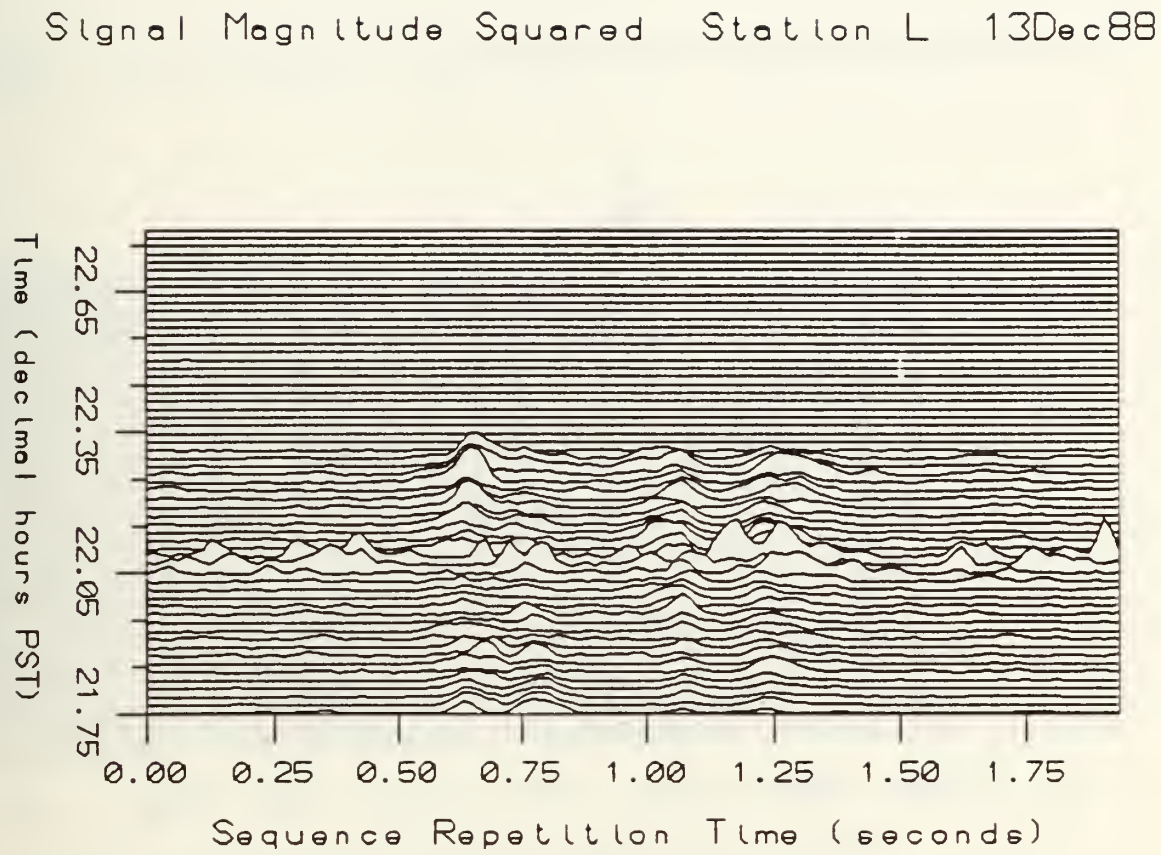

Figure 67: Tomographic signal, coherently averaged 16 times then magnitude squared. Station L, 2148 to 2242 13Dec88.

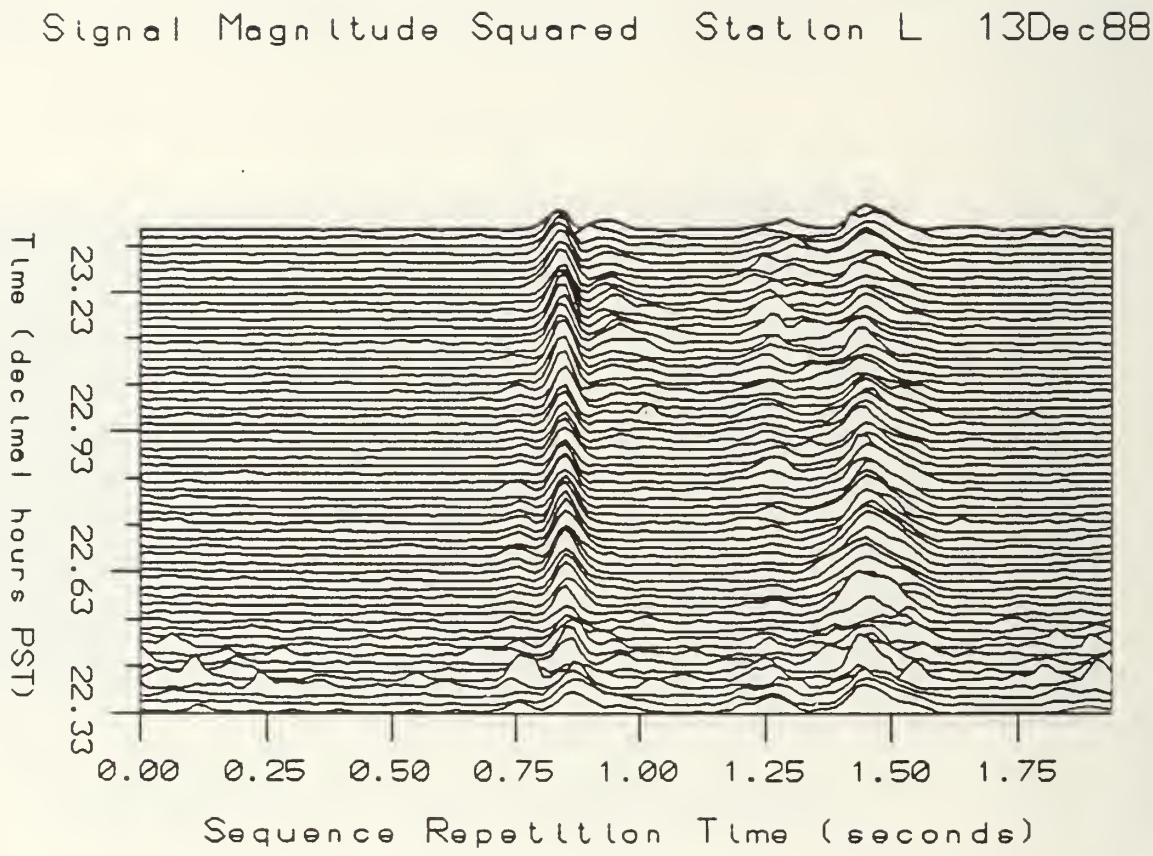

Figure 68: Tomographic signal, coherently averaged 16 times then magnitude squared. Station L, 2218 to 2312 13Dec88.

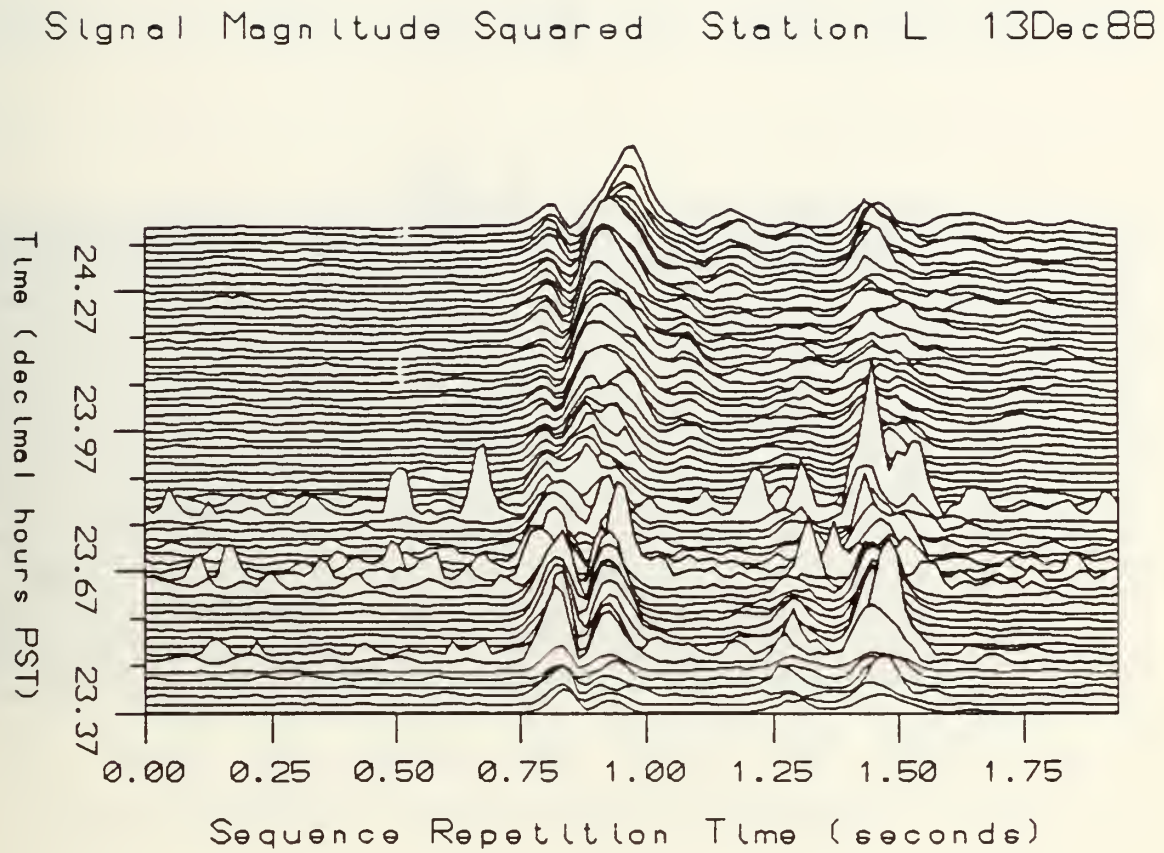

Figure 69: Tomographic signal, coherently averaged 16 times then magnitude squared. Station L, 2324 13 Dec88 to 0018 14Dec88.

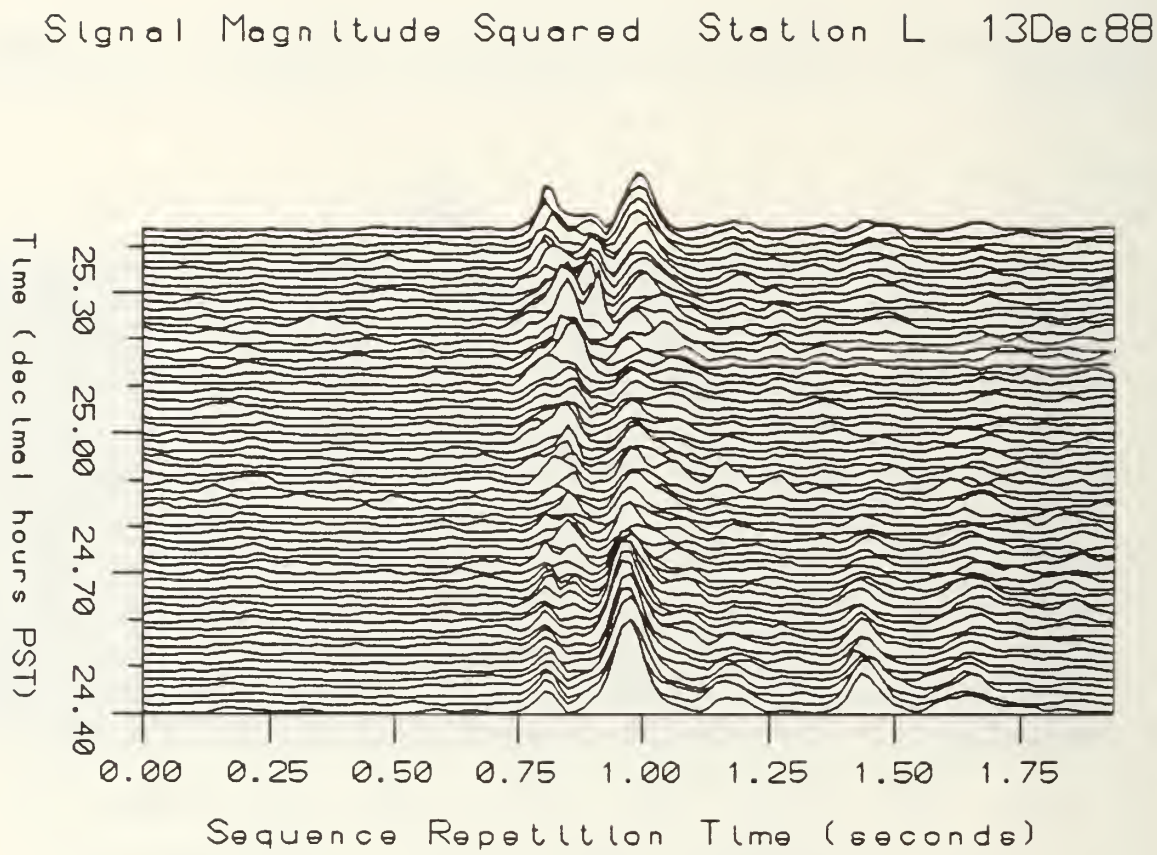

Figure 70: Tomographic signal, coherently averaged 16 times then magnitude squared. Station L, 0024 to 0118 14Dec88.

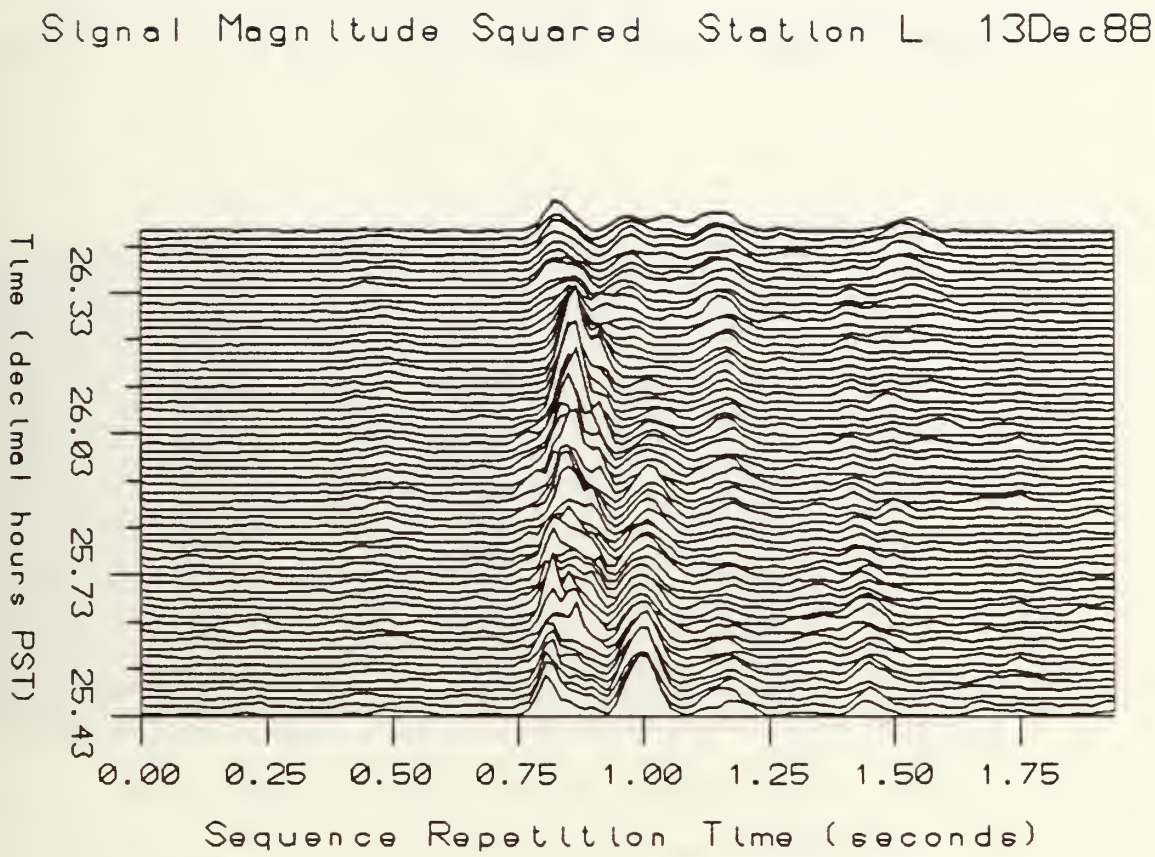

Figure 71: Tomographic signal, coherently averaged 16 times then magnitude squared. Station L, 0124 to 0218 14Dec88.

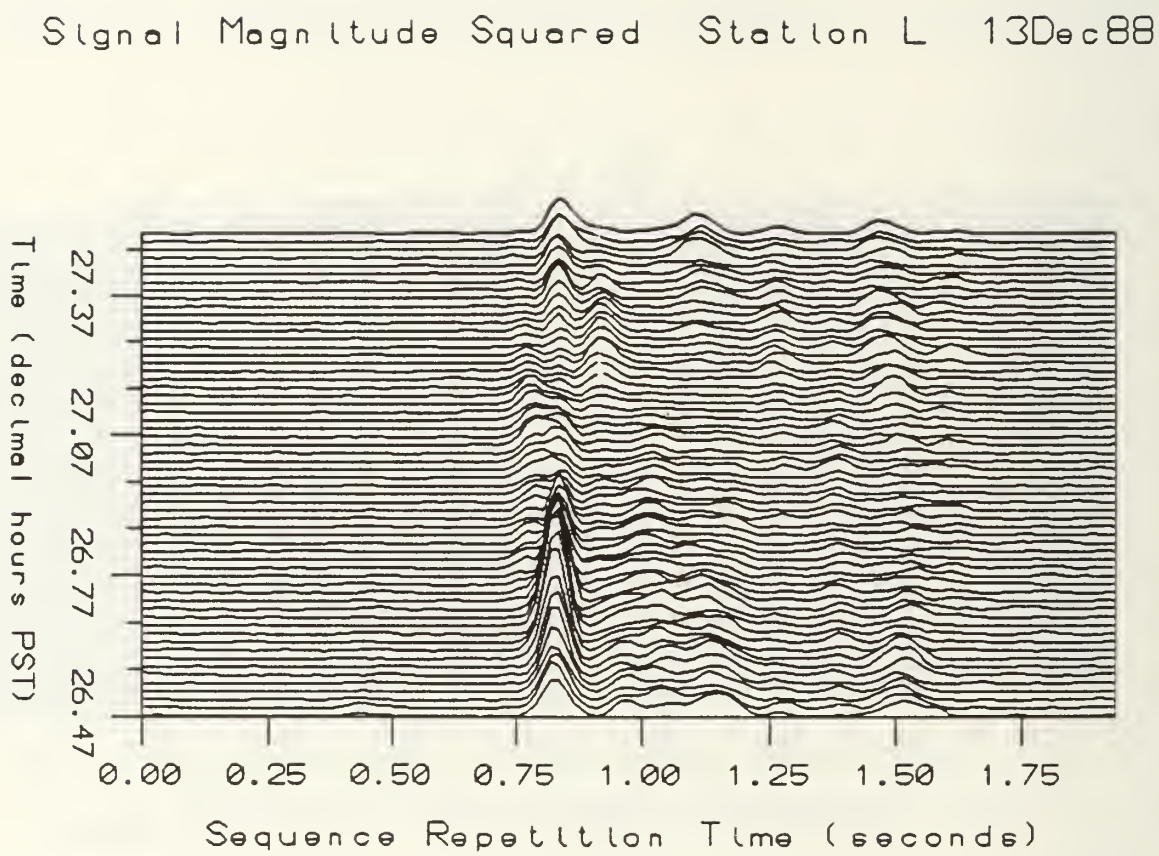

Figure 72: Tomographic signal, coherently averaged 16 times then magnitude squared. Station L, 0230 to 0324 14Dec88.

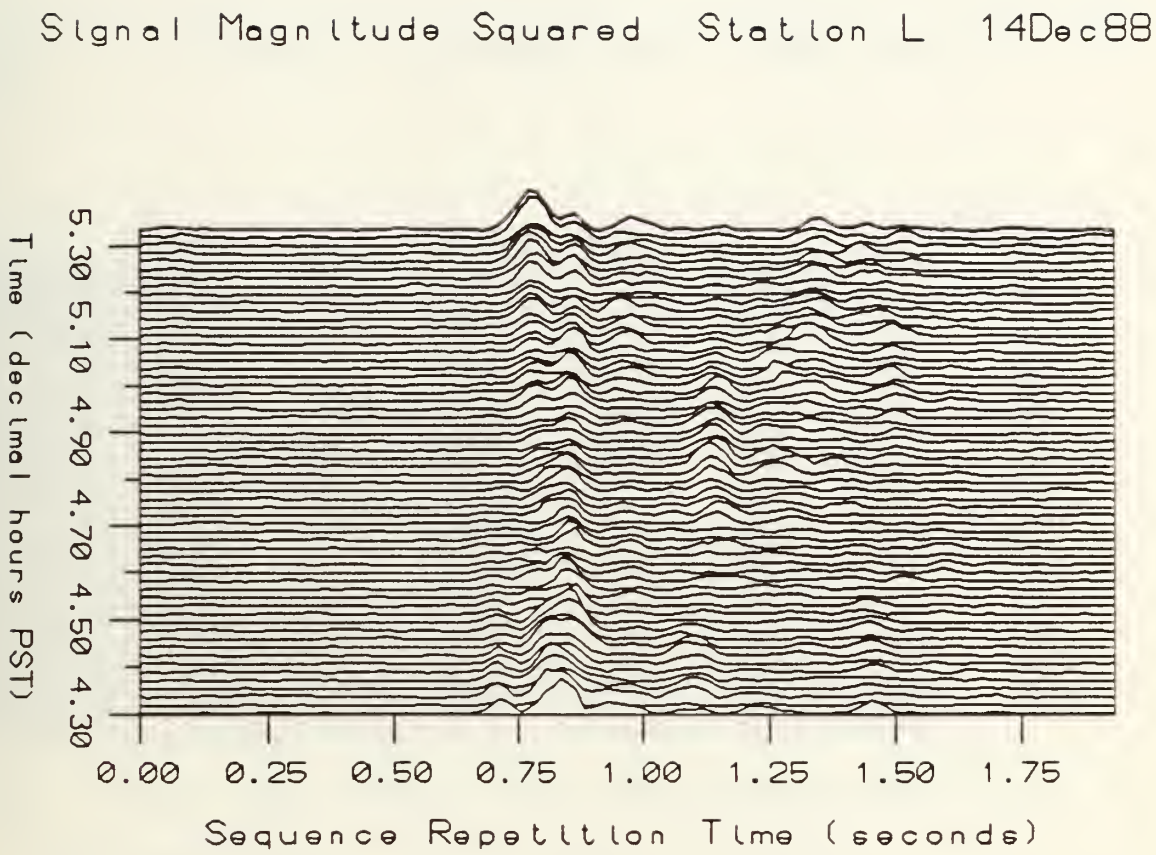

Figure 73: Tomographic signal, coherently averaged 16 times then magnitude squared. Station L, 0418 to 0518 14Dec88.

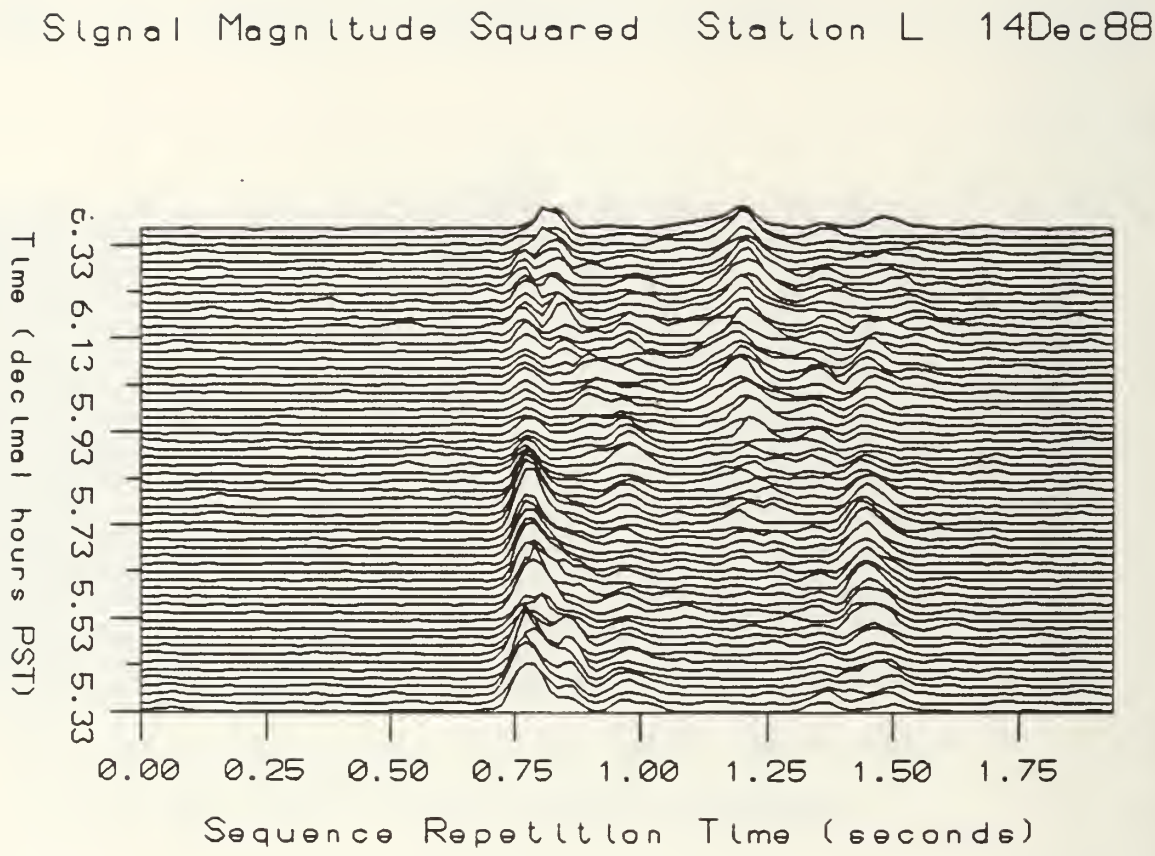
Signal Magnitude Squared Station L 14Dec88
Time (decimal hours PST)
6.33 6.13 5.93 5.73 5.53 5.33
0.00 0.25 0.50 0.75 1.00 1.25 1.50 1.75
Sequence Repetition Time (seconds)

Figure 74: Tomographic signal, coherently averaged 16 times then magnitude squared. Station L, 0518 to 0618 14Dec88.

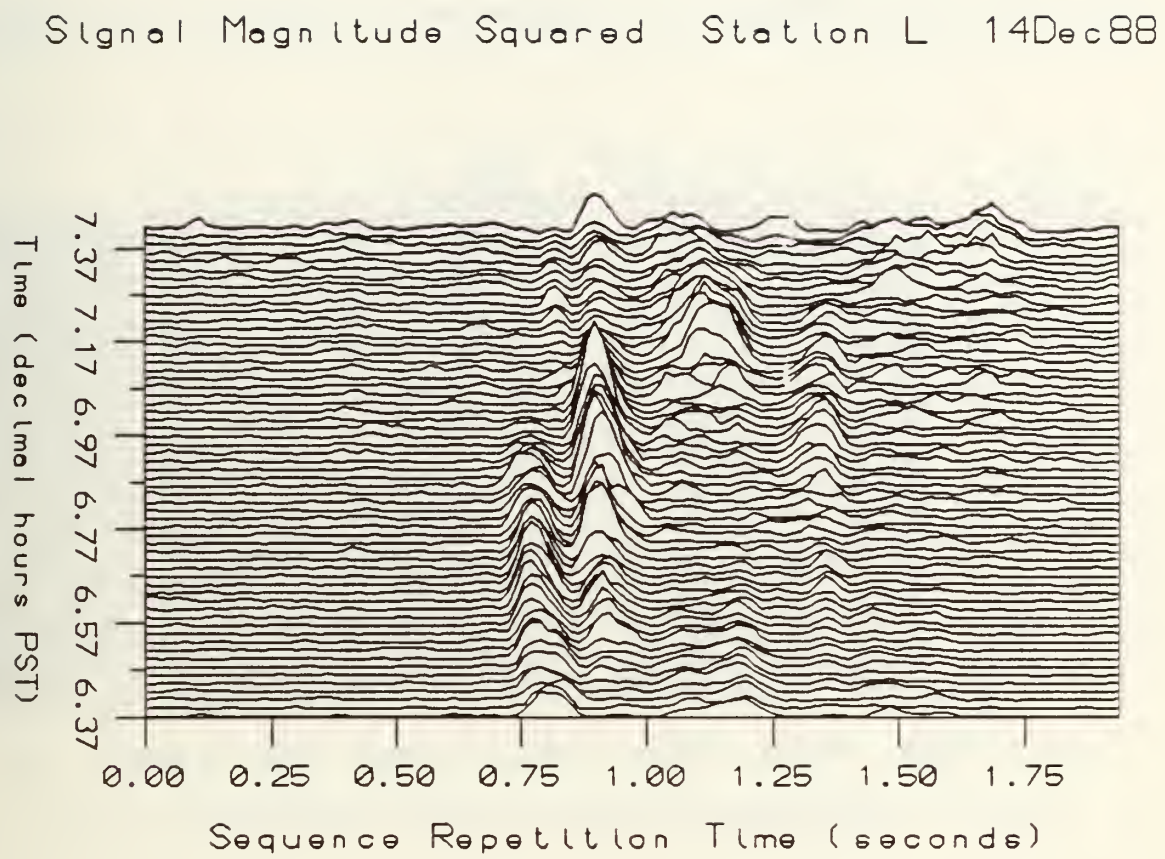
Signal Magnitude Squared Station L 14Dec88
Time (decimal hours PST)
7.37 7.17 6.97 6.77 6.57 6.37
0.00 0.25 0.50 0.75 1.00 1.25 1.50 1.75
Sequence Repetition Time (seconds)

Figure 75: Tomographic signal, coherently averaged 16 times then magnitude squared. Station L, 0624 to 0724 14Dec88.

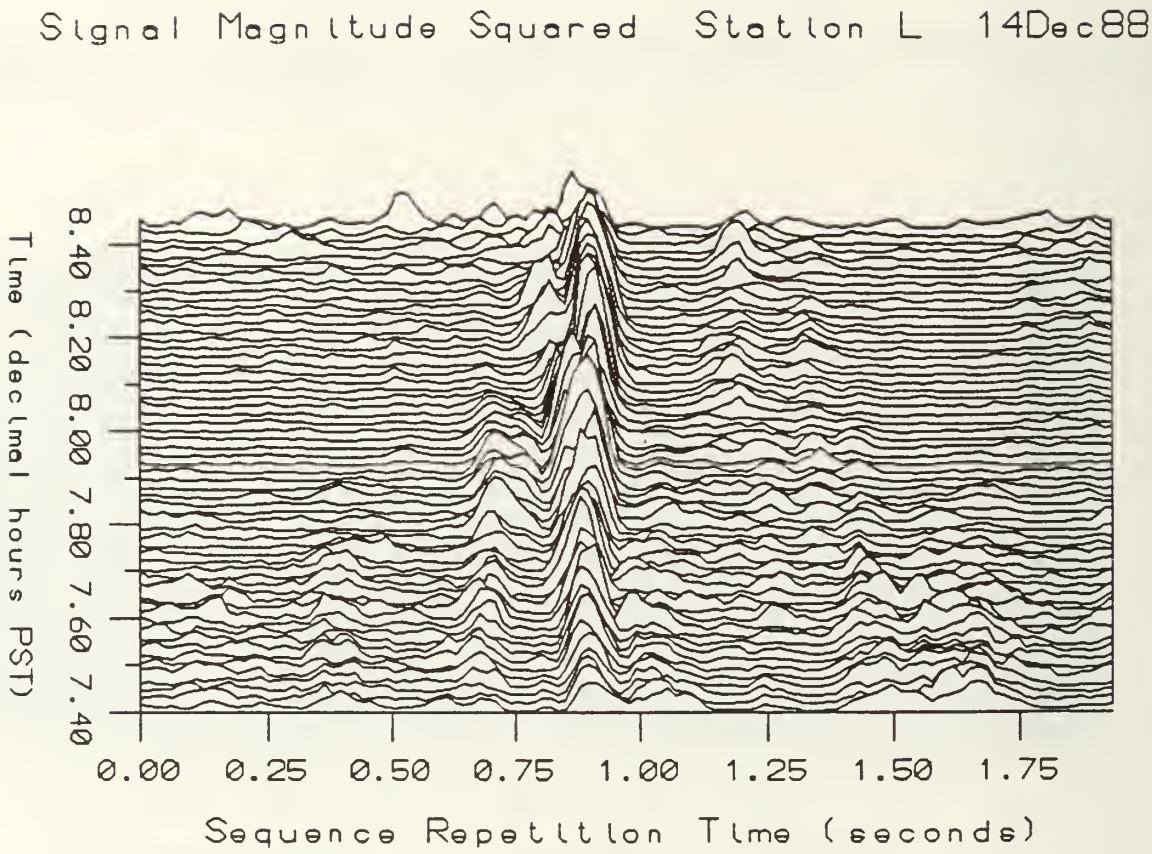
Signal Magnitude Squared Station L 14Dec88
Time (decimal hours PST)
8.40 8.20 8.00 7.80 7.60 7.40
0.00 0.25 0.50 0.75 1.00 1.25 1.50 1.75
Sequence Repetition Time (seconds)

Figure 76: Tomographic signal, coherently averaged 16 times then magnitude squared. Station L, 0724 to 0824 14Dec88.

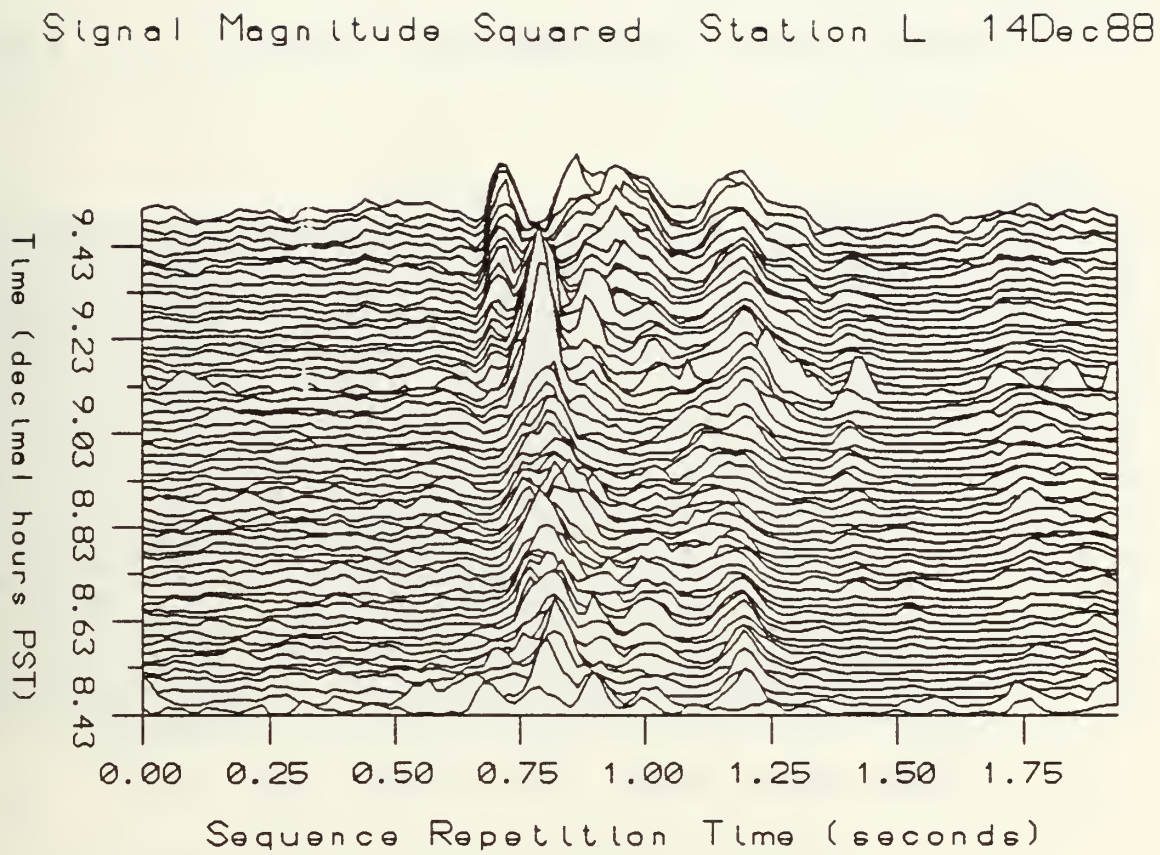
Signal Magnitude Squared Station L 14Dec88
Time (decimal hours PST)
9.43 9.23 9.03 8.83 8.63 8.43
0.00 0.25 0.50 0.75 1.00 1.25 1.50 1.75
Sequence Repetition Time (seconds)

Figure 77: Tomographic signal, coherently averaged 16 times then magnitude squared. Station L, 0824 to 0924 14Dec88.

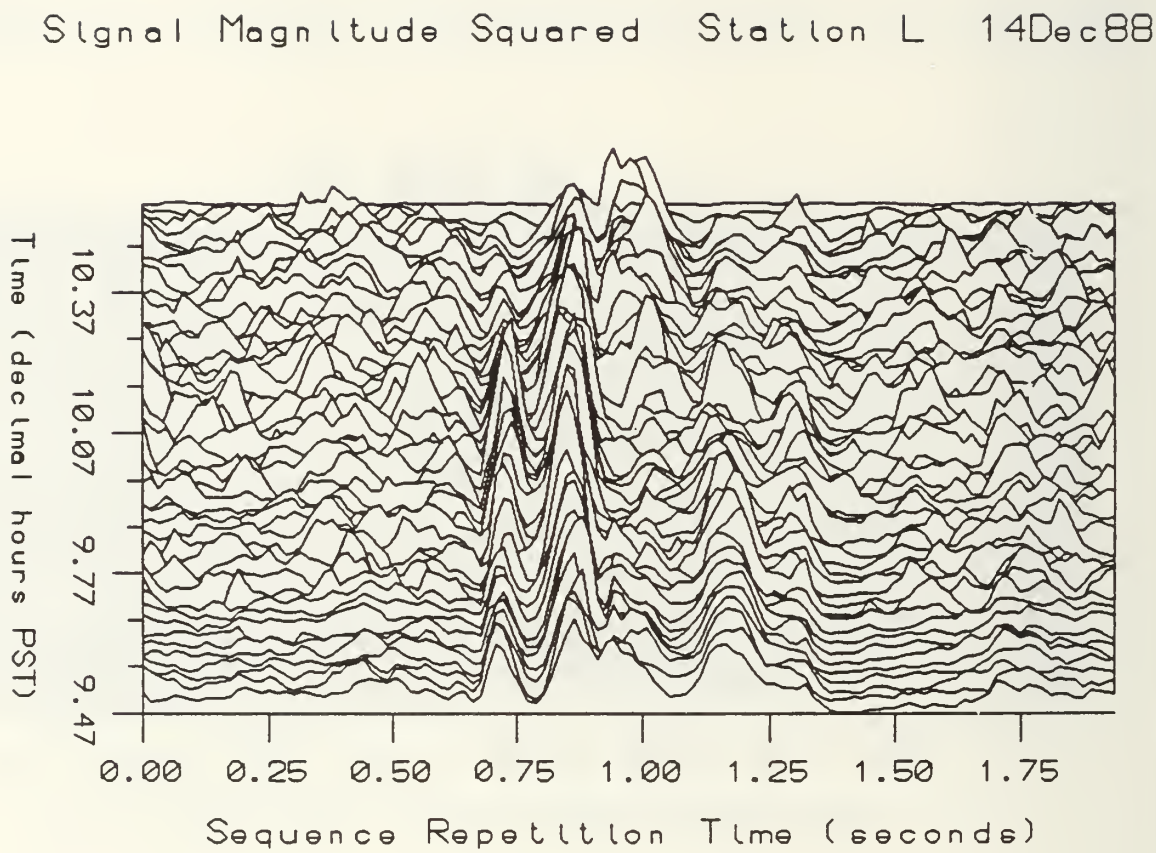

Figure 78: Tomographic signal, coherently averaged 16 times then magnitude squared. Station L, 0924 to 1024 14Dec88.

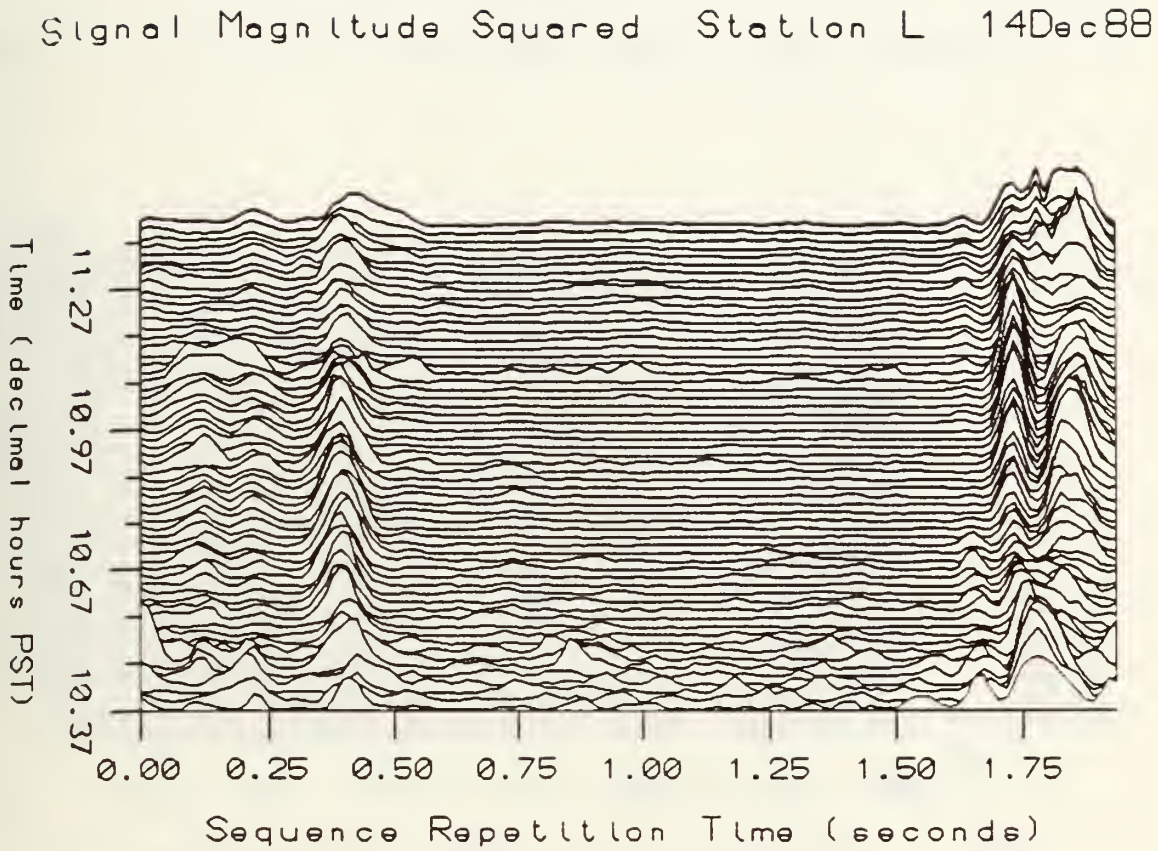

Figure 79: Tomographic signal, coherently averaged 16 times then magnitude squared. Station L, 1024 to 1124 14Dec88.

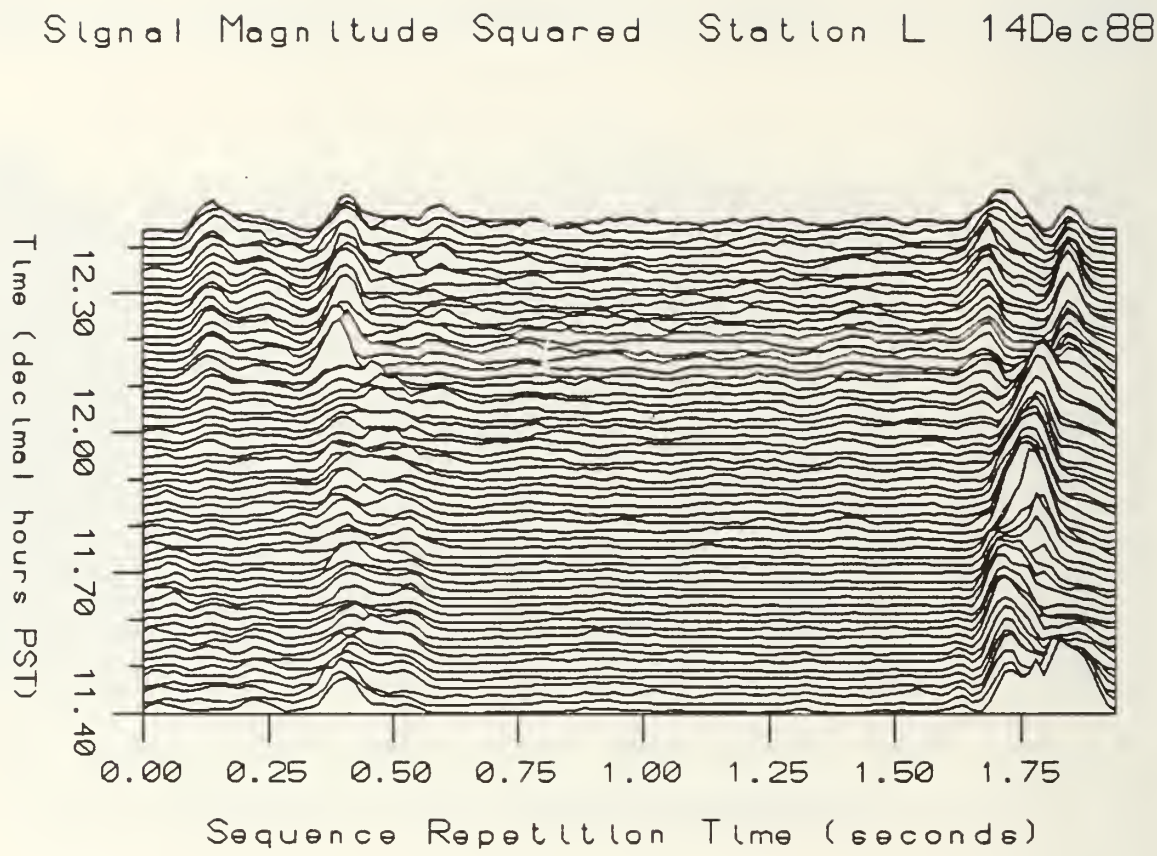

Figure 80: Tomographic signal, coherently averaged 16 times then magnitude squared. Station L, 1124 to 1218 14Dec88.

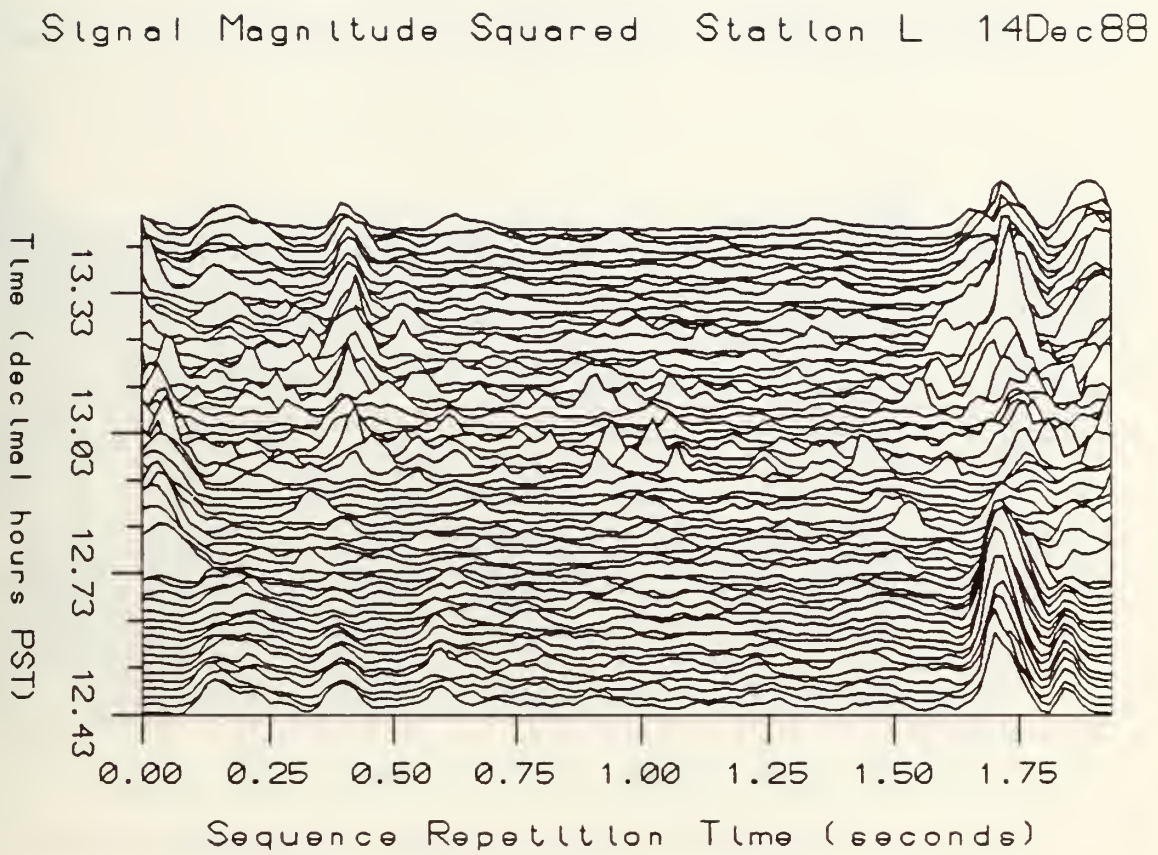

Figure 81: Tomographic signal, coherently averaged 16 times then magnitude squared. Station L, 1224 to 1318 14Dec88.

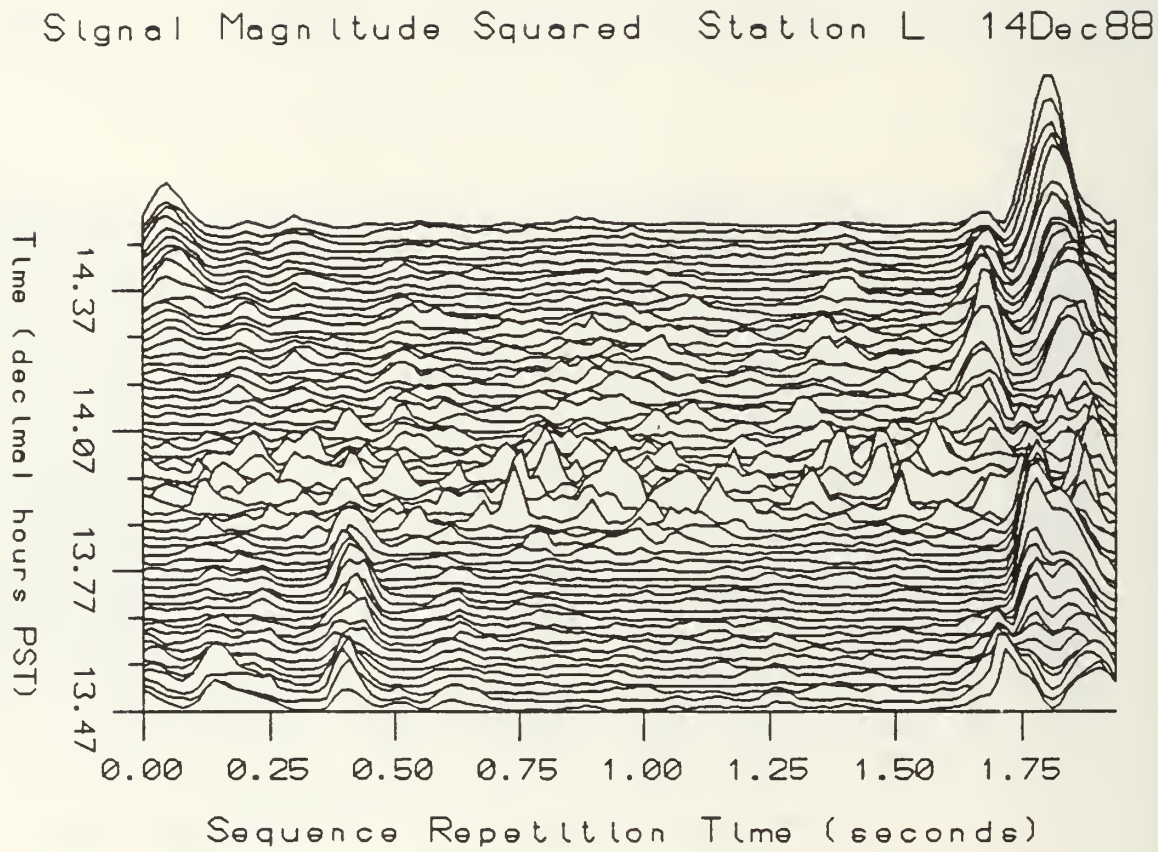

Figure 82: Tomographic signal, coherently averaged 16 times then magnitude squared. Station L, 1330 to 1424 14Dec88.

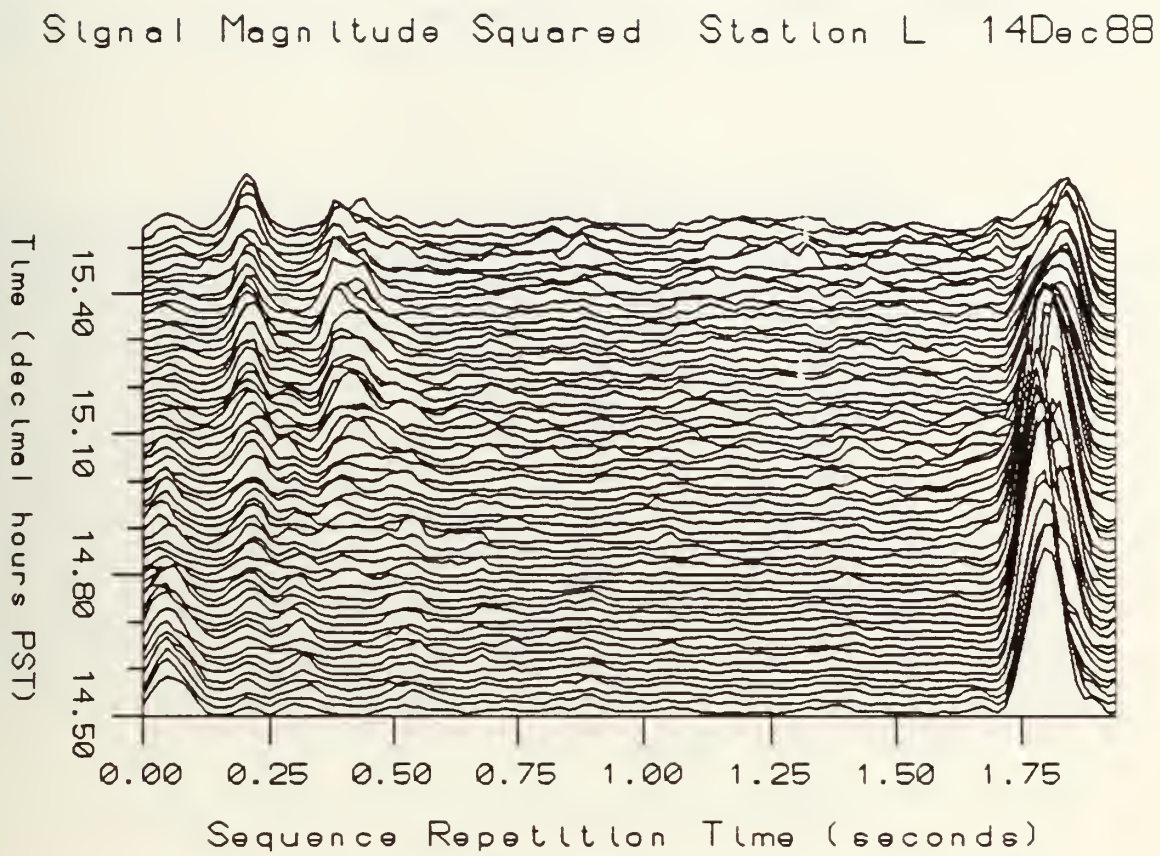

Figure 83: Tomographic signal, coherently averaged 16 times then magnitude squared. Station L, 1430 to 1524 14Dec88.

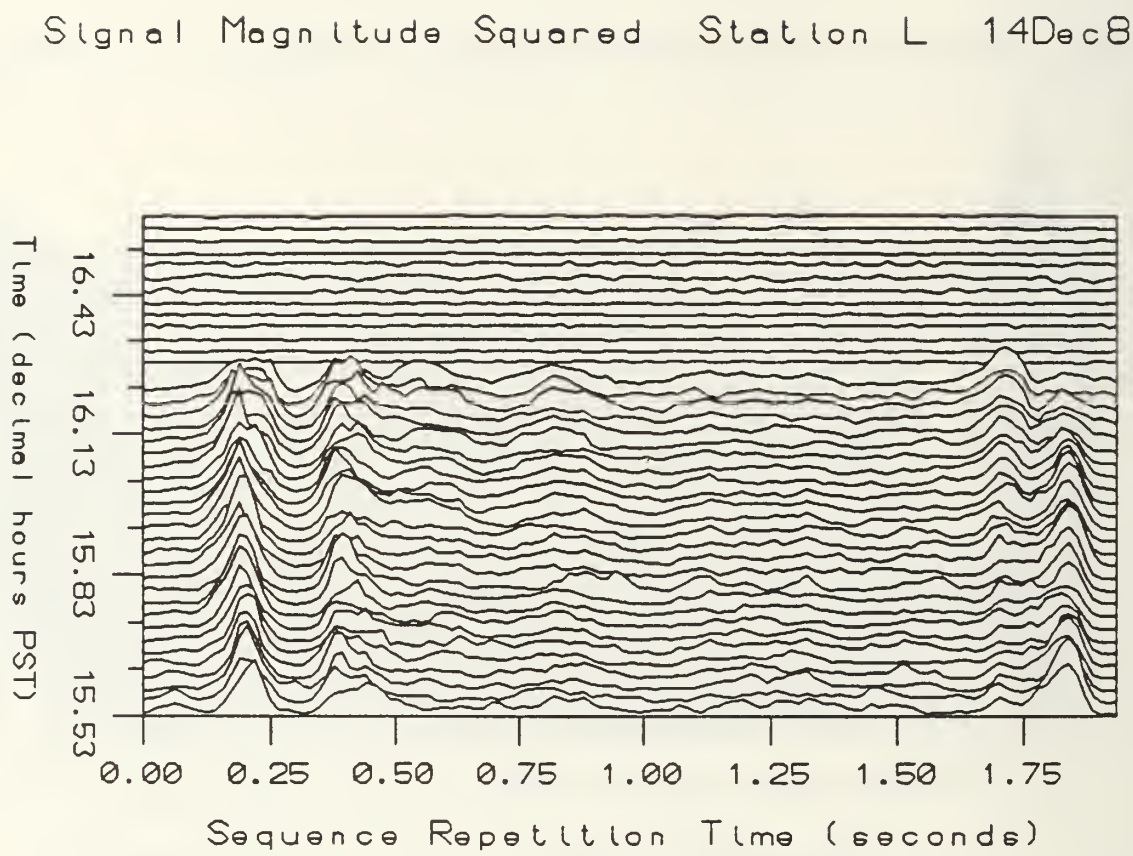

Figure 84: Tomographic signal, coherently averaged 16 times then magnitude squared. Station L, 1530 to 1624 14Dec88.

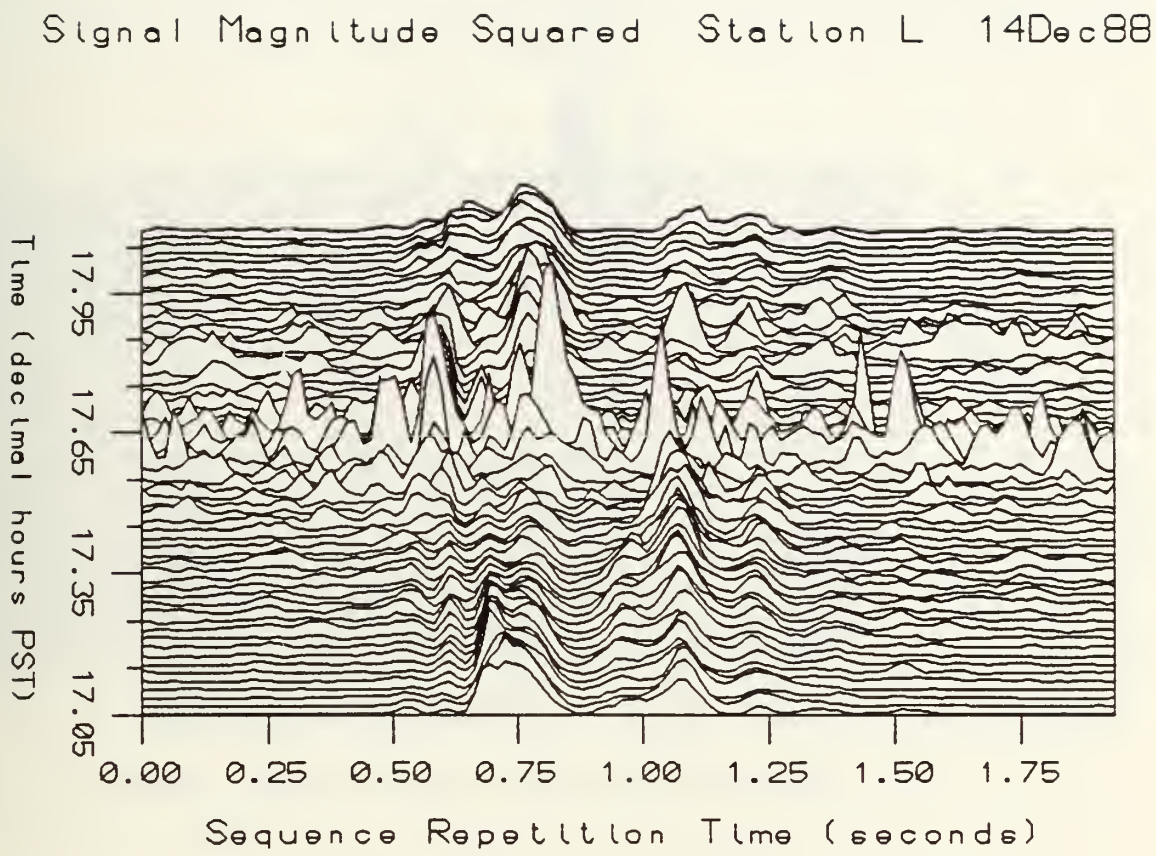

Figure 85: Tomographic signal, coherently averaged 16 times then magnitude squared. Station L, 1703 to 1757 14Dec88.

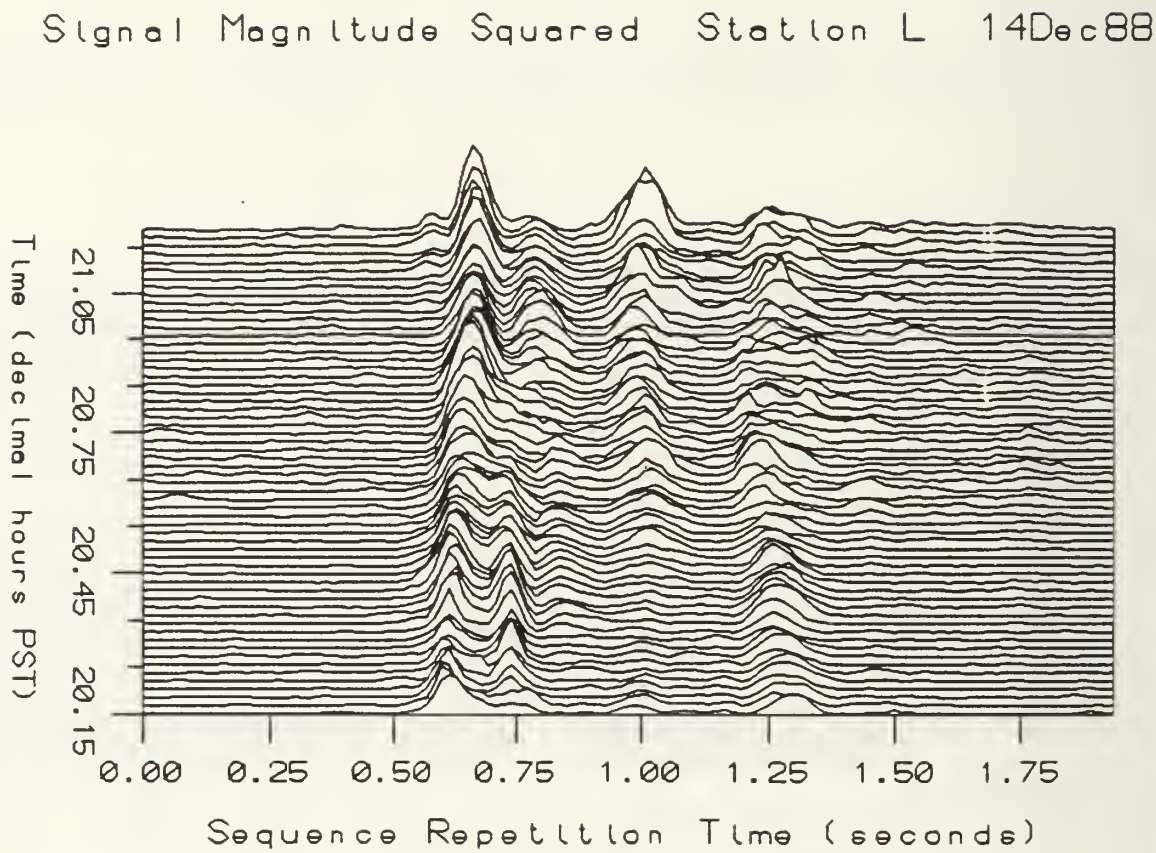

Figure 86: Tomographic signal, coherently averaged 16 times then magnitude squared. Station L, 2109 to 2103 14Dec88.

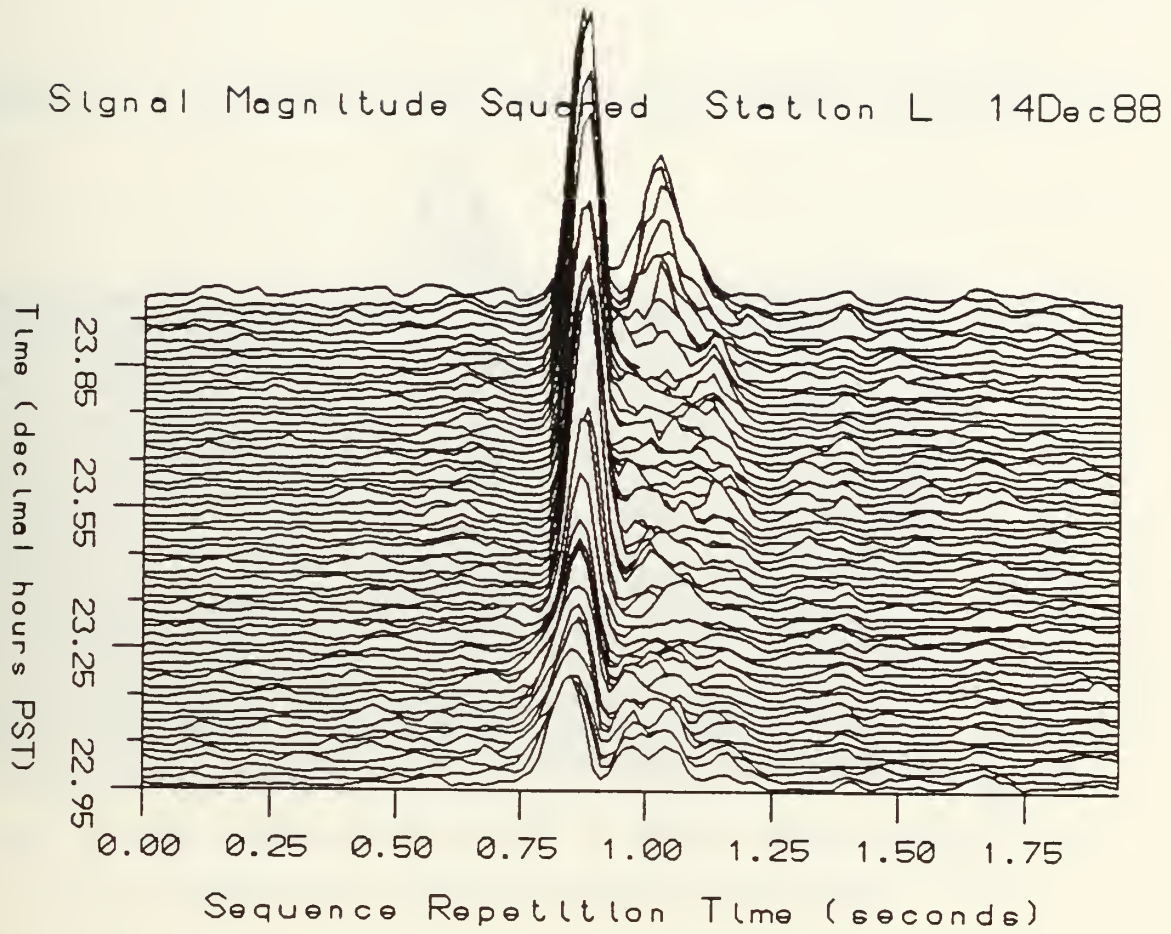

Figure 87: Tomographic signal, coherently averaged 16 times then magnitude squared. Station L, 2257 to 2351 14Dec88.

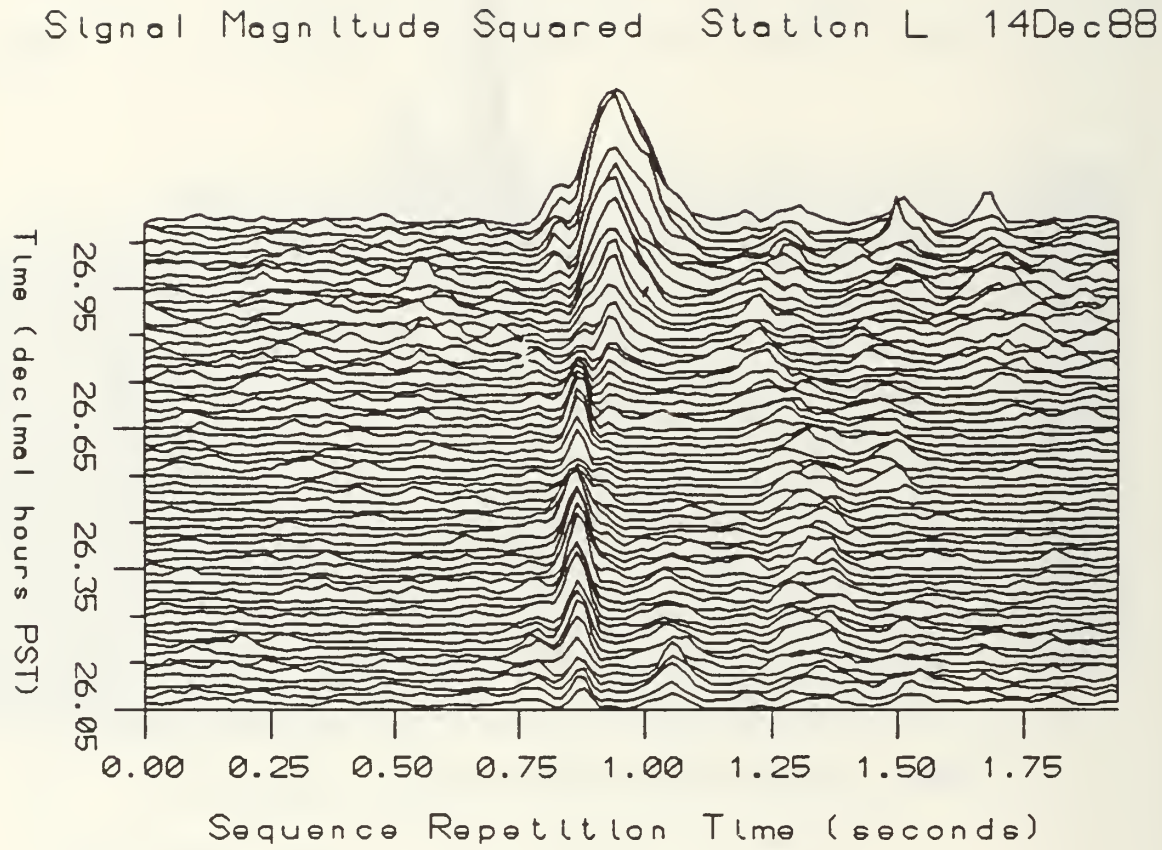

Figure 88: Tomographic signal, coherently averaged 16 times then magnitude squared. Station L, 0203 to 0257 15Dec88.

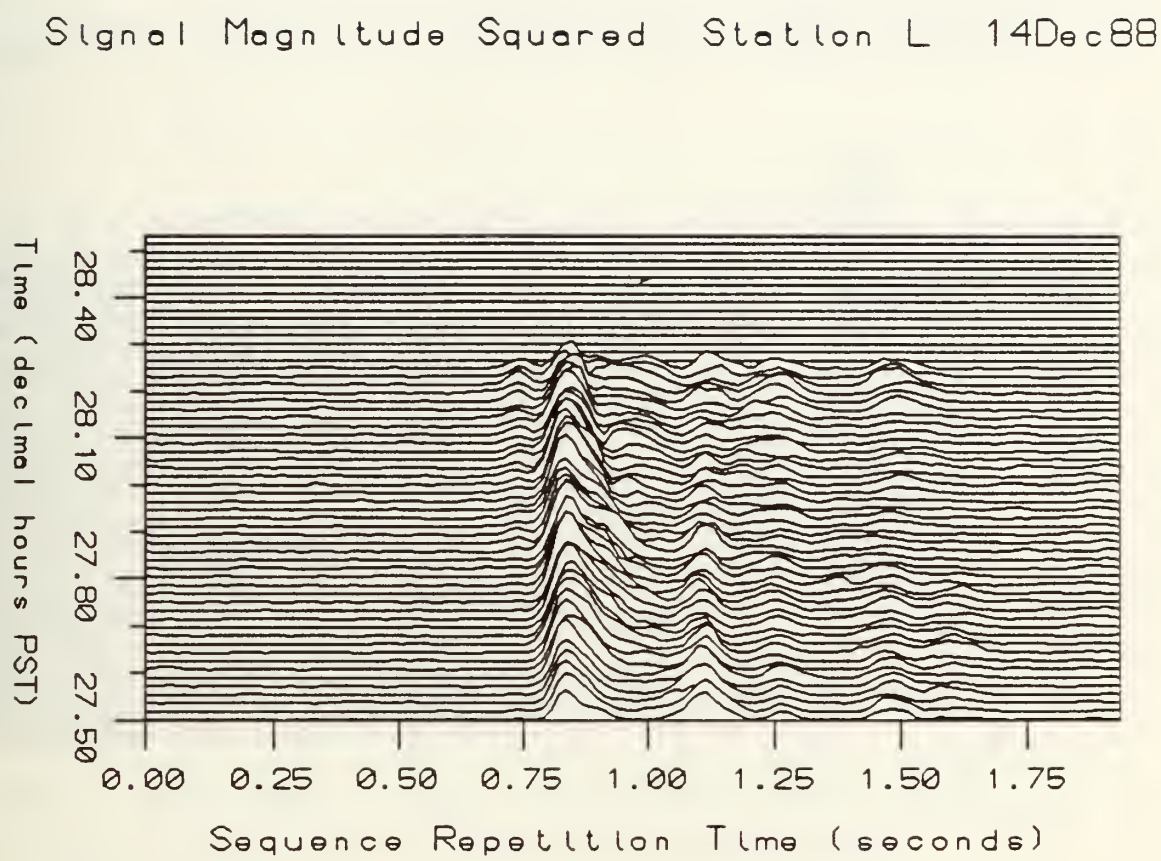

Figure 89: Tomographic signal, coherently averaged 16 times then magnitude squared. Station L, 0330 to 0424 15Dec88.

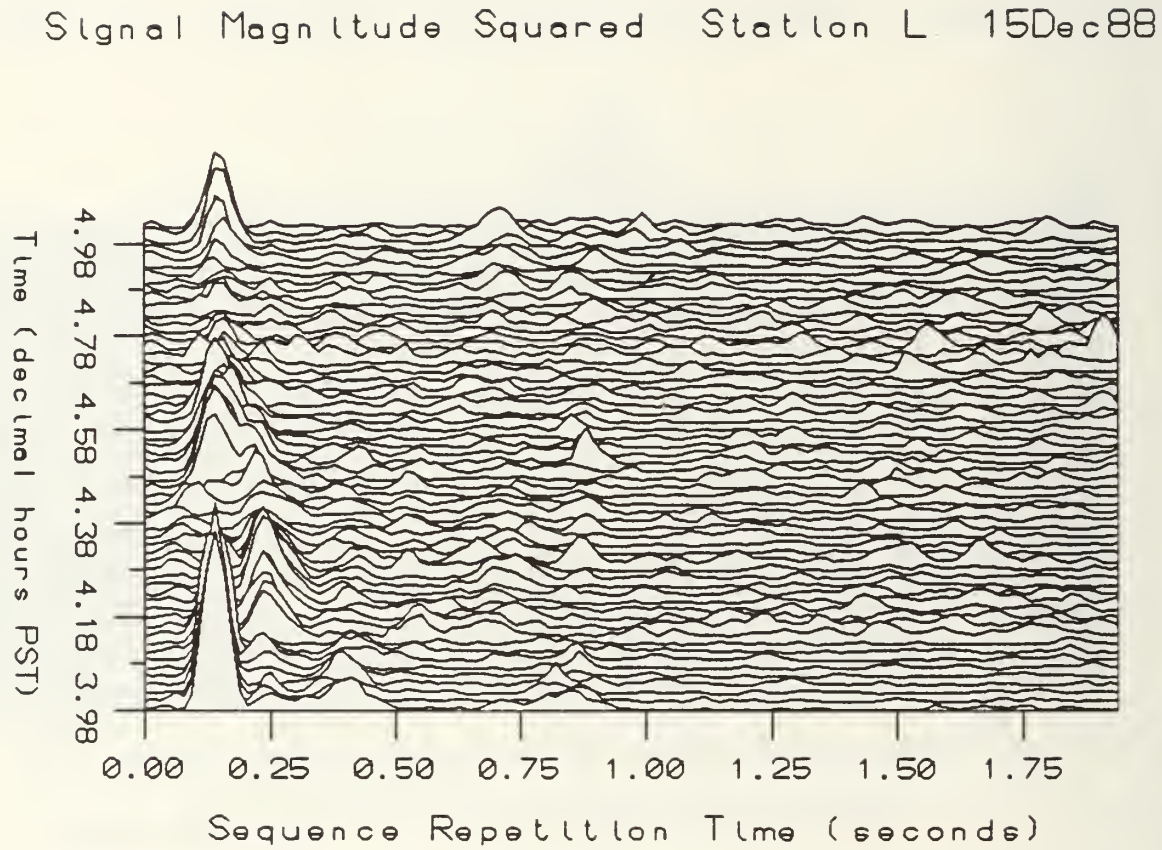

Figure 90: Tomographic signal, coherently averaged 16 times then magnitude squared. Station L, 0359 to 0459 15Dec88.

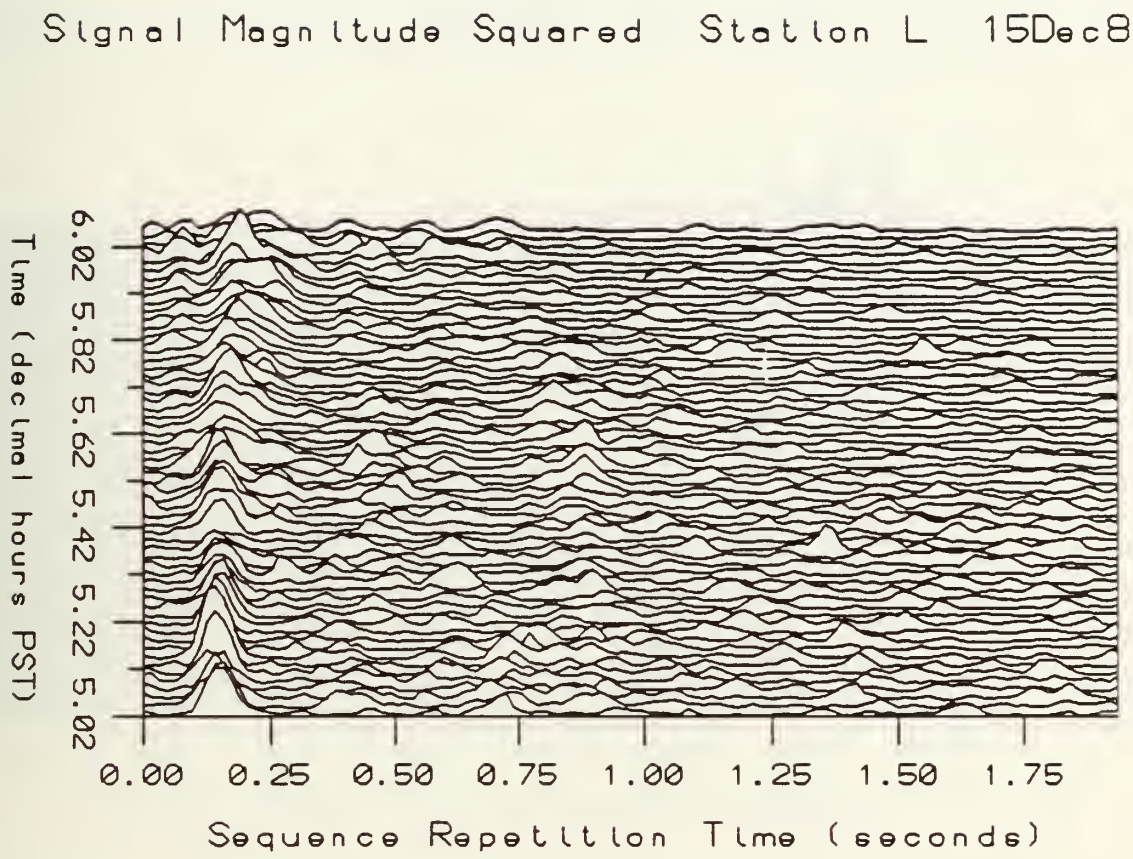
Signal Magnitude Squared Station L 15Dec88
Time (decimal hours PST)
6.02 5.82 5.62 5.42 5.22 5.02
0.00 0.25 0.50 0.75 1.00 1.25 1.50 1.75
Sequence Repetition Time (seconds)

Figure 91: Tomographic signal, coherently averaged 16 times then magnitude squared. Station L, 0501 to 0601 15Dec88.

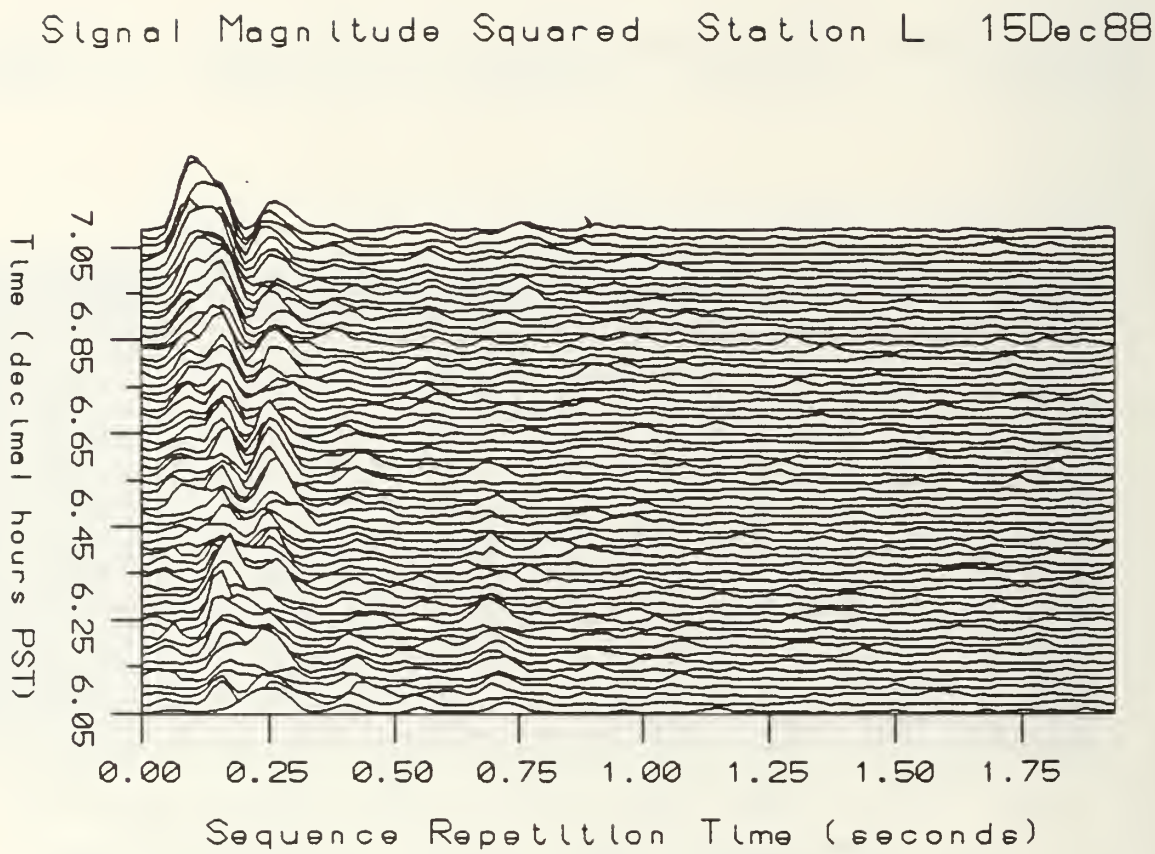
Signal Magnitude Squared Station L 15Dec88
Time (decimal hours PST)
7.05 6.85 6.65 6.45 6.25 6.05
0.00 0.25 0.50 0.75 1.00 1.25 1.50 1.75
Sequence Repetition Time (seconds)

Figure 92: Tomographic signal, coherently averaged 16 times then magnitude squared. Station L, 0603 to 0703 15Dec88.

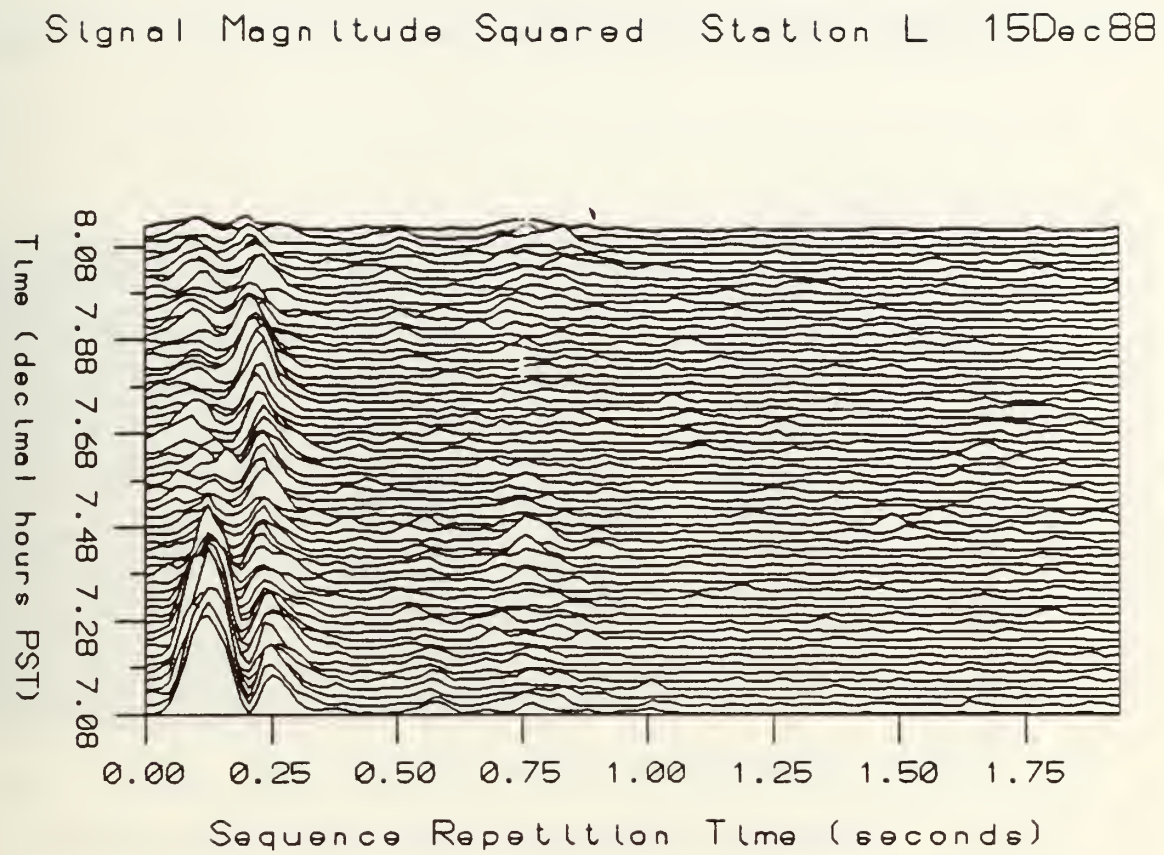
Signal Magnitude Squared Station L 15Dec88
Time (decimal hours PST)
8.08 7.88 7.68 7.48 7.28 7.08
0.00 0.25 0.50 0.75 1.00 1.25 1.50 1.75
Sequence Repetition Time (seconds)

Figure 93: Tomographic signal, coherently averaged 16 times then magnitude squared. Station L, 0705 to 0805 15Dec88.

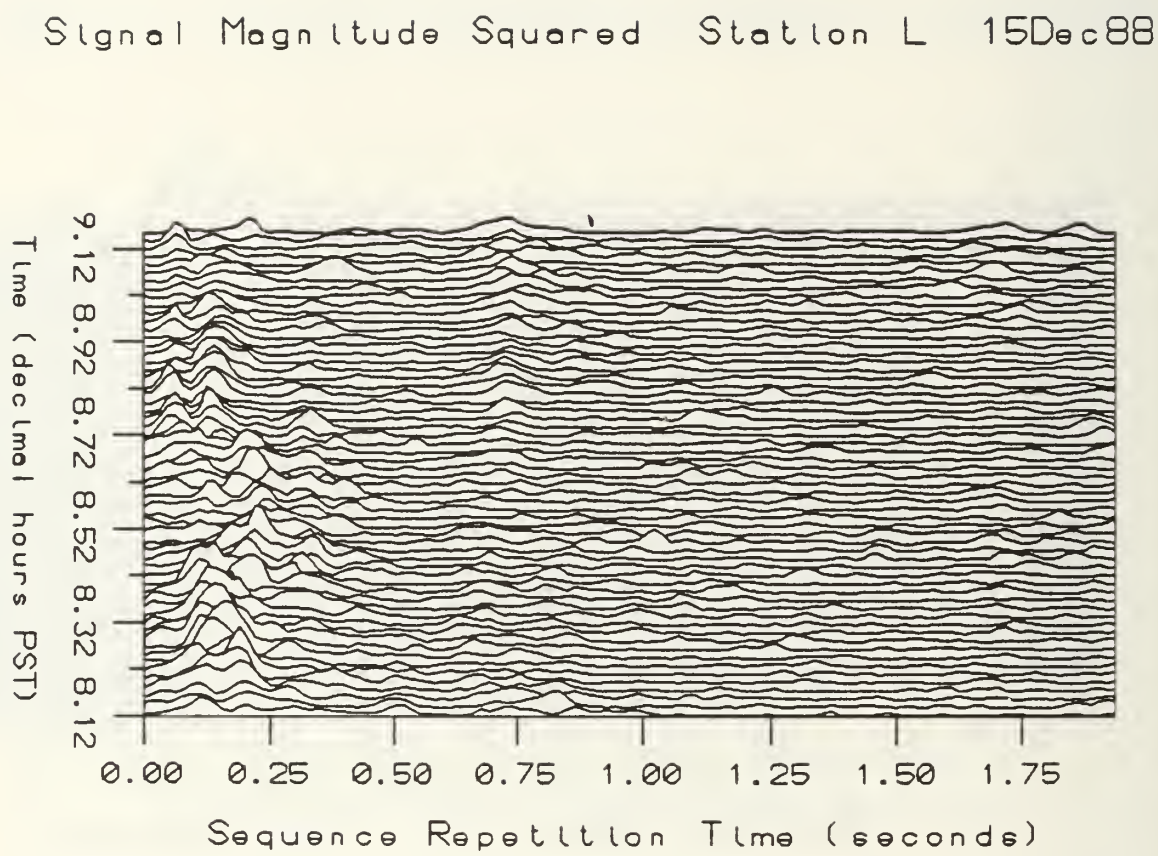
Signal Magnitude Squared Station L 15Dec88
Time (decimal hours PST)
9.12 8.92 8.72 8.52 8.32 8.12
0.00 0.25 0.50 0.75 1.00 1.25 1.50 1.75
Sequence Repetition Time (seconds)

Figure 94: Tomographic signal, coherently averaged 16 times then magnitude squared. Station L, 0807 to 0907 15Dec88.

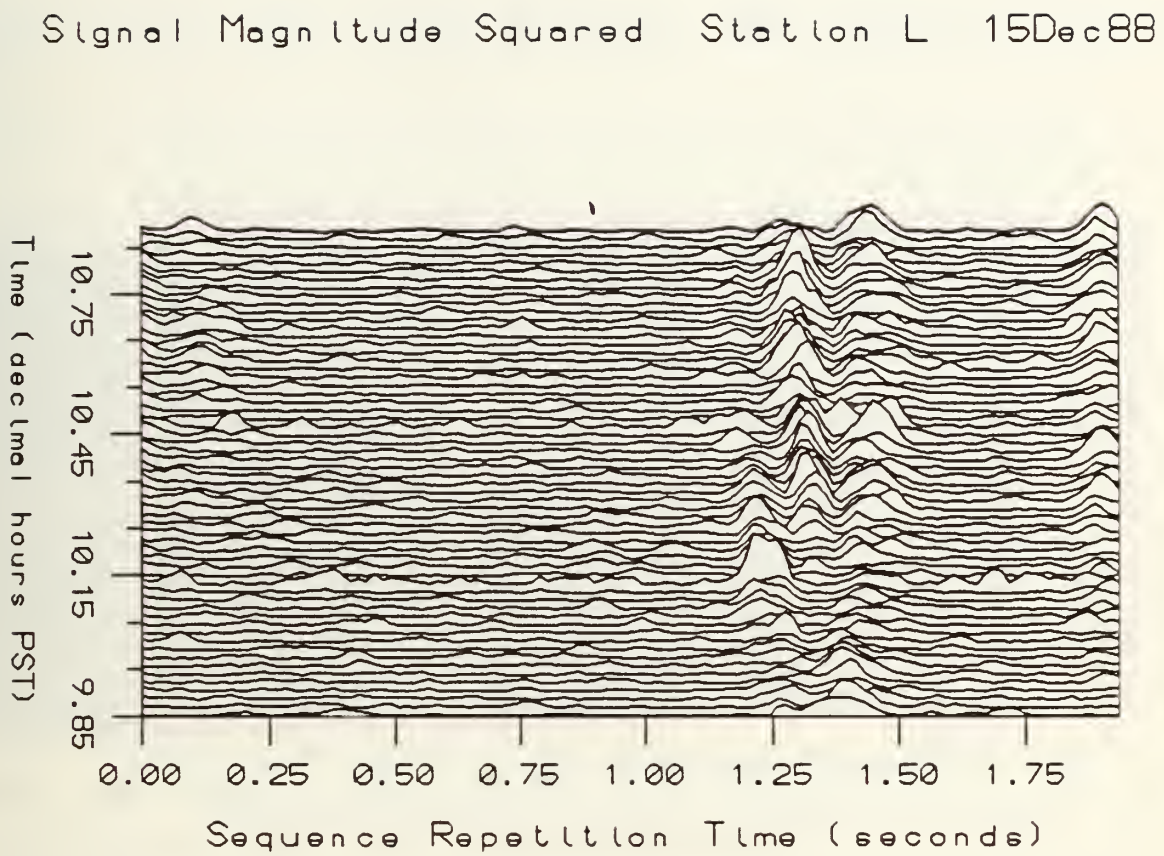

Figure 95: Tomographic signal, coherently averaged 16 times then magnitude squared. Station L, 0951 to 1045 15Dec88.

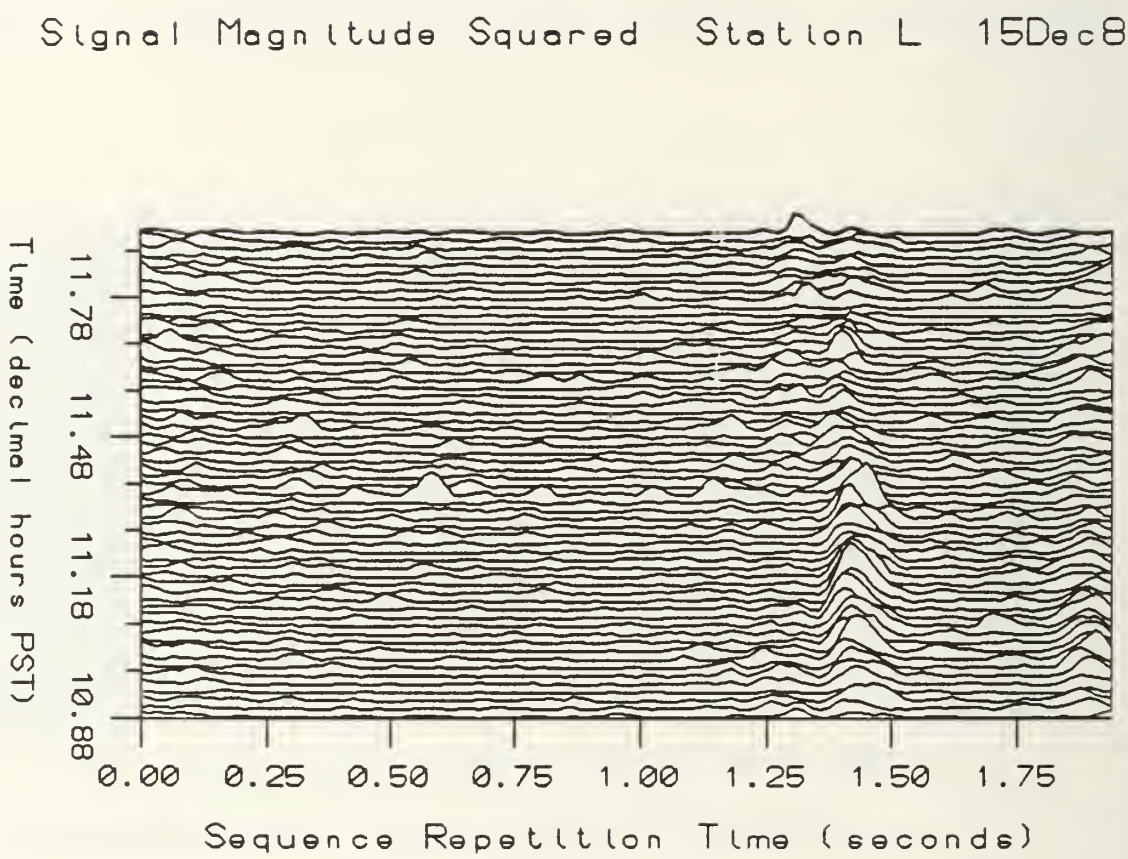

Figure 96: Tomographic signal, coherently averaged 16 times then magnitude squared. Station L, 1053 to 1147 15Dec88.

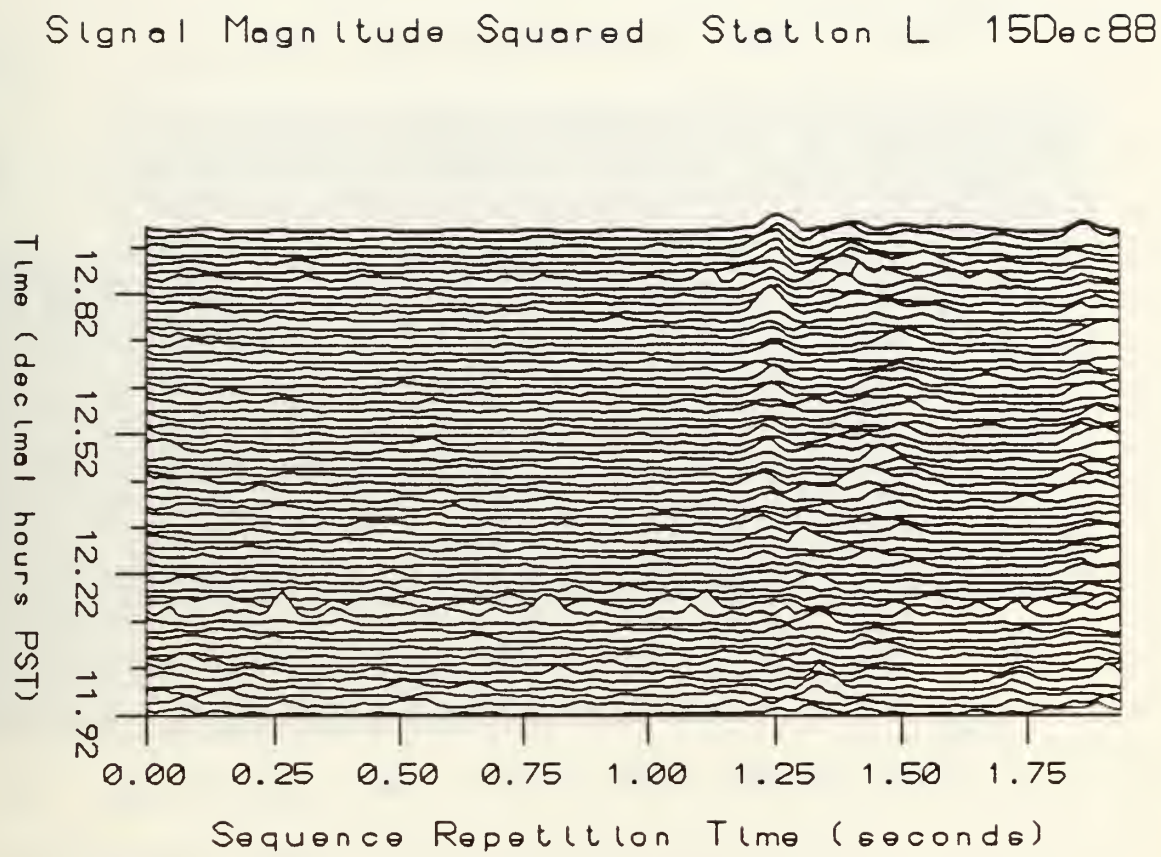

Figure 97: Tomographic signal, coherently averaged 16 times then magnitude squared. Station L, 1155 to 1249 15Dec88.

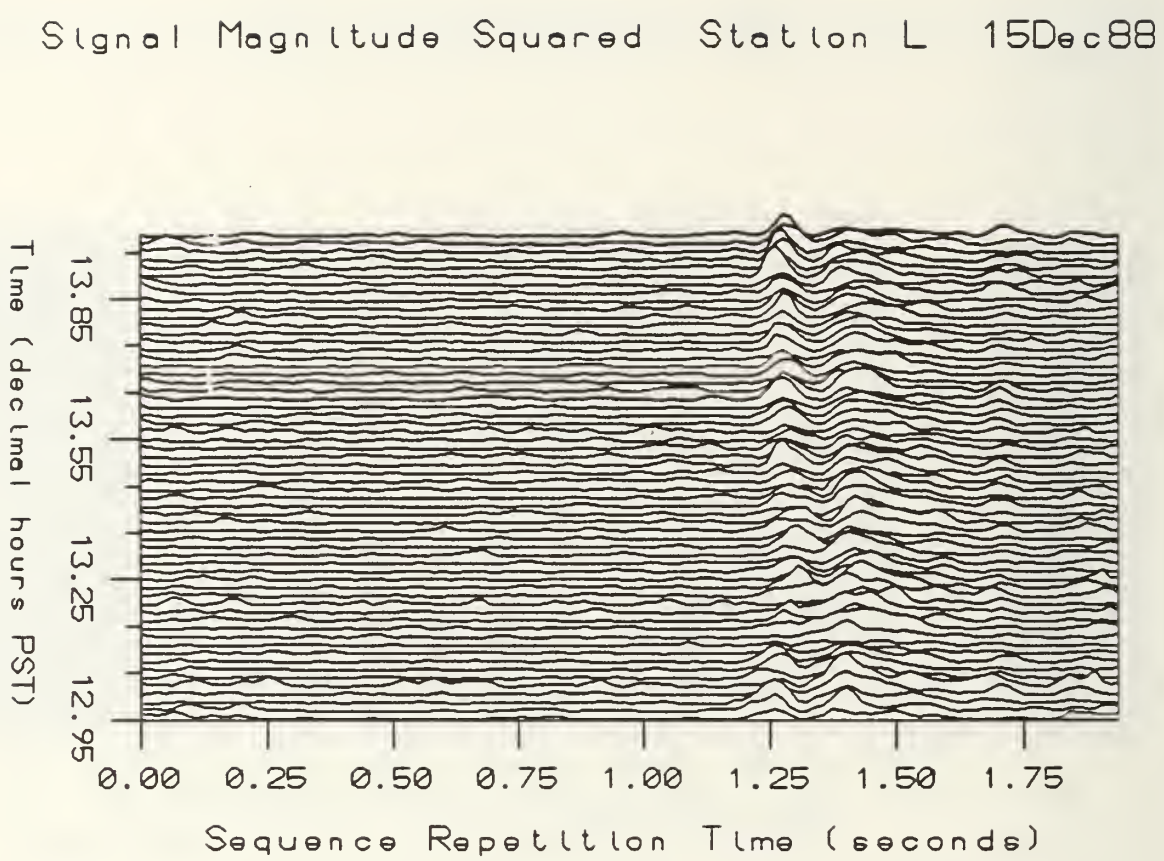

Figure 98: Tomographic signal, coherently averaged 16 times then magnitude squared. Station L, 1257 to 1351 15Dec88.

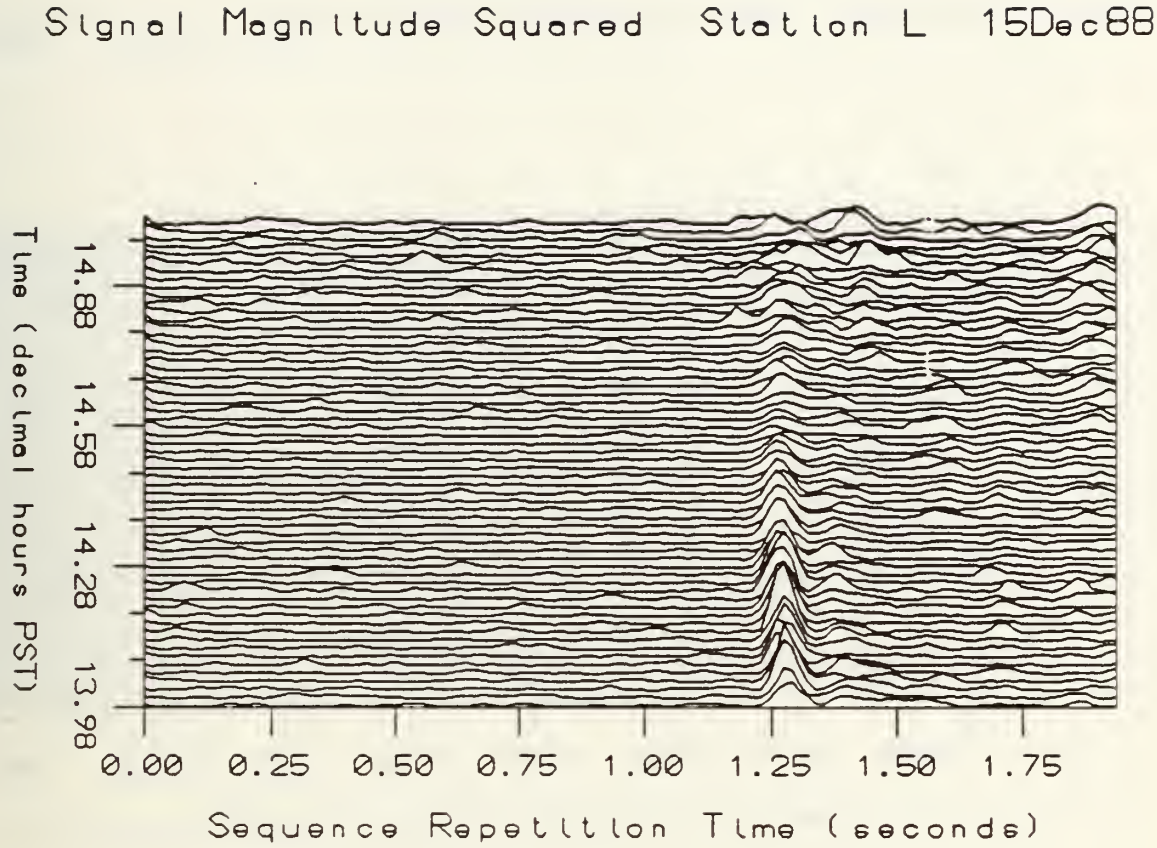

Figure 99: Tomographic signal, coherently averaged 16 times then magnitude squared. Station L, 1359 to 1453 15Dec88.

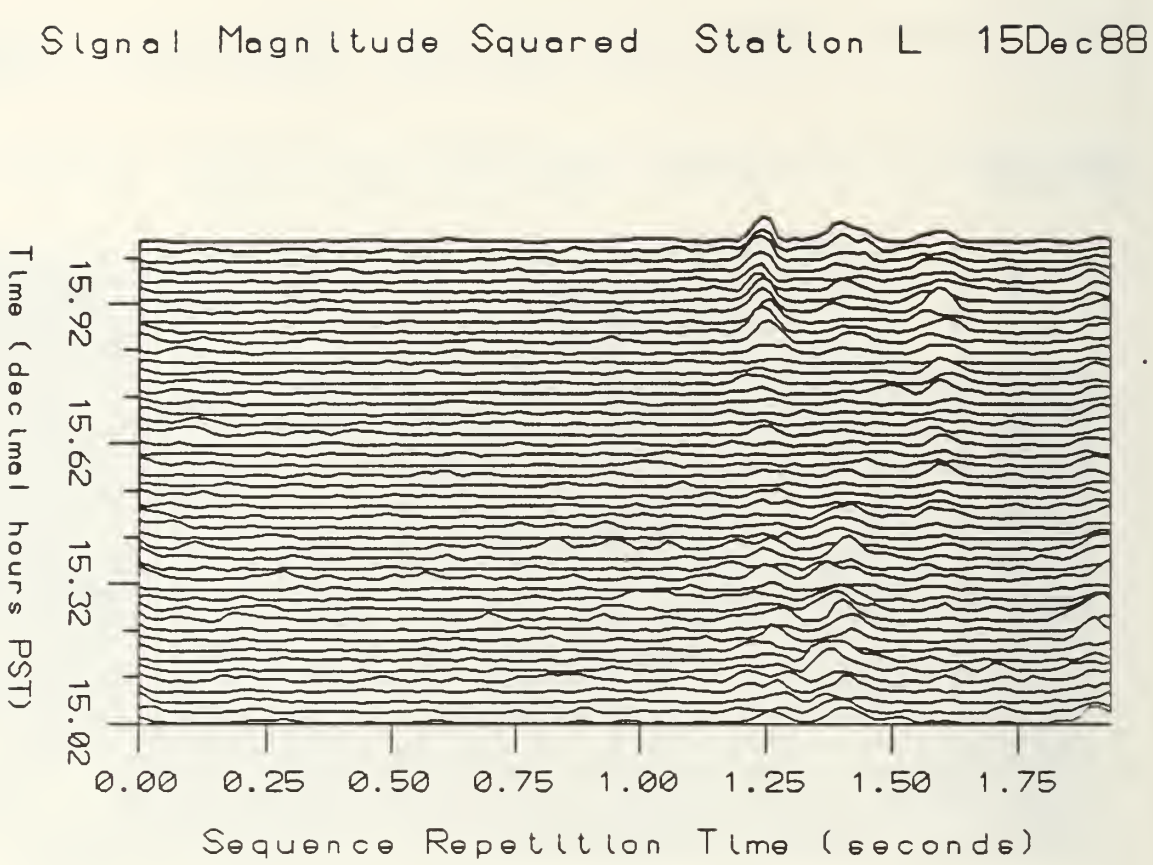

Figure 100: **Tomographic signal, coherently averaged 16 times then magnitude squared. Station L, 1501 to 1555 15Dec88.**

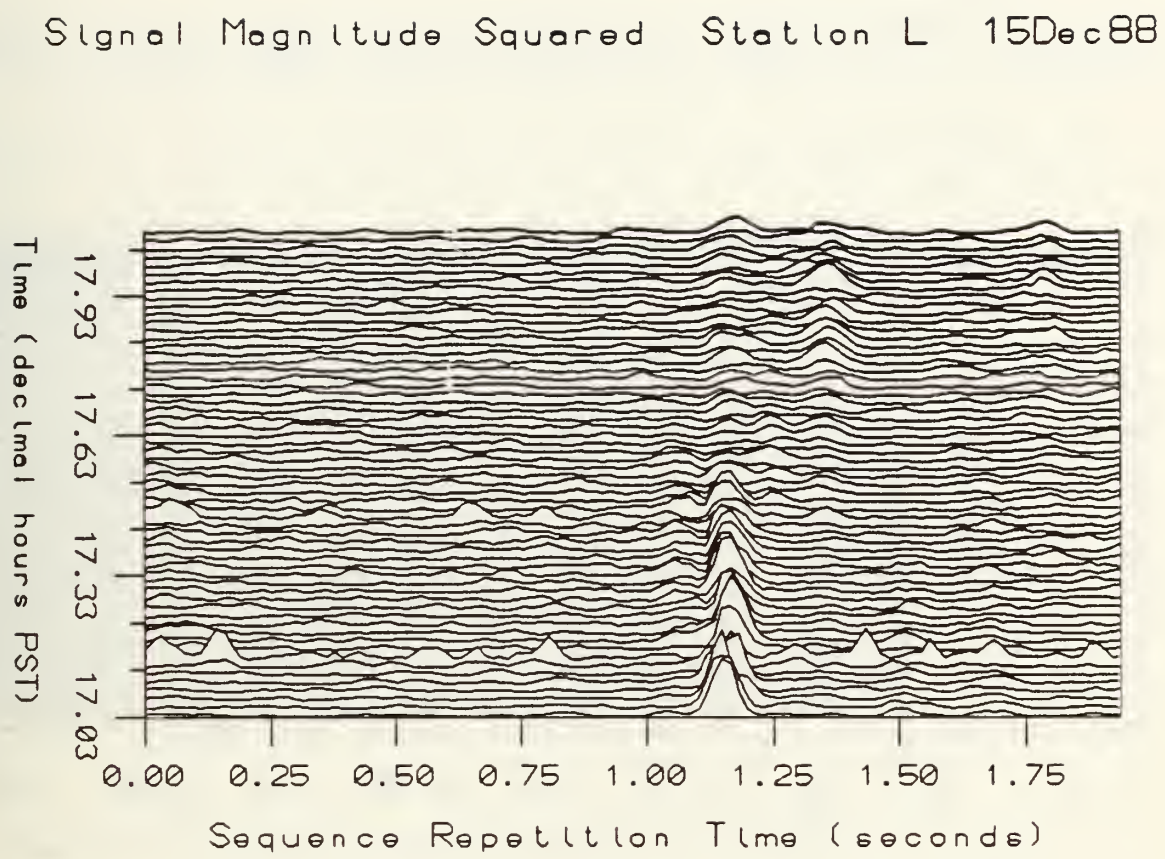

Figure 101: **Tomographic signal, coherently averaged 16 times then magnitude squared. Station L, 1702 to 1756 15Dec88.**

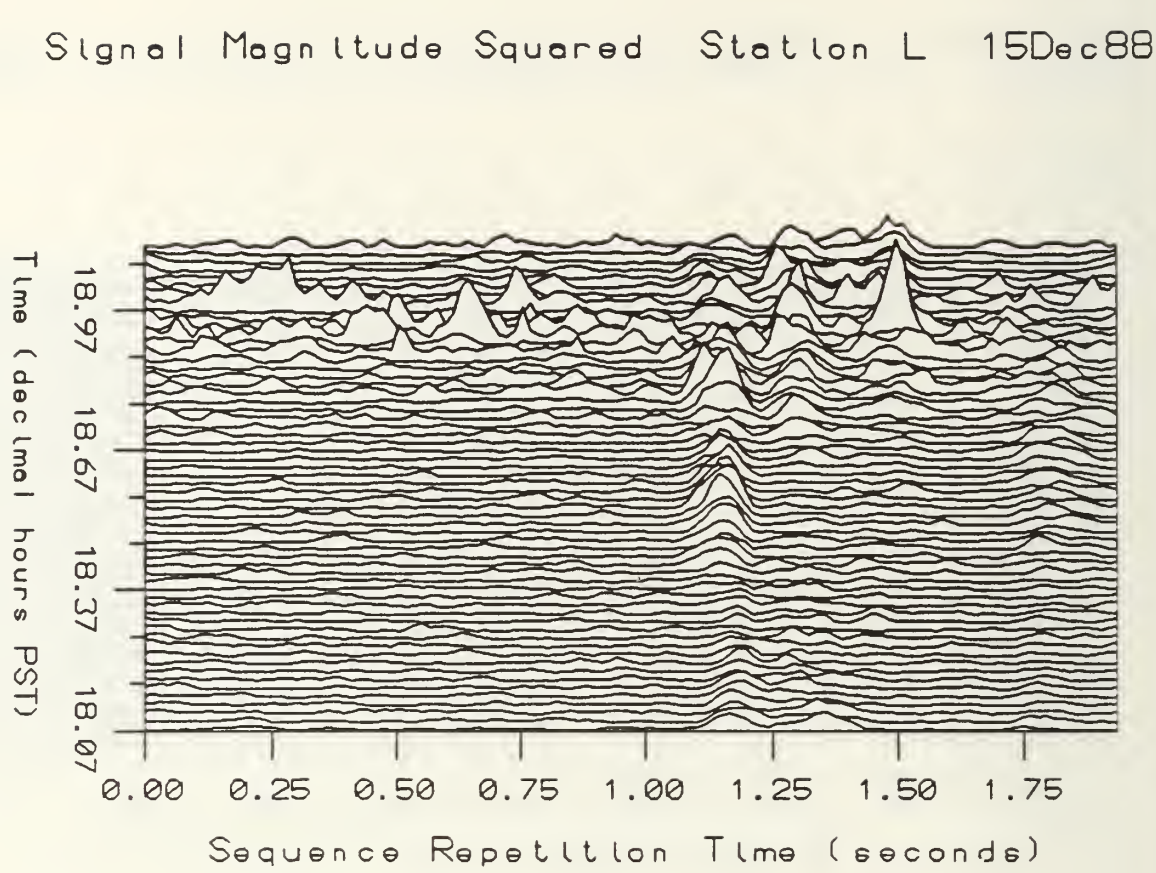

Figure 102: **Tomographic signal, coherently averaged 16 times then magnitude squared. Station L, 1804 to 1858 15Dec88.**

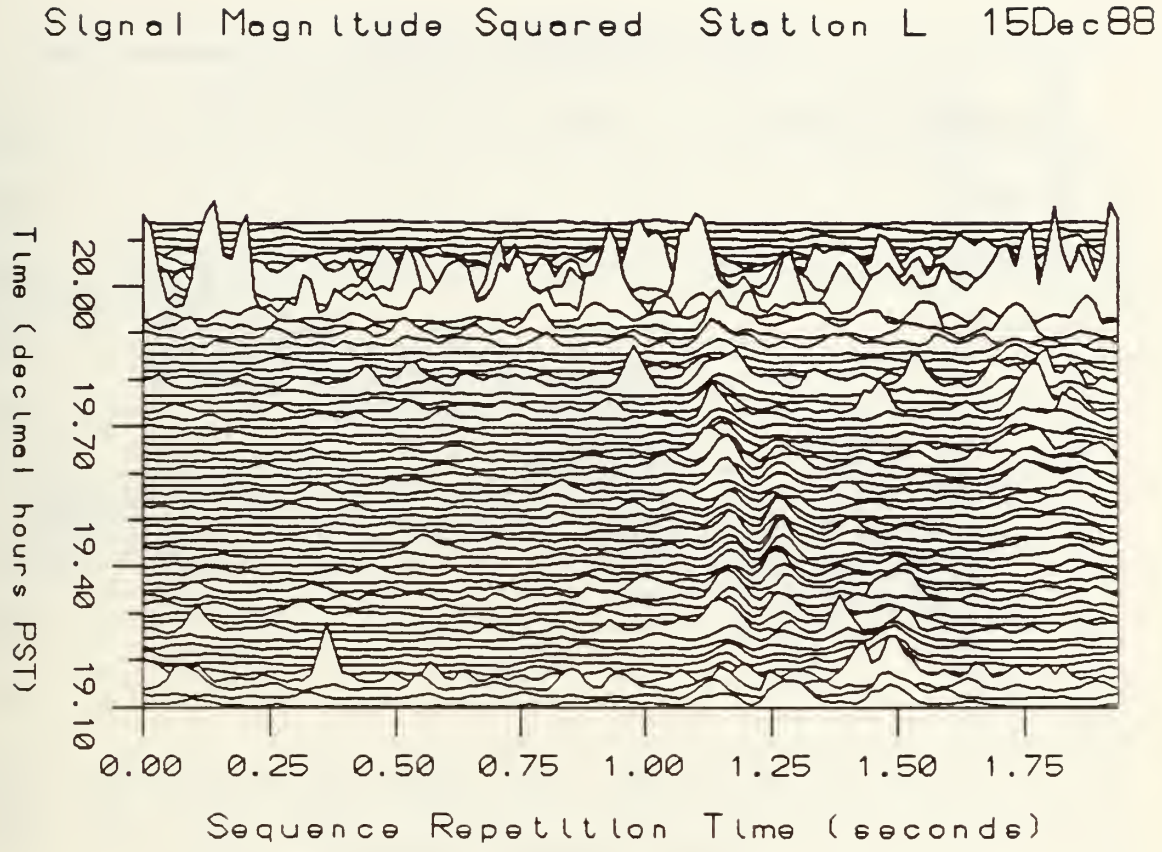

Figure 103: **Tomographic signal, coherently averaged 16 times then magnitude squared. Station L, 1906 to 2000 15Dec88.**

B. ARRIVAL TIME ESTIMATES

All arrival time estimates were filtered with an eighth order Chebyshev with a .02581 Hz cutoff frequency.

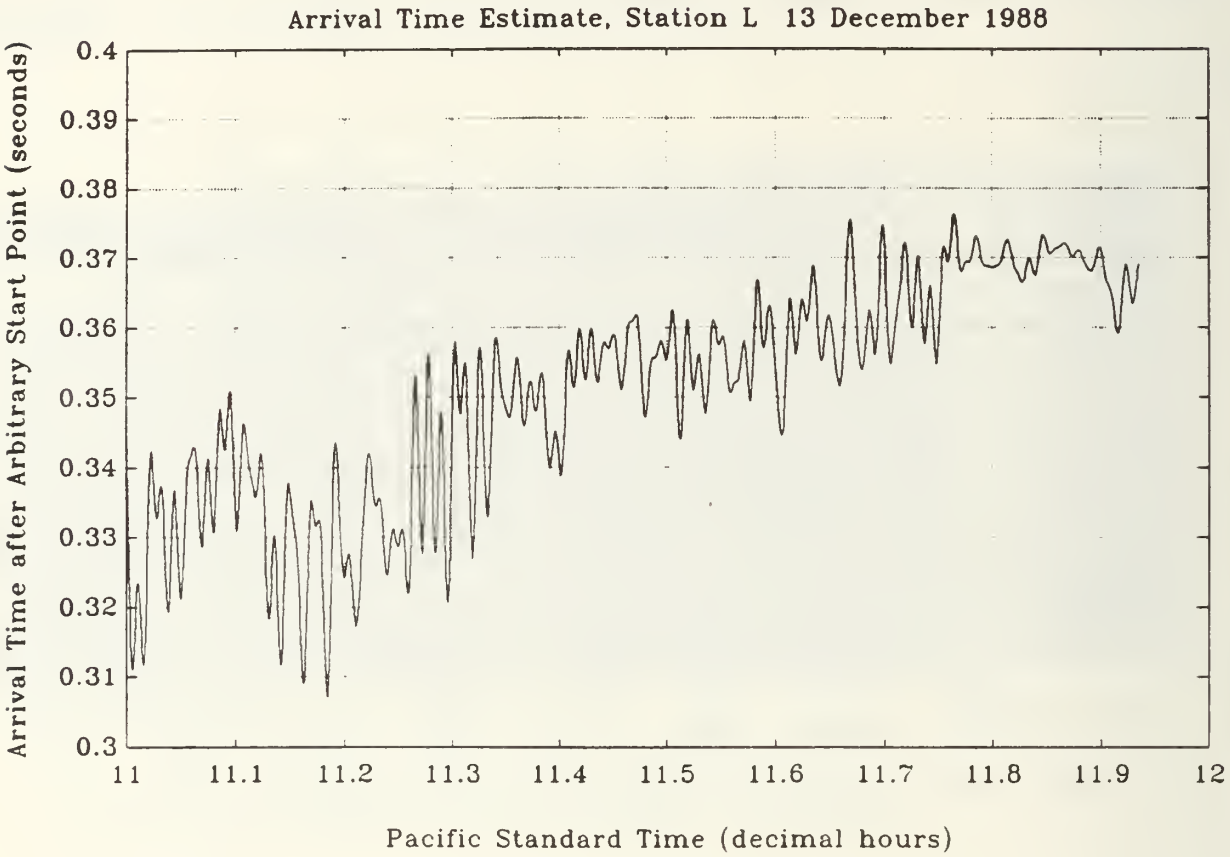

Figure 104: **Arrival time estimate for Station L from 1100 to 1200 PST 13Dec88. The fast fluctuations in the arrival time are caused by surface waves changing the path length.**

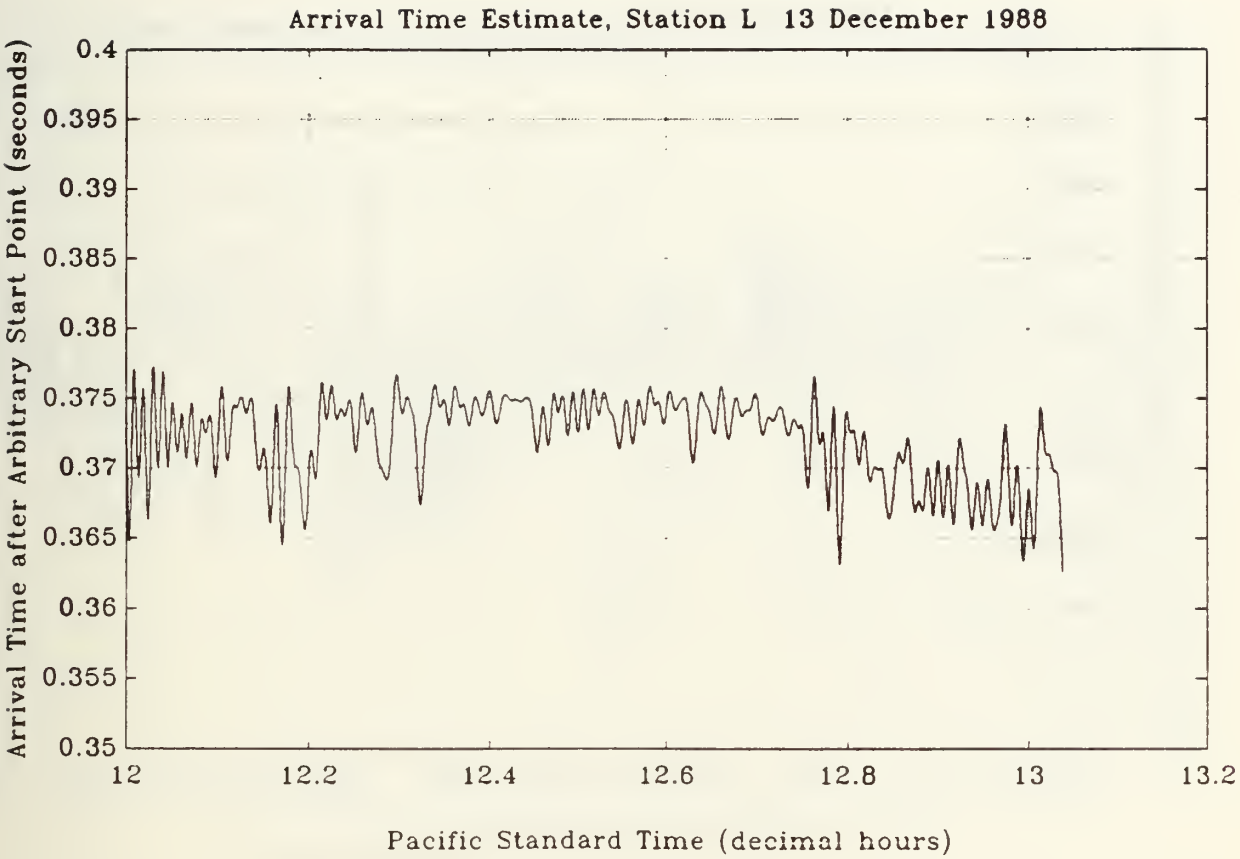

Figure 105: Arrival time estimate for Station L from 1200 to 1312 PST 13Dec88. The fast fluctuations in the arrival times are caused by surface waves changing the path length.

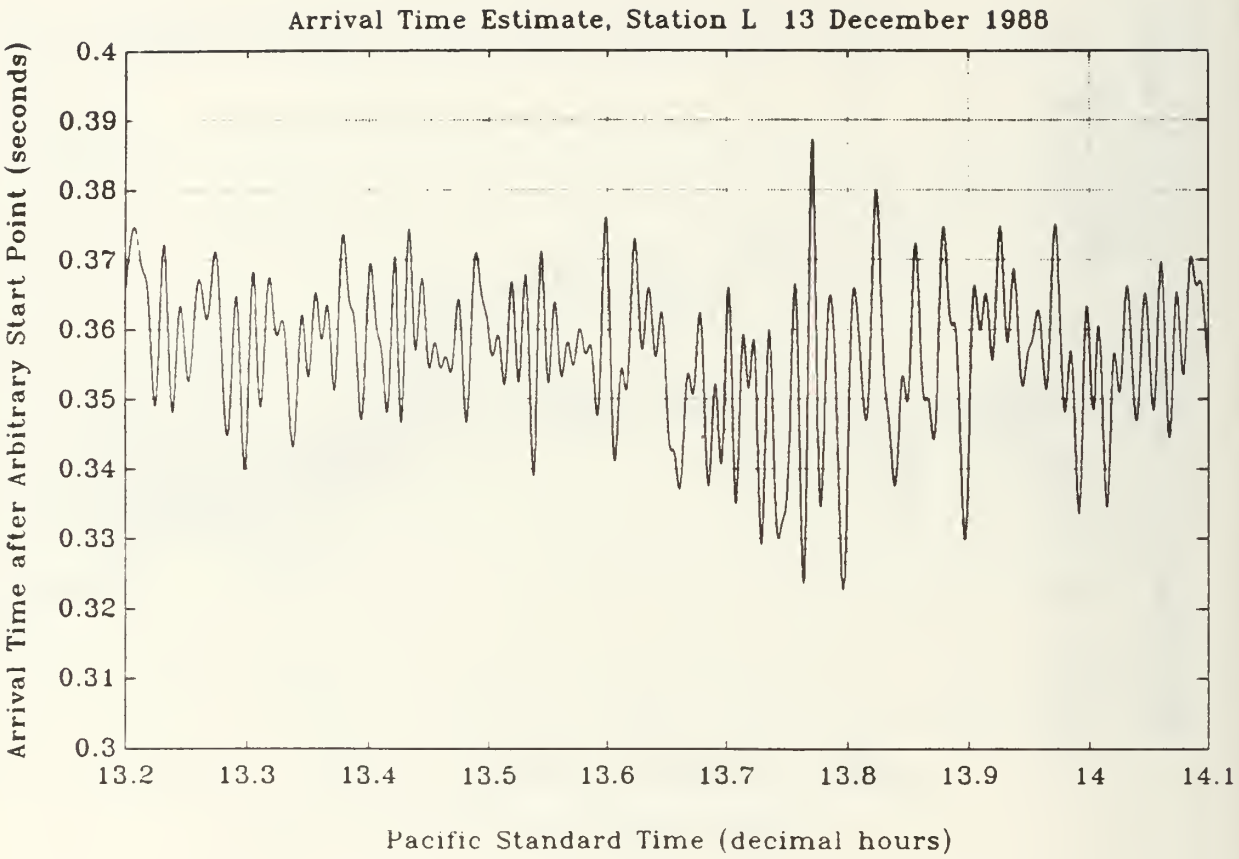

Figure 106: Arrival time estimate for Station L from 1312 to 1406 PST 13Dec88. The fast fluctuations in the arrival times are caused by surface waves changing the path length.

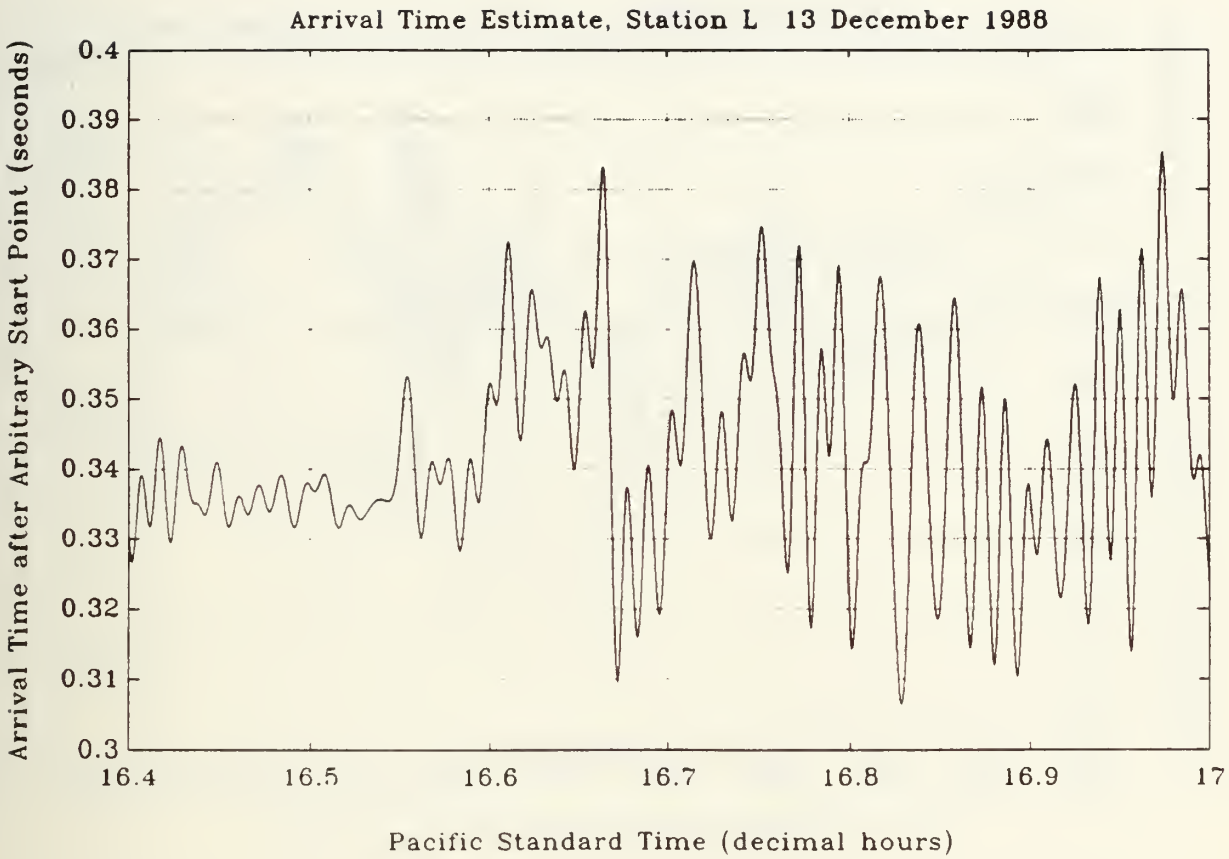

Figure 107: Arrival time estimate for Station L from 1200 to 1312 PST 13Dec88. The fast fluctuations in the arrival times are caused by surface waves changing the path length.

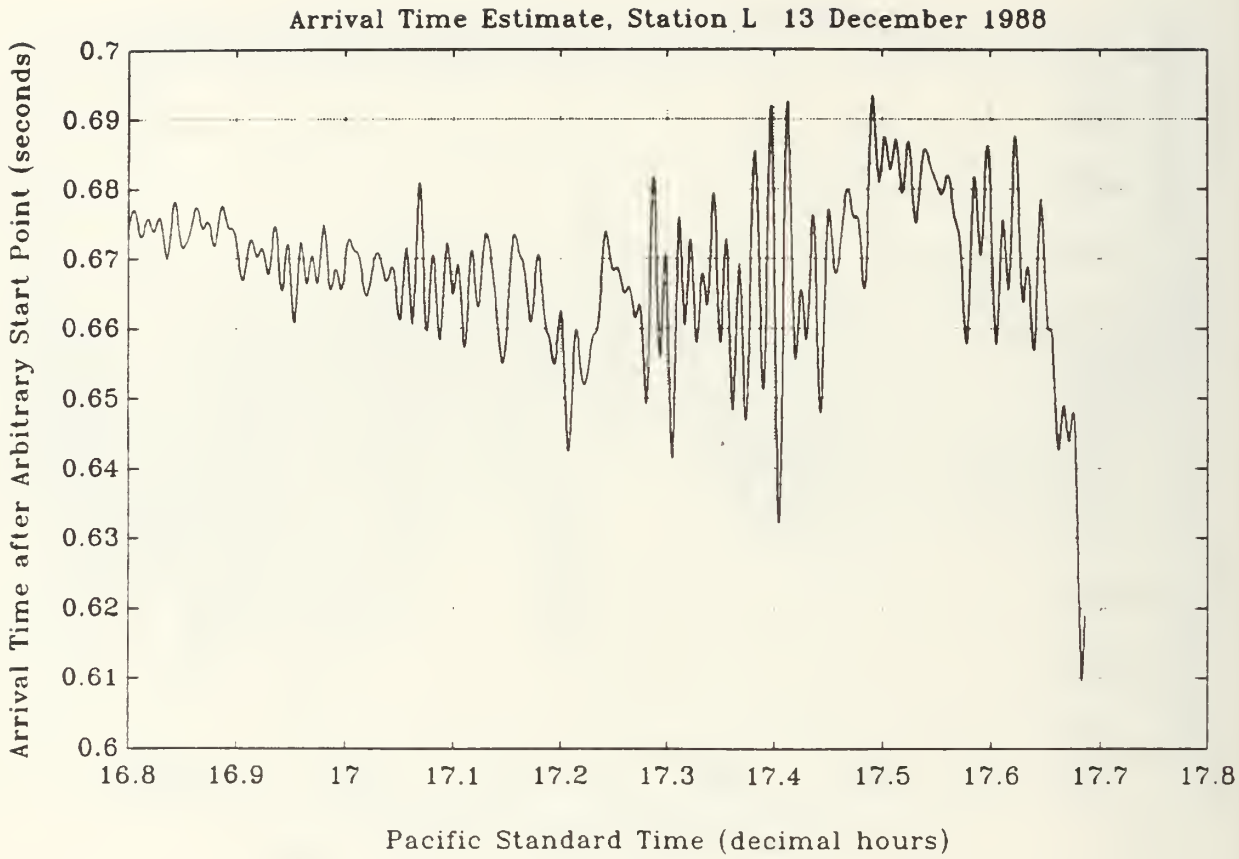

Figure 108: Arrival time estimate for Station L from 1624 to 1700 PST 13Dec88. The fast fluctuations in the arrival times are caused by surface waves changing the path length.

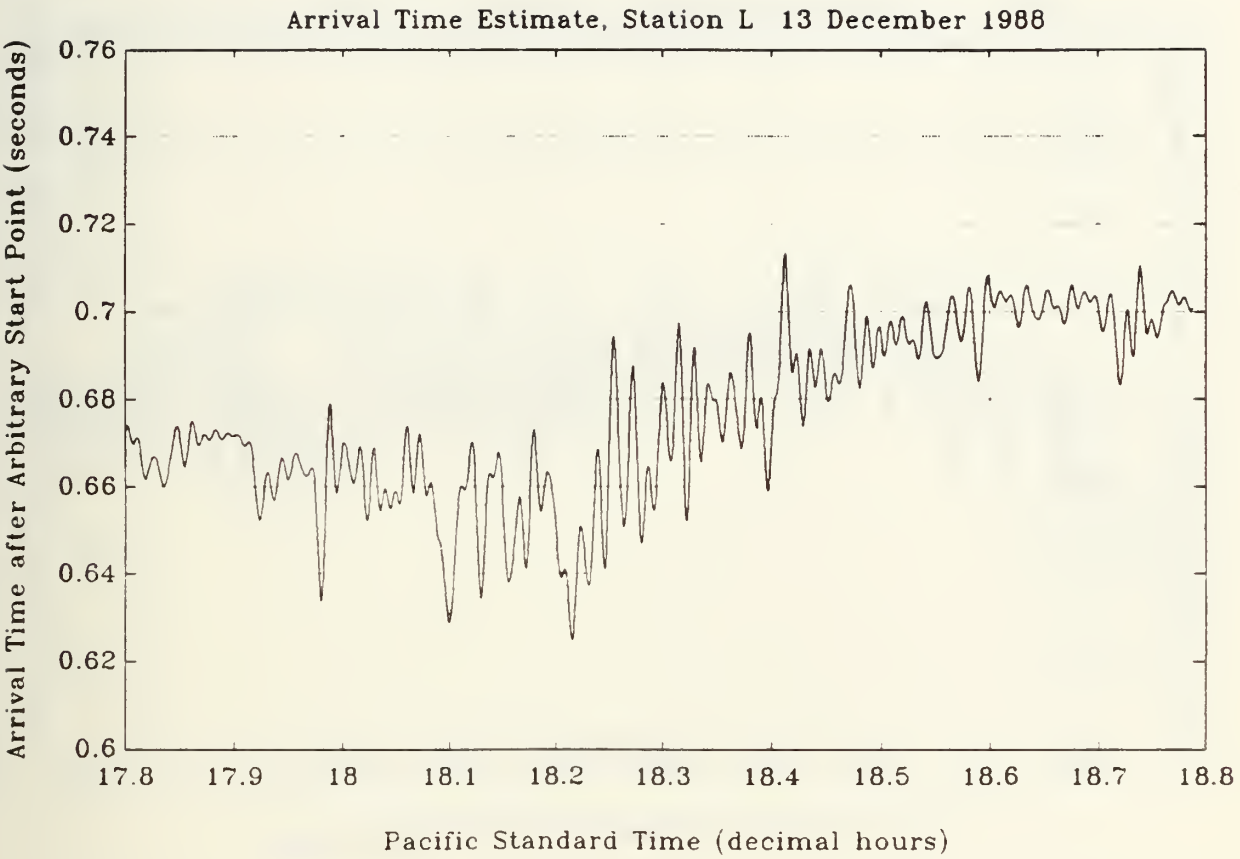

Figure 109: Arrival time estimate for Station L from 1748 to 1848 PST 13Dec88. The fast fluctuations in the arrival times are caused by surface waves changing the path length.

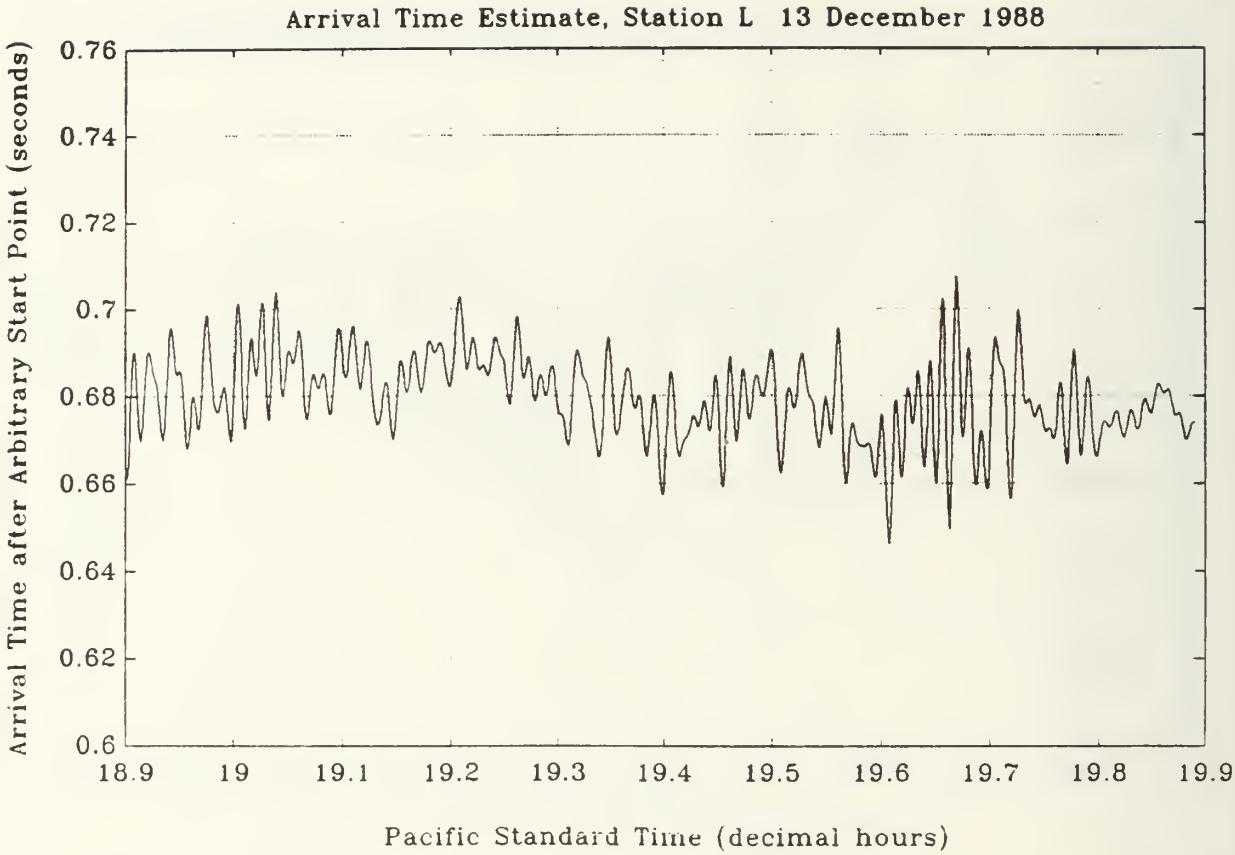

Figure 110: Arrival time estimate for Station L from 1854 to 1954 PST 13Dec88. The fast fluctuations in the arrival times are caused by surface waves changing the path length.

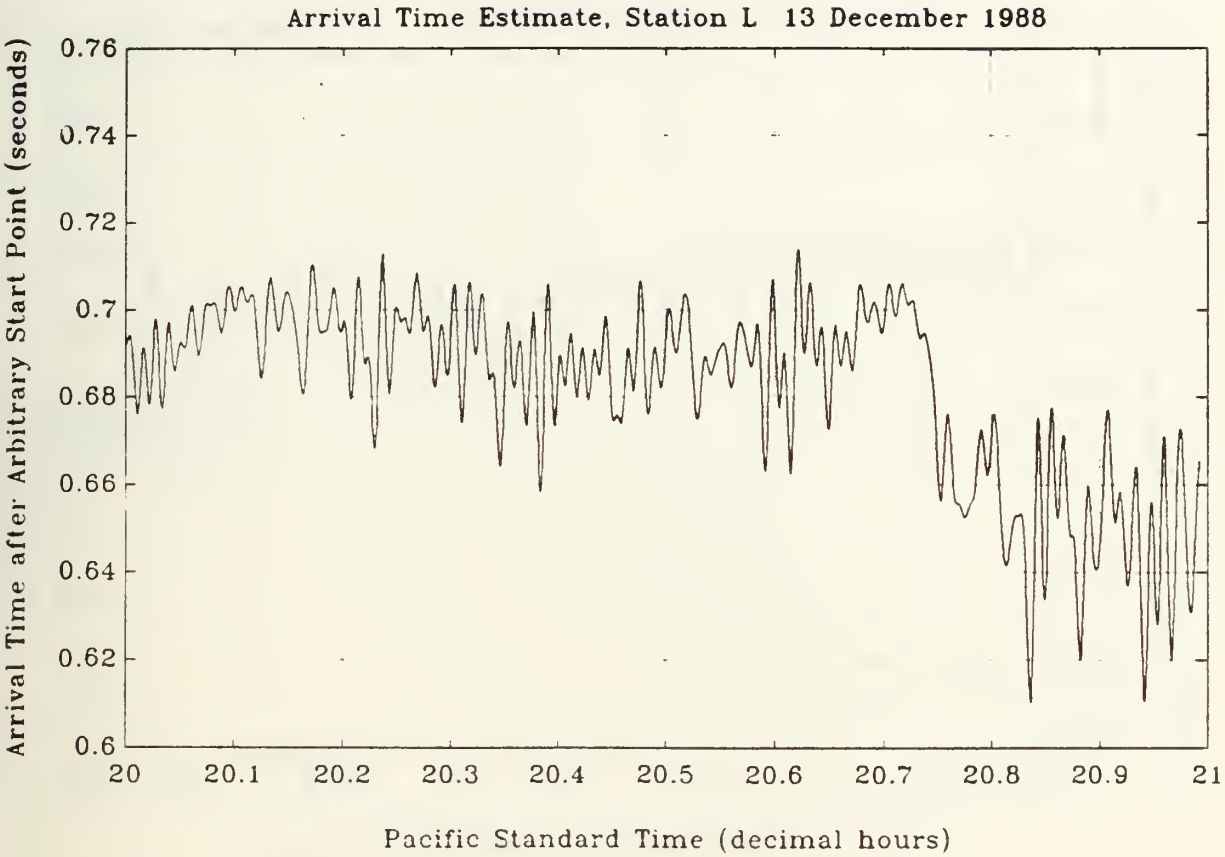

Figure 111: Arrival time estimate for Station L from 2000 to 2100 PST 13Dec88. The fast fluctuations in the arrival times are caused by surface waves changing the path length.

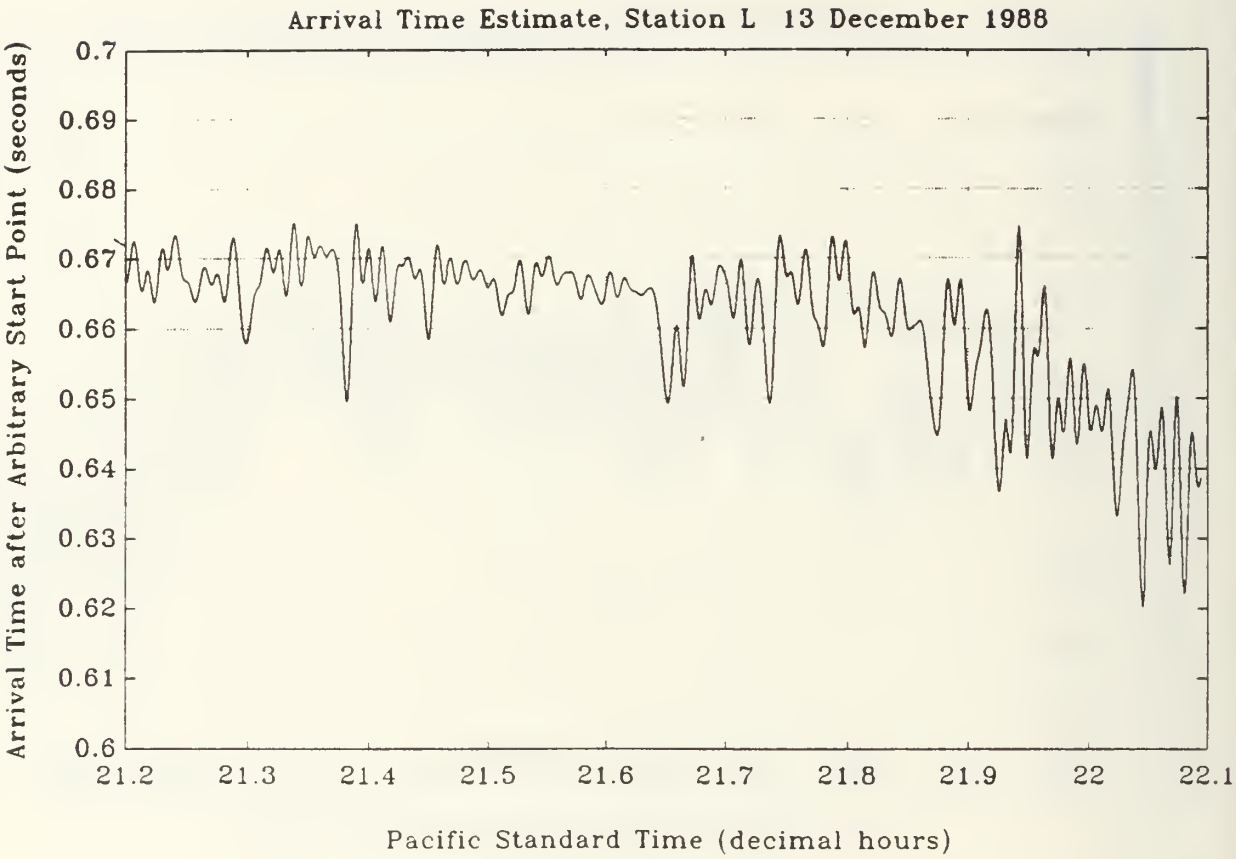

Figure 112: Arrival time estimate for Station L from 2112 to 2206 PST 13Dec88. The fast fluctuations in the arrival times are caused by surface waves changing the path length.

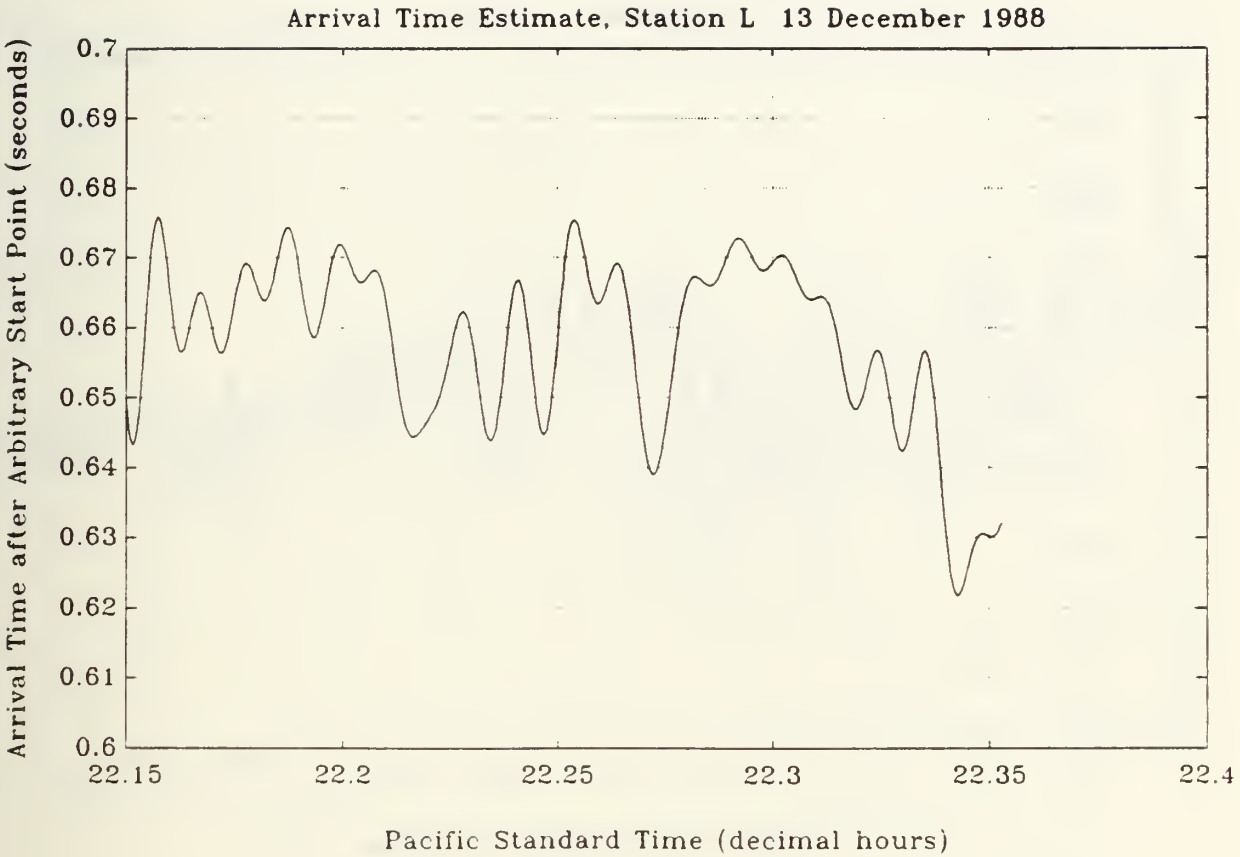

Figure 113: Arrival time estimate for Station L from 2209 to 2224 PST 13Dec88. The fast fluctuations in the arrival times are caused by surface waves changing the path length.

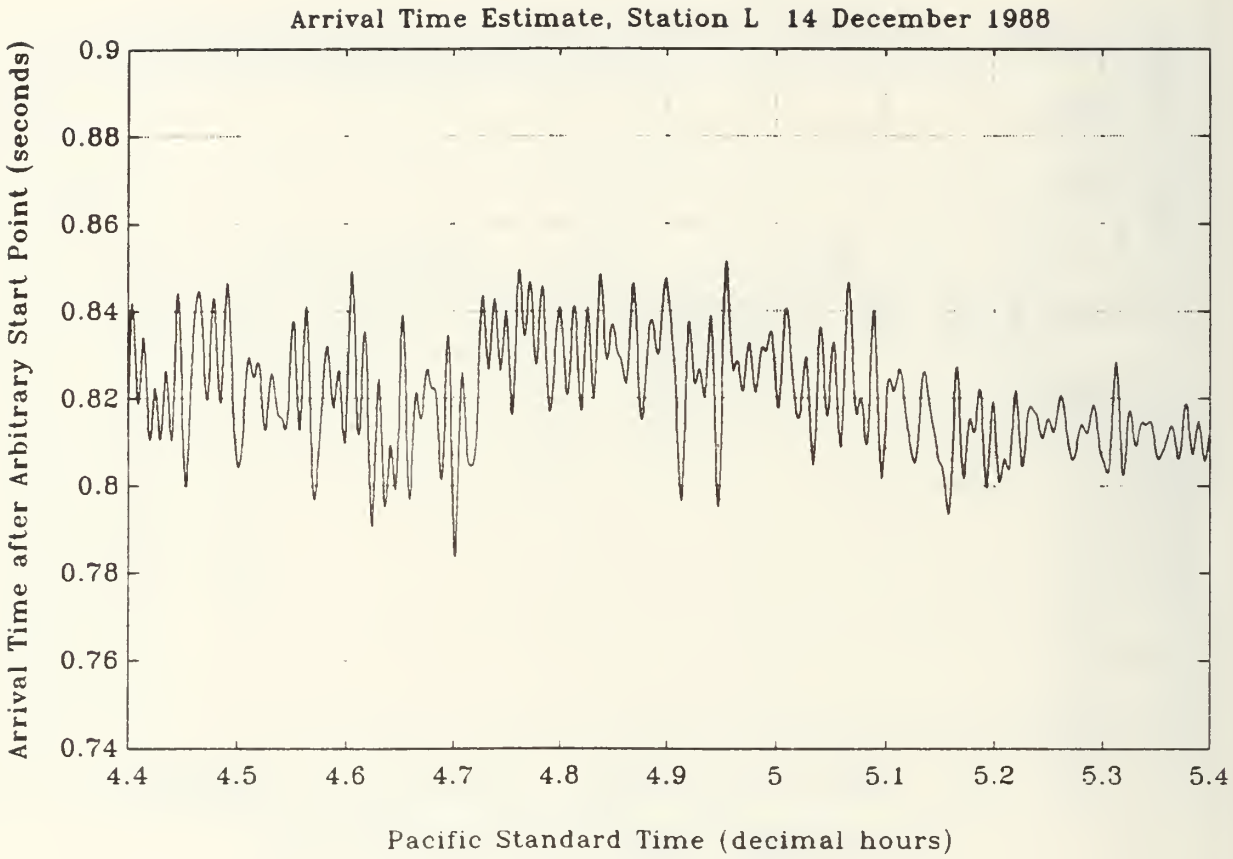

Figure 114: Arrival time estimate for Station L from 0424 to 0524 PST 14Dec88. The fast fluctuations in the arrival times are caused by surface waves changing the path length.

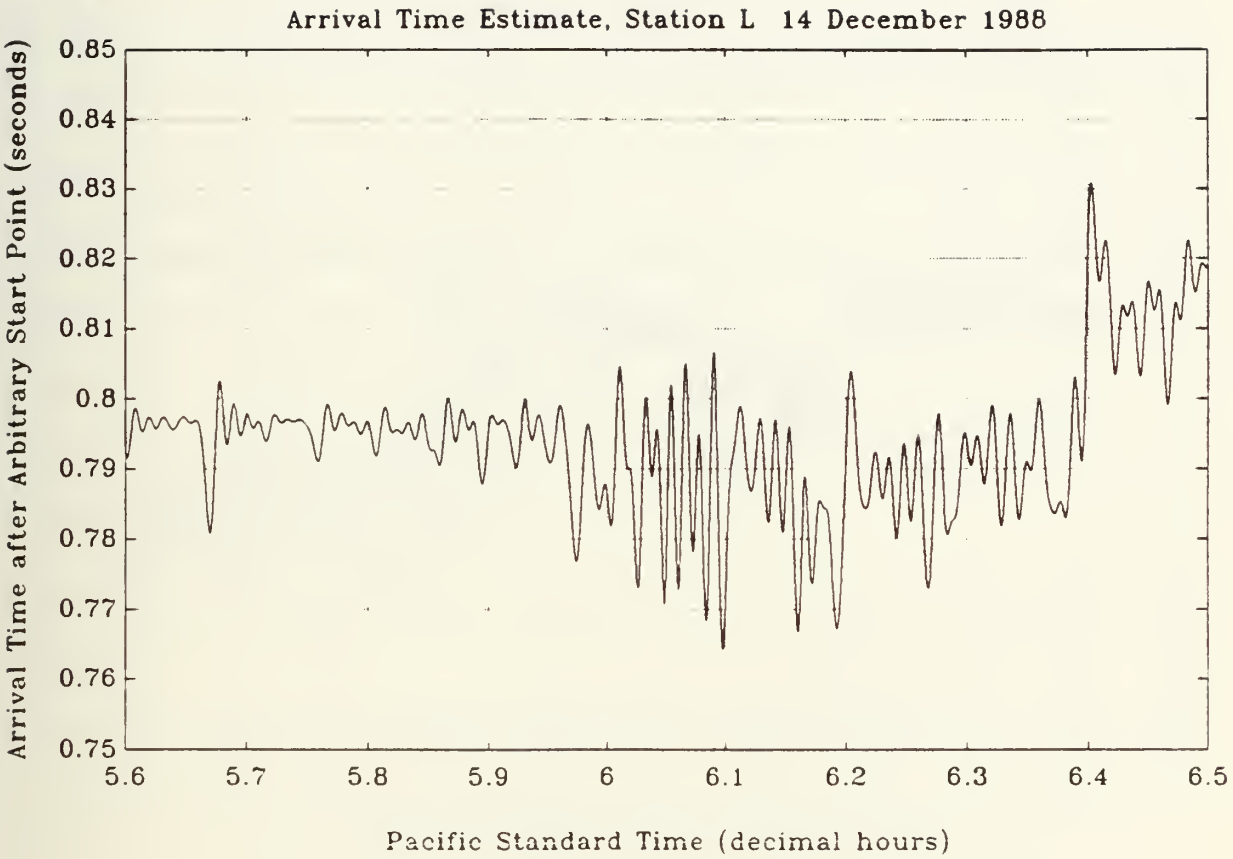

Figure 115: Arrival time estimate for Station L from 0536 to 0630 PST 14Dec88. The fast fluctuations in the arrival times are caused by surface waves changing the path length.

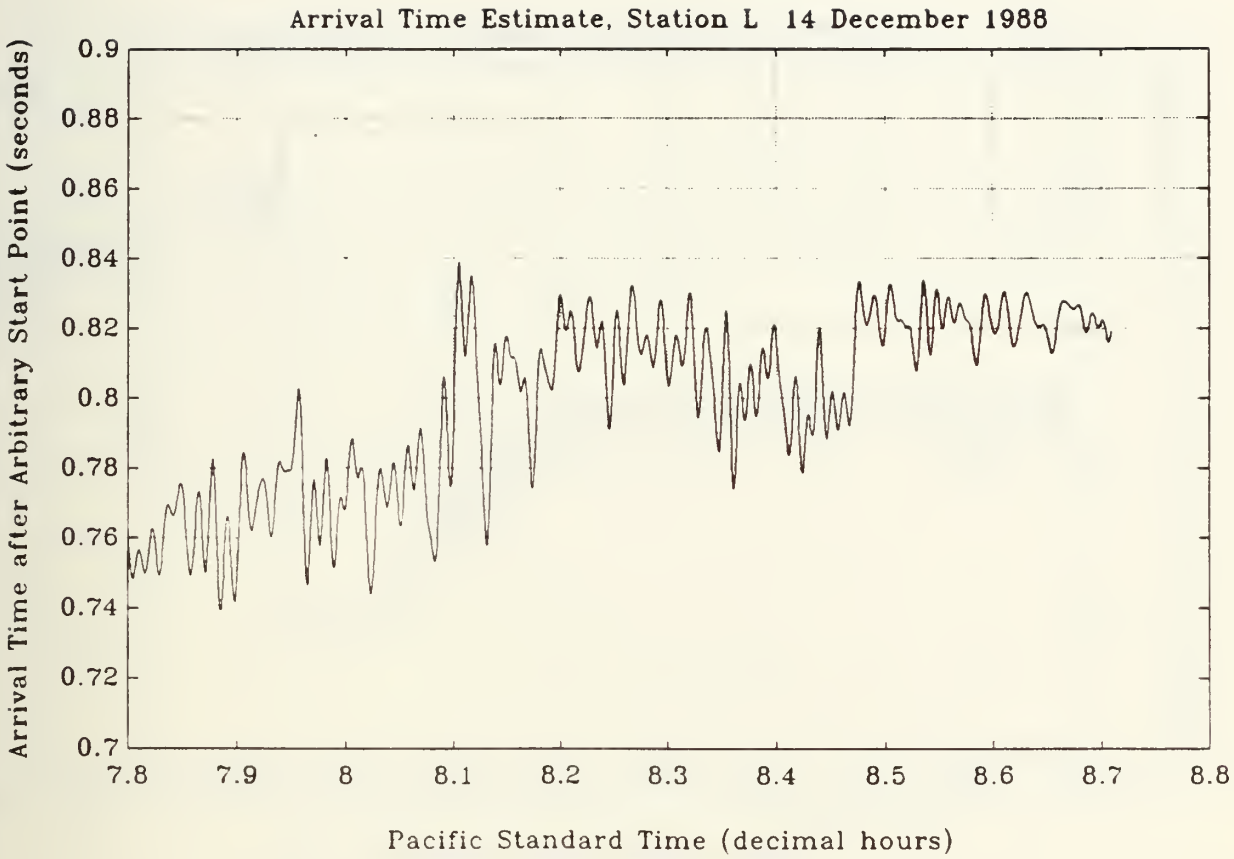

Figure 117: Arrival time estimate for Station L from 0748 to 0848 PST 14Dec88. The fast fluctuations in the arrival times are caused by surface waves changing the path length.

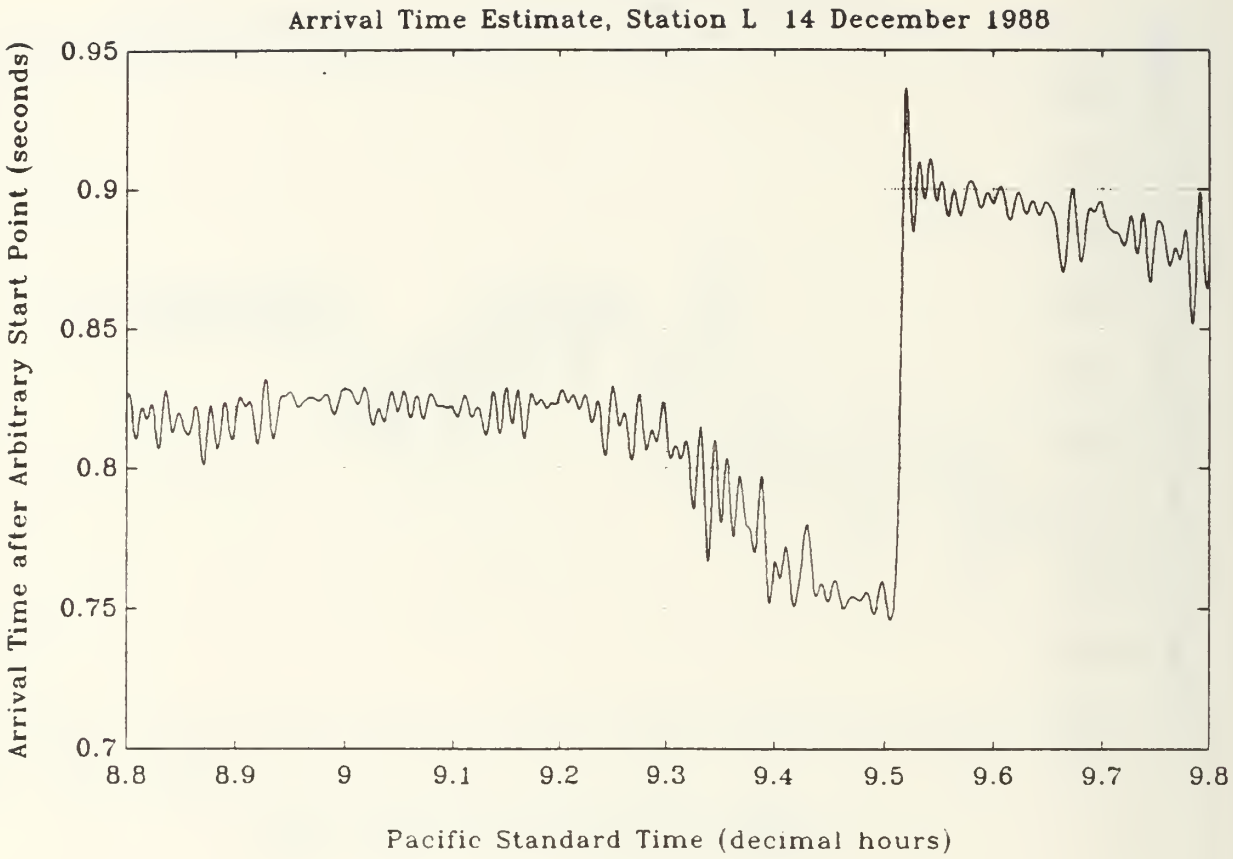

Figure 118: Arrival time estimate for Station L from 0848 to 0948 PST 14Dec88. The fast fluctuations in the arrival times are caused by surface waves changing the path length.

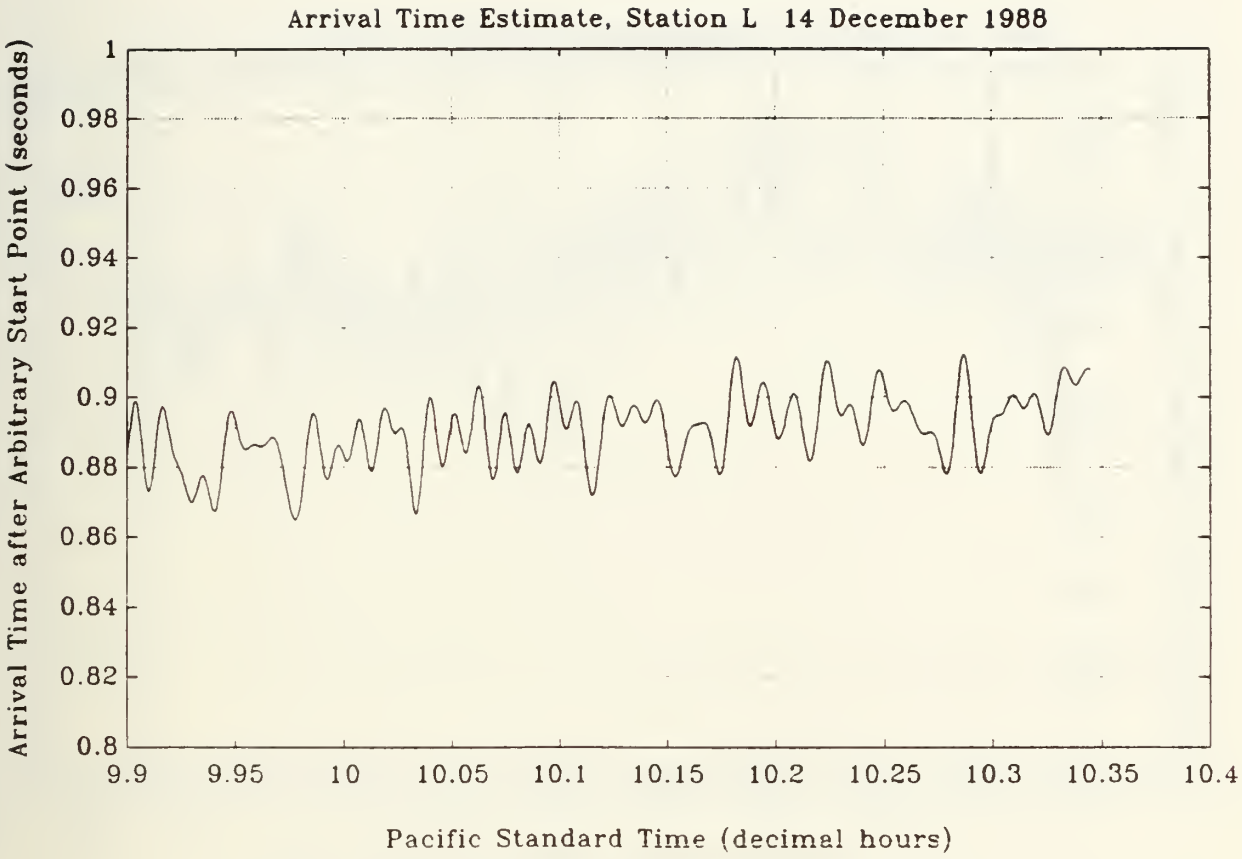

Figure 119: Arrival time estimate for Station L from 0954 to 1024 PST 14Dec88. The fast fluctuations in the arrival times are caused by surface waves changing the path length.

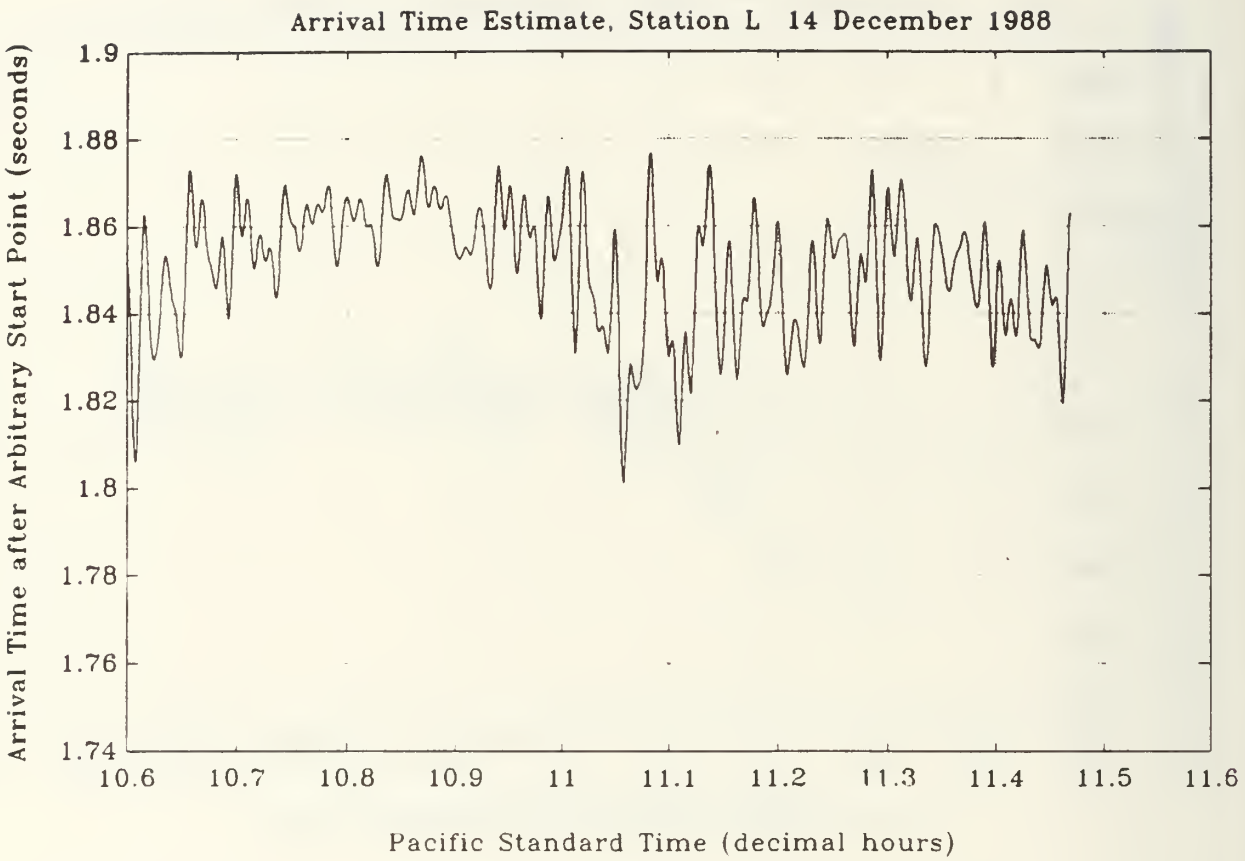

Figure 120: Arrival time estimate for Station L from 1036 to 1136 PST 14Dec88. The fast fluctuations in the arrival times are caused by surface waves changing the path length.

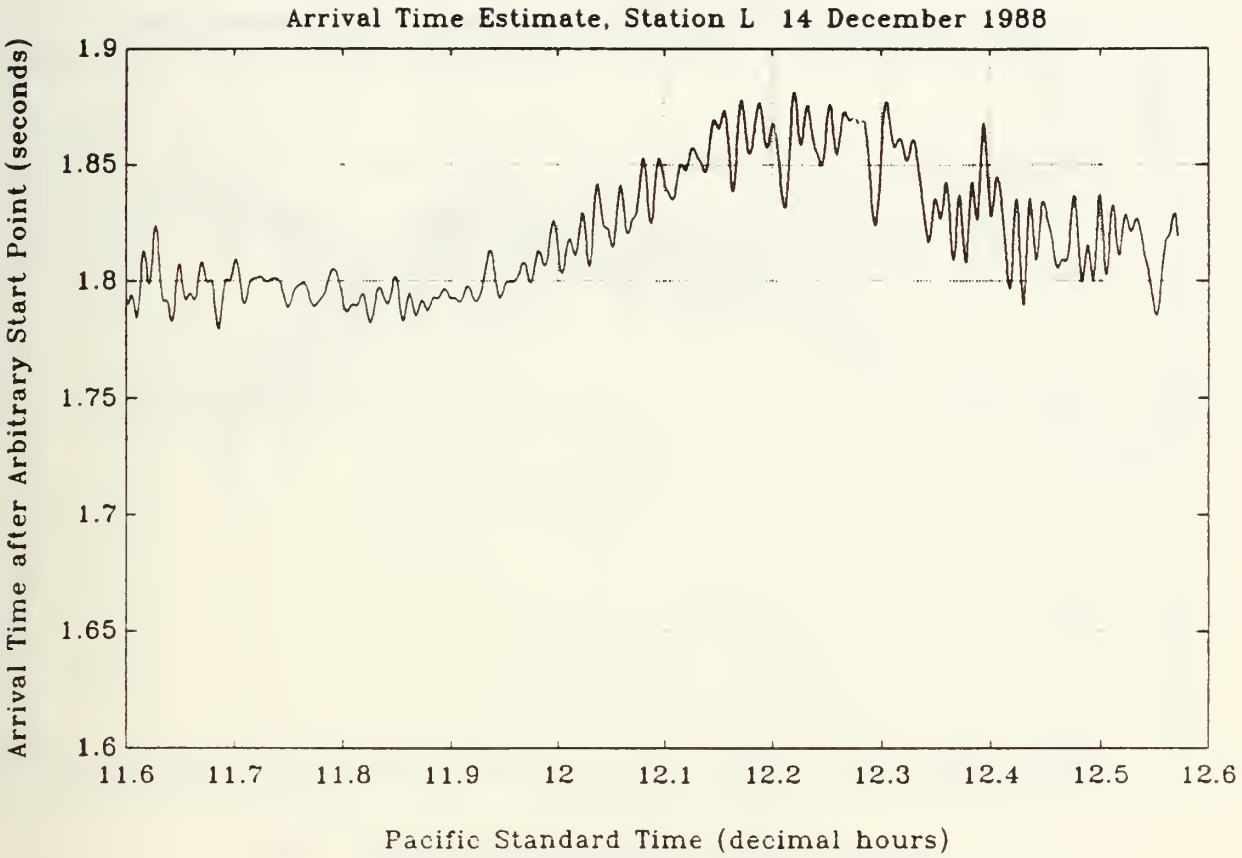

Figure 121: Arrival time estimate for Station L from 1136 to 1236 PST 14Dec88. The fast fluctuations in the arrival times are caused by surface waves changing the path length.

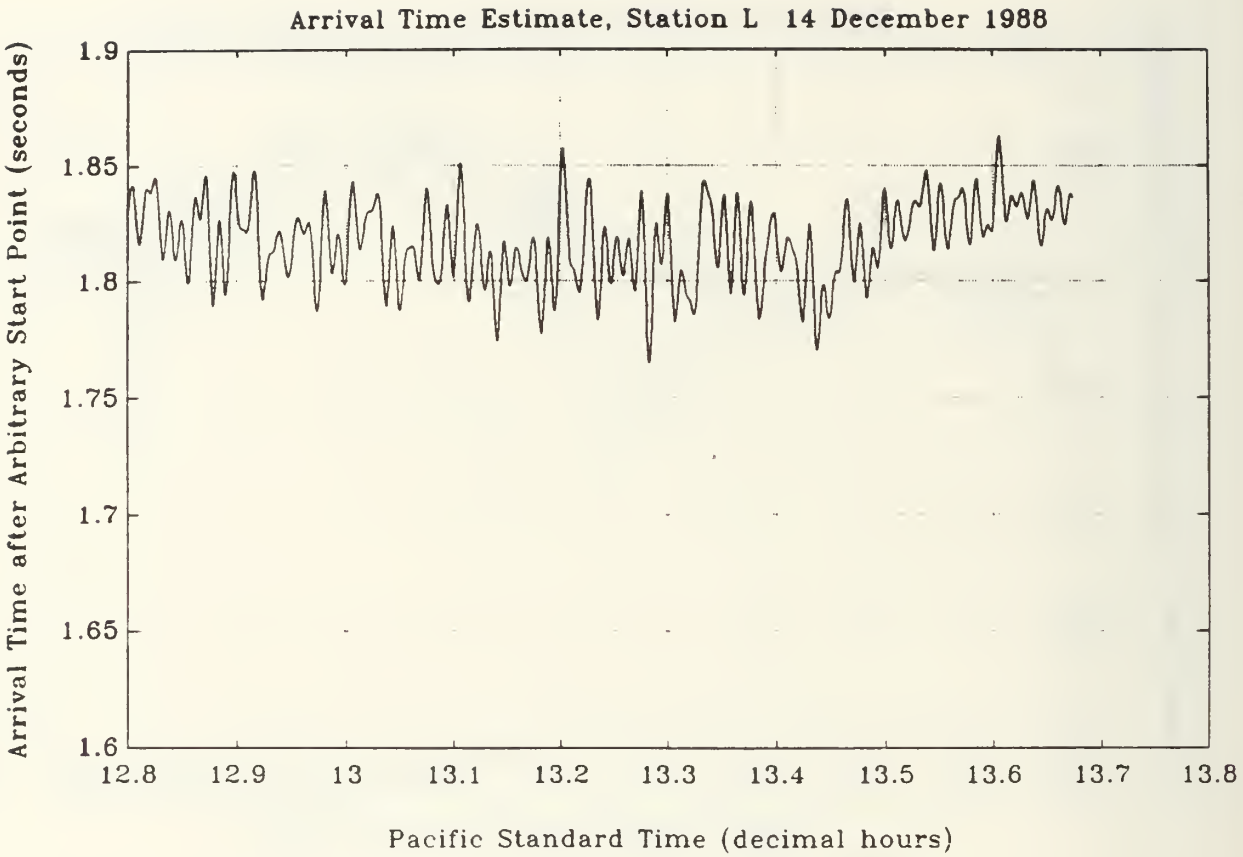

Figure 122: Arrival time estimate for Station L from 1248 to 1348 PST 14Dec88. The fast fluctuations in the arrival times are caused by surface waves changing the path length.

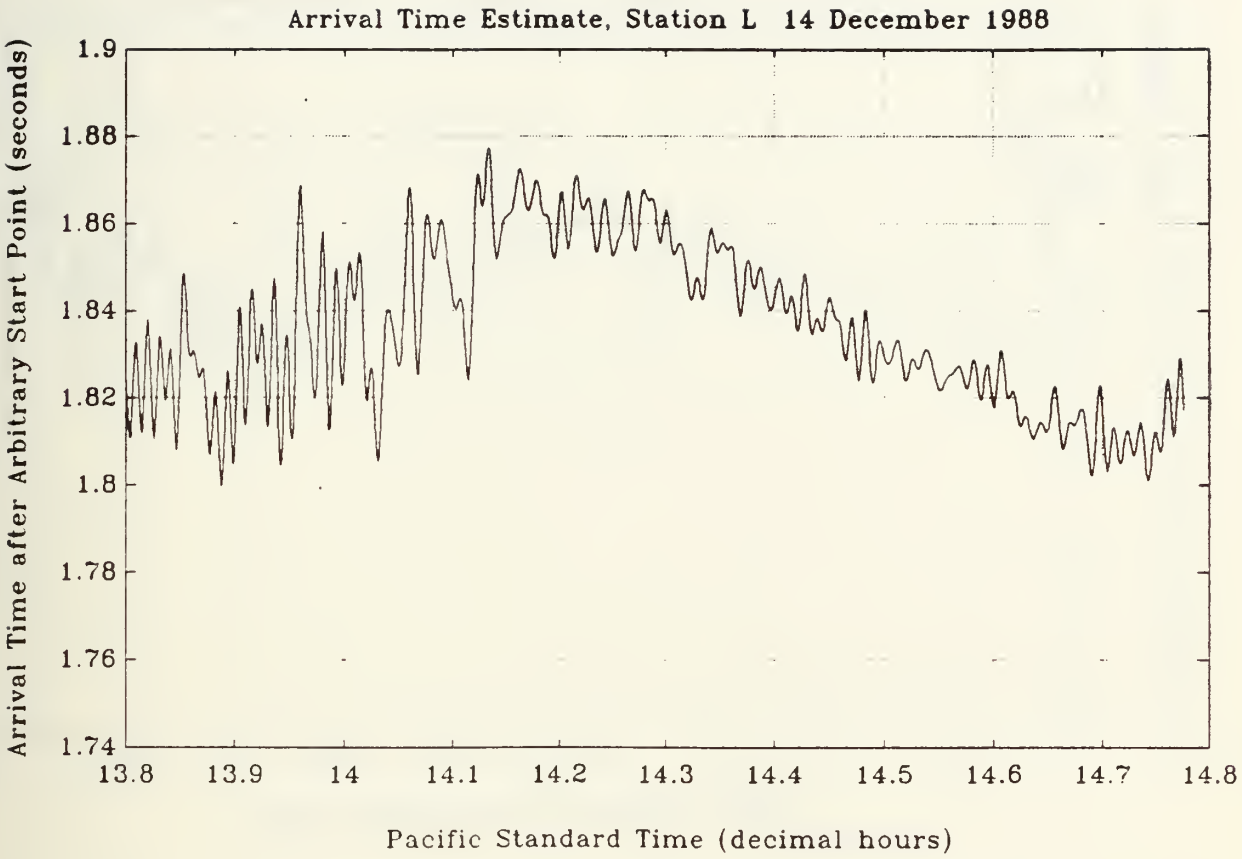

Figure 123: Arrival time estimate for Station L from 1348 to 1448 PST 14Dec88. The fast fluctuations in the arrival times are caused by surface waves changing the path length.

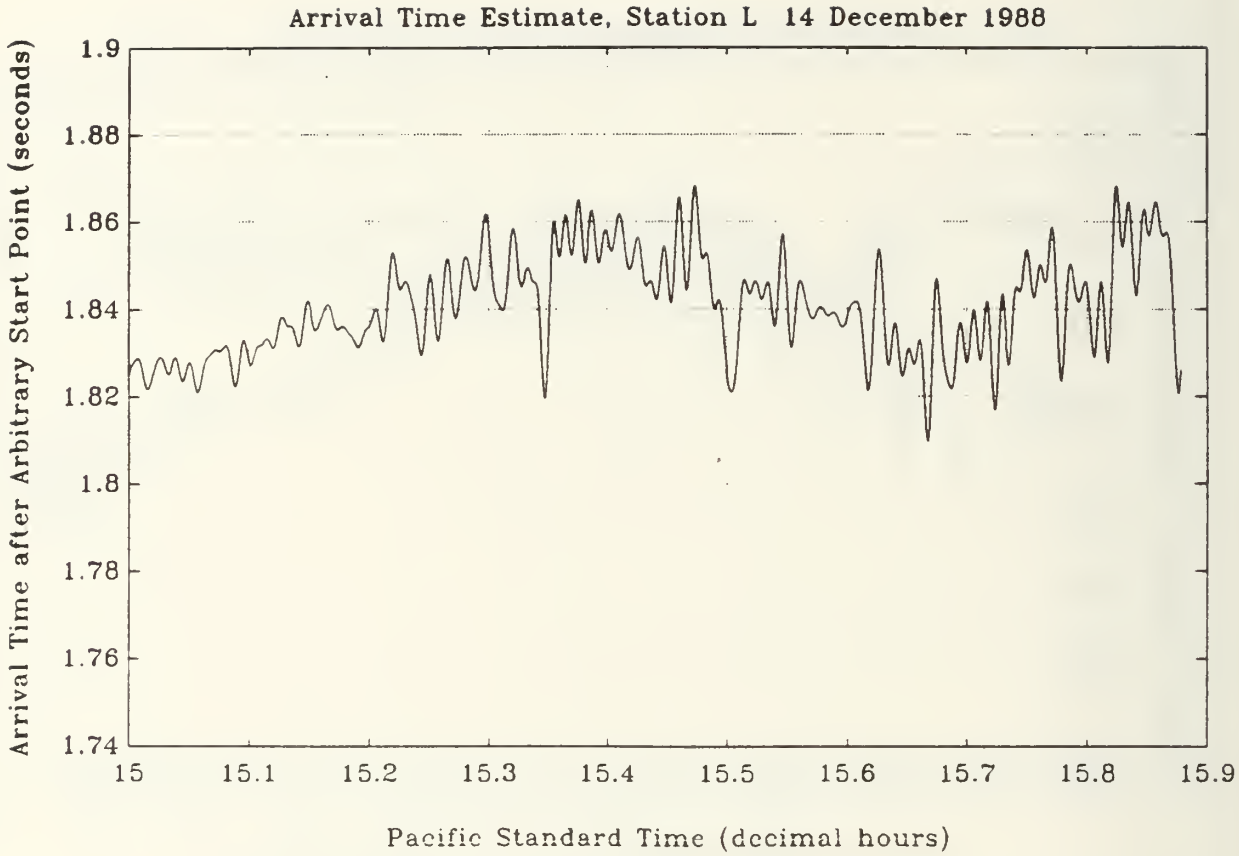

Figure 124: Arrival time estimate for Station L from 1500 to 1554 PST 14Dec88. The fast fluctuations in the arrival times are caused by surface waves changing the path length.

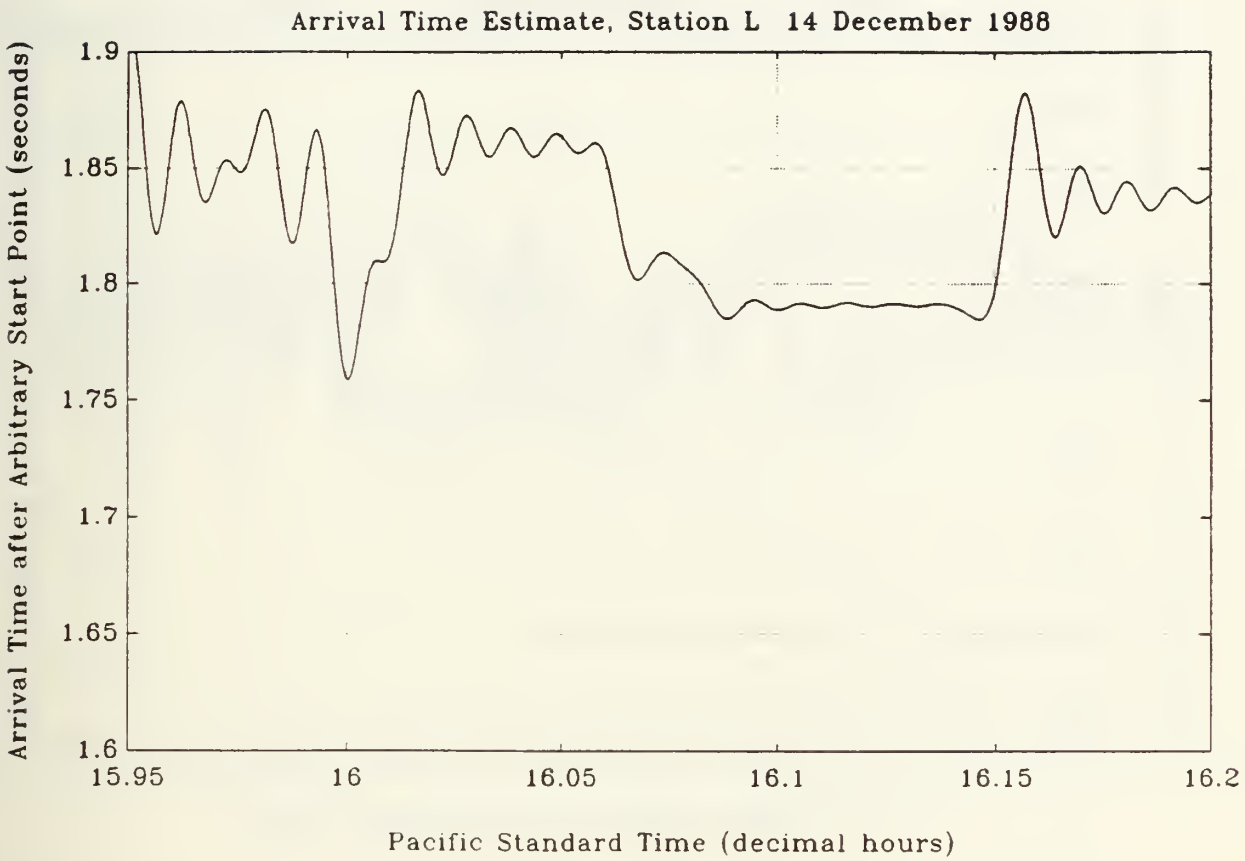

Figure 125: Arrival time estimate for Station L from 1557 to 1612 PST 14Dec88. The fast fluctuations in the arrival times are caused by surface waves changing the path length.

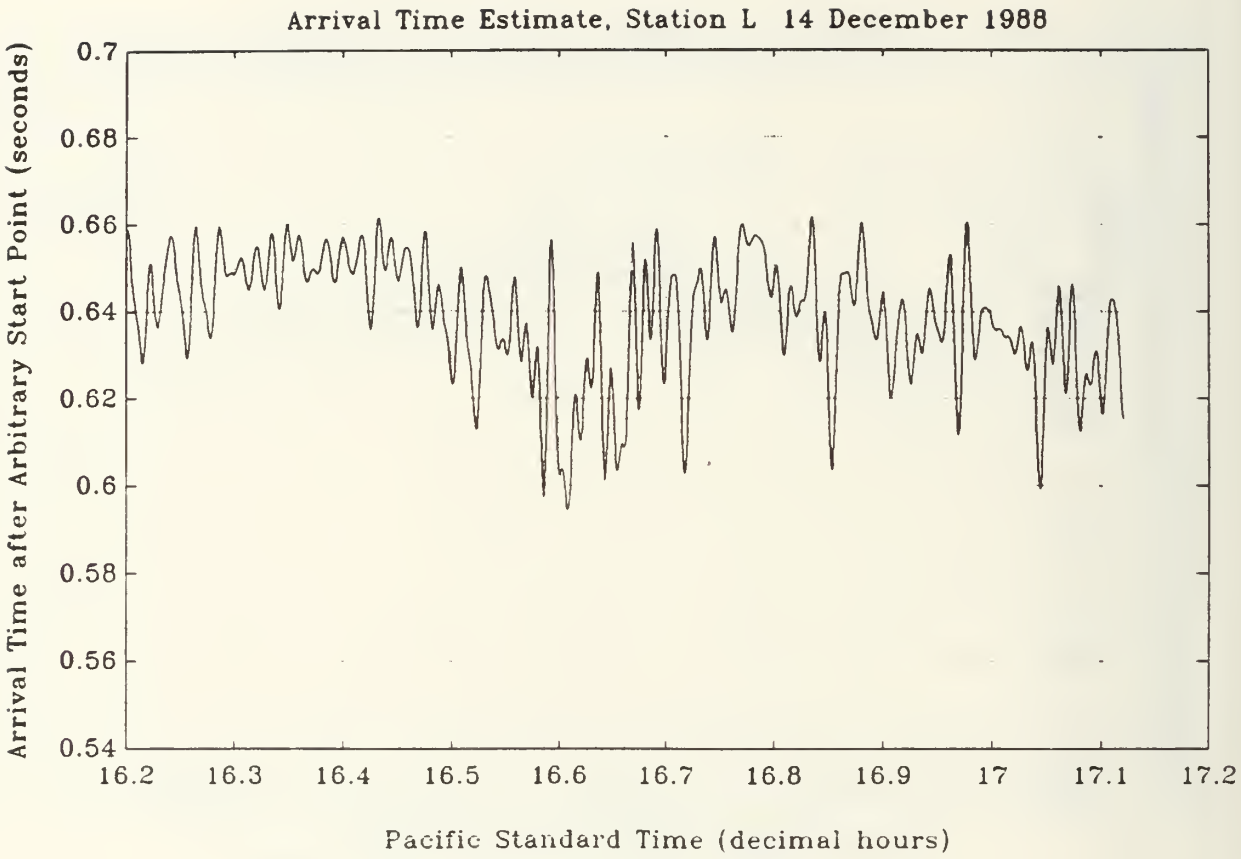

Figure 126: Arrival time estimate for Station L from 1612 to 1712 PST 14Dec88. The fast fluctuations in the arrival times are caused by surface waves changing the path length.

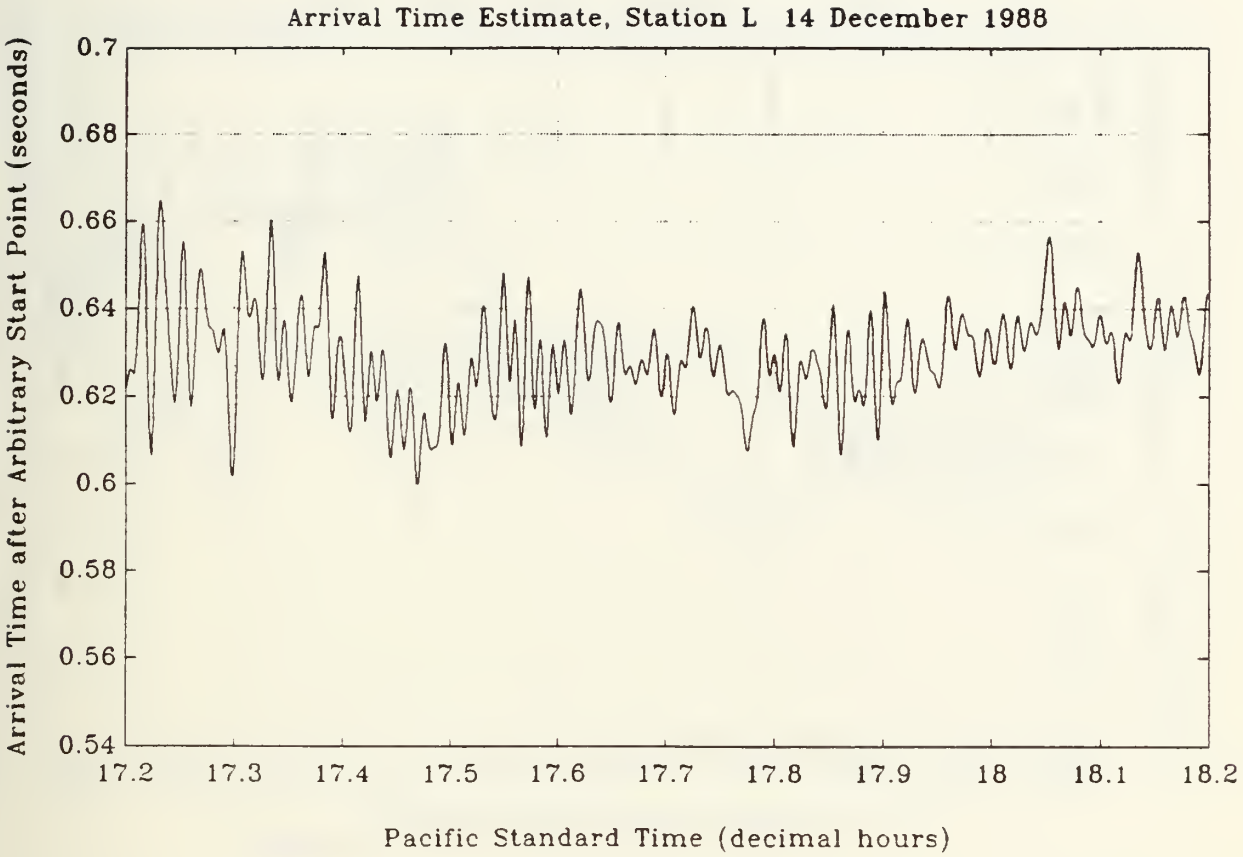

Figure 127: Arrival time estimate for Station L from 1712 to 1812 PST 14Dec88. The fast fluctuations in the arrival times are caused by surface waves changing the path length.

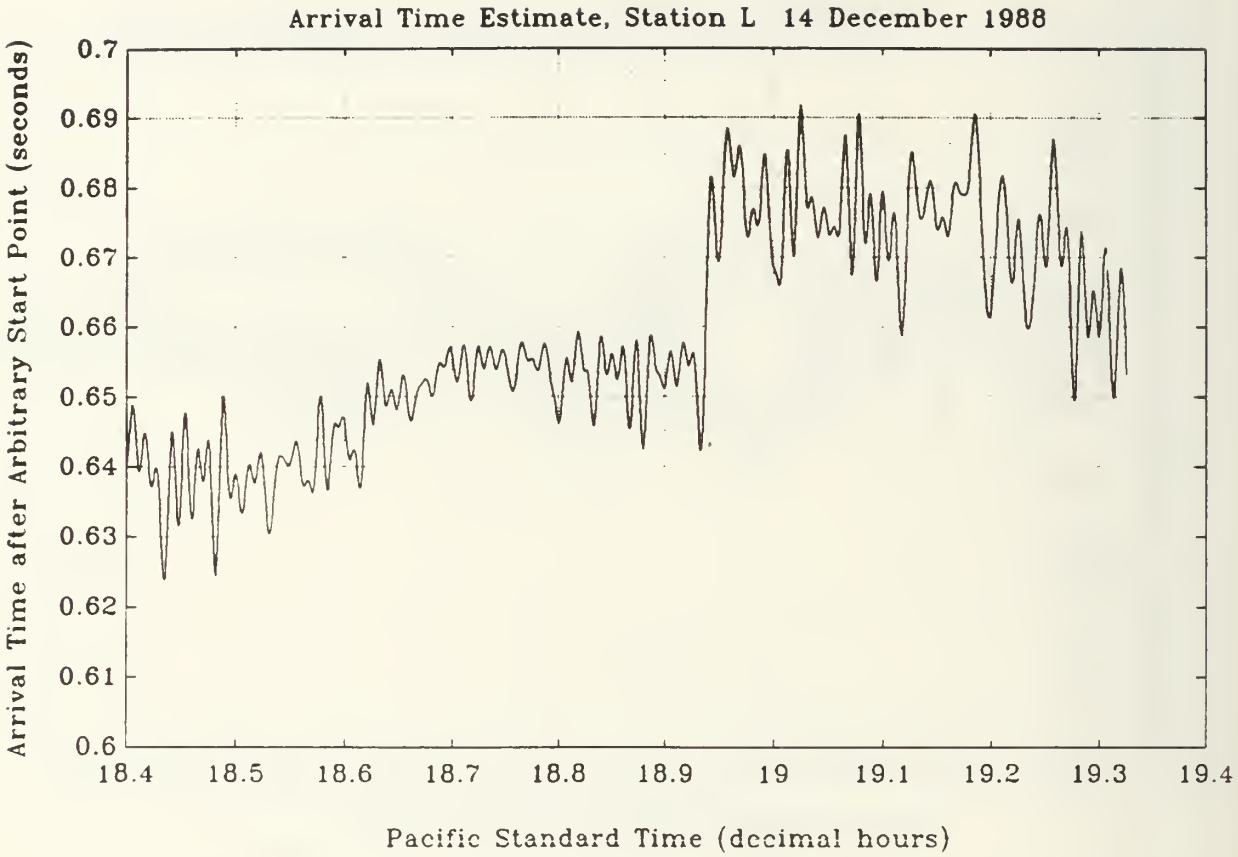

Figure 128: Arrival time estimate for Station L from 1824 to 1924 PST 14Dec88. The fast fluctuations in the arrival times are caused by surface waves changing the path length.

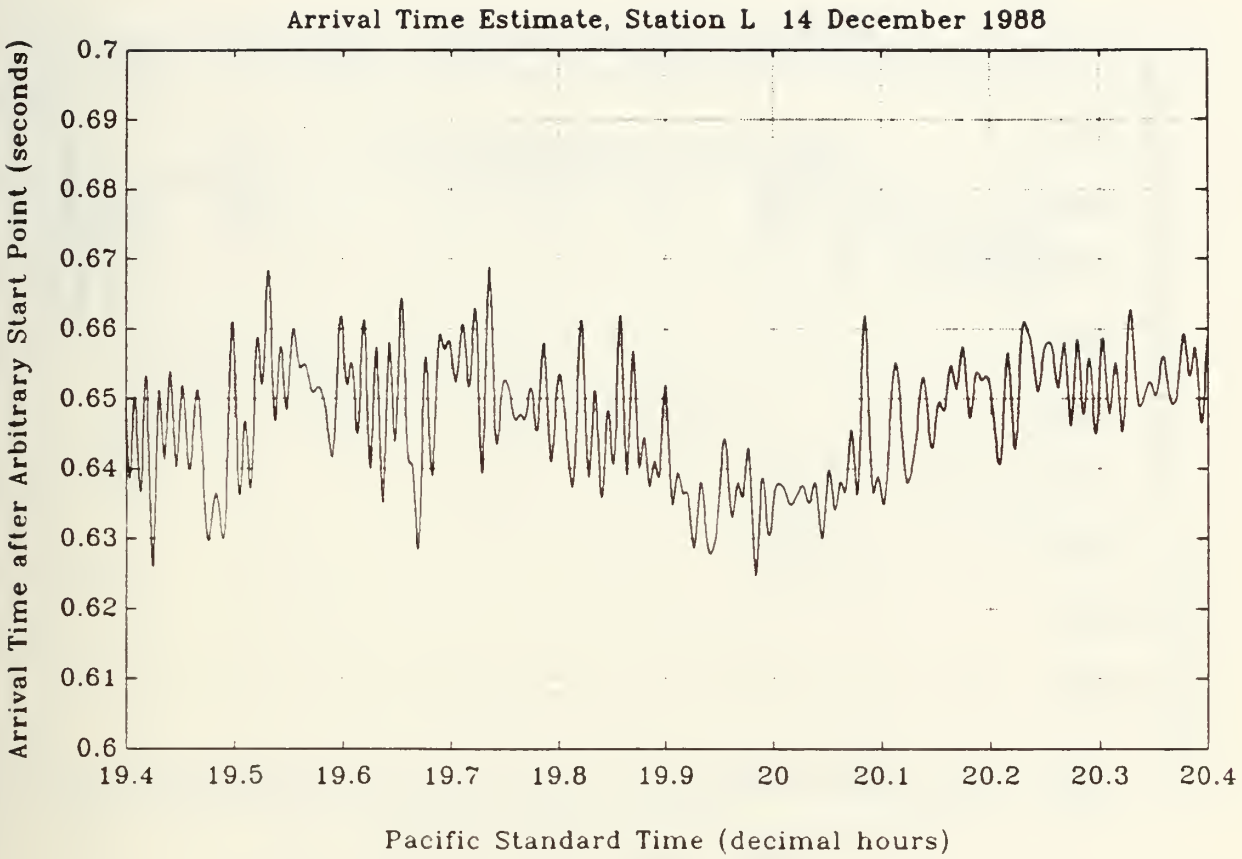

Figure 129: Arrival time estimate for Station L from 1924 to 2024 PST 14Dec88. The fast fluctuations in the arrival times are caused by surface waves changing the path length.

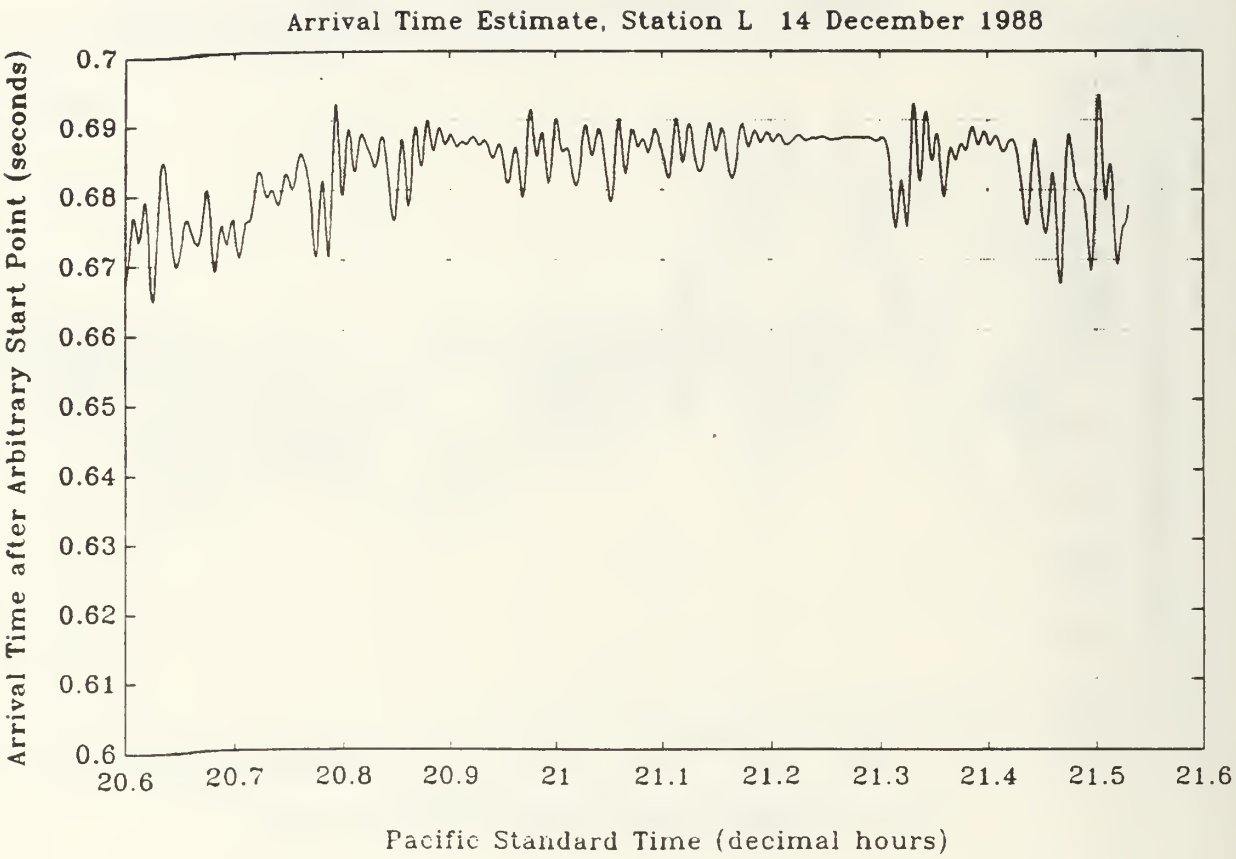

Figure 130: Arrival time estimate for Station L from 2036 to 2136 PST 14Dec88. The fast fluctuations in the arrival times are caused by surface waves changing the path length.

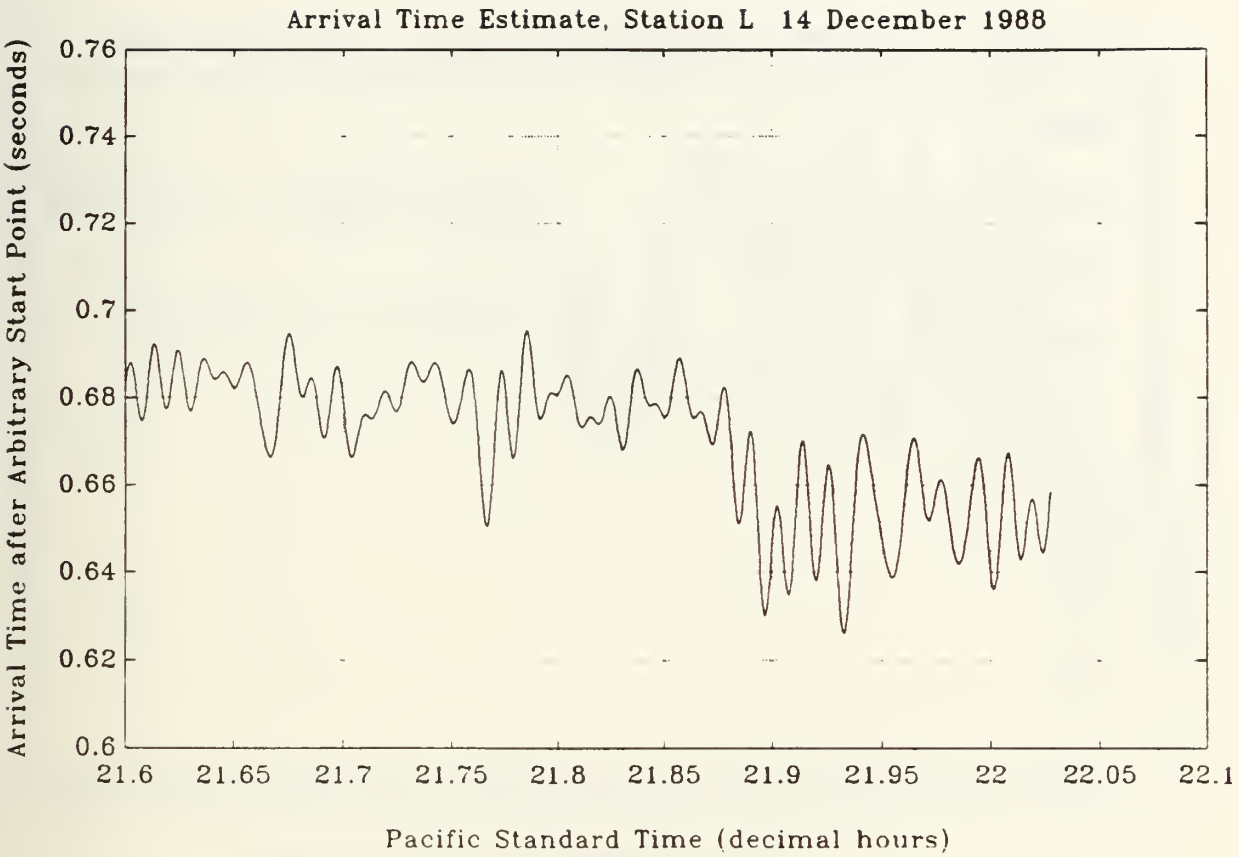

Figure 131: Arrival time estimate for Station L from 2136 to 2206 PST 14Dec88. The fast fluctuations in the arrival times are caused by surface waves changing the path length.

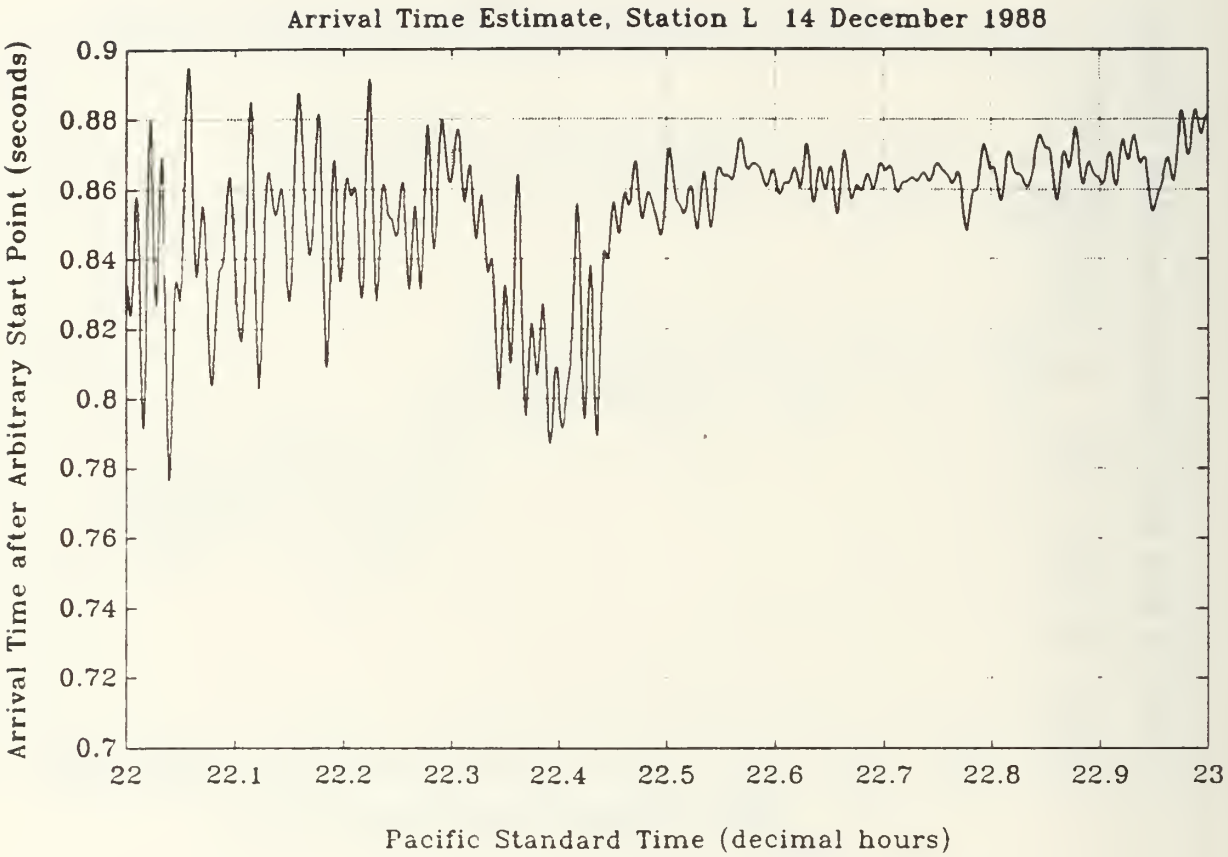

Figure 132: Arrival time estimate for Station L from 2200 to 2300 PST 14Dec88. The fast fluctuations in the arrival times are caused by surface waves changing the path length.

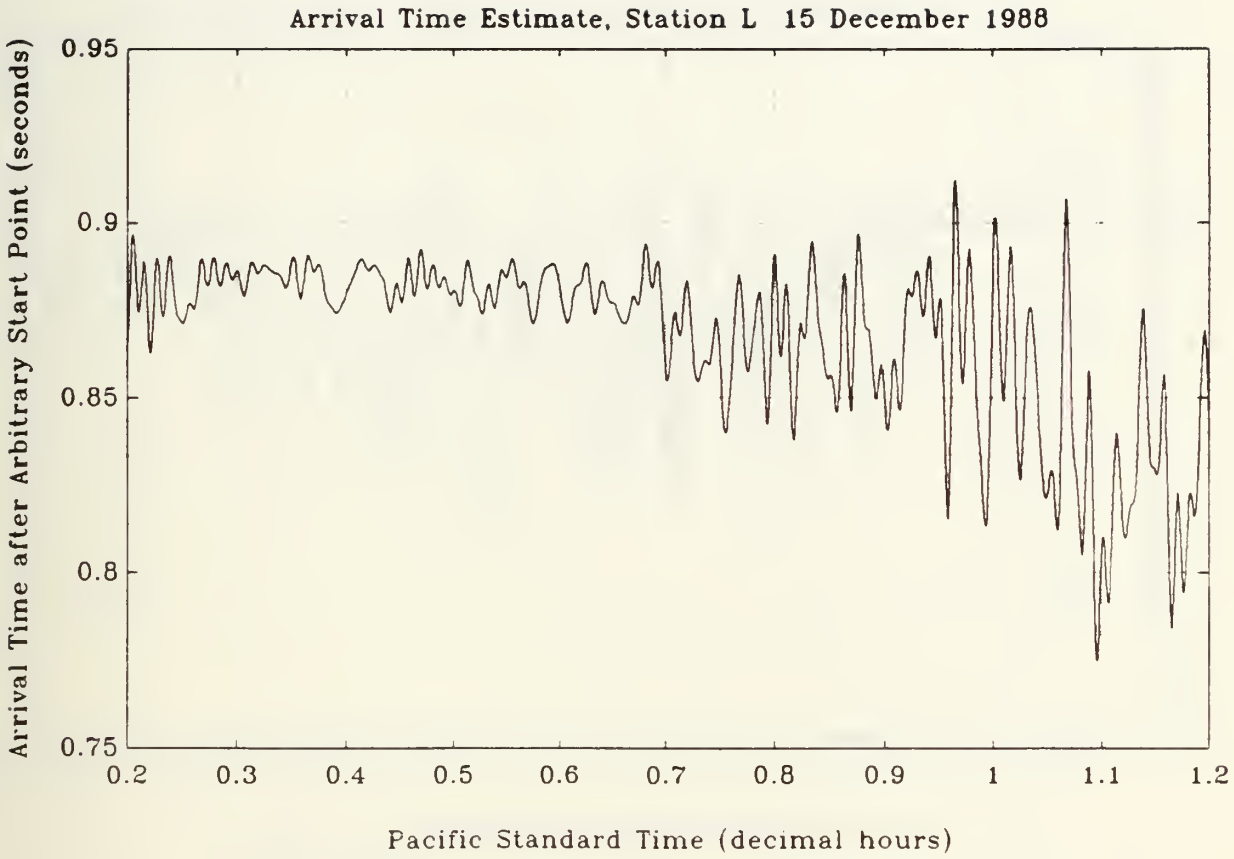

Figure 133: Arrival time estimate for Station L from 0012 to 0112 PST 15Dec88. The fast fluctuations in the arrival times are caused by surface waves changing the path length.

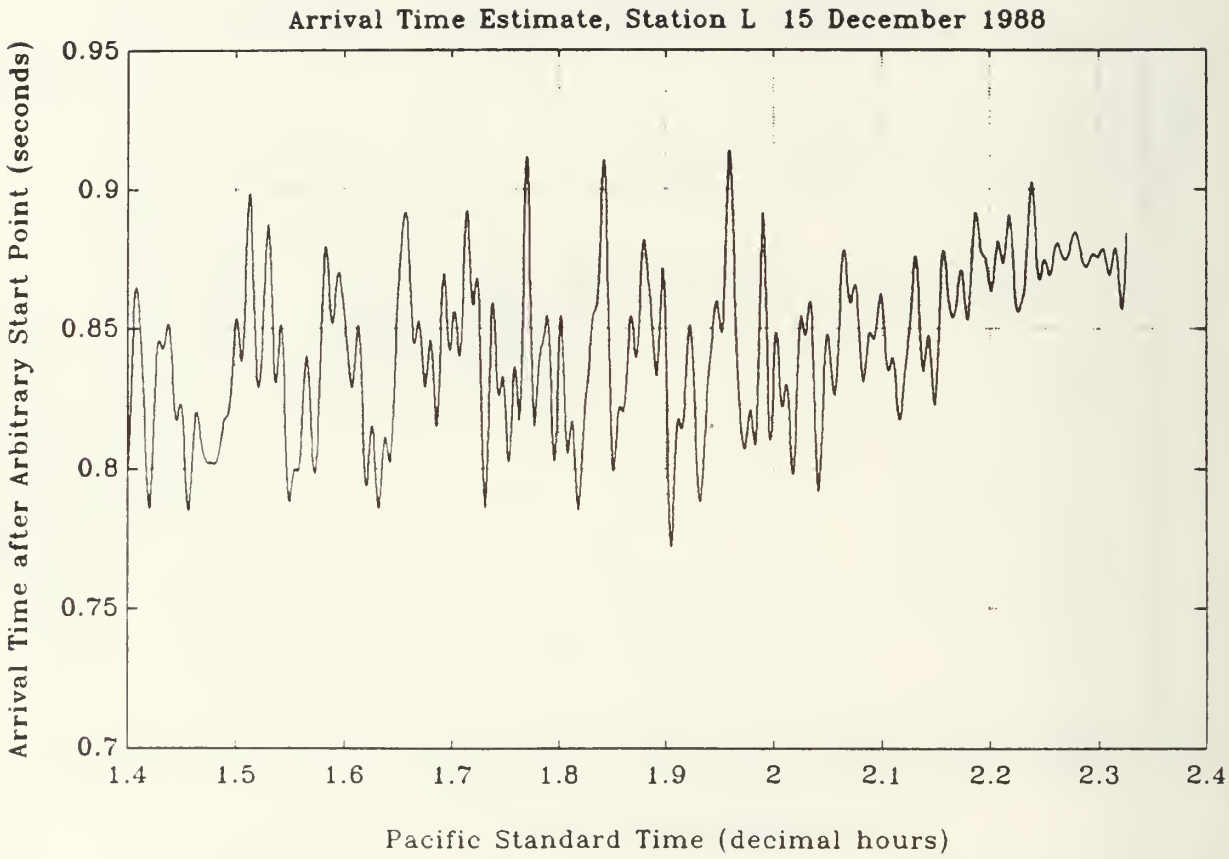

Figure 134: Arrival time estimate for Station L from 0124 to 0224 PST 15Dec88. The fast fluctuations in the arrival times are caused by surface waves changing the path length.

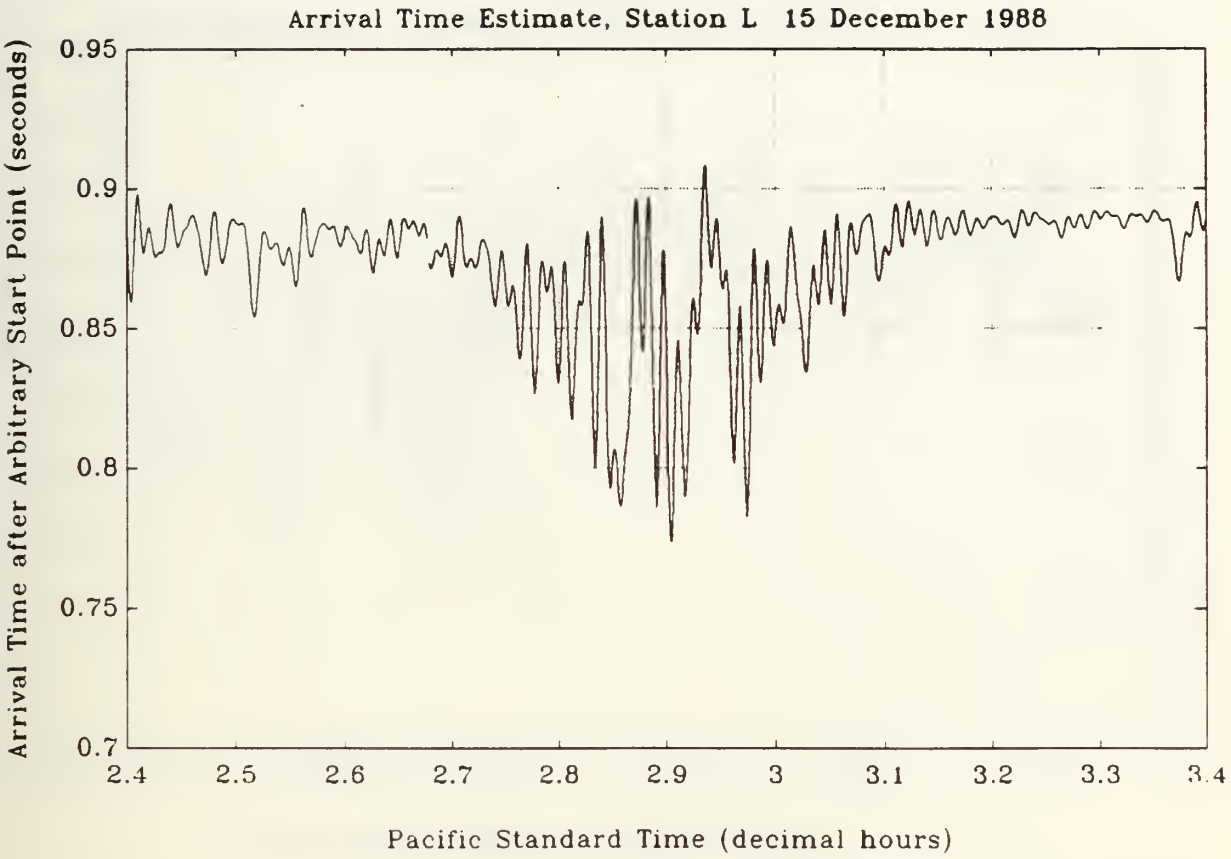

Figure 135: Arrival time estimate for Station L from 0224 to 0324 PST 15Dec88. The fast fluctuations in the arrival times are caused by surface waves changing the path length.

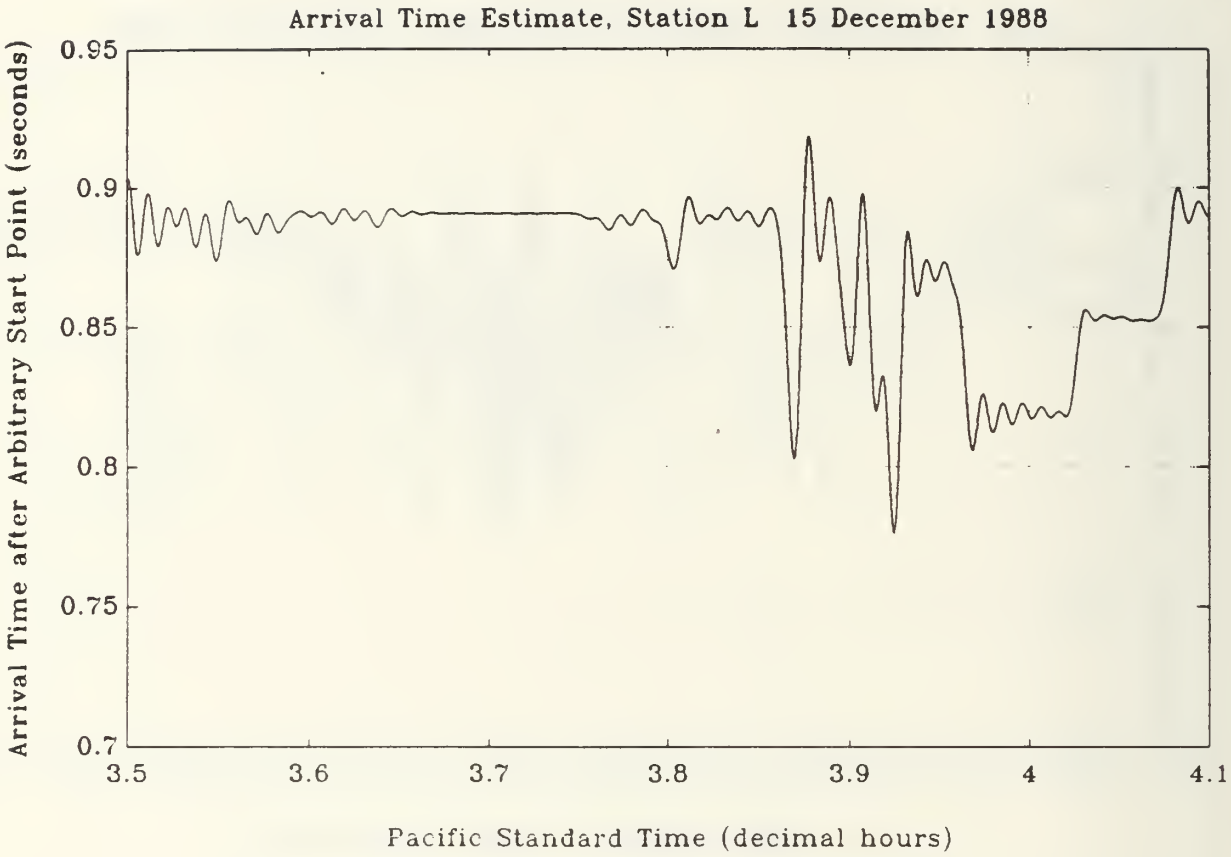

Figure 136: Arrival time estimate for Station L from 0330 to 0406 PST 15Dec88. The fast fluctuations in the arrival times are caused by surface waves changing the path length.

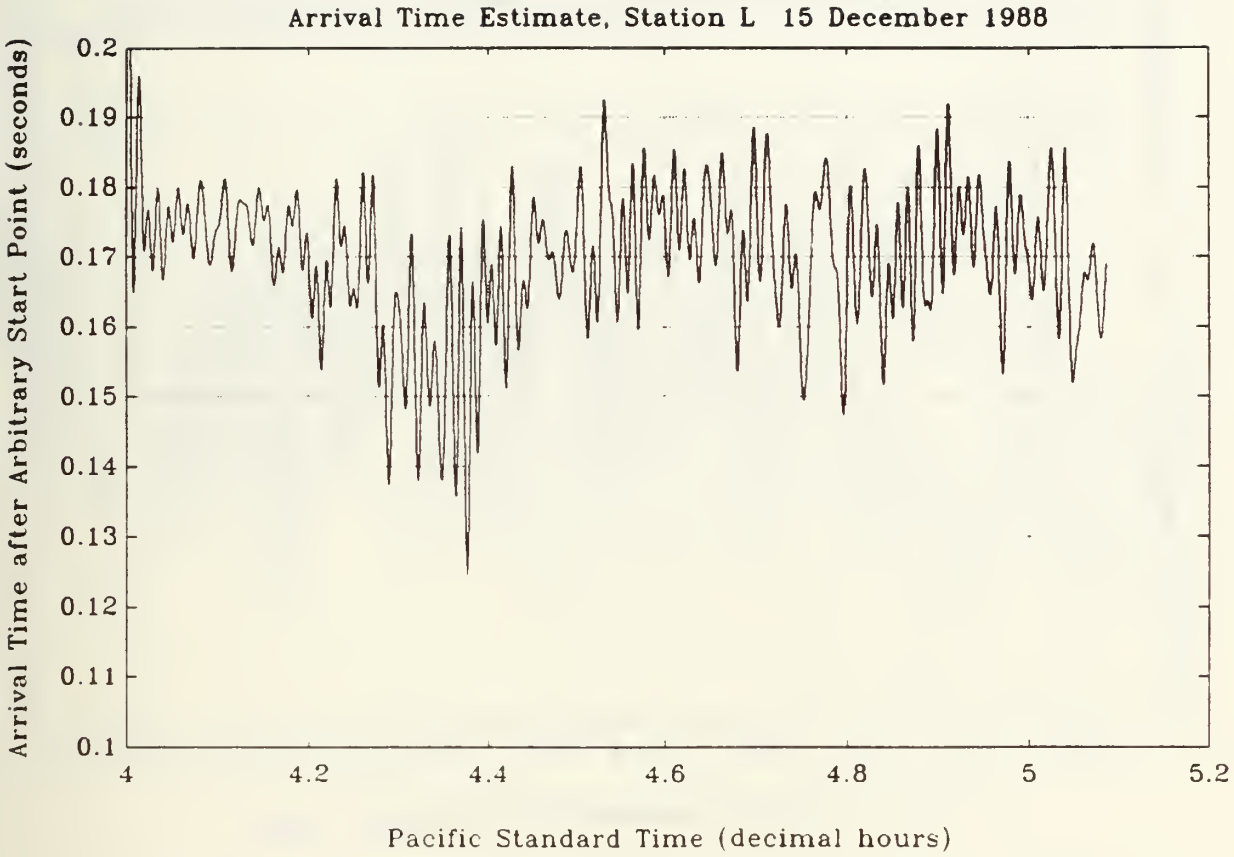

Figure 137: Arrival time estimate for Station L from 0400 to 0512 PST 15Dec88. The fast fluctuations in the arrival times are caused by surface waves changing the path length.

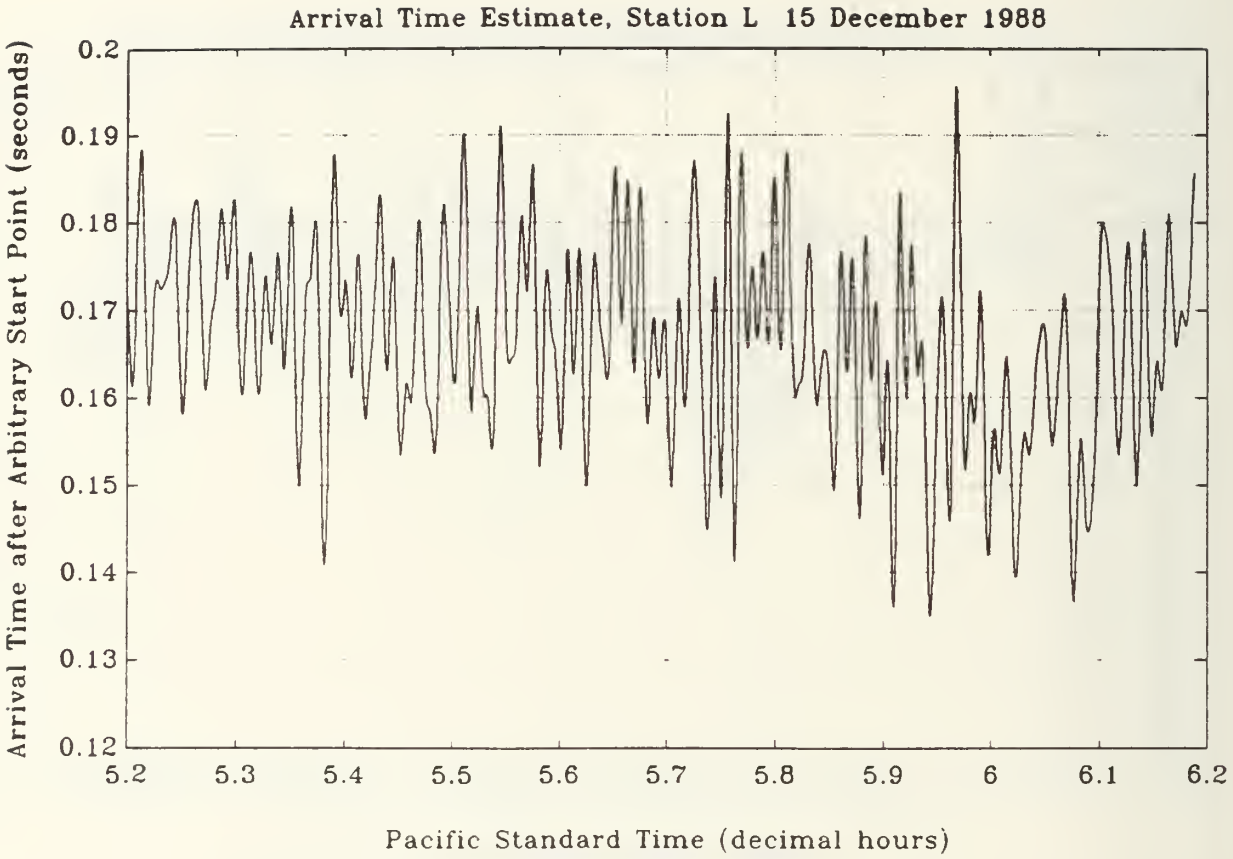

Figure 138: Arrival time estimate for Station L from 0512 to 0612 PST 15Dec88. The fast fluctuations in the arrival times are caused by surface waves changing the path length.

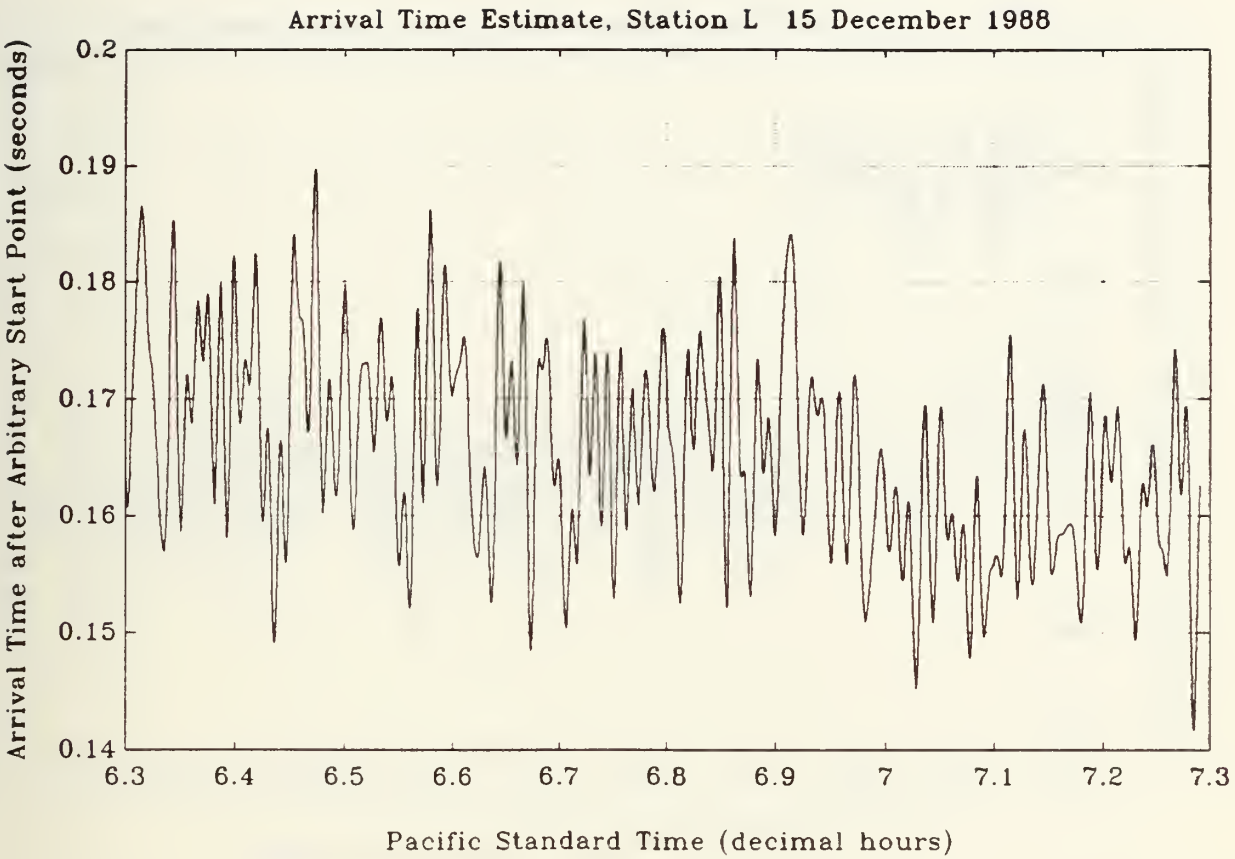

Figure 139: Arrival time estimate for Station L from 0618 to 0718 PST 15Dec88. The fast fluctuations in the arrival times are caused by surface waves changing the path length.

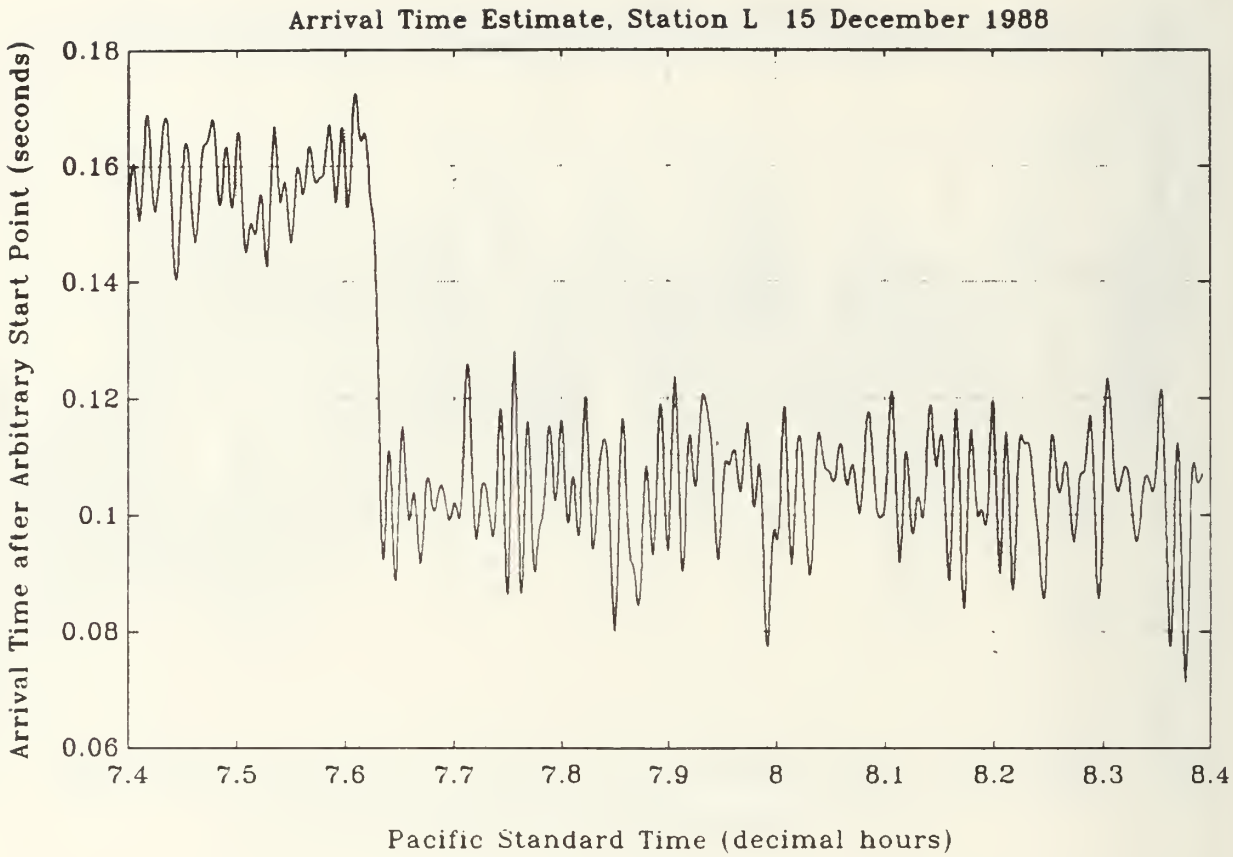

Figure 140: Arrival time estimate for Station L from 0724 to 0824 PST 15Dec88. The fast fluctuations in the arrival times are caused by surface waves changing the path length.

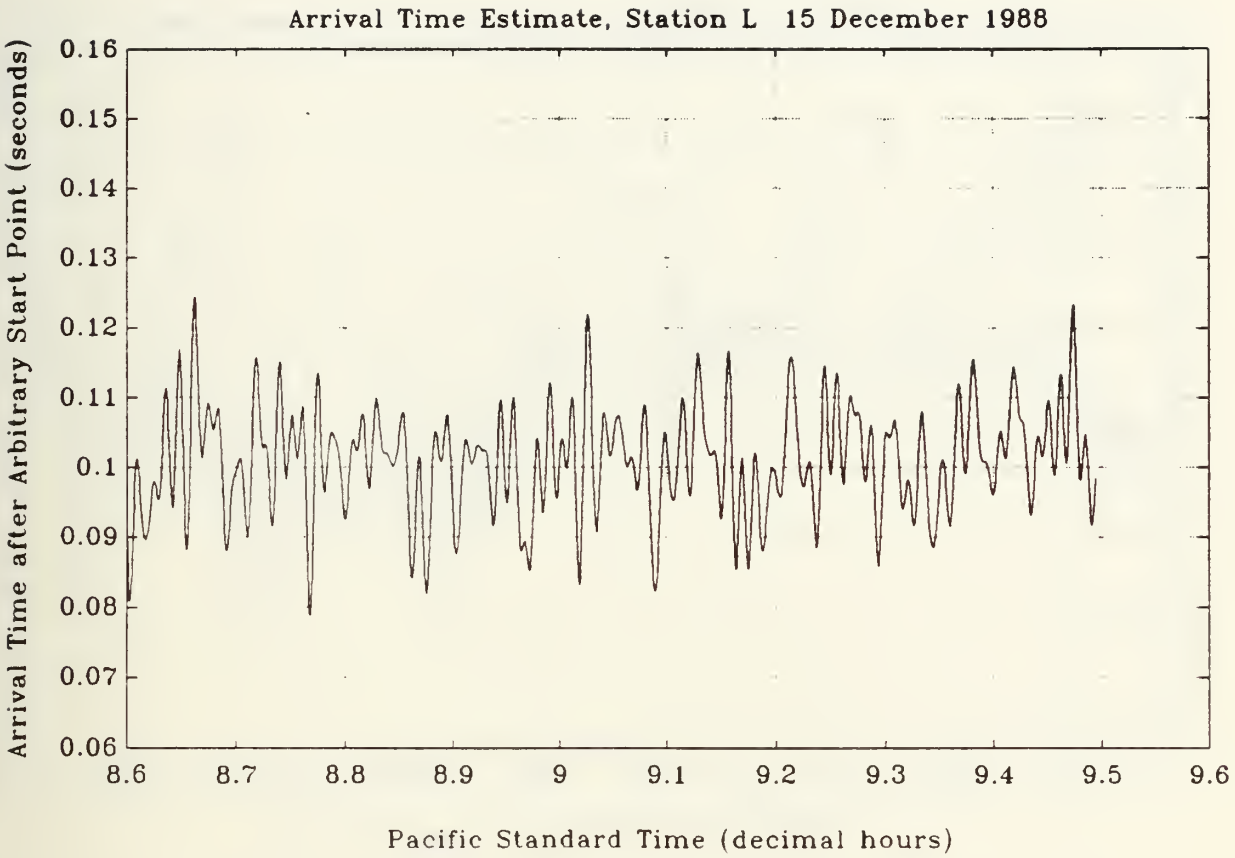

Figure 141: Arrival time estimate for Station L from 0836 to 0936 PST 15Dec88. The fast fluctuations in the arrival times are caused by surface waves changing the path length.

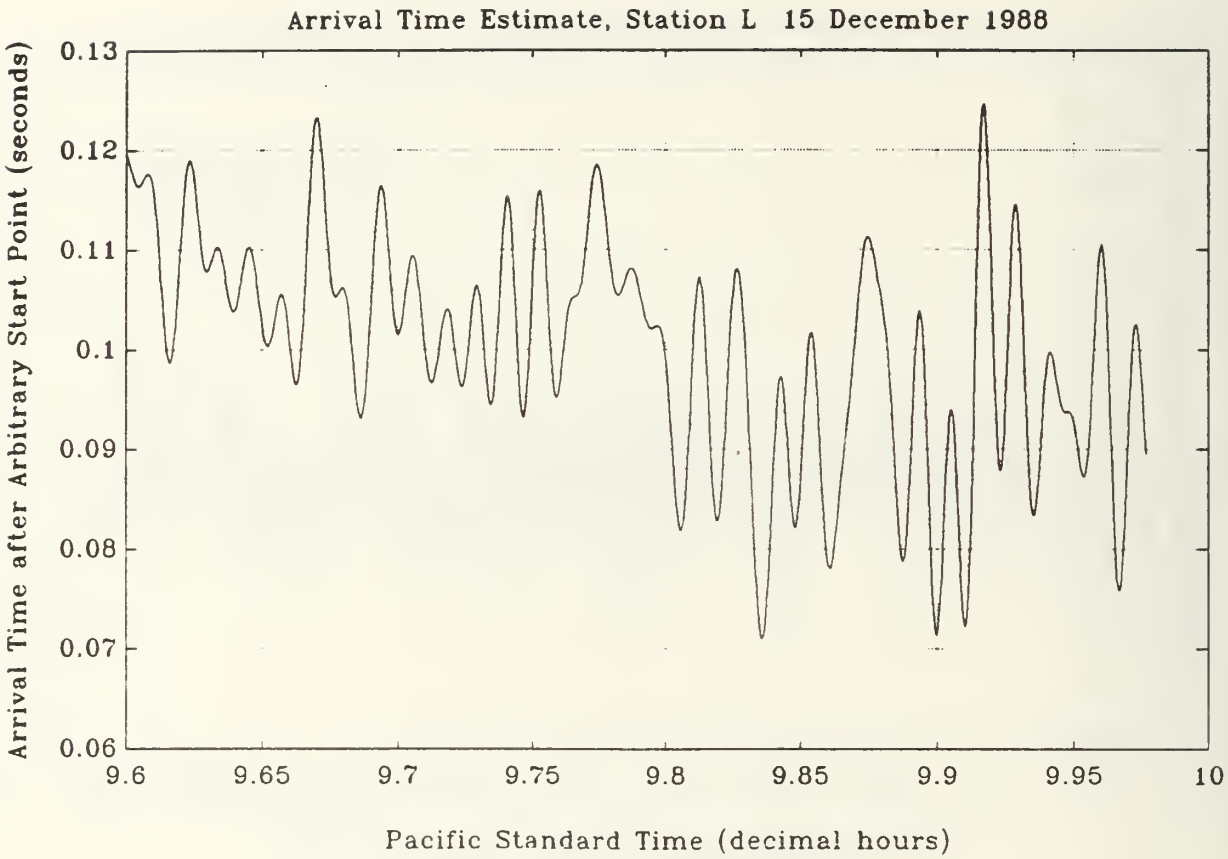

Figure 142: Arrival time estimate for Station L from 0936 to 1000 PST 15Dec88. The fast fluctuations in the arrival times are caused by surface waves changing the path length.

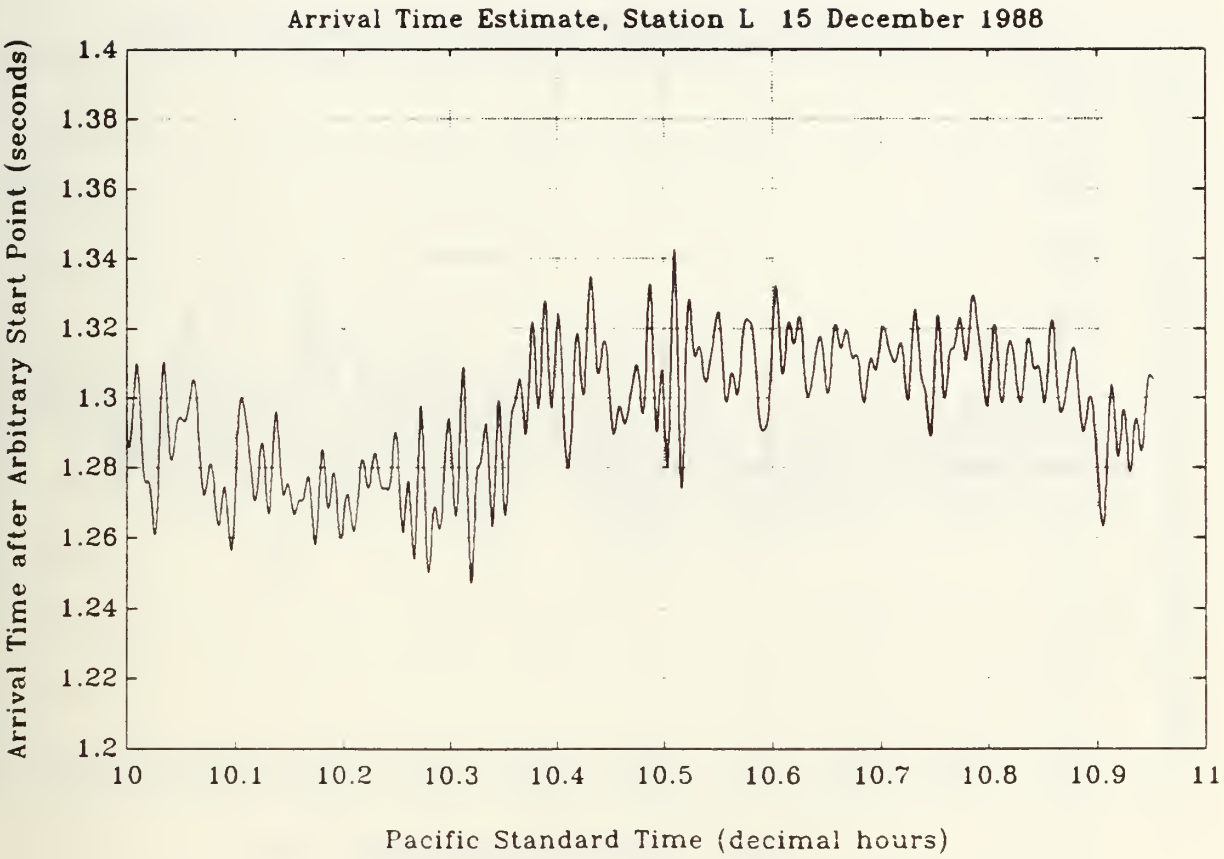

Figure 143: Arrival time estimate for Station L from 1000 to 1100 PST 15Dec88. The fast fluctuations in the arrival times are caused by surface waves changing the path length.

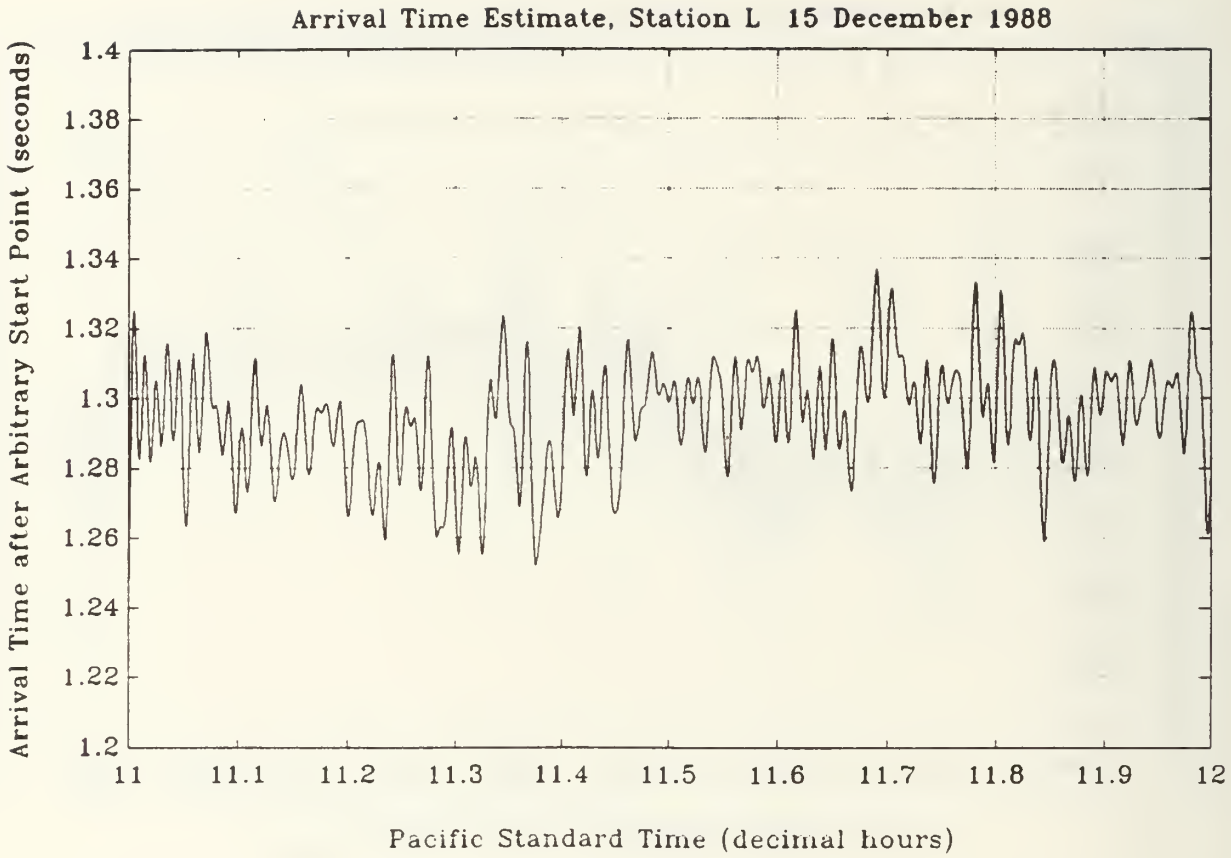

Figure 144: Arrival time estimate for Station L from 1100 to 1200 PST 15Dec88. The fast fluctuations in the arrival times are caused by surface waves changing the path length.

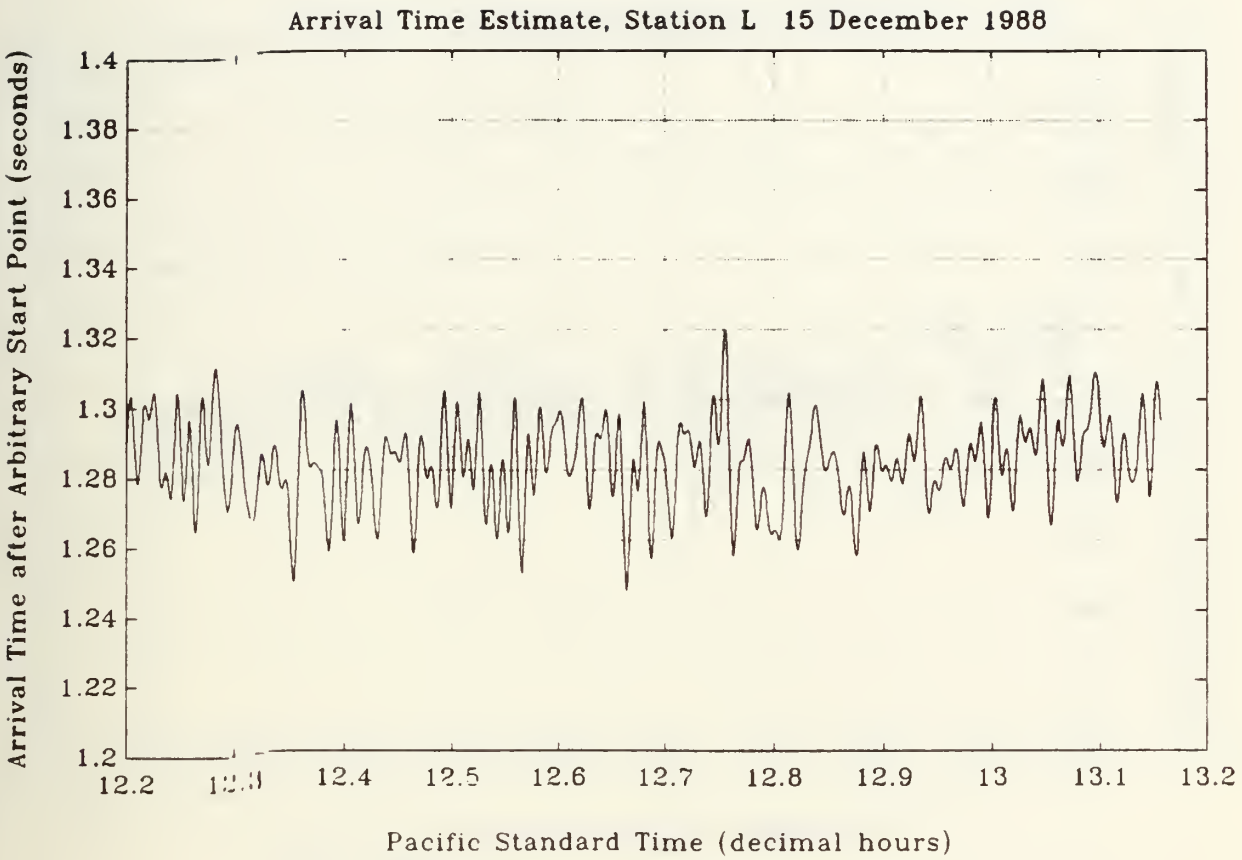

Figure 145: Arrival time estimate for Station L from 1212 to 1312 PST 15Dec88. The fast fluctuations in the arrival times are caused by surface waves changing the path length.

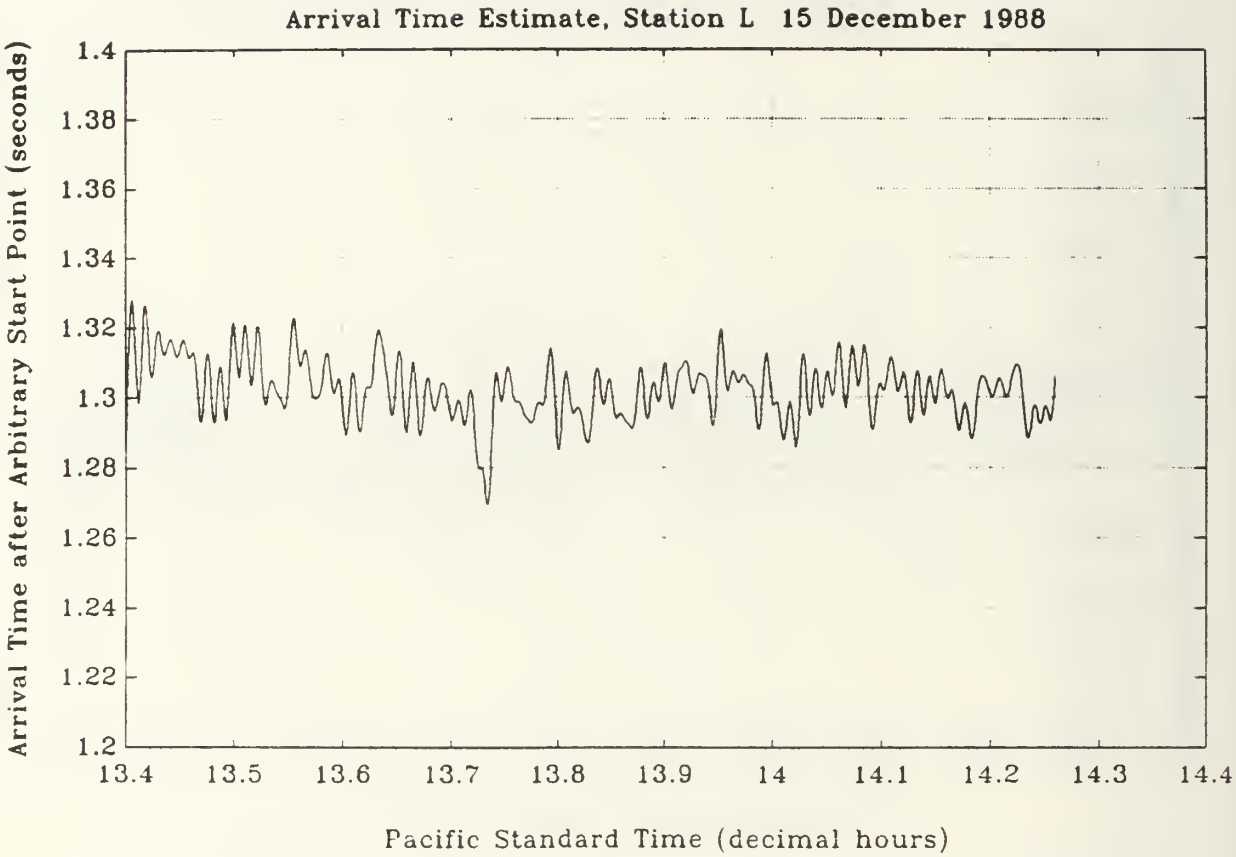

Figure 146: Arrival time estimate for Station L from 1324 to 1424 PST 15Dec88. The fast fluctuations in the arrival times are caused by surface waves changing the path length.

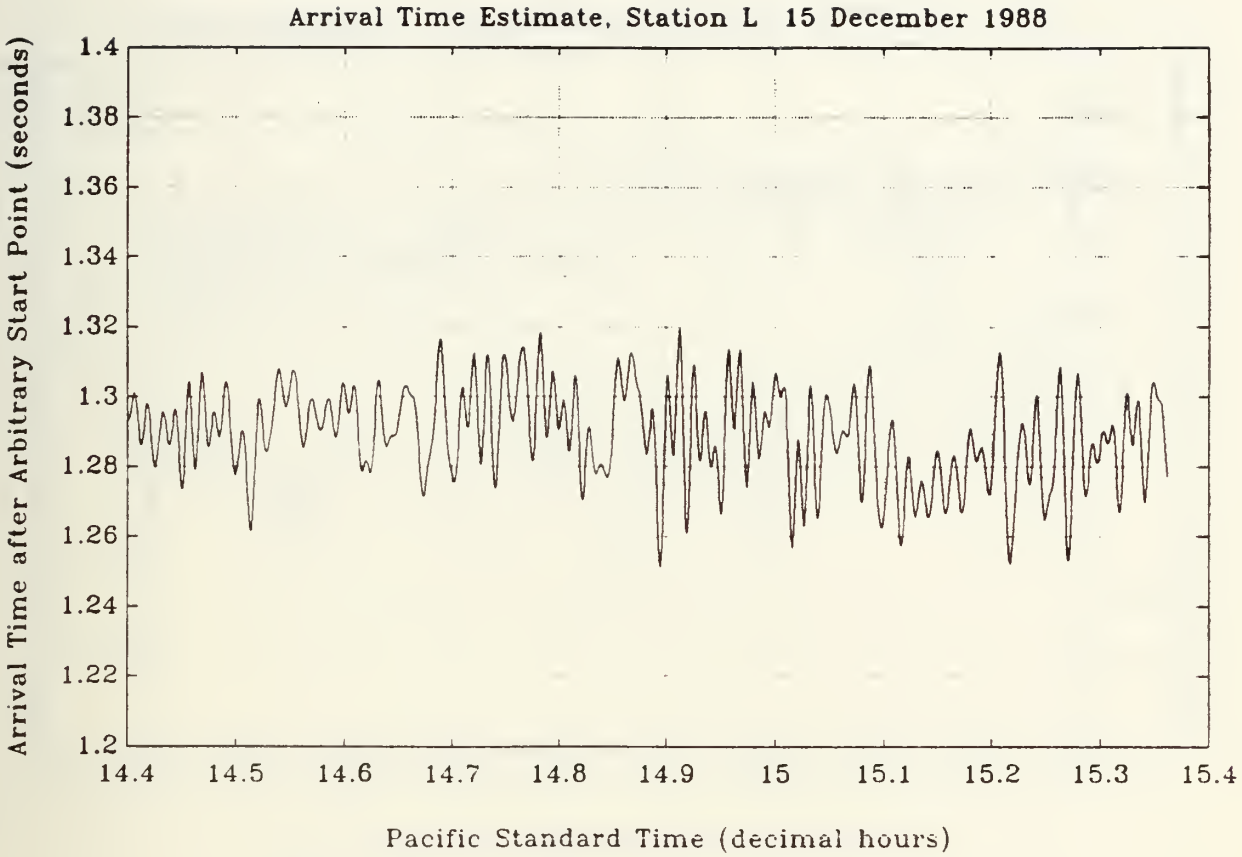

Figure 147: Arrival time estimate for Station L from 1424 to 1524 PST 15Dec88. The fast fluctuations in the arrival times are caused by surface waves changing the path length.

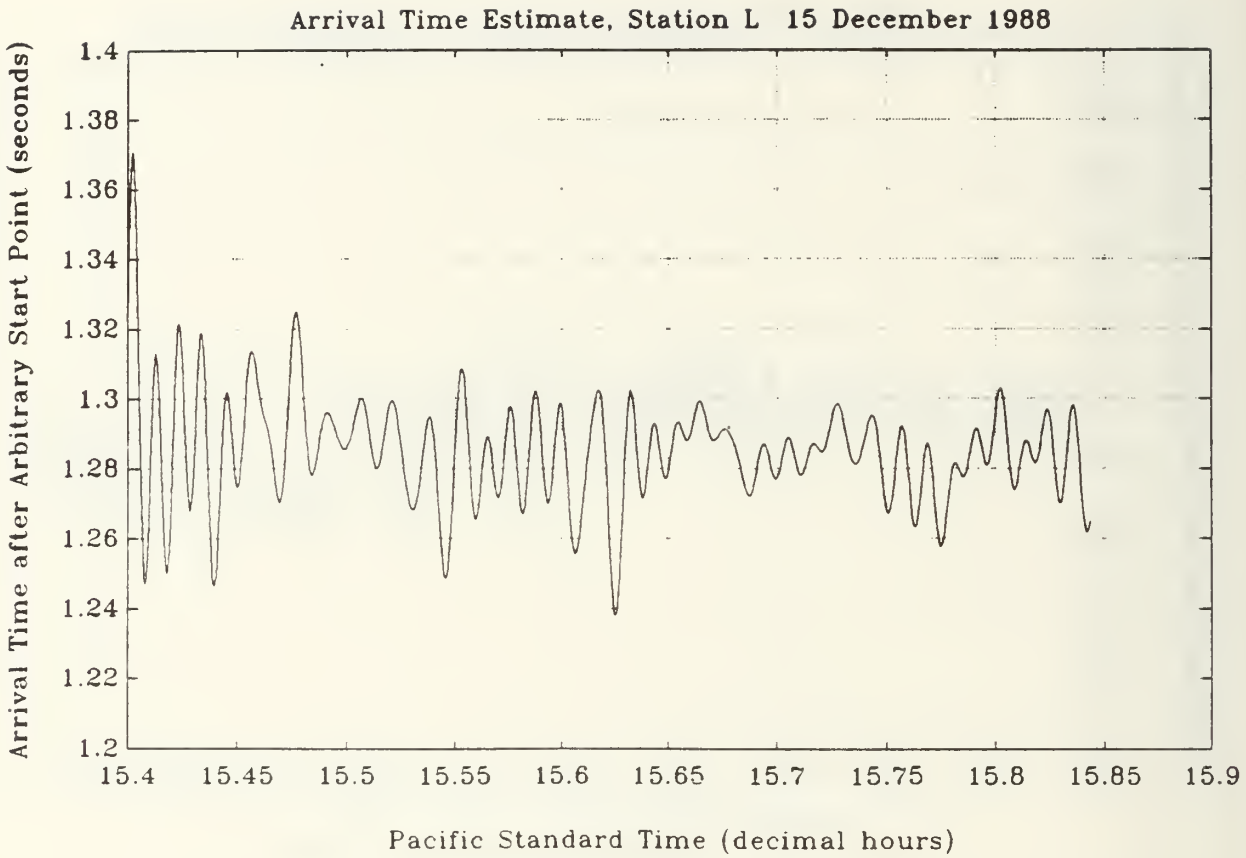

Figure 148: Arrival time estimate for Station L from 1524 to 1554 PST 15Dec88. The fast fluctuations in the arrival times are caused by surface waves changing the path length.

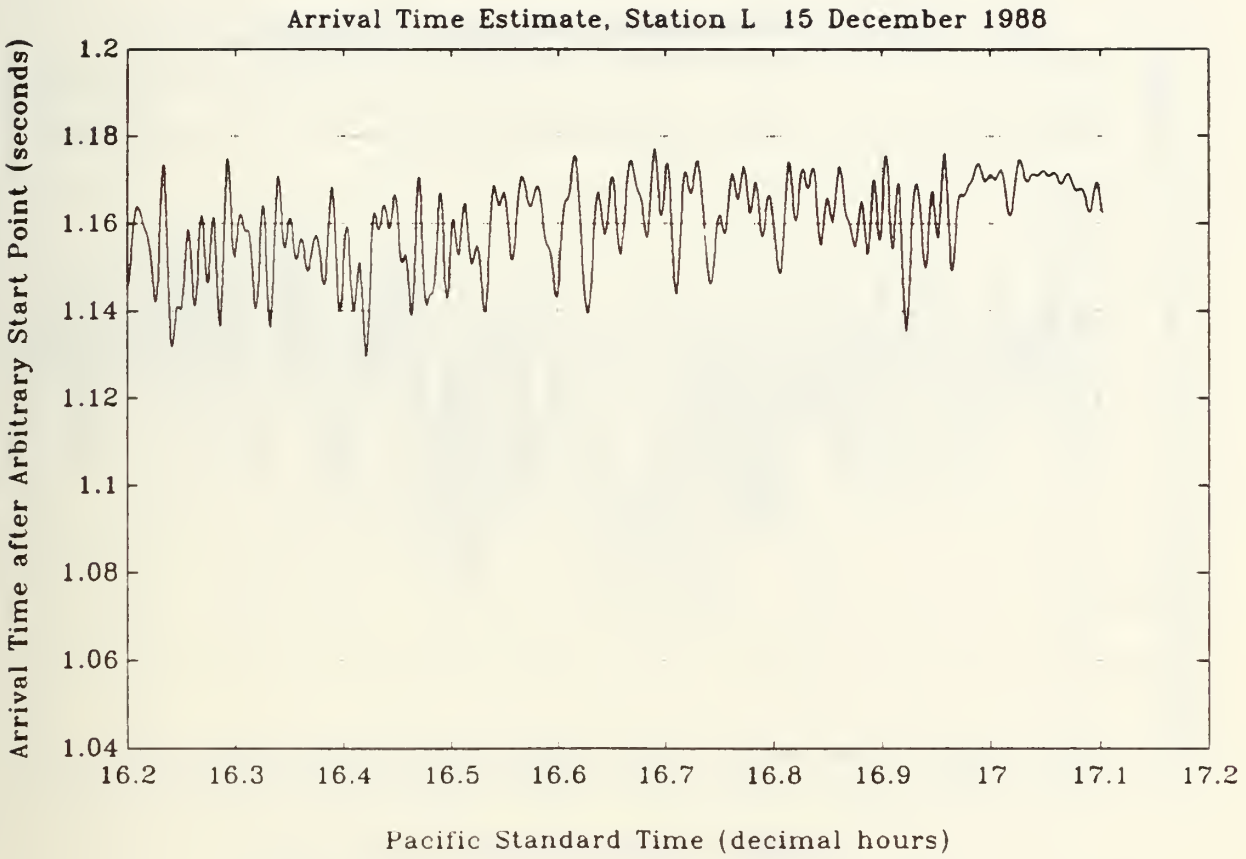

Figure 149: Arrival time estimate for Station L from 1612 to 1712 PST 15Dec88. The fast fluctuations in the arrival times are caused by surface waves changing the path length.

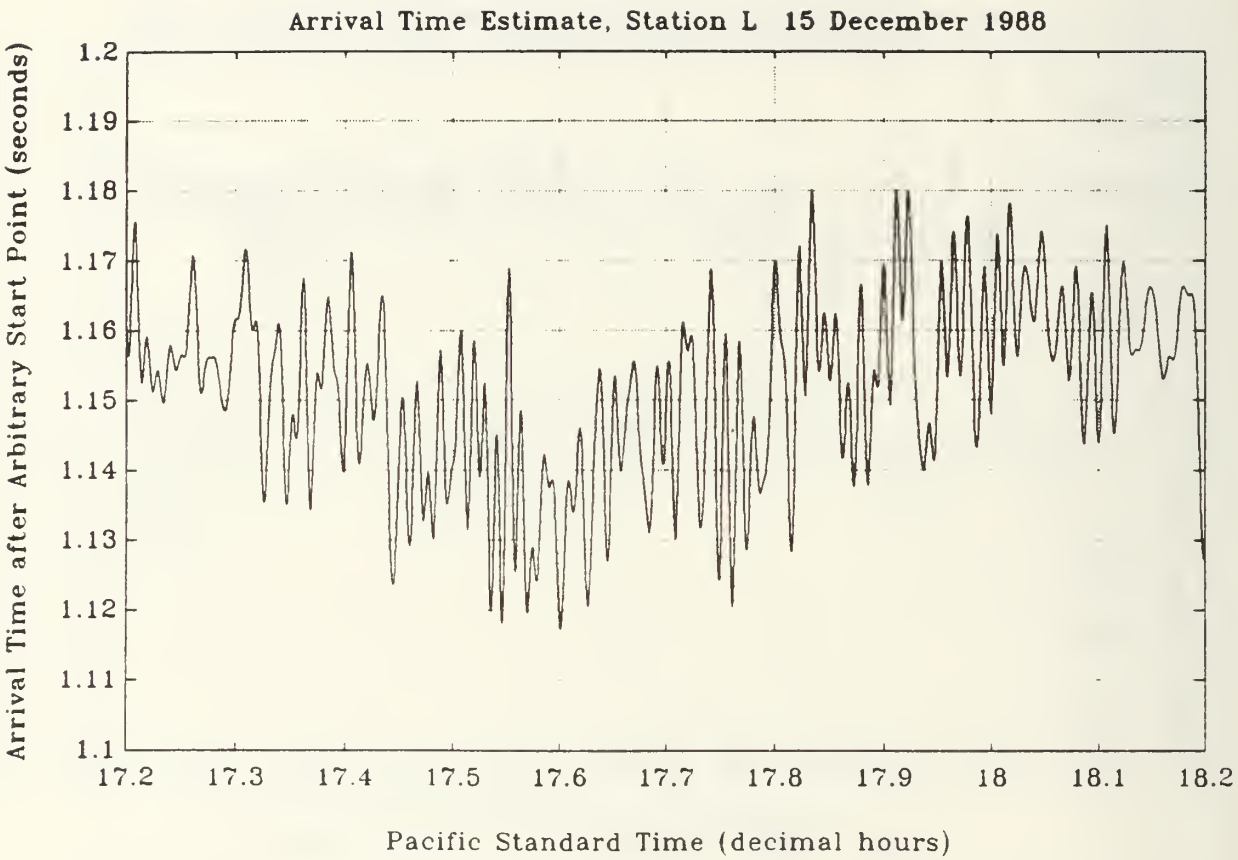

Figure 150: Arrival time estimate for Station L from 1712 to 1812 PST 15Dec88. The fast fluctuations in the arrival times are caused by surface waves changing the path length.

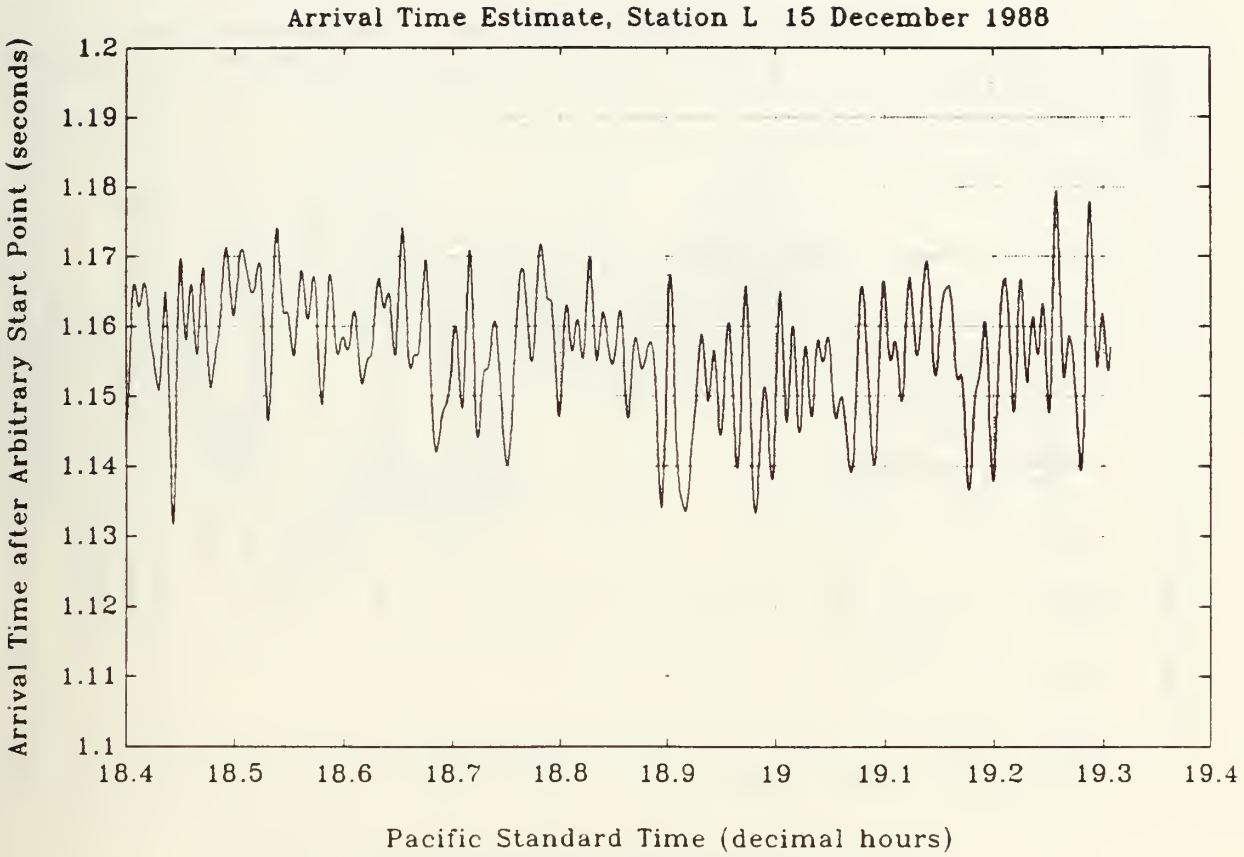

Figure 151: Arrival time estimate for Station L from 1824 to 1924 PST 15Dec88. The fast fluctuations in the arrival times are caused by surface waves changing the path length.

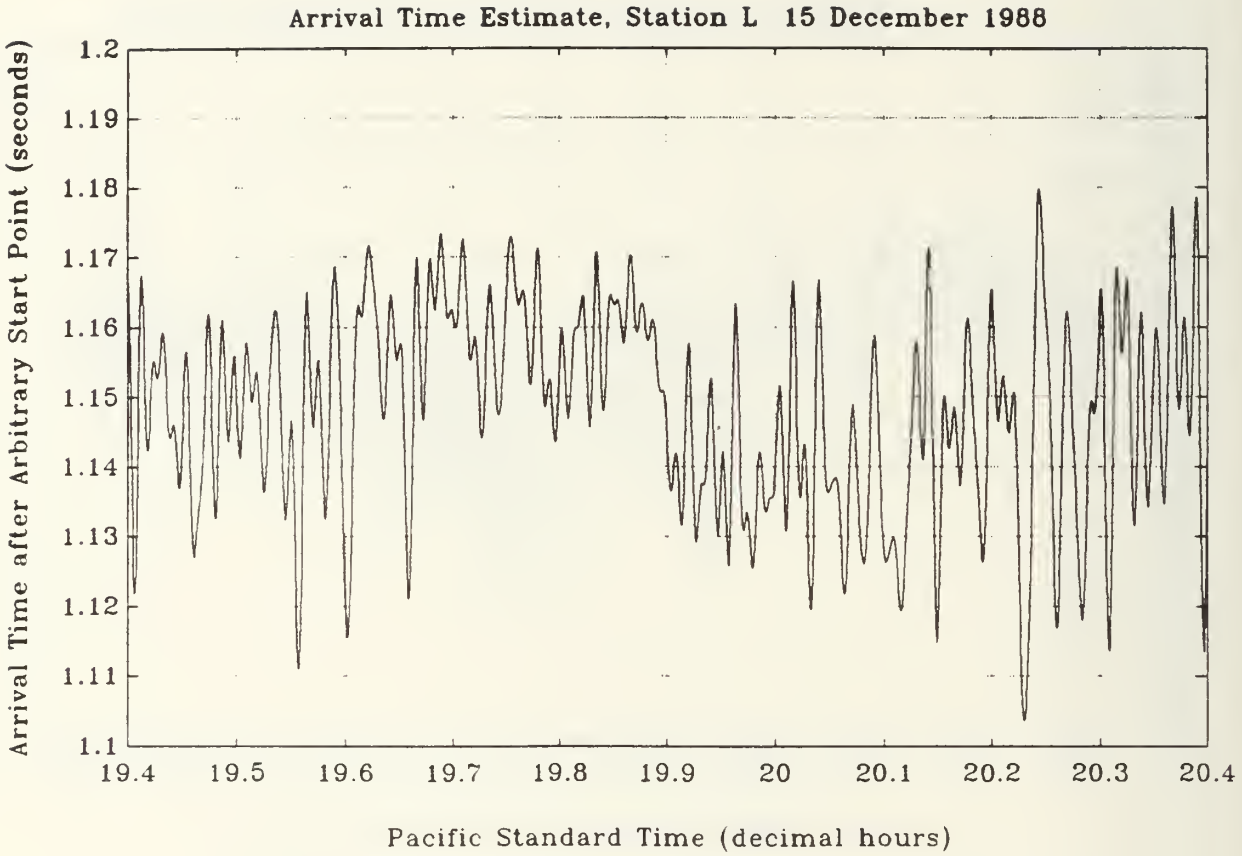

Figure 152: Arrival time estimate for Station L from 1924 to 2024 PST 15Dec88. The fast fluctuations in the arrival times are caused by surface waves changing the path length.

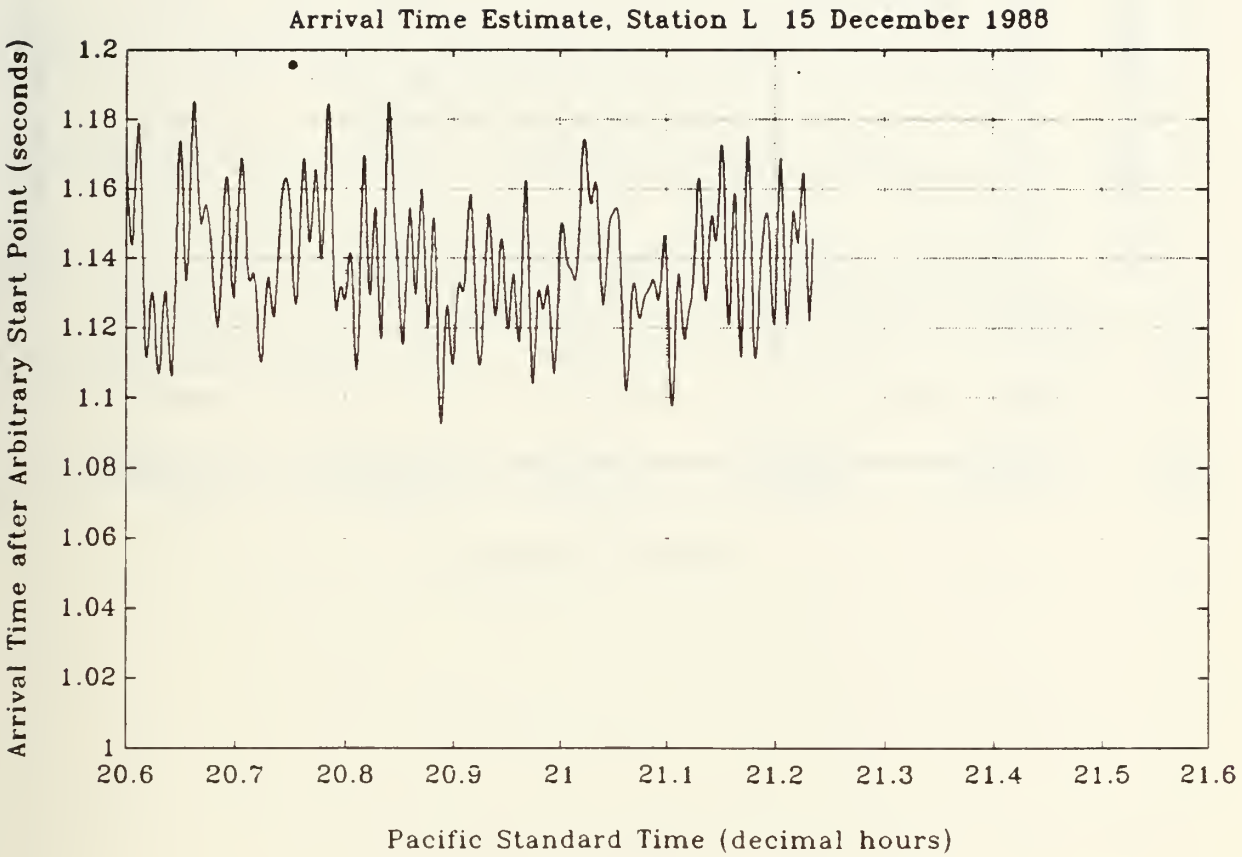

Figure 153: Arrival time estimate for Station L from 2036 to 2136 PST 15Dec88. The fast fluctuations in the arrival times are caused by surface waves changing the path length.

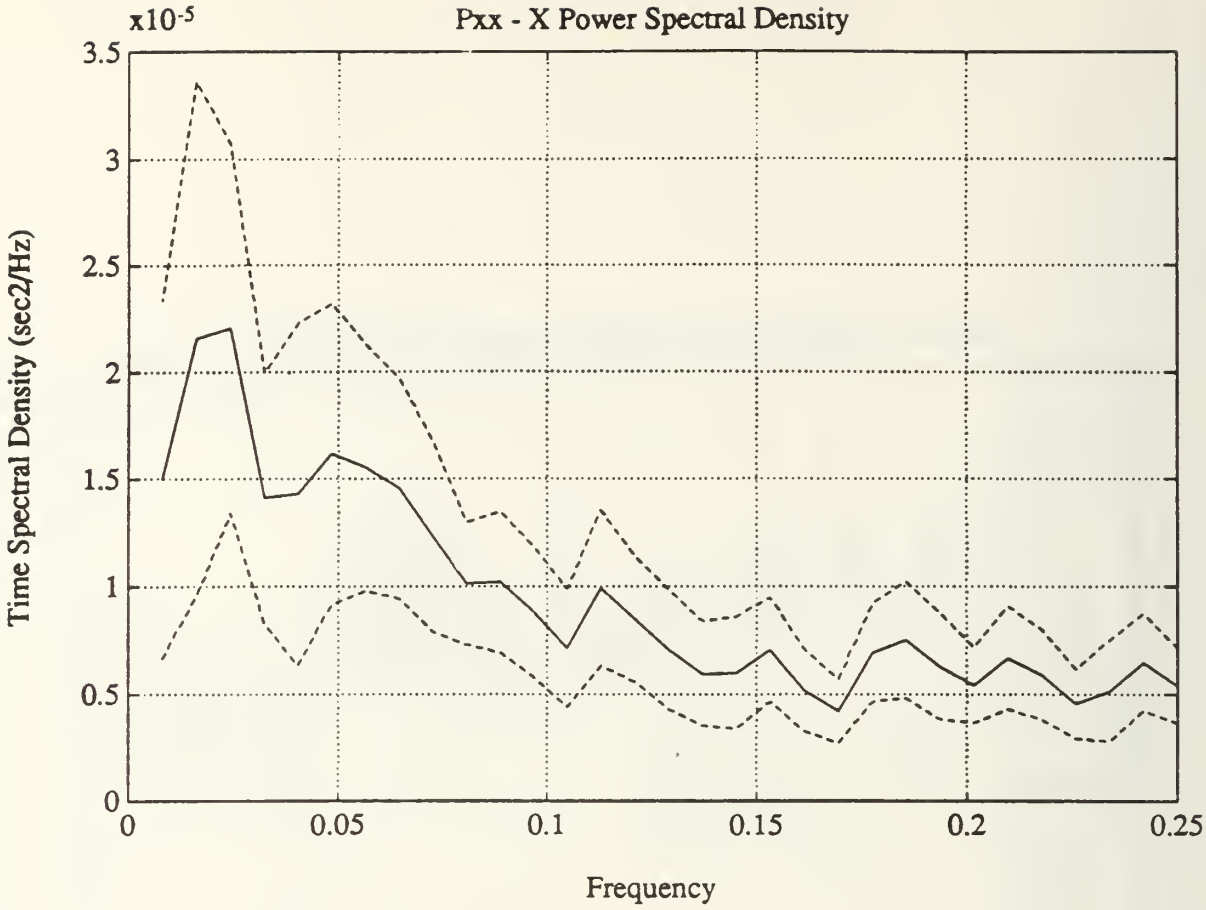

Figure 154: Arrival time power spectrum for Station L. Spectrum from 2.2 hours of arrival time series, 1100 to 1312 PST 13Dec88 including 95% confidence interval.

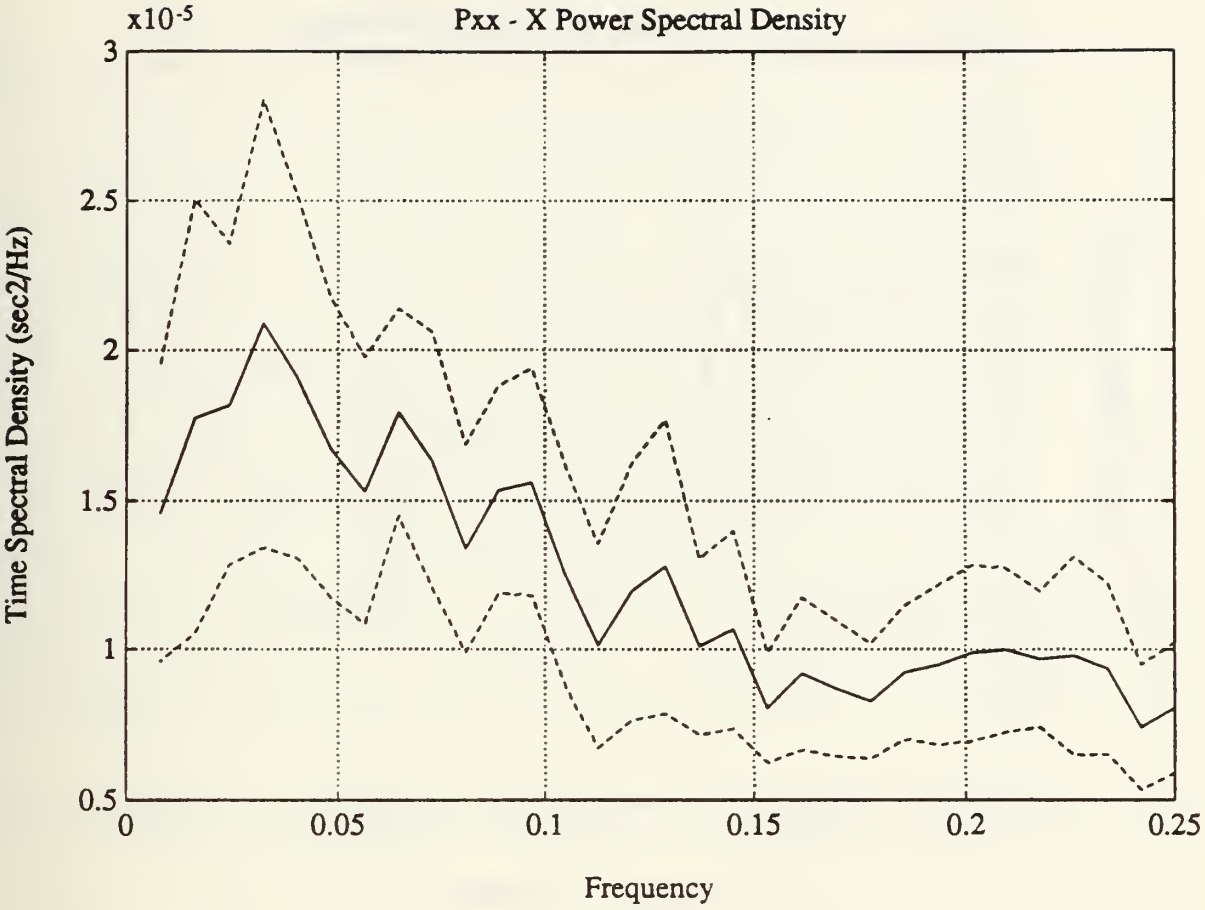

Figure 155: Arrival time power spectrum for Station L. Spectrum from 2.2 hours of arrival time series, 1312 to 1524 PST 13Dec88 including 95% confidence interval.

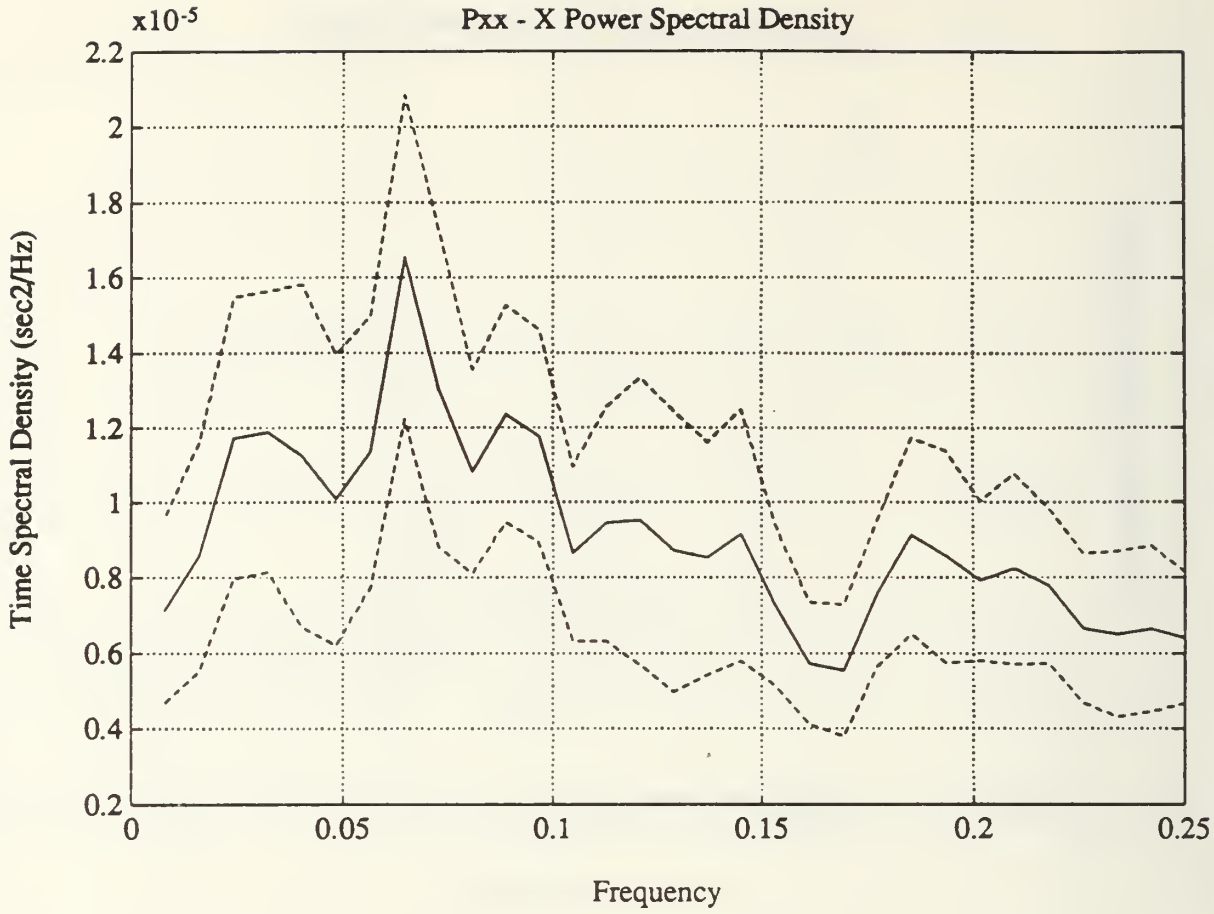

Figure 156: Arrival time power spectrum for Station L. Spectrum from 2.2 hours of arrival time series, 1524 to 1748 PST 13Dec88 including 95% confidence interval.

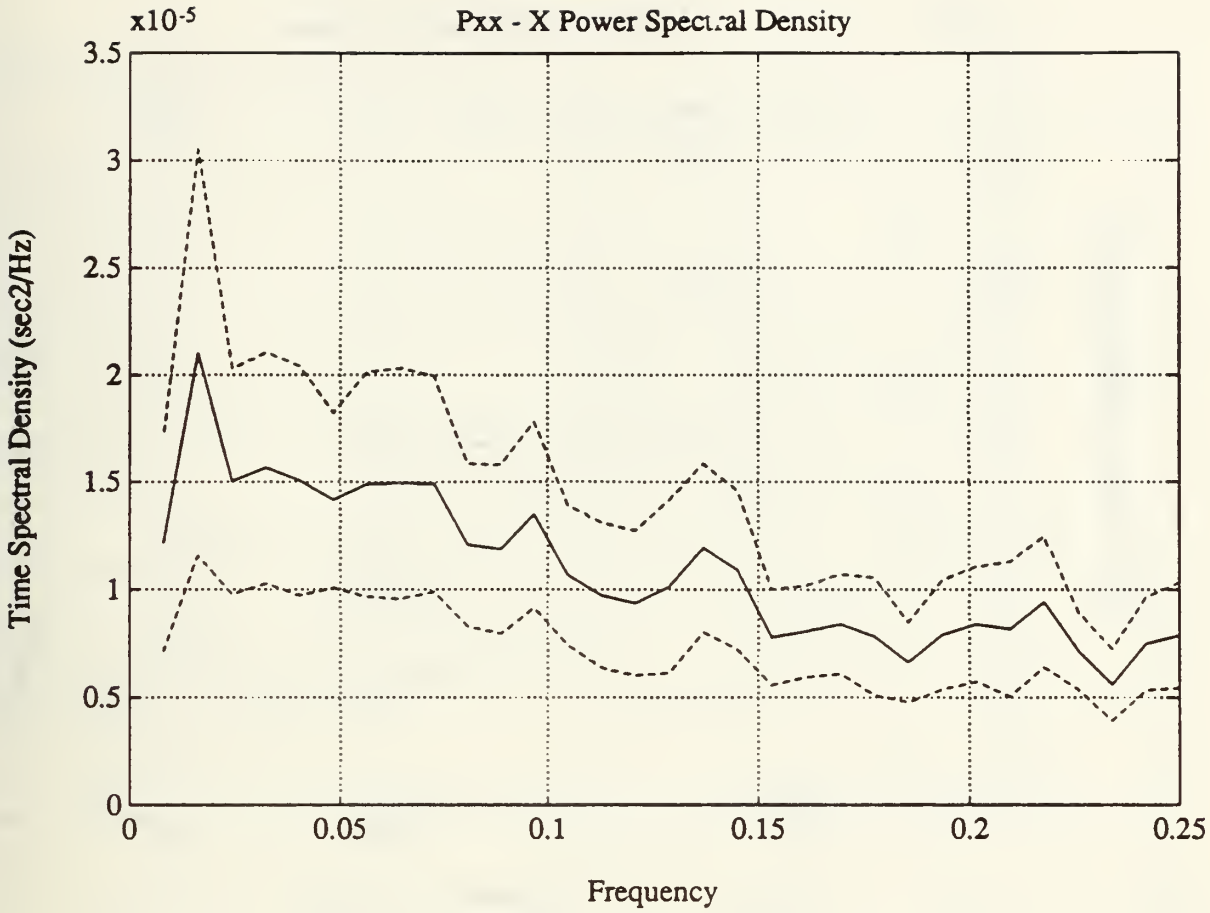

Figure 157: Arrival time power spectrum for Station L. Spectrum from 2.2 hours of arrival time series, 1748 to 2000 PST 13Dec88 including 95% confidence interval.

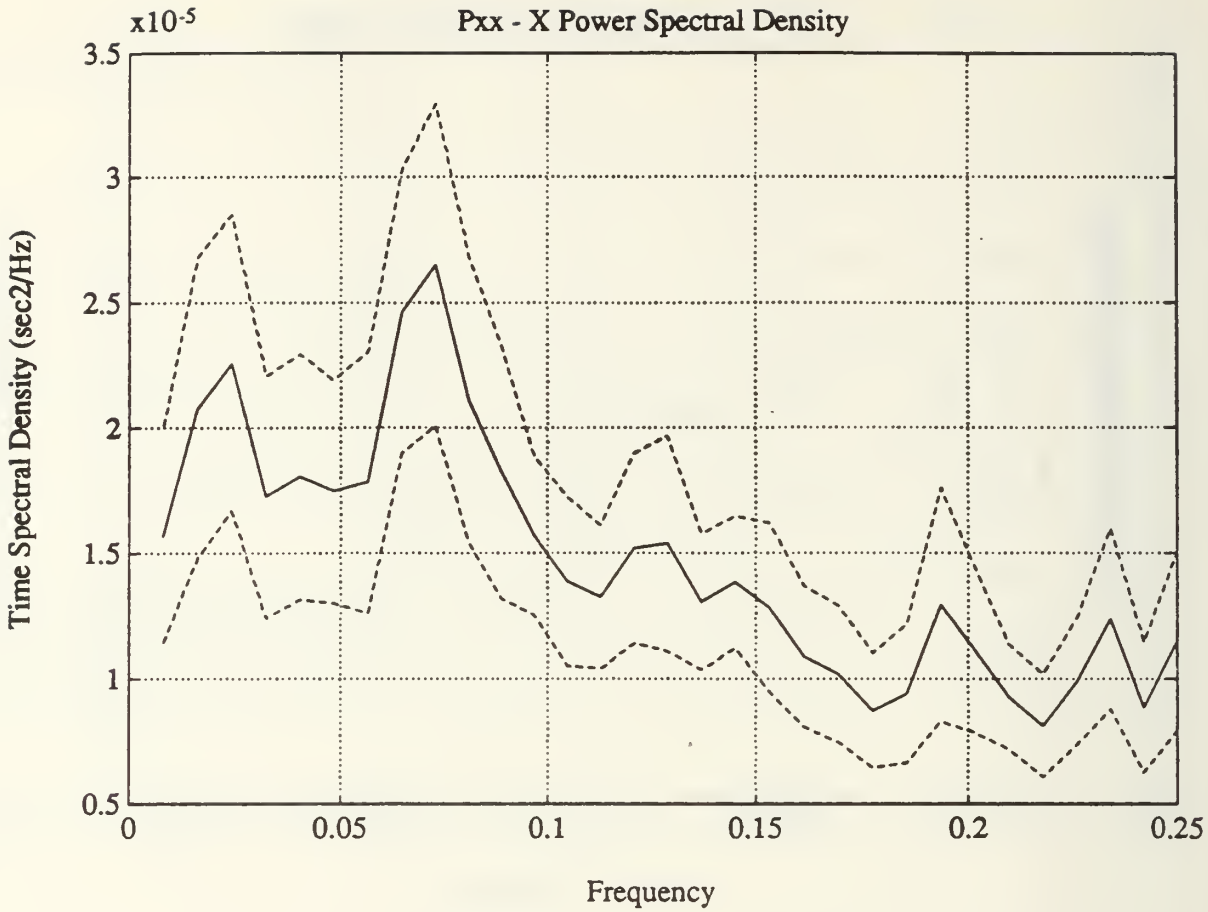

Figure 158: Arrival time power spectrum for Station L. Spectrum from 2.2 hours of arrival time series, 0024 to 0236 PST 14Dec88 including 95% confidence interval.

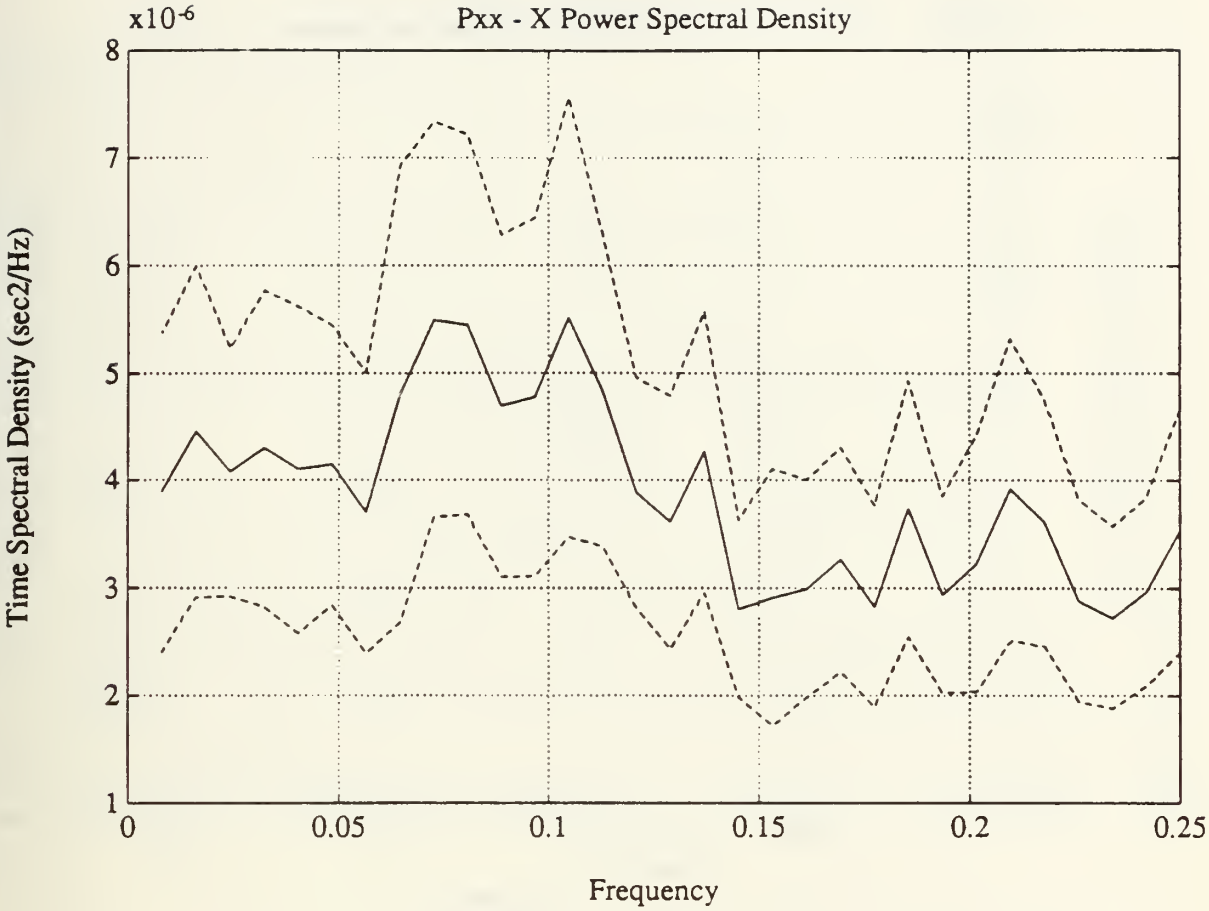

Figure 159: Arrival time power spectrum for Station L. Spectrum from 2.2 hours of arrival time series, 0236 to 0448 PST 14Dec88 including 95% confidence interval.

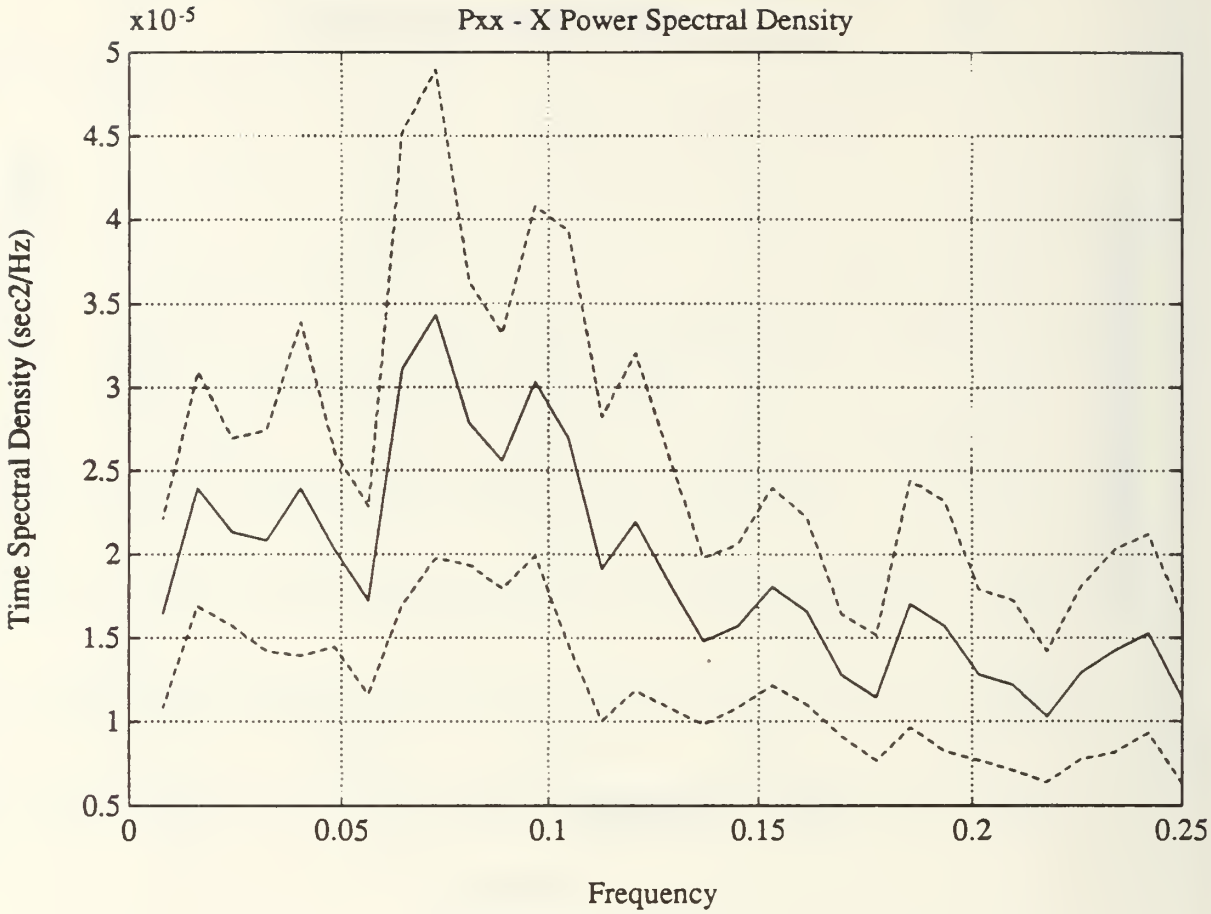

Figure 160: Arrival time power spectrum for Station L. Spectrum from 2.2 hours of arrival time series, 0412 to 0624 PST 14Dec88 including 95% confidence interval.

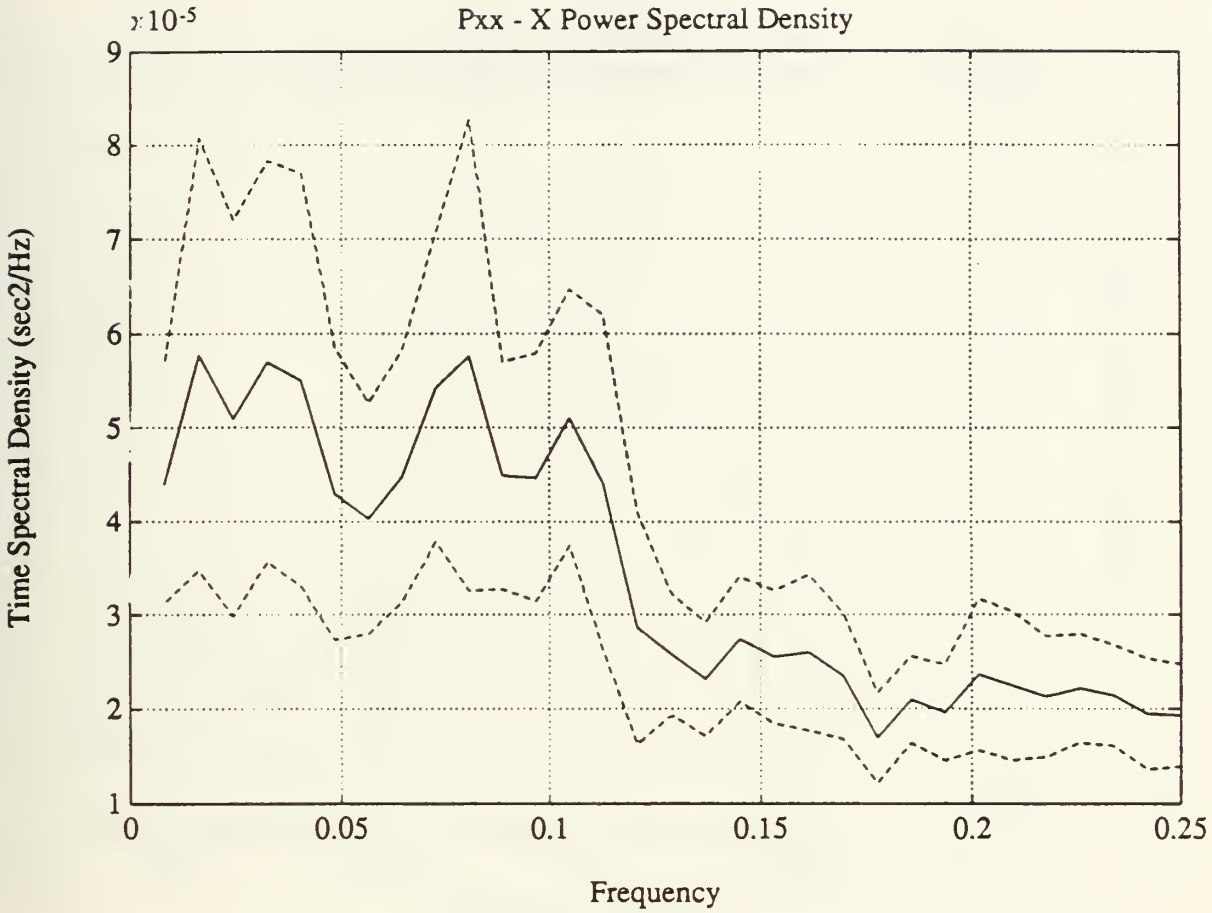

Figure 161: Arrival time power spectrum for Station L. Spectrum from 2.2 hours of arrival time series, 0624 to 0836 PST 14Dec88 including 95% confidence interval.

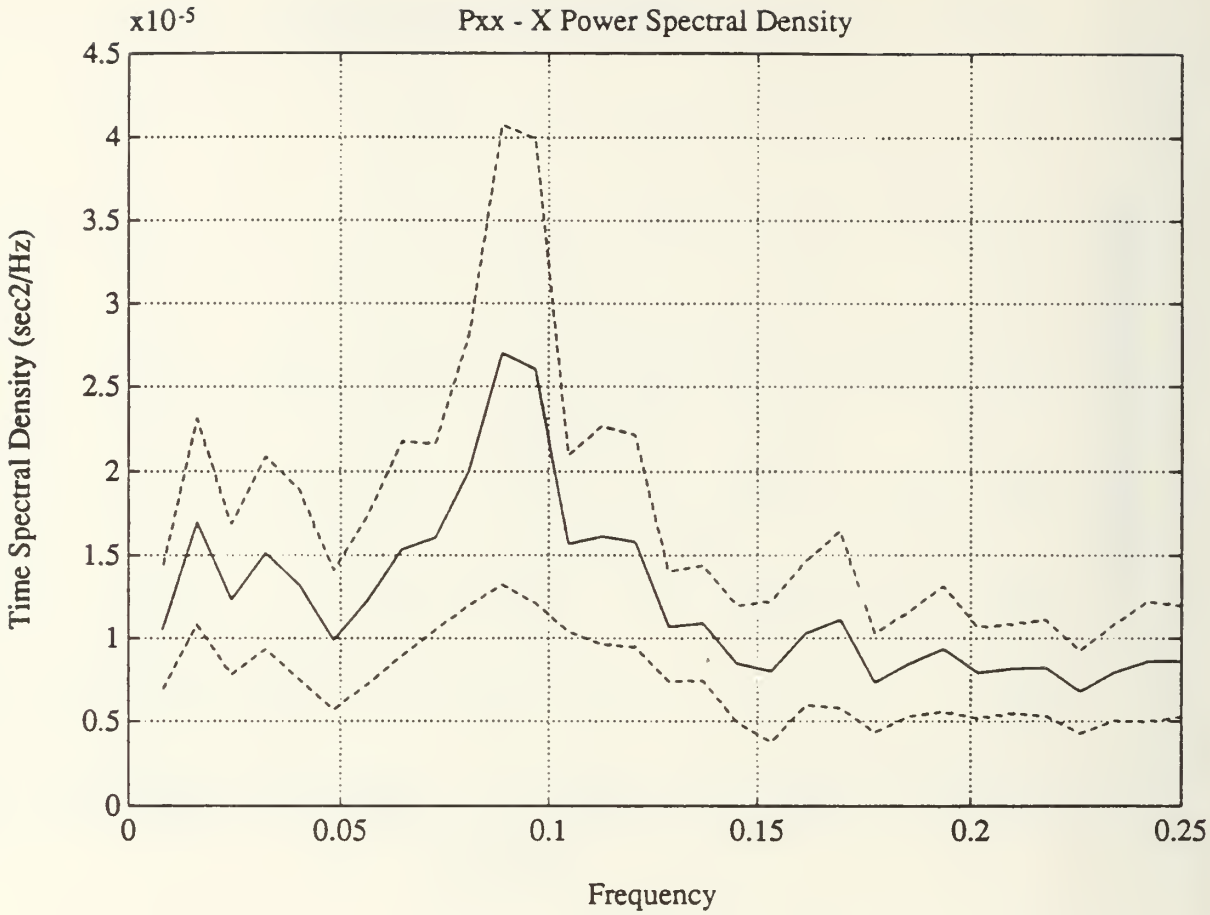

Figure 162: Arrival time power spectrum for Station L. Spectrum from 2.2 hours of arrival time series, 0836 to 1048 PST 14Dec88 including 95% confidence interval.

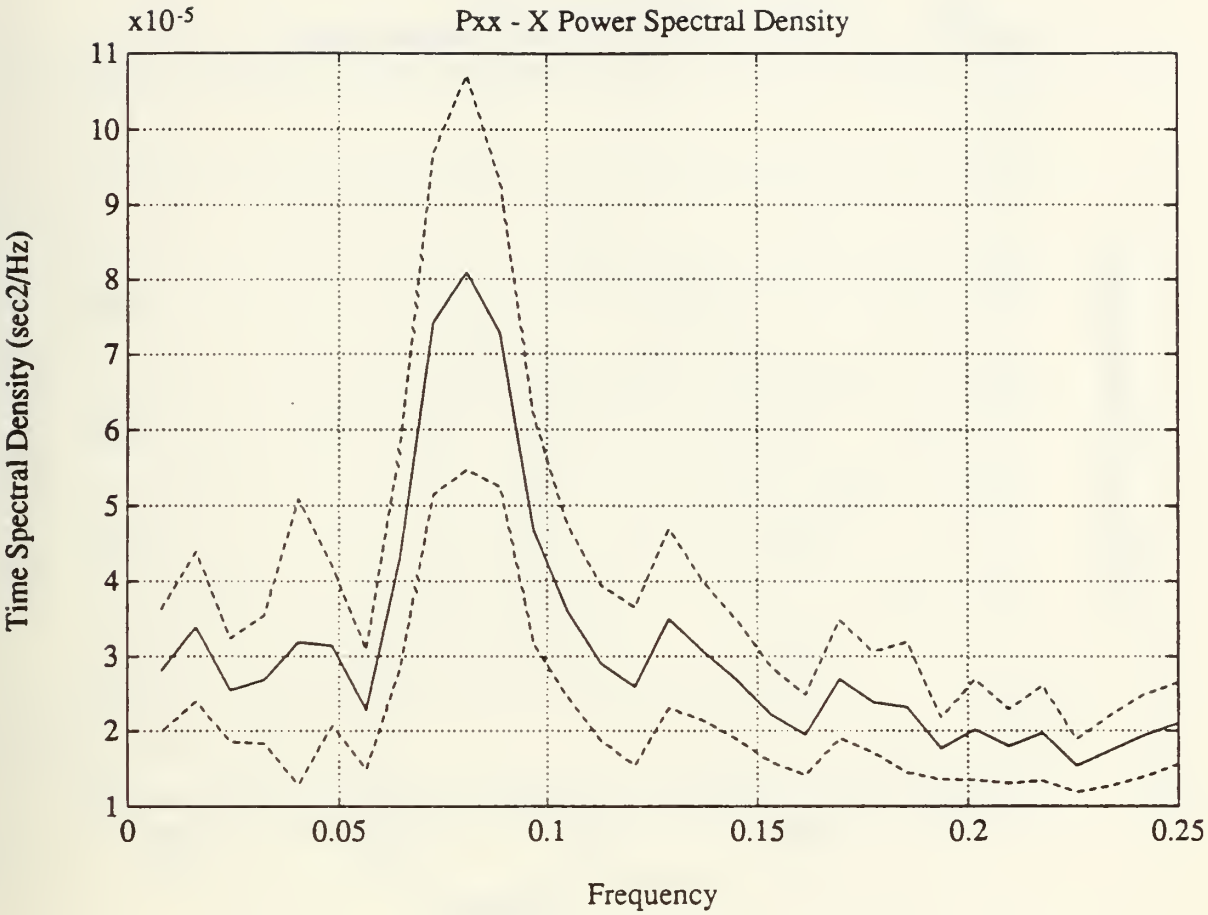

Figure 163: Arrival time power spectrum for Station L. Spectrum from 2.2 hours of arrival time series, 1048 to 1300 PST 14Dec88 including 95% confidence interval.

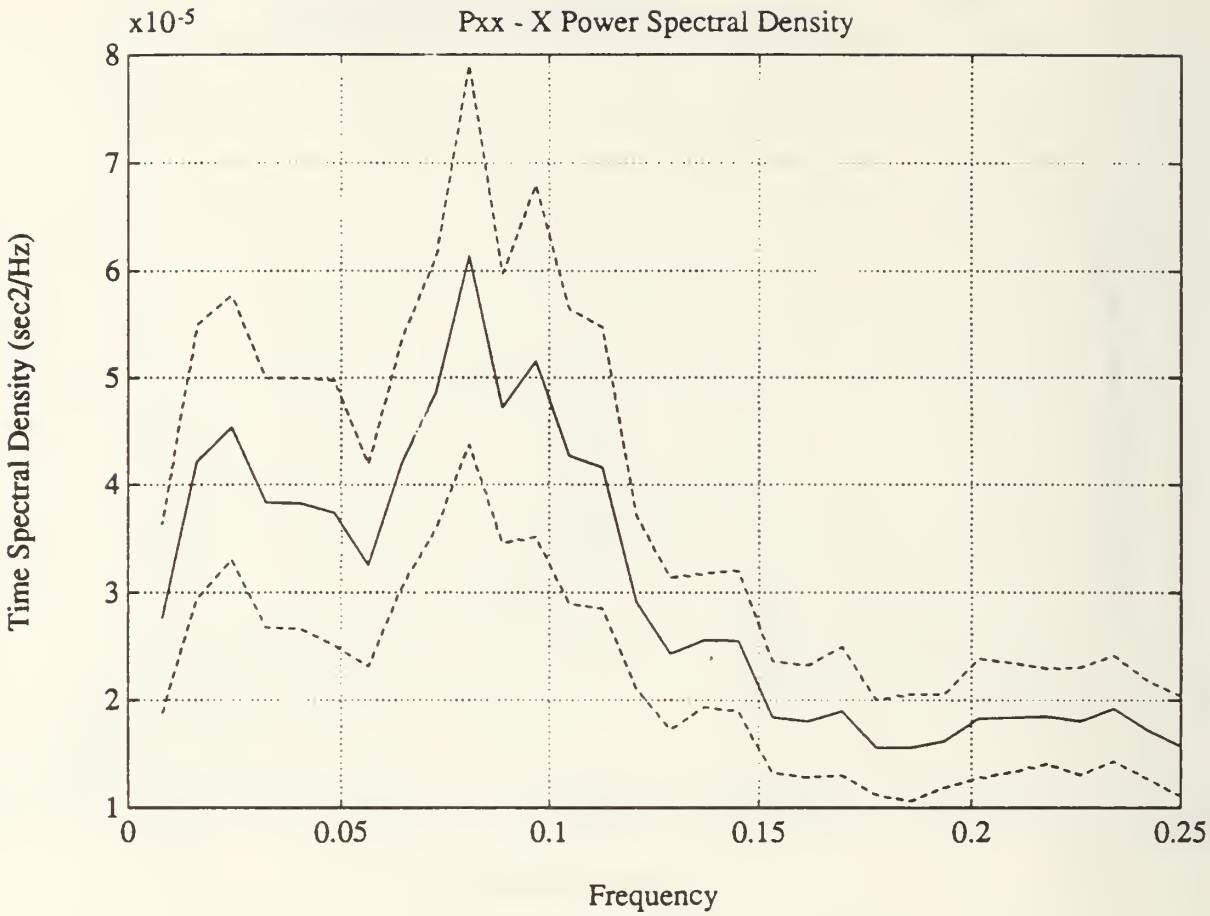

Figure 164: Arrival time power spectrum for Station L. Spectrum from 2.2 hours of arrival time series, 1300 to 1512 PST 14Dec88 including 95% confidence interval.

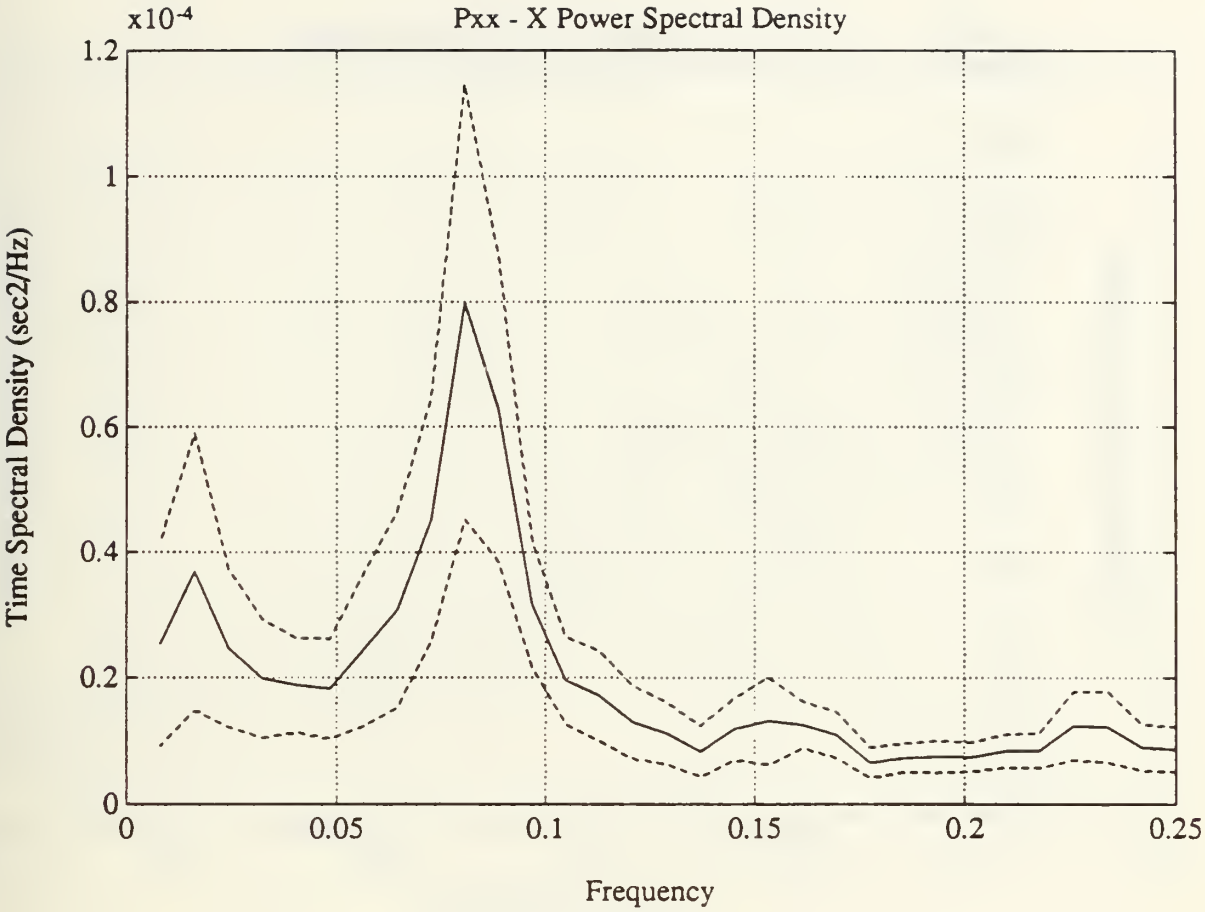

Figure 165: Arrival time power spectrum for Station L. Spectrum from 2.2 hours of arrival time series, 1512 to 1724 PST 14Dec88 including 95% confidence interval.

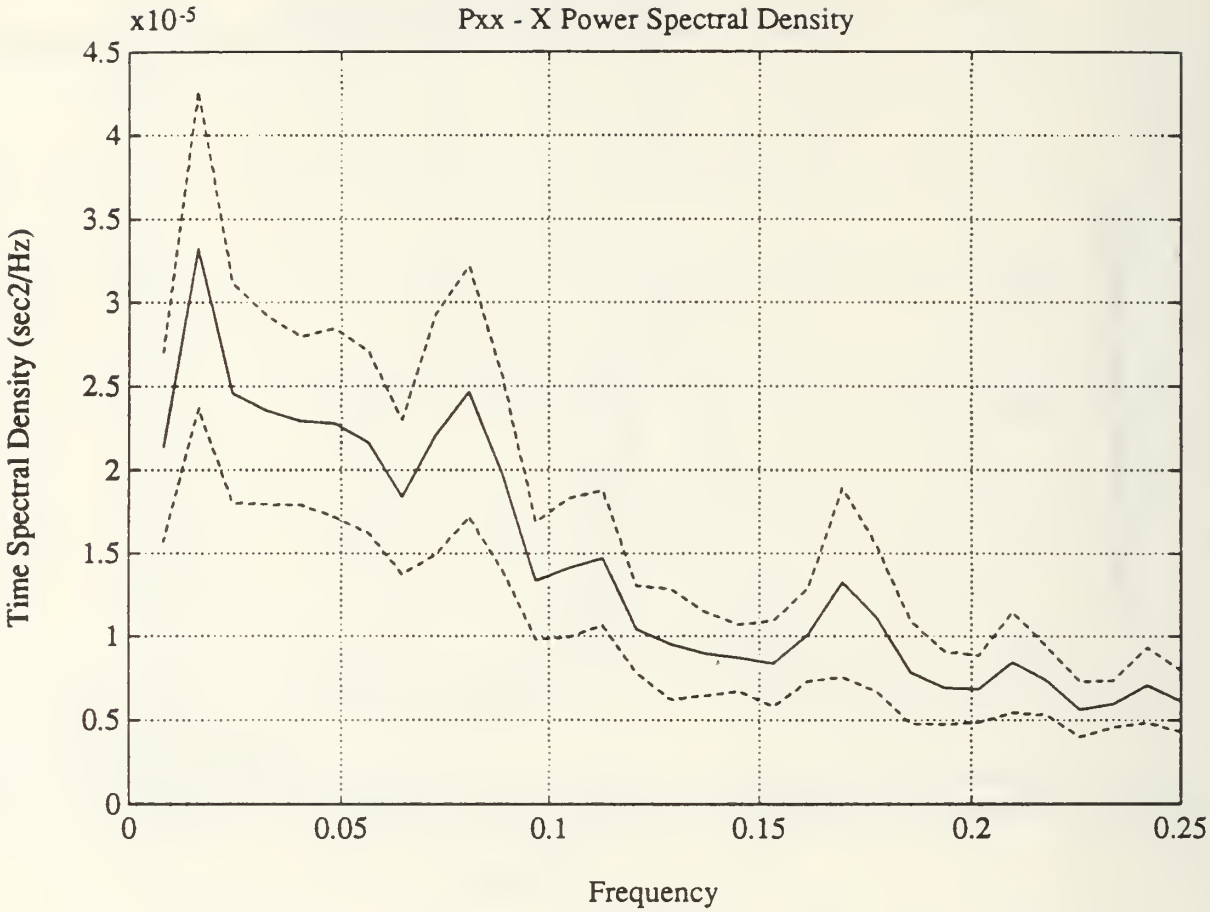

Figure 166: Arrival time power spectrum for Station L. Spectrum from 2.2 hours of arrival time series, 1724 to 1936 PST 14Dec88 including 95% confidence interval.

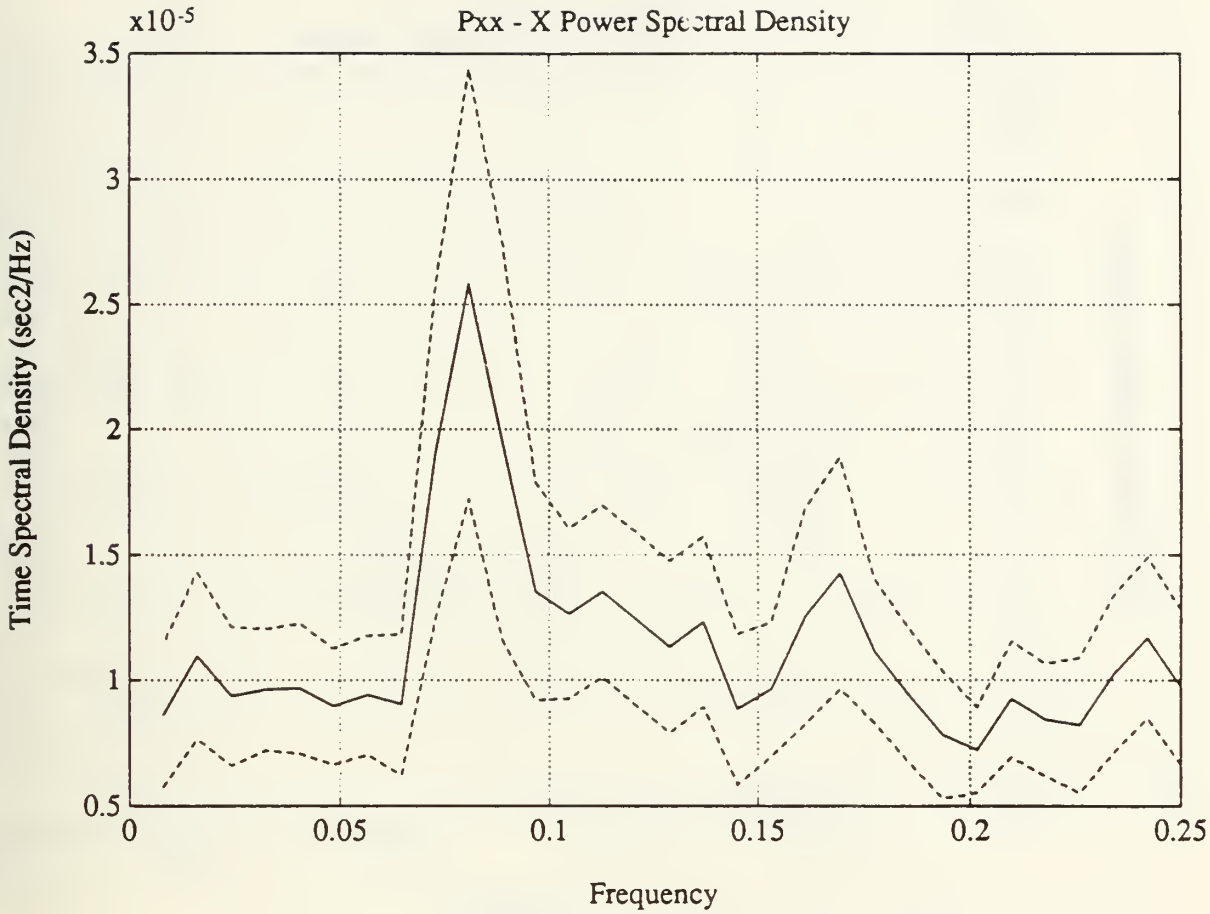

Figure 167: Arrival time power spectrum for Station L. Spectrum from 2.2 hours of arrival time series, 1936 to 2148 PST 14Dec88 including 95% confidence interval.

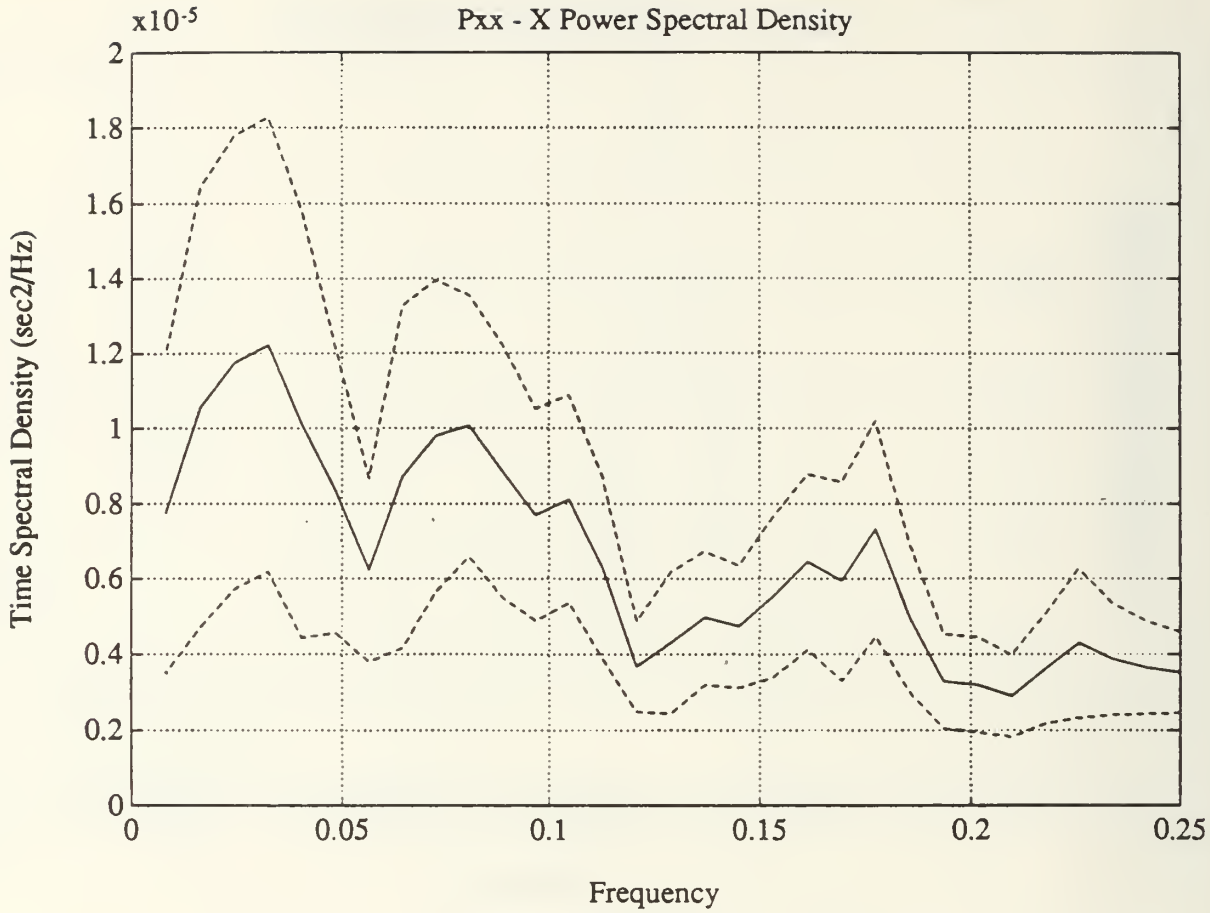

Figure 168: Arrival time power spectrum for Station L. Spectrum from 2.2 hours of arrival time series, 2148 to 2400 PST 14Dec88 including 95% confidence interval.

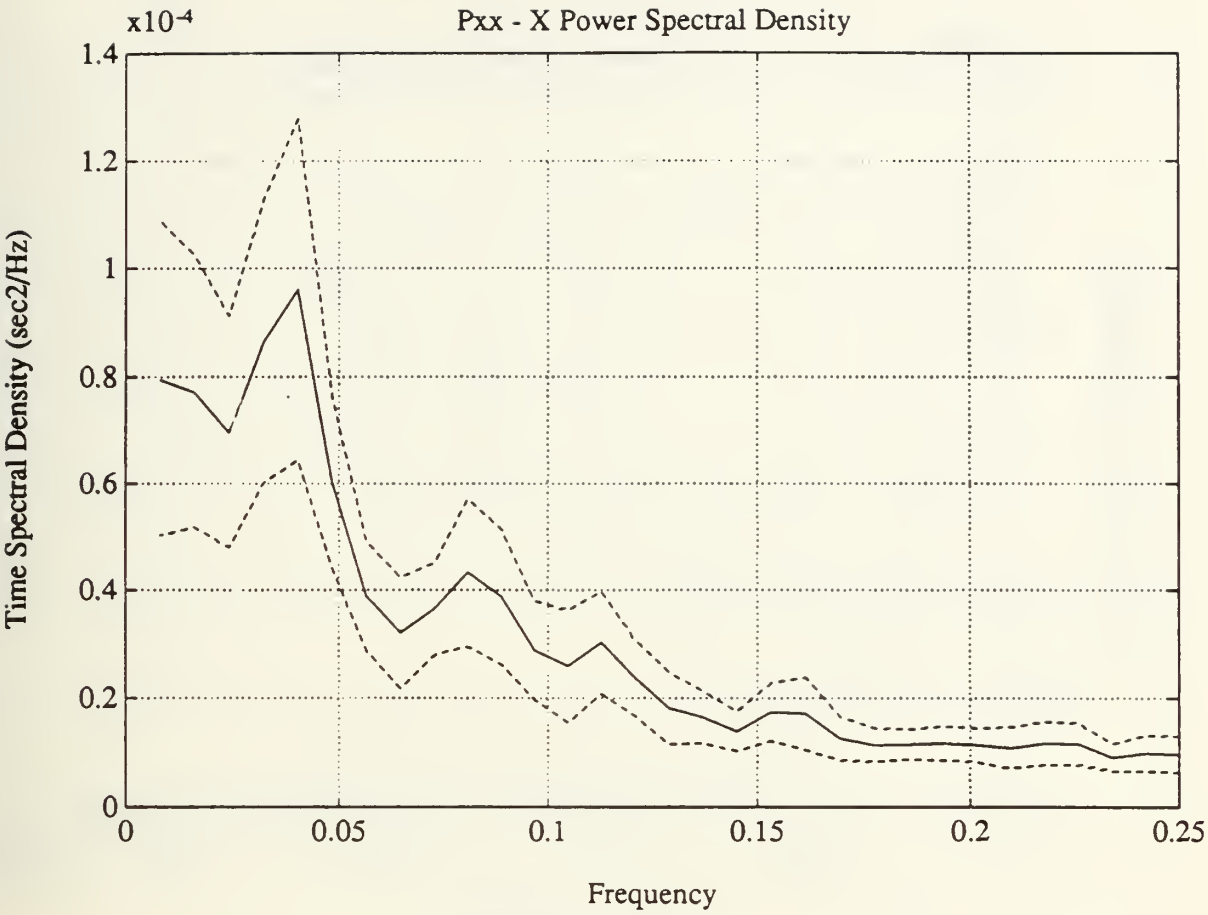

Figure 169: Arrival time power spectrum for Station L. Spectrum from 2.2 hours of arrival time series, 0212 to 0424 PST 15Dec88 including 95% confidence interval.

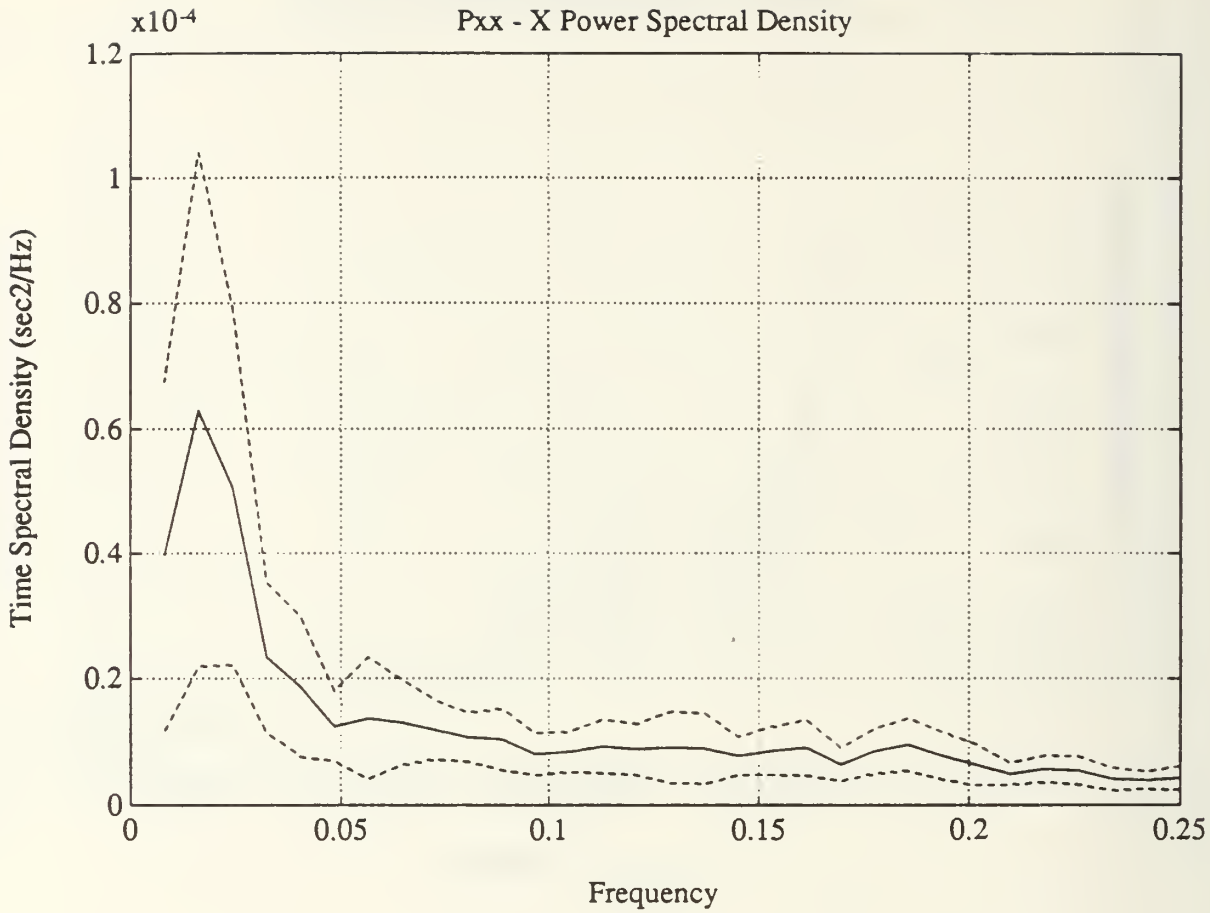

Figure 170: Arrival time power spectrum for Station L. Spectrum from 2.2 hours of arrival time series, 0424 to 0636 PST 15Dec88 including 95% confidence interval.

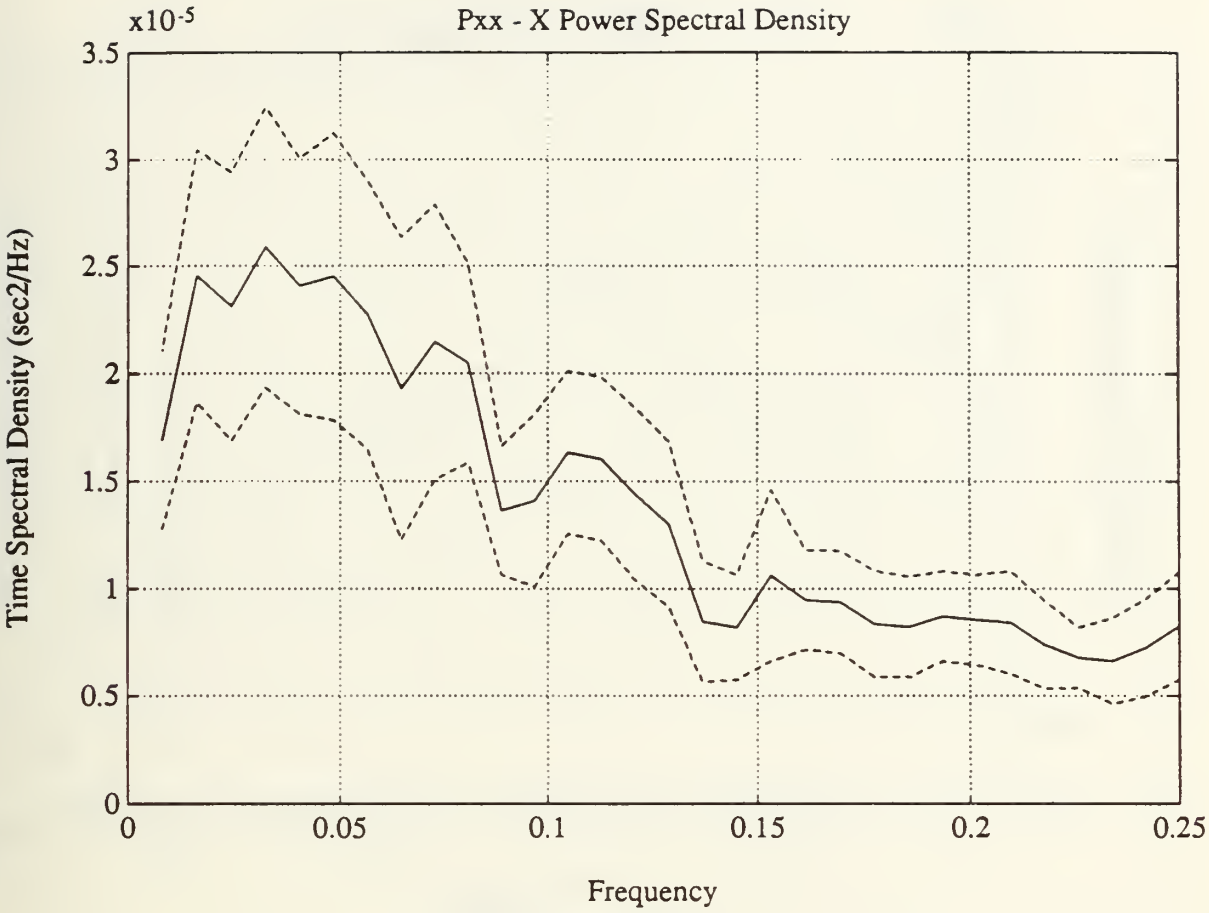

Figure 171: Arrival time power spectrum for Station L. Spectrum from 2.2 hours of arrival time series, 0848 to 1100 PST 15Dec88 including 95% confidence interval.

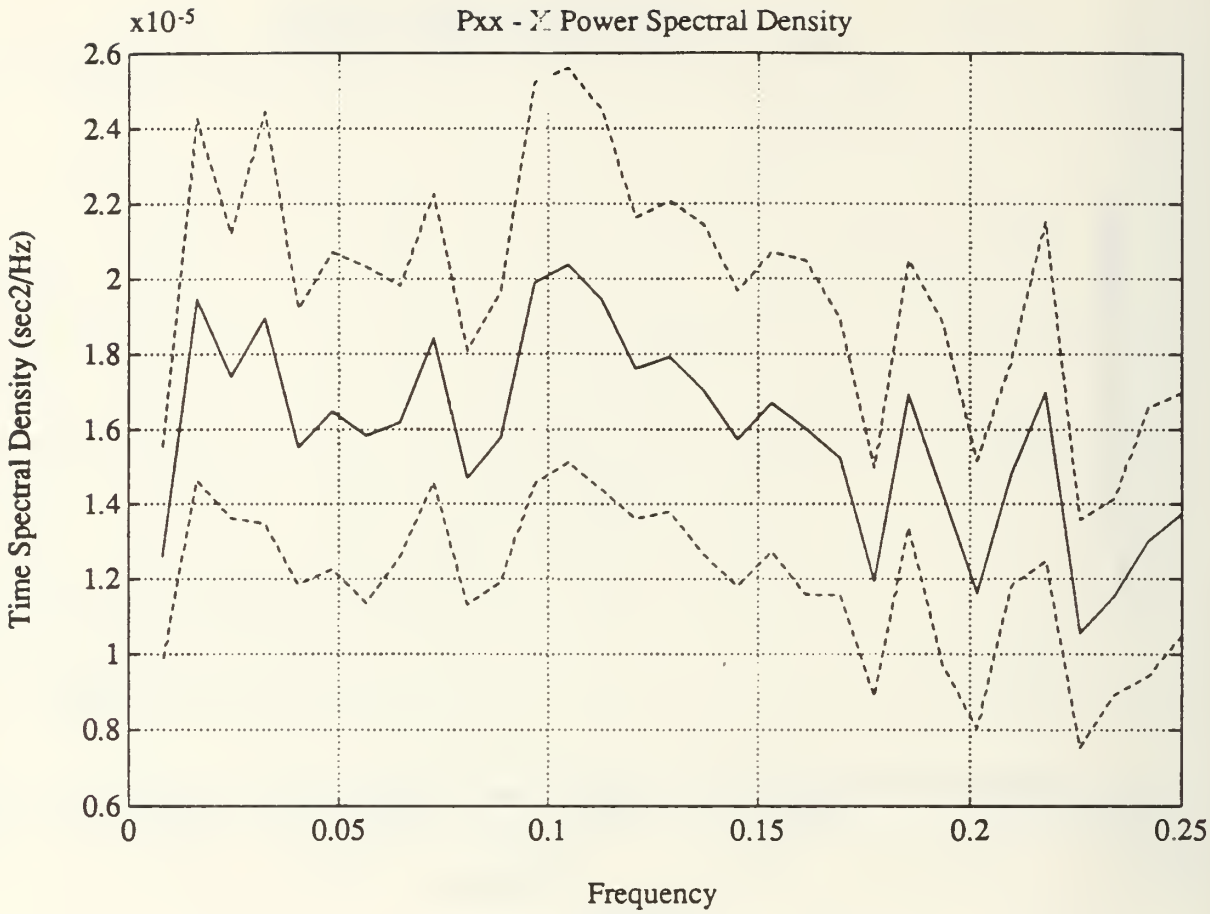

Figure 172: Arrival time power spectrum for Station L. Spectrum from 2.2 hours of arrival time series, 1124 to 1312 PST 15Dec88 including 95% confidence interval.

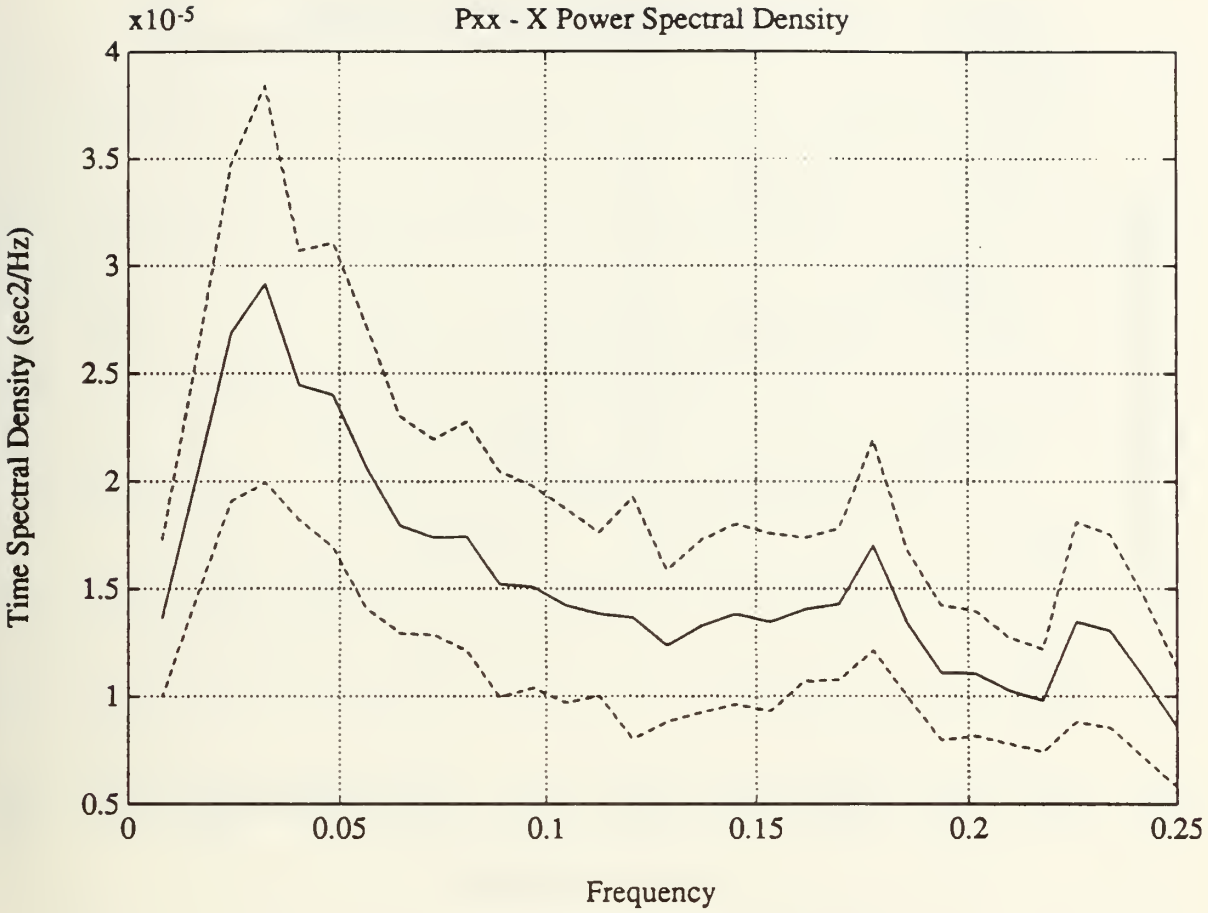

Figure 173: Arrival time power spectrum for Station L. Spectrum from 2.2 hours of arrival time series, 1312 to 1524 PST 15Dec88 including 95% confidence interval.

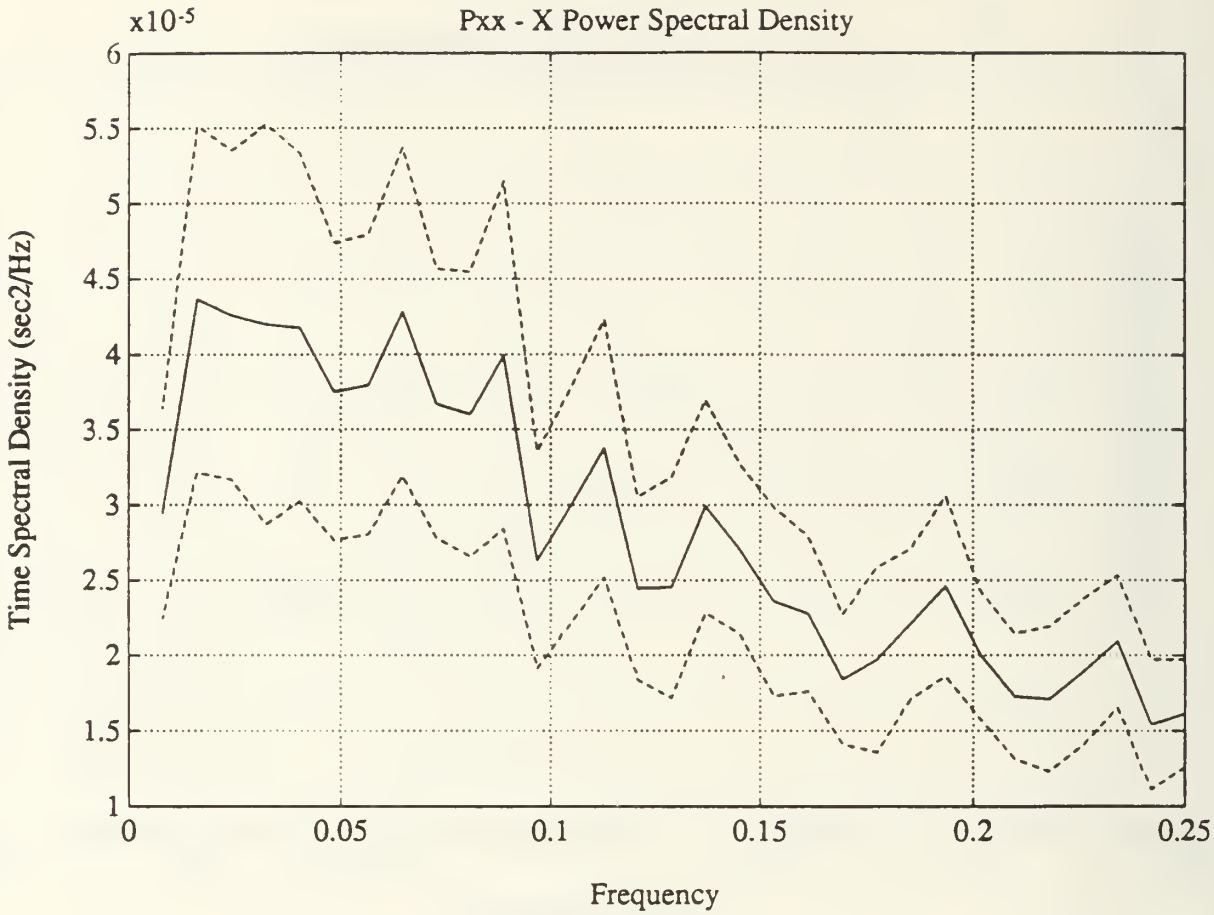

Figure 174: **Arrival time power spectrum for Station L. Spectrum from 2.2 hours of arrival time series, 1524 to 1736 PST 15Dec88 including 95% confidence interval.**

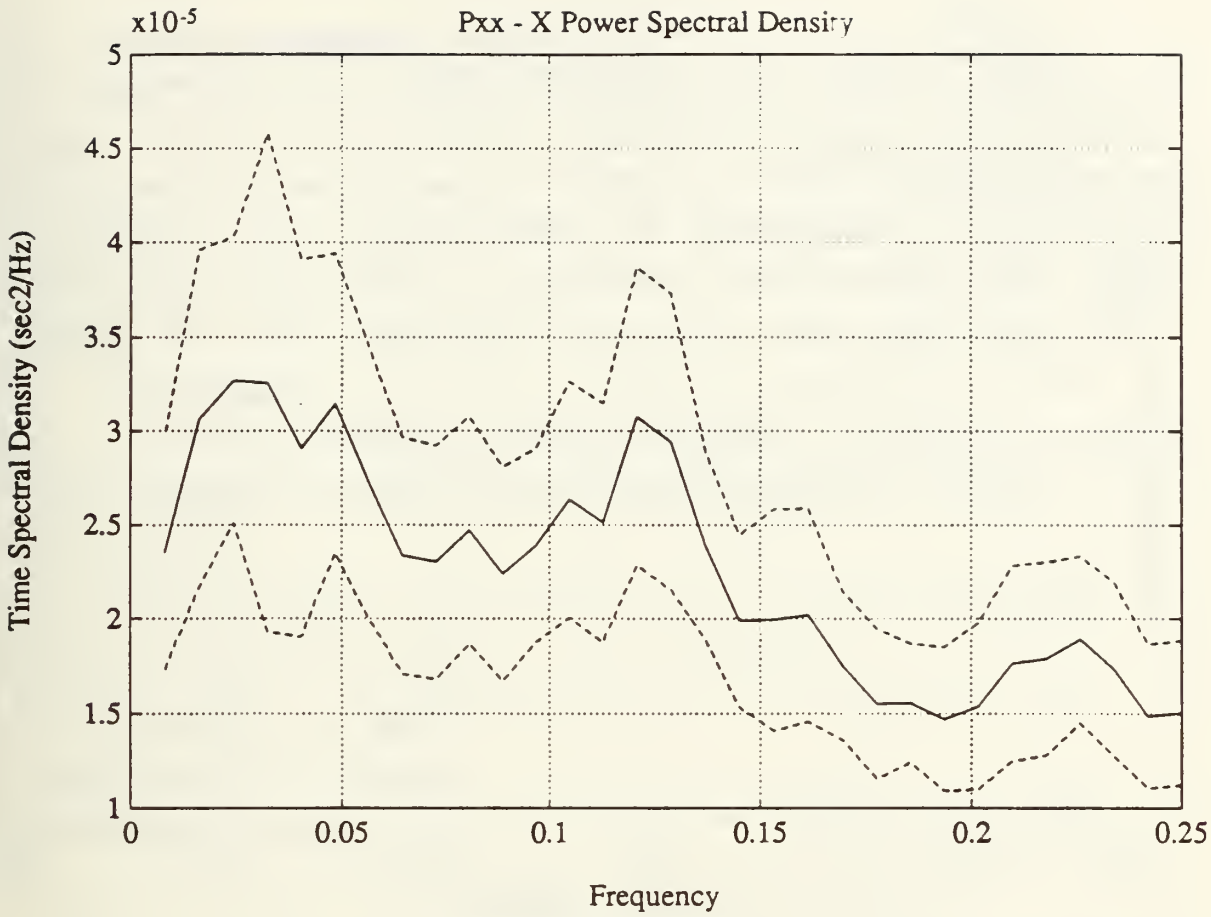

Figure 175: Arrival time power spectrum for Station L. Spectrum from 2.2 hours of arrival time series, 1736 to 1948 PST 15Dec88 including 95% confidence interval.

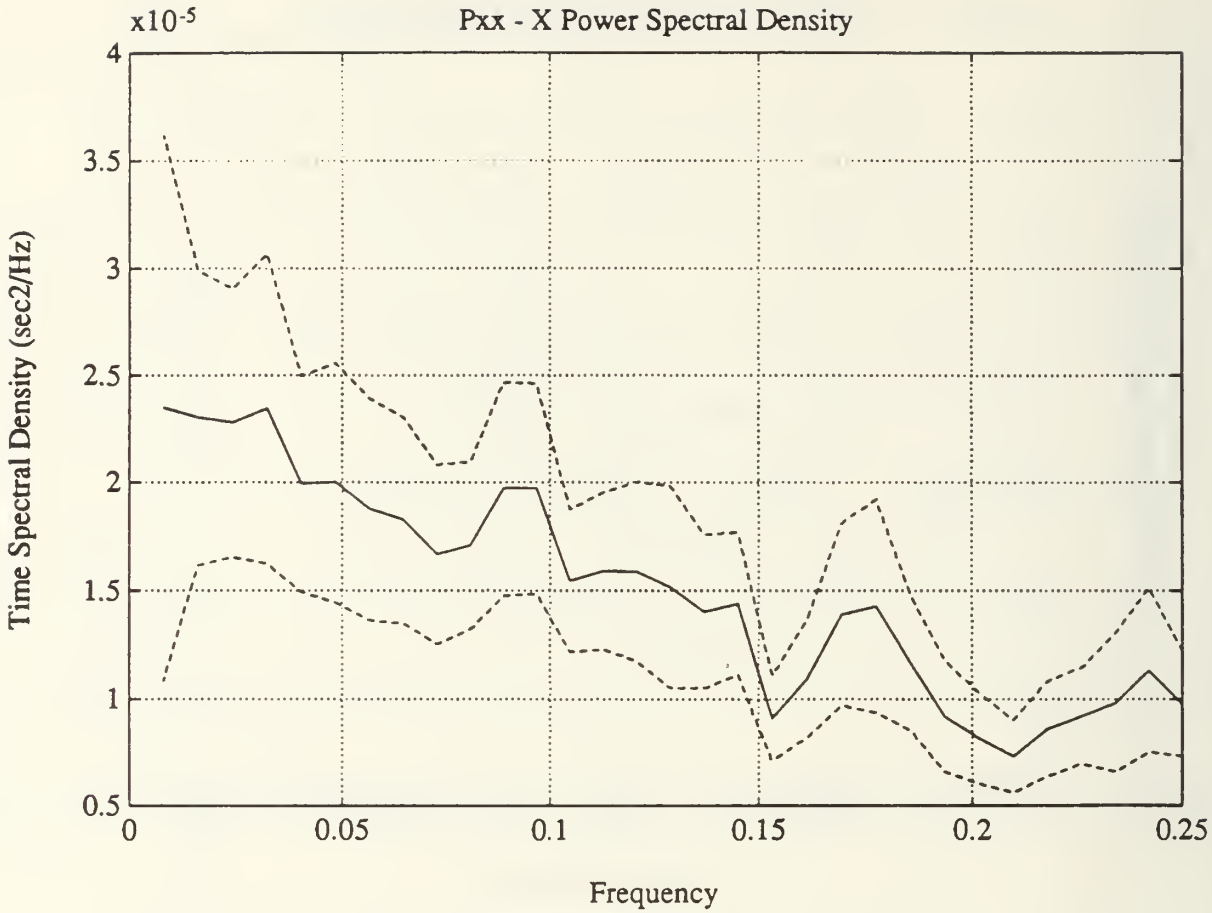

Figure 176: Arrival time power spectrum for Station L. Spectrum from 2.2 hours of arrival time series, 1948 to 2200 PST 15Dec88 including 95% confidence interval.

C. MATLAB PROGRAMS

The included MATLAB programs were used to process the data to the various forms presented throughout this thesis. They are included to make it easier for those processing other Stations from the Monterey Bay Experiment to be able to duplicate this output if required The programs will rum on either the IBM or Macintosh with only minor modifications.

1. Arrest1

This IBM MATLAB program displays one hour of arrival time estimates using the raw data produced by AGRAF1.

```
load a41604
time=a41604(:,1);
peak=a41604(:,2);
clear a41604
[b,a]=cheby(8,.5,.1);
fpeak=filter(b,a,peak);
plot(time,fpeak)
title('Arrival Time Estimate, Station L  14 December 1988')
xlabel('Pacific Standard Time (decimal hours)')
ylabel('Arrival Time after Arbitrary Start Point (seconds)')
grid
```

2. Varloop2

This Macintosh MATLAB program loads varying hours worth of data from AGRAF1 generating variables of required lengths to be further processed by the MATLAB programs Perturb and Pwrspec1.

```
clear
load a40401.mat
time=a40401(:,1);
peak=a40401(:,2);
time1=[time1;time];
peak1=[peak1;peak];
clear a40401
```

```
load a40402.mat
time=a40402(:,1);
peak=a40402(:,2);
time1=[time1;time];
peak1=[peak1;peak];
clear a40402
pack
```

3. Perturb

This Macintosh MATLAB program produces Arrival Time Perturbations from the Varloop2 output.

```
clg
[b,a]=cheby1(8,.5,.01);
dpeak=detrend(peak1);
fpeak=filter(b,a,dpeak);
clear dpeak
plot(time1,fpeak)
title('Arrival Time Perturbation, Station L  15 December 1988')
xlabel('Pacific Standard Time (hours)')
ylabel('Arrival Perturbation (seconds)')
grid
```

4. Pwrspec1

This Macintosh MATLAB program produces power spectral densities over a 2.2 hour period from the output of Varloop2.

```
clg
format long e
dpeak=detrend(peak1);
p=spectrum(dpeak,64);
specplot(p,.51613);
ylabel('Time Spectral Density (sec^2/Hz)')
grid
```

LIST OF REFERENCES

1. Clay, C. S. and Medwin, H., Acoustical Oceanography: Principles and Applications, p. 2, John Wiley & Sons, 1977.

2. Munk, W. and Wunsch, C., "Ocean Acoustic Tomography: A Scheme for Large Scale Monitoring", Deep-Sea Research, v. 26A, pp. 123-161, 1979.

3. Behringer, D., and others, "A demonstration of ocean acoustic tomography," Nature, v. 299(5879), pp. 121-125, 9 September 1982.

4. Spiesberger, J. L., and Worcester, P. F., "Perturbations in travel time and ray geometry due to mesoscale disturbances: A comparison of exact and approximate calculations," The Journal of the Acoustical Society of America, v. 74(1), pp. 219-225, July 1983.

5. Munk, W., and Wunsch, C., "Ocean acoustic tomography: a scheme for large scale monitoring," Deep-Sea Research, v. 26A, pp. 123-161, 1979.

6. Spindel, R. C., "Signal processing in ocean tomography", Adaptive Methods in Underwater Acoustics, pp. 687-710, 1985.

7. Rowan, T. M., Monterey Bay Acoustic Tomography: Ray Tracing and Environmental Assessment, Master's Thesis, Naval Postgraduate School, Monterey, California, September 1988.

8. Spindel, R. C., "Ocean Acoustic Tomography: a Review," Current Practices and New Technology in Ocean Engineering, v. 11, pp. 7-13, 1986.

9. DeFrance, J. J., Communications Electronics Circuits, 2d ed., pp. 188-196, Rinehart Press, 1972.

10. Miller, J. H., "Cruise Plan; Monterey Bay Acoustic Tomography Experiment 12-16 December 1988," distributed to participants at the Naval Postgraduate School, Monterey, California, 11 December 1988.

11. Ziomek, L. J., UNDERWATER ACOUSTICS, A Linear Systems Theory Approach, pp. 176-193, Academic Press, Inc., 1985.

12. National Semiconductor Corporation, Linear Databook 3, pp. 9-42 - 9-46, 1988.

13. Maxim Integrated Products Corporation, Maxim 1989 Integrated Circuits Data Book, pp. 9-1 - 9-16, 1989.

14. Texas Instruments Incorporated, The TTL Data Book, v. 2, pp. 3-471 - 3-476, 1985.

15. National Semiconductor Corporation, LS/S/TTL Logic Databook, pp. 2-141 - 2-143, 1987.

16. Signetics Corporation, Fast Data Manual, 1988.

17. Signetics Corporation, Linear LSI Data and Applications Manual, pp. 9-57 - 9-73, 1985.

18. RCA Corporation, Integrated Circuits for Linear Applications Databook, pp. 836-841, 1986.

19. RCA Corporation, Integrated Circuits for Linear Applications Databook, pp. 225-232, 1986.

20. Johnson, David E., Introduction to Filter Theory, pp. 41-47, Prentice-Hall, Inc., 1976.

21. Hilburn, J. L., and Johnson, D. E., Manual of Active Filter Design, 2d ed., McGraw-Hill Company, 1983.

22. National Semiconductor Corporation, Hybrid Products Catalog, 1988.

23. Lancaster, D., Active Filter Cookbook, pp. 156-168, Howard W. Sams & Co., Inc., 1975.

24. Analog Devices Inc. Integrated Circuits, 1984.

25. Dees, Robert C., Monterey Bay Acoustic Tomography: ,MS Thesis, Naval Postgraduate School, Monterey, CA, June 1989.

26. Cooley Electronics Laboratory Report 216, Modulation by Linear-Maximal Shift Register Sequences: Amplitude, Biphase and Complement-Phase Modulation, by Theodore G. Birdsall, Richard M. Heitmeyer, and Kurt Metzger, December 1971.

27. Cooley Electronics Laboratory Report 165, Study of Linear Sequence Generators, by C. C. Hoopes and R. Randall, June 1966.

28. Haykin, S., Communications Systems, 2d ed., pp. 179-218, John Wiley & Sons Inc., 1983.

INITIAL DISTRIBUTION LIST

		No. Copies
1.	Defense Technical Information Center Cameron Station Alexandria, Virginia 22304-6145	2
2.	Library, Code 0142 Naval Postgraduate School Monterey, California 93943-5002	2
3.	Prof. James H. Miller, Code 62Mr Department of Electrical and Computer Engineering Naval Postgraduate School Monterey, California 93943	7
4.	Prof. Ching-Sang Chiu, Code 68Ci Department of Oceanography Naval Postgraduate School Monterey, California 93943	1
5.	Dr. James F. Lynch Department of Applied Ocean Physics and Engineering Woods Hole Oceanographic Institution Woods Hole, Maine 02543	1
6.	LT Kevin P. Schaaff, USN 11507 Lovejoy Street Silver Spring, Maryland 20902	2

7. Floyd L. York, Code 68Yk 1
Department of Oceanography
Naval Postgraduate School
Monterey, California 93943

8. Sönke Paulsen, Code 62Pa 1
Department of Electrical and Computer Engineering
Naval Postgraduate School
Monterey, California 93943

9. Thomas L. Walton 1
The MITRE Corporation/MITRE C^3I Division
7525 Colshire Drive
McLean, Virginia 22102-3481

10. Dr. Garry M. Jacyna 1
The MITRE Corporation/MITRE C^3I Division
7525 Colshire Drive
McLean, Virginia 22102-3481

11. CDR Phillip D. Voss 1
Commanding Officer, VS-27
NAS Cecil Field, Florida

12. LT Robert C. Dees, USN 1
207 Lauber Lane
Derby, Kansas 67037

13. Dr. R. K. R. Cook 1
Strong Hall, Room 108
University of Kansas
Lawrence, Kansas 66045

14. Dr. Kurt Metzger, Jr. 1
Communications and Signal Processing Laboratory
Department of Electrical Engineering and Computer Science
University of Michigan
Ann Arbor, Michigan 48109

15. Dr. Marshall Orr 1
Office of Naval Research, Code 11250A
800 North Quincy Street
Arlington, Virginia 22217-5000

16. Dr. Robert C. Spindel 1
Director, Applied Physics Laboratory
University of Washington
1013 Northeast 40th Street
Seattle, Washington 98105

17. Mrs. Theresa Rowan, Code 742 1
Naval Training Systems Center
12350 Research Parkway
Orlando, Florida 32826

18. Dr. Warren Denner 1
SAIC
205 Montecito Avenue
Monterey, California 93940

19. Dr. John Stockhausen 1
Defense Research Establishment Atlantic
Grove Street, P. O. Box 1012
Dartmouth, Nova Scotia, Canada B2Y3Z7

20. Chief of Naval Operations 1
OP-71
Attn: LCDR J. Woodbury
Code 714C
Washington, D. C. 20350-2000

21. Prof. Lawrence J. Ziomek, Code 62Zm 1
Department of Electrical and Computer Engineering
Naval Postgraduate School
Monterey, California 93943

Thesis
S2436
c.1

Schaaff
Monterey Bay acoustic tomography : signal processing using multi-channel data-synchronized quadrature phase demodulation.

Thesis
S2436
c.1

Schaaff
Monterey Bay acoustic tomography : signal processing using multi-channel data-synchronized quadrature phase demodulation.

AMERICAN BINDERY
TOPEKA KANSAS

thesS2436
Monterey Bay acoustic tomography : signa
3 2768 000 85915 1
DUDLEY KNOX LIBRARY